Magnetometry and Thermodynamic Studies of Anisotropic Honeycomb and Hyperhoneycomb Magnets



Kylie MacFarquharson

Keble College

University of Oxford

A thesis submitted for the degree of

Doctor of Philosophy

Trinity 2023

Acknowledgements

I would like to thank all of the people whose support and guidance made this thesis possible. In particular, my supervisor Radu Coldea, whose deep insight into the field has directed a great deal of my research over the past four years, and his attention to detail has encouraged me to complete projects I may have otherwise left unpolished. I would additionally like to thank Amalia Coldea for teaching me the wonderful torque magnetometry technique, and for her guidance on research more broadly.

The novel materials studied in this thesis were synthesised by Ryutaro Okuma. I would like to thank him for his vital contribution to the work, and for his perfectionism which led to the lovely single crystals reported in this thesis.

A number of other members of the quantum materials group, and especially those with whom I have shared an office, have kept me enjoying working on this project, and I would like to thank them for their entertaining and occasionally productive conversations, and I hope that at least one of them keeps up with the puzzles when I leave. In particular I would like to thank Matthew Pearce who worked very closely with me on a number of projects, and who provided me a great understanding of cryogenics, high magnetic field research, and experimental physics more broadly.

Much of the research published here was undertaken at EMFL high magnetic field facilities. I would like to thank those there who made that possible, including the instrument scientists who I worked with: Toni Helm and Yurii Skourski at HZDR Dresden, and Alix McCollam, Roos Leenen, and Uli Zeitler at HFML Nijmegen. As well as these I would like to thank all the others at the labs, who keep them running and administrate them to have them open for researchers like me to use. And I extend this thanks to the cryomagnetics group, and administrators at the University of Oxford for working behind the scenes to allow a research project like this to take place.

I would finally like to thank my family, friends, loved ones, crew-mates, and assorted parental figures who supported me emotionally, financially, or mechanically over the last four years.

The research reported in this thesis, as well as my graduate studentship funding were supported by a grant from the European Research Council under the European Union's Horizon 2020 research and innovation programme, Grant Agreement Number 788814 (EQFT), with my supervisor as Principal Investigator.

Abstract

This thesis presents results from high-sensitivity piezocantilever single-crystal torque magnetometry, magnetisation, and calorimetry measurements on the magnetically ordered phases of four related quantum magnetic materials, linked by their tricoordinated honeycomb and hyperhoneycomb magnetic sublattices and strong spin-orbit coupling.

The first two materials investigated, honeycomb α-Na_2PrO_3 , and its hyperhoneycomb polymorph β-Na_2PrO_3 , are candidates to display unconventional magnetic behaviour from bond-dependent Kitaev interactions. That these physics may occur in the $4f$ rare-earths has remained experimentally largely unexplored. In both cases, this is the first time high-quality single crystals of the material have been magnetically characterised.

In α-Na_2PrO_3 I find a sharp transition to long range order below $T_N = 4.6\,\mathrm{K}$, and strongly contrasting angular dependence of torque in three crystal planes, and show that this can be naturally explained by a canted antiferromagnetic structure. I also propose a minimal anisotropic exchange model, compatible with crystal symmetry, explaining the observed magnetic structure. Finally, I report torque magnetometry up to $35\,\mathrm{T}$, showing clear evidence of a spin-flop transition for certain orientations of the magnetic field, consistent with the minimal model and observe non-monotonic field dependence of crossover between spin-flop and paramagnetic phases.

In β-Na_2PrO_3 , I find a sharp transition to magnetic order below $T_N = 5.2\,\mathrm{K}$ and show torque magnetometry consistent with the four sublattice non-collinear magnetic structure found in neutron diffraction experiments. I explore the proposed bond-anisotropic minimal magnetic model with mean field calculations and show that it predicts a metamagnetic spin-flop transition for certain field orientations. Additionally, I report torque magnetometry up to $67\,\mathrm{T}$, finding the predicted field-driven phase transition at $26\,\mathrm{T}$ as well as a high-field transition to the polarised state.

The final two materials investigated in this thesis are the honeycomb transition metal titanates $CoTiO_3$ and $FeTiO_3$. These materials are isostructural with honeycomb layers of magnetic ions, ordering as an easy-plane and easy-axis antiferromagnet respectively. Previously published neutron scattering experiments found evidence for in-plane anisotropy in $CoTiO_3$, driven by a quantum zero-point fluctuation mechanism. In this thesis I use torque magnetometry to directly probe the in-plane anisotropy of both $CoTiO_3$ and $FeTiO_3$ and in both cases find clear evidence of six-fold clock anisotropy which cannot be attributed to single-ion anisotropy.

Contents

List of Figures **xi**

1 Introduction **1**

2 Introduction to Quantum Magnetism **3**
2.1 Origin of the Magnetic Moment 3
2.2 Paramagnetism 7
2.3 Interactions 8
2.4 Magnetic Order 9
2.5 Field Induced Phase Transitions 11
2.6 Frustration and Exotic Phases 14

3 Experimental Methods **21**
3.1 Linear Magnetometry 21
3.1.1 Overview 21
3.1.2 Vibrating Sample Magnetometry 22
3.1.3 Pulsed-Field Extraction Magnetometry 23
3.2 Torque Magnetometry 25
3.2.1 Overview 25
3.2.2 Theory 25
3.2.3 Experimental Approach 27
3.2.4 Example: Uniaxial Paramagnet 30
3.3 Heat Capacity 32
3.3.1 Overview 32
3.3.2 AC Calorimetry 35
3.4 X-ray Diffraction Crystallography 37
3.4.1 Overview 37
3.4.2 Experimental Details 39

4 General Optimisation Algorithm to Find Classical Magnetic Ground States **43**
4.1 Introduction 43
4.2 Example: Phase diagram of an Ising-like antiferromagnet on a square lattice for general orientation of magnetic field. 45
4.3 General formalism for multi-sublattice magnetic systems 51
4.4 Riemannian Optimisation Algorithm 55

5 Canted antiferromagnetic magnetic order in honeycomb α-Na_2PrO_3 revealed by single crystal torque measurements 63
5.1 Introduction . . . 64
5.2 Crystal Structure . . . 65
5.3 Single Ion Physics . . . 70
5.4 Previous Reports . . . 73
5.5 DC Field Torque Magnetometry up to 4T . . . 73
5.6 Magnetic Structure . . . 79
5.7 Exchange Parameters and Models . . . 83
5.8 Powder Magnetisation in Pulsed Field up to 60T . . . 91
5.9 DC Field Torque Magnetometry up to 35T . . . 93
5.10 Conclusions . . . 97

6 Magnetic order and high-field magnetic phase transitions in hyperhoneycomb β-Na_2PrO_3 103
6.1 Introduction . . . 104
6.2 Crystal Structure . . . 104
6.3 Single Ion Physics . . . 109
6.4 Heat Capacity . . . 111
6.5 DC Field Torque Magnetometry up to 16T . . . 112
6.6 Magnetic Structure . . . 117
6.7 Candidate Spin Hamiltonians . . . 125
6.7.1 Minimal $J\Gamma\Gamma'$ model . . . 127
6.7.2 $JK\Gamma$ model . . . 135
6.8 Pulsed-Field Torque Magnetometry up to 67T . . . 137
6.9 DC Field Torque Magnetometry up to 35T . . . 147
6.10 Pulsed-Field Magnetisation up to 67T . . . 151
6.11 Discussion/Conclusions . . . 152

7 Six-fold clock-anisotropy in honeycomb titanates $CoTiO_3$ and $FeTiO_3$ 157
7.1 Six-Fold Clock Anisotropy in $CoTiO_3$ . . . 158
7.1.1 Crystal Structure of $CoTiO_3$ . . . 158
7.1.2 Single Ion Physics of Co^{2+}in $CoTiO_3$ . . . 160
7.1.3 Magnetic Structure of $CoTiO_3$ . . . 163
7.1.4 Exchange Interactions and Magnetic Anisotropy . . . 163
7.1.5 Single Crystal Vibrating Sample Magnetometry studies of $CoTiO_3$ 169
7.1.6 Single Crystal Torque Magnetometry Studies of $CoTiO_3$ . . . 172
7.2 Six-Fold Clock Anisotropy in $FeTiO_3$ . . . 184
7.2.1 Single ion physics of Fe^{2+}ions in $FeTiO_3$ . . . 185
7.2.2 Torque magnetometry studies of $FeTiO_3$ . . . 188
7.3 Conclusions . . . 195

8 Concluding Remarks **197**

Appendices

A Appendix - Magnetic order and high-field magnetic phase transitions in hyper-honeycomb β-Na_2PrO_3 **201**

A.1 Character tables 201

List of Figures

2.1 Schematic diagram showing a Néel order antiferromagnet on a square lattice. 10
2.2 Phase diagram of uniaxial anisotropic antiferromagnets. 13
2.3 $JK\Gamma$ phase diagram for honeycomb and hyperhoneycomb lattices. . . . 16

3.1 Schematic view of torque cantilever 27
3.2 Photographs of piezoresistive and capacitive torque cantilevers 29
3.3 Calculated angular dependence of energy and torque for uniaxial paramagnet. 31
3.4 Plots showing Landau free energy, entropy, and heat capacity for first and second order phase transitions 34
3.5 Schematic showing heat capacity probe 36

4.1 Schematic diagram showing a Néel order antiferromagnet on a square lattice. 45
4.2 Phase diagram showing magnetisation for XXZ model. 49
4.3 Field dependence of magnetisation and torque for XXZ model. 50
4.4 Schematic showing some properties of the spherical S^2 manifold. . . . 58

5.1 X-ray diffraction pattern and crystal morphology of α-Na_2PrO_3 66
5.2 Observed vs calculated Bragg peak intensities. 68
5.3 Model showing the crystal structure of α-Na_2PrO_3 69
5.4 Schematic diagram showing the level splitting of an isolated Pr^{4+}ion. . 71
5.5 Angular and temperature dependence of torque in the $\boldsymbol{ac}$ plane. 74
5.6 Angular dependence of torque in the $\boldsymbol{ac}$ plane showing both rotation directions. 75
5.7 Angular and field dependence of magnetic torque of α-Na_2PrO_3 in the $\boldsymbol{ac}$ plane. 76
5.8 Angular dependence of magnetic torque in $\boldsymbol{ab}$ plane. 78
5.9 Angular dependence of magnetic torque in $\boldsymbol{bc}^*$ plane. 80
5.10 Model showing the proposed magnetic structure of α-Na_2PrO_3 in the monoclinic setting. 83
5.11 Schematic showing honeycomb bonds in the basal plane of α-Na_2PrO_3 . 84
5.12 Calculation of angular dependence of magnetic torque in orthogonal crystal planes. 86
5.13 Calculated field dependence of single crystal magnetisation. 88
5.14 Calculated phase diagram of α-Na_2PrO_3 89

5.15 Calculated field dependence of powder magnetisation. 90
5.16 Measured field dependence of powder magnetisation of α-Na_2PrO_3 . . . 92
5.17 Field dependence of magnetic torque up to 35T. 94
5.18 Field dependence of thermometer calibration. 95
5.19 Temperature dependence of torque close to $\boldsymbol{H} \sim\parallel \boldsymbol{c}^*$ 96

6.1 Single crystal X-ray diffraction pattern OF β-Na_2PrO_3 105
6.2 Observed vs calculated Bragg peak intensities for β-Na_2PrO_3 106
6.3 Model showing the crystal structure of β-Na_2PrO_3 107
6.4 Schematic diagram showing level splitting of an isolated Pr^{4+}ion. . . . 109
6.5 Temperature dependence of heat capacity at 0T and 16T 110
6.6 Angular dependence of torque and fitted temperature dependence amplitude parameter for rotations in $\boldsymbol{ac}$ plane and $\boldsymbol{bc}$ planes. 113
6.7 Angular dependence of torque and fitted temperature dependence amplitude parameter for rotations in $\boldsymbol{ab}$ plane. 116
6.8 Models showing magnetic basis vectors. 118
6.9 Model showing fitted magnetic structure. 124
6.10 Field dependence of magnetic basis vector components for proposed $J\Gamma\Gamma'$ model. 128
6.11 Calculated trace of the differential susceptibility tensor for proposed $J\Gamma\Gamma'$ model. 129
6.12 Field dependence of torque components for proposed $J\Gamma\Gamma'$ model. . . . 132
6.13 Field dependence of torque amplitude in $\boldsymbol{ac}$ plane and magnetisation along crystal axes. 134
6.14 Calculated trace of the differential susceptibility tensor for alternative $J\Gamma\Gamma'$ model. 135
6.15 Field dependence of magnetic basis vector components for $JK\Gamma$ model. 136
6.16 Photograph showing mounted β-Na_2PrO_3 crystal on piezoresistive cantilever. 138
6.17 Field dependence of torque for $\boldsymbol{H} \parallel \boldsymbol{a}$ 139
6.18 Field and temperature dependence of torque for $\boldsymbol{H} \parallel \boldsymbol{a}$ 140
6.19 Field and angle dependence of torque for $\boldsymbol{H} \sim\parallel \boldsymbol{a}$ 141
6.20 Field and temperature dependence of torque for $\boldsymbol{H} \sim\parallel \boldsymbol{b}$ 142
6.21 Field and angle dependence of torque for field in $\boldsymbol{bc}$ plane. 144
6.22 SEM image of β-Na_2PrO_3 crystal and torque in $\boldsymbol{ab}$ plane 145
6.23 Field and angle dependence of torque for field in $\boldsymbol{ab}$ plane. 146
6.24 DC Field - field and temperature dependence of torque for field in $\boldsymbol{ab}$ plane. 148
6.25 Colour plot showing derivative of torque with field $\frac{\partial \tau}{\partial H}$ for fields in the $\boldsymbol{ab}$ planes. 149

6.26 DC Field - field and temperature dependence of torque for field in $\boldsymbol{ac}$ plane, close tp $\boldsymbol{H} \parallel \boldsymbol{a}$. 150
6.27 Co-aligned β-Na_2PrO_3 crystals for magnetisation measurements. 151

7.1 Model showing crystal structure of $CoTiO_3$ 158
7.2 Calculated Bragg peak intensities for two structural domains of $CoTiO_3$. 160
7.3 Schematic diagram showing the level splitting of isolated Co^{2+}ion. . . . 162
7.4 Model showing magnetic unit cell of $CoTiO_3$ 164
7.5 Calculated angular dependence of effective site anisotropy energy. . . . 168
7.6 Temperature dependence of susceptibility and inverse susceptibility in $CoTiO_3$ 170
7.7 Field dependence of magnetisation and susceptibility in $CoTiO_3$ 172
7.8 Photographs of $CoTiO_3$ single crystals mounted on piezocantilever. . . . 173
7.9 Angular dependence of magnetic torque in ac plane 174
7.10 Fitted torque amplitudes against predicted torque amplitudes in $CoTiO_3$. 175
7.11 Angular and field dependence of magnetic torque in $CoTiO_3$ $\boldsymbol{ab}$ plane. . 177
7.12 Field dependence of fitted torque components in $CoTiO_3$ $\boldsymbol{ab}$ plane. . . . 178
7.13 Angular dependence of magnetic torque for select fields in $CoTiO_3$ $\boldsymbol{ab}$ plane. 179
7.14 Field dependence of calculated total anisotropy energy. 180
7.15 Angular dependence of magnetic torque in $\boldsymbol{ab}$ plane with calculation. . 182
7.16 Previously published Temperature dependence of susceptibility in $FeTiO_3$ 185
7.17 Schematic diagram showing the level splitting of isolated Fe^{2+}ion . . . 187
7.18 Photograph of $FeTiO_3$ single crystals mounted on piezocantilever. . . . 188
7.19 Angular and temperature dependence of magnetic torque in $\boldsymbol{a^*c}$ plane of $FeTiO_3$ 189
7.20 Fitted torque amplitudes against predicted torque amplitudes in $FeTiO_3$. 189
7.21 Angular dependence of magnetic torque in $\boldsymbol{ab}$ plane of $FeTiO_3$ alongside calculation. 191
7.22 Field dependence of fitted torque amplitudes in $\boldsymbol{ab}$ plane. 192
7.23 Angular and temperature dependence of magnetic torque in $\boldsymbol{ab}$ plane of $FeTiO_3$ and temperature dependence of fitted torque amplitudes. 194

1 Introduction

This thesis reports research into magnetic structures of periodic crystals where the magnetic ions exist on tricoordinated honeycomb or hyper-honeycomb lattices. The primary experimental technique used to study these materials is piezocantilever torque magnetometry, many of the experiments reported were performed in the Clarendon Laboratories at the University of Oxford. However, in order to access stronger magnetic fields, additional experiments were performed alongside instrument scientists at the European Magnetic Field Lab facilities: HFML Nijmegen in The Netherlands and HZDR Dresden in Germany. Alongside these torque magnetometry results, I report data from other techniques such as X-ray diffraction for crystal structure, AC calorimetry to study heat capacity anomalies in phase transitions, and both single-crystal and powder magnetisation. I support these experimental results with mean-field calculations of the response of the magnetic systems to applied magnetic field.

In the following Chapter 2 of this thesis I introduce the basics of quantum magnetism, to provide an overview of the motivation for this research. This starts with an explanation of the origin of the magnetic moment in isolated magnetic ions, followed by an explanation of how these magnetic ions interact and stabilise magnetic order at low temperatures. Finally, the so-called J, K, Γ model on a honeycomb or hyper-honeycomb lattice is explored to motivate the materials investigated in this thesis.

This is followed by explanations of each of the experimental methods used in this project. As well as these, Chapter 4 introduces and explains the Riemannian optimisation algorithm used for the mean-field calculations reported later in the thesis.

The final three chapters report experimental results. Firstly, the Kitaev-candidate honeycomb magnet α-Na_2PrO_3 is reported, starting from structure using X-ray diffraction of single-crystals. This is followed by the single-crystal physics of the Pr^{4+}ions and a discussion of the previously published data on powder samples. I then report torque magnetometry in three orthogonal rotation planes, and up to $35\,\mathrm{T}$, revealing a canted antiferromagnetic structure for the first time. This is accompanied by calculations to support a minimal model to stabilise this magnetic structure.

The next material reported is the hyper-honeycomb polymorph of the same material, β-Na_2PrO_3 . This chapter reports torque magnetometry and AC calorimetry revealing magnetic ordering below $5.2\,\mathrm{K}$. This is followed by a discussion of the magnetic structure revealed by currently unpublished neutron diffraction studies, and an exploration of Hamiltonians which could stabilise the reported magnetic structure. Finally, I report torque magnetometry up to $65\,\mathrm{T}$, revealing high magnetic field phase transitions.

The final results chapter reports torque magnetometry in isostructural honeycomb antiferromagnets $CoTiO_3$ and $FeTiO_3$. These follow recently published results which predict a 6-fold clock anisotropy in easy-plane $CoTiO_3$ from analysis of inelastic neutron scattering (INS) data. With high resolution torque magnetometry I find clear direct evidence for such clock anisotropy, and am able to estimate the energy scale of the effect to within the same order of magnitude as the estimate from INS data. This is followed by the same treatment for easy-axis $FeTiO_3$, which finds the same effect with a much larger energy scale. In both cases, single-ion anisotropy can be rejected as the origin, and I discuss possible origins of the effect.

2

Introduction to Quantum Magnetism

2.1 Origin of the Magnetic Moment

In an insulator, the electrons on each ion are localised in orbitals around the ion. These electrons can be treated as moving in a spherically symmetric potential from the nucleus, and interacting with every other electron in the ion. This system has an electronic ground state configuration consisting of degenerate energy levels E_{nl} with quantum numbers n, l such that $l < n$ and degeneracy $2(2l+1)$. These make up shells, which fill from lowest energy to form an overall energy configuration.

For each electron in the ion, spin and orbital angular momentum operators can be defined $\hat{\boldsymbol{s}}$ and $\hat{\boldsymbol{l}}$ respectively. These contribute to a magnetic moment, the operator of which can be defined

$$\hat{\boldsymbol{\mu}}_e = \mu_B \left(g_l \hat{\boldsymbol{l}} + g_s \hat{\boldsymbol{s}} \right) \tag{2.1}$$

where $g_l = 1$, $g_s = 2 + \mathcal{O}(\alpha)$ including additional contributions from the fine-structure constant $\alpha \approx {}^1/_{137}$.

For the ion, total spin and angular momentum operators can be defined

$$\hat{\boldsymbol{S}} = \sum_i \hat{\boldsymbol{s}}_i \tag{2.2}$$

$$\hat{\boldsymbol{L}} = \sum_i \hat{\boldsymbol{l}}_i \tag{2.3}$$

and so can a total magnetic moment operator

$$\hat{\boldsymbol{\mu}} = \mu_B \left(g_l \hat{\boldsymbol{L}} + g_s \hat{\boldsymbol{S}} \right) \tag{2.4}$$

For every full shell in the electronic configuration, the angular momenta and spins sum to zero, so they do not contribute to the total spin or orbital angular momentum for the ion. Instead, the only electrons which contribute are those in partially filled electron shells. Because of this, reported electronic configurations normally specify just the outermost, partially filled (valence) shell of electrons. For example, the Co^{2+}ion has a $3d^7$ valence shell, specifying that there are 7 electrons in the $n = 3, l = 2$ outermost shell. As free ions are spherically symmetric, the energy cannot change under a rotation. The degenerate ground state manifold is then best described by quantum numbers L, S such that $\hat{\boldsymbol{L}} \cdot \hat{\boldsymbol{L}} \left|\phi_{L,S}\right\rangle = L(L+1) \left|\phi_{L,S}\right\rangle$ and similarly with S. These manifolds of states with a given L, S have degeneracies $(2L+1)(2S+1)$.

If the electrons in the outermost valence shell are treated as non-interacting, all the combinations of L and S will be degenerate in energy. A more realistic treatment to find the ground state L and S manifold is called Hund's rules [1–3]. This specifies that (1): S will be maximised, and (2): given (1) L will be maximised. The third rule includes spin-orbit coupling which is treated separately here. In the Co^{2+}example, this results in an $L = 3$, $S = {}^3\!/_2$, 28-fold degenerate ground state, ignoring spin-orbit coupling.

The next leading order perturbation considered is a relativistic correction to the energy levels, spin-orbit coupling (SOC). SOC adds a contribution to the energy

$$\hat{\mathcal{H}}_{\text{SO}} = \lambda \hat{\boldsymbol{L}} \cdot \hat{\boldsymbol{S}} \tag{2.5}$$

where the spin-orbit coupling constant λ is positive for shells less than half full, and negative for shells more than half full. If a total angular momentum operator is defined

$$\hat{\boldsymbol{J}} = \hat{\boldsymbol{L}} + \hat{\boldsymbol{S}} \tag{2.6}$$

with quantum number J, defined similarly to L and S. $\hat{\boldsymbol{J}}$ commutes with the spin-orbit Hamiltonian, so J is a good quantum number, while L and S are not. This splits the L, S manifolds of states into $J = |L-S|, |L-S|+1, \ldots, L+S$ multiplets, each with degeneracy $2J+1$. In the Co^{2+}example, $\lambda < 0$ and the ground state is $J = L + S = {}^9\!/_2$ with additional multiplets at $J = {}^7\!/_2, {}^5\!/_2, {}^3\!/_2$ in increasing order of energy.

The total magnetic moment operator can be written in terms of this new total angular momentum operator as

$$\hat{\boldsymbol{\mu}} = \mu_B g_J \hat{\boldsymbol{J}} \tag{2.7}$$

where g_J is the Landé g-factor [4] which evaluates as

$$g_J \approx \frac{3}{2} + \frac{S(S+1) - L(L+1)}{J(J+1)} \tag{2.8}$$

Note that the time-reversal symmetry of the Hamiltonian enforces $\langle \hat{\boldsymbol{\mu}} \rangle = 0$ over any degenerate multiplet of states. The moment $\hat{\boldsymbol{\mu}}$ couples to a magnetic field by the Zeeman energy

$$\hat{\mathcal{H}}_{\text{Zeeman}} = -\hat{\boldsymbol{\mu}} \cdot \boldsymbol{B} \tag{2.9}$$

which is sufficient to break the symmetry and produce a non-zero moment, even for an infinitesimally small field B.

This gives the free-ion ground state, however in crystals the electrons in the ion will feel an electrostatic potential which is not spherically symmetric. In general, the continuous spherical symmetry will be broken into discrete symmetries, depending on the point group symmetry of the ion. This will typically lift the degeneracy of the multiplets of states. In some cases, this can be treated as a perturbation on the spin-orbit ground state. However, in all the systems of interest in this thesis, it at least comparably strong to the SOC. The additional contribution from the crystal environment is called the crystal-electric field (CEF), and its energy contribution can be written in terms of Stevens operators O_k^q [5]

$$\hat{\mathcal{H}}_{\text{CEF}} = \sum_{k \in \{2,4,6\}} \sum_{q=-k}^{k} B_k^q O_k^q \tag{2.10}$$

where the coefficients B_k^q are constrained by the point group symmetry of the environment. For example, in a cubic octahedral O_h environment the only non-zero terms are $B_4^0, B_4^4, B_6^0, B_6^0$ under the constraints $B_4^4 = 5B_4^0$, $B_6^4 = -21B_6^0$ [5, 6]. This means that the octahedral crystal field (OCF) CEF Hamiltonian can be written as

$$\mathcal{H}_{\text{OCF}} = B_4^0(O_4^0 + 5O_4^4) + B_6^0(O_6^0 - 21O_6^4) \tag{2.11}$$

These Stevens operators are caused by an energy dependence on the orbitals involved in the state. This comes from the interactions between these orbitals and the crystal environment, for example an octahedral environment of O^{2-}ions as is seen in all the materials of interest in this thesis. The electronic states whose wave-functions have large overlap with the oxygen ions develop a higher energy than the electrons with a smaller overlap, which lifts the degeneracy of the free ion multiplet. Because this effect is dependent only on the orbital degree of freedom, the Stevens operators can be written in terms of only polynomials of the orbital angular momentum operators $\hat{L}_z, \hat{L}_+, \hat{L}_-$. For example

$$O_4^0 = \hat{L}_z^4 - (30L(L+1) - 25)\hat{L}_z^2 + (3L^2(L+1)^2 - 6L(L+1))\mathbb{I} \tag{2.12}$$

$$O_4^4 = \frac{1}{2}(\hat{L}_+^4 + \hat{L}_-^4) \tag{2.13}$$

where $\mathbb{I}$ is the identity operator. These operators are straightforward to compute [7] and are tabulated up to $k = 6$ [5, 8]. In all of the systems investigated in this thesis, the most straightforward approach to including both SOC and the CEF is numerically, computing the Hamiltonian and diagonalising to give the energy levels. Frequently, an effective angular momentum j_{eff} will be defined for the resulting ground state multiplet. This is defined such that the degeneracy of this multiplet is $2j_{\text{eff}} + 1$. The g-factor of this multiplet can be defined in terms of the moment operator by taking the limit of a small magnetic field (here along a nominal $\boldsymbol{z}$ axis)

$$g = \lim_{B \to 0} \frac{|\langle \hat{\mu_z} \rangle|}{\mu_B j_{\text{eff}}} \tag{2.14}$$

where the expectation value $\langle \hat{\mu_z} \rangle$ is the expectation of the ground state, once a small field has been applied along the $\boldsymbol{z}$ axis. This means that the magnetic moment has the same form as the free-ion case

$$\hat{\boldsymbol{\mu}}_z = \mu_B g \hat{\boldsymbol{j}}_{\text{eff}}^z \tag{2.15}$$

Given some ground state multiplet with non-zero g a magnetic field $\boldsymbol{B} = B\hat{\boldsymbol{z}}$ applied parallel to the $\hat{\boldsymbol{z}}$ axis will be split by the Zeeman Hamiltonian (2.9)

$$\hat{\mathcal{H}}_{\text{Zeeman}} = -\hat{\boldsymbol{\mu}} \cdot \boldsymbol{B} \tag{2.16}$$

$$= -\mu_B g B \hat{j}_{\text{eff}}^z \tag{2.17}$$

This splits the multiplet into $2j_{\text{eff}} + 1$ separate levels described by the $\hat{j}^z_{\text{eff}}$ eigenvalue $m \in \{-j_{\text{eff}}, -j_{\text{eff}} + 1, \ldots, j_{\text{eff}}\}$. These levels have a magnetic moment $\mu_z = \mu_B g m$, and energy $E_m = -\mu_B g m B$.

Note that the g-factor is not isotropic in general. This extension can be included by defining a g-factor tensor $\mathbb{G}$ such that

$$\hat{\boldsymbol{\mu}} = \mu_B \mathbb{G} \hat{\boldsymbol{j}}_{\text{eff}} \tag{2.18}$$

which is used frequently later in the thesis.

2.2 Paramagnetism

Given a collection of isolated (non-interacting) magnetic moments, the behaviour in finite temperature can be described by statistical mechanics. For the sake of brevity, j_{eff} here is written as j. Given the energy splittings above, the partition function [9] can be written

$$Z = \sum_m \exp(m\beta g \mu_B B) \tag{2.19a}$$

$$= \sum_m \exp(mx) \tag{2.19b}$$

where $x \coloneqq \beta g \mu_B B$ and $\beta = \frac{1}{k_B T}$. From this, the expectation value of m can be written

$$\langle m \rangle = \frac{1}{Z} \sum_m m \exp(mx) \tag{2.20a}$$

$$= \frac{1}{Z} \frac{\partial Z}{\partial x} = \frac{\partial \ln Z}{\partial x} \tag{2.20b}$$

$$= j B_j(jx) \tag{2.20c}$$

where $B_j(jx)$ is the Brillouin function [10]. This shows that in the large-field, low-temperature limit $\beta B \to \infty$, the expectation value $\langle m \rangle \to j$. In the inverse high temperature case, $\beta B \to 0$ this expectation tends towards zero. The expectation value of the moment is then $\langle \mu_z \rangle = g \mu_B \langle m \rangle$. This expression itself gives the behaviour of the magnetic moment in a small field and finite temperature. One commonly measured observable is the temperature dependent magnetic susceptibility χ, defined as

$$\chi \coloneqq \lim_{B \to 0} \frac{n \mu_0 \langle \mu_z \rangle}{B} \tag{2.21}$$

$$= \frac{n \mu_0 \mu^2_{\text{eff}}}{3 k_B T} \tag{2.22}$$

for number density n and *effective* moment $\mu_{\text{eff}}^2 = g^2\mu_B^2 j(j+1)$. This is a Curie relationship [3].

In real materials, there are additional multiplets at higher energies. The most straightforward way of computing their effect on the temperature dependent magnetisation is to numerically compute the Hamiltonian, including SOC, CEF, and Zeeman terms, and to then diagonalise and compute the expectation value of the moment operator over all of the energy levels. Fitting this to experimental data can be used to determine the values of spin-orbit coupling and crystal-electric-field parameters.

2.3 Interactions

In a crystal at low temperatures, the interactions between magnetic ions become important to understand how the material orders magnetically. For the sake of convention, the effective angular momentum operators are written $\hat{\boldsymbol{S}}_i$. The canonical minimal example of an interaction term between spins i, j is the Heisenberg interaction, which can originate as an exchange energy from the Coulomb repulsion of the electrons, when combined with the Pauli exclusion principle. The Heisenberg Hamiltonian can be written

$$\hat{\mathcal{H}} = \frac{1}{2}\sum_{i,j} J_{ij}\hat{\boldsymbol{S}}_i \cdot \hat{\boldsymbol{S}}_j \tag{2.23}$$

where J_{ij} is the exchange term between spins i, j, and the half is needed as each bond is summed over twice. Terms with $J_{ij} < 0$ prefer spins i, j to be parallel i.e. ferromagnetic; $J_{ij} > 0$ prefers spins to be antiparallel i.e. antiferromagnetic.

The Heisenberg Hamiltonian is completely isotropic, it only favours a relative orientation of spins. In general, interactions can come from higher order processes such as superexchange and can be anisotropic, depending on the symmetry of the bond. At second-order perturbation theory these will come about as bilinear terms in the spin operators, and can be written in the most general form as

$$\hat{\mathcal{H}} = \sum_{\langle i,j\rangle}\sum_{\alpha\beta} J_{ij}^{\alpha\beta}\hat{S}_i^{\alpha}\hat{S}_j^{\beta} \tag{2.24}$$

where the sum over $\langle i, j\rangle$ indexes each bond only once, and $\alpha, \beta \in \{x, y, z\}$. This means that the bilinear interaction on each bond is given as a tensor $J_{ij}^{\alpha\beta}$. This can capture common anisotropic interactions such as XXZ

$$\hat{\mathcal{H}}_{\text{XXZ}}^{ij} = J_{ij}\left(\hat{S}_i^x \hat{S}_j^x + \hat{S}_i^y \hat{S}_j^y + \Delta \hat{S}_i^z \hat{S}_j^z\right) \tag{2.25}$$

which is sufficient to prefer a particular axis. If $\Delta > 1$, this is called an easy-axis or Ising-type XXZ interaction, otherwise if $\Delta < 1$ this is an easy-plane interaction.

Another important type of interaction which appears in this thesis, is Dzyaloshinskii–Moriya interaction (DMI), or antisymmetric exchange. This has the form

$$\hat{\mathcal{H}}_{\text{DMI}}^{ij} = \boldsymbol{D}_{ij} \cdot \left(\hat{\boldsymbol{S}}_i \times \hat{\boldsymbol{S}}_j\right) \tag{2.26}$$

and can also be written as an antisymmetric component to the $J_{ij}^{\alpha\beta}$ interaction tensor. This type of interaction is antisymmetric under swapping of the two spins. This means that if DMI is present, the interaction tensor has to be specified on a *directed* bond.

A particular model of interest is the Kitaev model [11] on a honeycomb lattice with

$$\hat{\mathcal{H}}_{\text{Kitaev}} = \sum_{\langle i,j\rangle\gamma} K \hat{S}_i^\gamma \hat{S}_j^\gamma \tag{2.27}$$

where $\langle i, j\rangle$ indexes over nearest-neighbour honeycomb bonds and $\gamma \in \{x, y, z\}$ is dependent on the bond direction. This model is discussed more in a later section.

The origin of the anisotropy seen in each of these cases is the anisotropy of the electronic orbitals in the crystal. In order to couple this to the spin degrees of freedom, the spin must be coupled to the orbital levels. This means that spin-orbit coupling is a requirement for anisotropic interactions.

2.4 Magnetic Order

In an ideal paramagnetic phase, in the low-field limit, every level in the degenerate multiplet with degeneracy $2j+1$ will be populated equally. This will result in an entropy of

$$S = k_B \ln(2j + 1) \tag{2.28}$$

per particle. As the temperature of the system approaches zero, the effect of interactions becomes more dominant, and in conventional magnetic materials the system will undergo a symmetry-breaking phase transition from the high-temperature paramagnetic state to a low-temperature ordered state with zero entropy at $T = 0$ (in the limit of large systems).

For example, in the ferromagnetic $J < 0$ Heisenberg system, time-reversal symmetry will be broken at the ordering temperature to produce a ferromagnet. This will have magnetisation as the order parameter for the transition.

In general, finding the quantum mechanical ground state for a system of many interacting spins and some specified interaction Hamiltonian is not straightforward or necessarily even feasible. An often fruitful approach is to consider the mean-field approximation, where spins are treated as classical vectors of fixed length S, replacing the operators S^x, S^y, S^z with their expectation values.

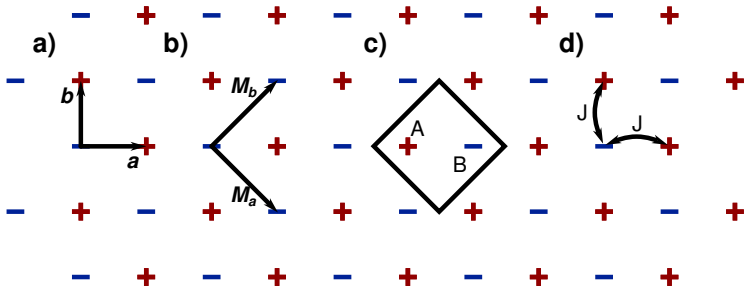


Figure 2.1: Schematic diagram showing a Néel order antiferromagnet on a square lattice. Red plus '+' symbols indicate spins along the $+z$ axis, out of the page. Blue minus '-' symbols indicate spins along the $-z$ axis, into the page. Overlaid diagrams show **a)** primitive lattice vectors $\boldsymbol{a}$, $\boldsymbol{b}$, **b)** magnetic unit cell lattice vectors $\boldsymbol{M}_a$, $\boldsymbol{M}_b$, **c)** magnetic unit cell outline with labelled sublattices A and B, and **d)** nearest-neighbour exchange path J.

In a crystal, the locations of the individual spins can be described by a Bravais lattice. For example, consider the square lattice, with only nearest-neighbour Heisenberg-type antiferromagnetic couplings. The energy on every bond can be minimised by setting every adjacent bond antiparallel, as is seen in Figure 2.1. This is known as Néel order [12], and breaks both time-reversal and translational symmetry. There is a new, magnetic unit cell, twice as large as the structural unit cell. An equivalent Néel order state will occur on any such bipartite model with only nearest-neighbour antiferromagnetic Heisenberg interactions.

In a more general case, rather than attempting to specify the spin orientation on every site on a crystal, magnetic orders can be described more succinctly in reciprocal space. This means that the spin on lattice vector $\boldsymbol{p}$ can be written in terms of Fourier components:

$$\boldsymbol{S_p} = \sum_{\boldsymbol{q}} \tilde{\boldsymbol{S}}_{\boldsymbol{q}} e^{2\pi i \boldsymbol{q}\cdot\boldsymbol{p}} \tag{2.29}$$

While in general, there are as many $\boldsymbol{q}$ vectors for which $\tilde{\boldsymbol{S}}_{\boldsymbol{q}}$ has to be specified as there are sites in the crystal, magnetic structures order periodically, so only a small number of these are non-zero. In many cases, only one $\tilde{\boldsymbol{S}}_{\boldsymbol{q}}$ is non-zero and the $\boldsymbol{q}$ where this occurs is referred to as the propagation vector of the magnetic order. In the square lattice Néel order example above, $\boldsymbol{S_p} = S\hat{\boldsymbol{z}}\cos\pi(p_x + p_y)$ so the system has $\boldsymbol{q} = (1/2, 1/2)^T$. There is no need in general for this $\boldsymbol{q}$ to be rational; if it is irrational the magnetic order is described as *incommensurate*. All the materials investigated in this thesis order as commensurate magnetic structures, so the magnetic unit cell is an integer multiple of the primitive structural unit cell.

2.5 Field Induced Phase Transitions

An interesting feature in many ordered systems is the presence of field-induced phase transitions. This occurs because the magnetic field couples to the Hamiltonian of the system through the Zeeman energy [13]

$$\hat{\mathcal{H}}_{\text{Zeeman}} = -\mu_B \sum_{i\mu\nu} \mathbb{G}^{\mu\nu} B^{\mu} S_i^{\nu} \tag{2.30}$$

where the g-factor tensor $\mathbb{G}$ allows for anisotropic g-factors, with arbitrary principal axes.

The most straightforward example of a field-induced transition is the transition to polarisation in a two-sublattice Heisenberg antiferromagnet. This has the Hamiltonian

$$\hat{\mathcal{H}} = J \sum_{\langle i,j \rangle} \boldsymbol{S}_i \cdot \boldsymbol{S}_j - \mu_B \sum_{i\mu\nu} g B^z S_i^z \tag{2.31}$$

where the magnetic field is chosen to apply along the $\boldsymbol{z}$ axis, and $\langle i, j \rangle$ selects nearest-neighbour bonds. Treating the spins as classical vectors, this can be rewritten in terms of sublattice magnetisations $\boldsymbol{S}_A$, $\boldsymbol{S}_B$ as

$$\mathcal{H} = nJ\boldsymbol{S}_A \cdot \boldsymbol{S}_B - g\mu_B B(S_A^z + S_B^z) \tag{2.32}$$

with n as the number of nearest-neighbours for each site. Taking the sublattice magnetisations $\boldsymbol{S}_A$, $\boldsymbol{S}_B$ as unit vectors, and defining parameters $\boldsymbol{A} = \frac{1}{2}(\boldsymbol{S}_A - \boldsymbol{S}_B)$, $\boldsymbol{F} = \frac{1}{2}(\boldsymbol{S}_A + \boldsymbol{S}_B)$ with the constraints $\boldsymbol{A} \cdot \boldsymbol{F} = 0$, $\boldsymbol{A}^2 + \boldsymbol{F}^2 = 1$, this can be rewritten as

$$\mathcal{H} = nJ - 2nJ\boldsymbol{A}^2 - 2g\mu_B B F_z \tag{2.33}$$

In this system with isotropic interactions, the ordered $\boldsymbol{A}$ vector can be chosen to be perpendicular to the field, in this example parallel to the $\boldsymbol{x}$ direction. As the magnetic field increases, so does F_z, and the spins cant towards the field. If the field is large enough, $A_x \ll 1$ and $F_z = \sqrt{1 - A_x^2} \approx 1 - \frac{1}{2}A_x^2 - \frac{1}{8}A_x^4 - \mathcal{O}(A_x^6)$ so the energy can be written as

$$\mathcal{H} \approx \mathcal{H}_0 - (2nJ - g\mu_B B)A_x^2 + \frac{1}{4}g\mu_B B A_x^4 + \mathcal{O}(A_x^6) \tag{2.34}$$

where $\mathcal{H}_0$ is a constant. This Hamiltonian can be understood in terms of Landau theory [14] to undergo a second order phase transition at $g\mu_B B_{\mathrm{P}} = 2nJ$ to a high-symmetry polarised $A_x = 0, F_z = 1$ phase for $B > B_{\mathrm{P}}$. This causes an anomaly in the differential susceptibility $-\dfrac{\partial^2 \mathcal{H}}{\partial B^2}$, which can be experimentally detected straightforwardly.

In the presence of magnetic anisotropy, there can be more complex magnetic phase transitions. Two simple examples include uniaxial anisotropy: easy-axis XXZ exchange anisotropy

$$\mathcal{H}_{\mathrm{XXZ}} = nJ(S_A^x S_B^x + S_A^y S_B^y + \Delta S_A^z S_B^z) - g\mu_B B(S_A^z + S_B^z) \tag{2.35}$$

and single-ion easy axis $-DS_z^2$ anisotropy

$$\mathcal{H}_{\mathrm{D}} = nJ\boldsymbol{S}_A \cdot \boldsymbol{S}_B - D({S_A^z}^2 + {S_B^z}^2) - g\mu_B B(S_A^z + S_B^z) \tag{2.36}$$

In both cases at low field the system orders into an A_z antiferromagnetic order along the $\boldsymbol{z}$ axis, which has a lower energy than A_x or A_y. Figure 2.2 shows the phase diagrams for the two cases, with magnetic field applied along the unique $\boldsymbol{z}$ axis. As field is increases, the ability to cant towards field lowers the energy of the (A_x, F_z) phase. At some point the energy of this phase is lower than the A_z state and the system undergoes a first-order magnetic phase transition called a spin-flop [12, 15, 16]. In the case of $-DS_z^2$ type anisotropy, if D is sufficiently large, the system will undergo a spin-flip transition from

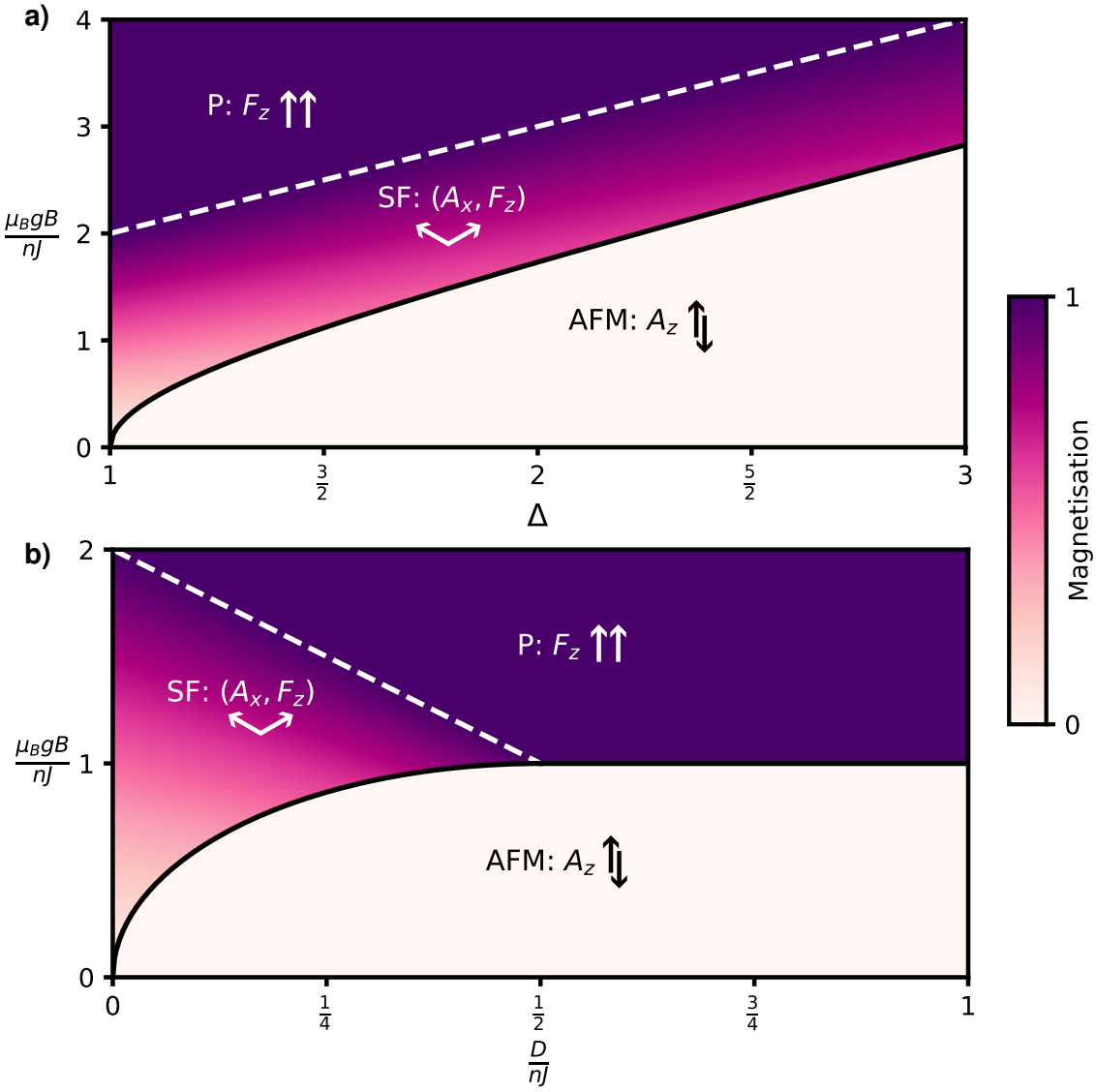


Figure 2.2: Phase diagram showing magnetisation, and phase boundaries of AFM, spin-flop (SF), and polarised (P) phases of **a)** XXZ Ising-type **b)** $-DS_z^2$ type uniaxial anisotropic antiferromagnets. Magnetic field is applied along the unique axis, labelled z. Solid and dashed lines indicate first and second order phase transitions respectively. Overlaid arrows indicate sublattice spin orientations. Phases are labelled with the magnetic basis vector contents as defined in the text.

A_z to F_z directly, without undergoing a spin-flop transition. Both spin-flop [17] and spin-flip [18] phase transitions have been realised in many materials experimentally.

More complex magnetic models can undergo a large variety of phase transitions in field. When these transitions are experimentally observed, this can reveal what model is governing the material's behaviour, and allow our understanding of fundamental theory to be tested. In frustrated magnetic systems, introduced next section, magnetic fields can induce transitions to many kinds of unconventional magnetically ordered phases. A large number of interesting field-induced phase transitions have been observed experimentally such as in α-$RuCl_3$ [19–21], polymorphs of Li_2IrO_3 [22, 23], triangular lattice antiferromagnet $2H$-$AgNiO_2$ [24], and Ising-chain $CoNb_2O_6$ [25].

2.6 Frustration and Exotic Phases

In many materials, it is not possible to minimise the energy on every bond simultaneously; when this is the case, the system is described as *frustrated*. One way this can happen is through geometric frustration, the canonical example of which is antiferromagnetic Heisenberg interactions on the triangular lattice. In these frustrated systems, there are large numbers of degenerate classical ground states [26], giving the potential for exotic quantum phases to occur. In the triangular lattice case, it was originally conjectured to form a resonating valence bond (RVB) state at low temperature [27]. This RVB state is a kind of quantum spin liquid (QSL), involving pairs of $S = 1/2$ spins coupling as spin singlets, fluctuating in a liquid-like fashion with long-range entanglement [28, 29]. In the end, it was shown that these triangular lattices order with spins at a 120° angle from their neighbours as predicted by a mean-field approximation, compromising to minimise total energy [30]. However, this exotic RVB-QSL phase is predicted to occur in other highly frustrated models [31, 32].

An alternate approach to achieving exotic magnetic phases is with frustration introduced by bond-dependent interactions. Such is the example of the Kitaev model [11] introduced earlier. The honeycomb lattice is bipartite, so antiferromagnetic Heisenberg interactions will stabilise a Néel order, and there is no geometric frustration. Instead, the Kitaev model introduces frustration by having mutually orthogonal Ising axes on each of

the three bonds which meet at a site on the honeycomb lattice. This means that there is no way to minimise the energy on all three bonds simultaneously. This model is important because it has an exactly solvable quantum spin liquid ground state, thereby proving that a QSL ground state can exist in 2D and beyond, and revealing exotic excitations including quasiparticles with generalised (anyonic) statistics. Theoretical work to understand how these interactions may be realised experimentally first predicted the honeycomb iridates as candidates [33–36]. An extensive search has been made for experimental realisation of a Kitaev quantum spin liquid, including Na_2IrO_3 [22, 37], α-Li_2IrO_3 [38], and α-$RuCl_3$ [21, 39]. Generalisations of this model to include Heisenberg interactions [34, 40] and symmetric off-diagonal exchange Γ gives the nearest-neighbour Hamiltonian

$$\mathcal{H} = \sum_{\langle i,j\rangle \in \alpha\beta(\gamma)} J\boldsymbol{S}_i \cdot \boldsymbol{S}_j + KS_i^\gamma S_j^\gamma + \Gamma(S_i^\alpha S_j^\beta + S_i^\beta S_j^\alpha) \tag{2.37}$$

Each bond has an associated Ising axis $\gamma \in \{x, y, z\}$ and $\alpha\beta(\gamma)$ refer to the orthogonal plane to this axis. This shows an incredibly complex phase diagram[41], as can be seen in Fig. 2.3**a, b)**. This includes a finite volume of phase space stabilising a QSL around the exactly solvable pure Kitaev model, as well as many regions of unconventional magnetic order, some of which have been experimentally realised in the candidate materials searched [20, 42]. This provided part of the motivation to search for possible realisations of models with frustrated bond-dependent interactions and unconventional magnetic order in the f-electron Na_2PrO_3 systems explored later in this thesis.

The Kitaev model, and its exact solutions, can be generalised onto three-dimensional tricoordinated lattices of spin-½ magnetic ions such as the hyperhoneycomb and harmonic honeycomb family of lattices [44, 45]. Some of these lattices have be realised as polymorphs of Li_2IrO_3 [46–49], but they seem to be experimentally rare. Much like the honeycomb case, this exactly solvable pure Kitaev model can be extended into a J, K, Γ model, which is predicted to show a rich phase diagram of exotic magnetic phases depending on the precise balance between the three terms in the model [43]. An overview of this phase diagram can be seen in Fig. 2.3**c, d)**.

This thesis reports studies on three materials: the honeycomb Kitaev-candidate α-Na_2PrO_3 [50], its hyperhoneycomb polymorph β-Na_2PrO_3 [51], and two honeycomb

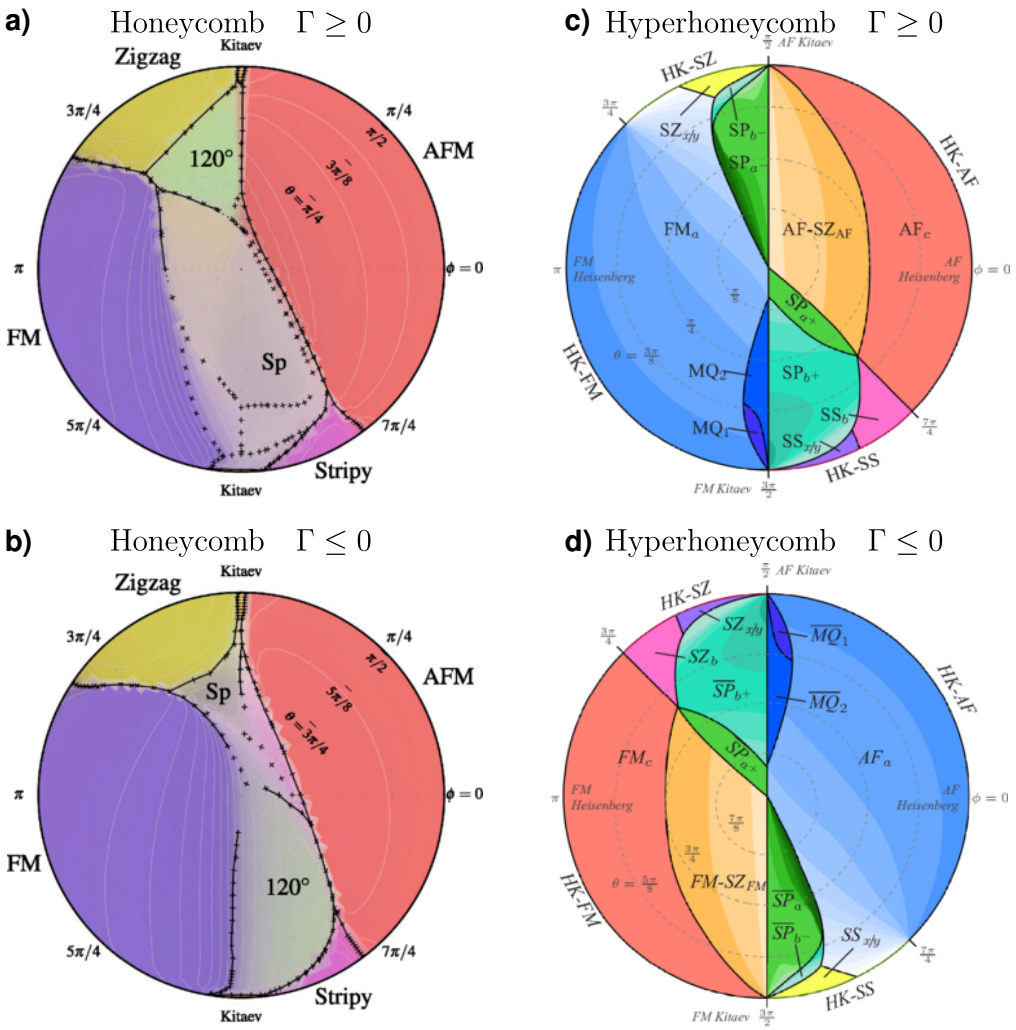


Figure 2.3: a, b) Phase boundaries from exact diagonalization of a 24-site cluster honeycomb $JK\Gamma$ exchange model. Reproduced with permission from [41]. **c, d)** Phase boundaries from classical calculation of hyperhoneycomb $JK\Gamma$ exchange model. Reproduced with permission from [43].

transition-metal oxides $FeTiO_3$ and $CoTiO_3$. The three materials are linked by their tricoordinated lattices of magnetic ions, and their anisotropic interactions driven by strong spin-orbit-coupling [52].

References

[1] F. Hund. *Linienspektren: Und Periodisches System der Elemente*. Vol. 4. Springer, 1927.

[2] J. C. Slater. "The theory of complex spectra". In: *Physical Review* 34.10 (1929), p. 1293.

[3] S. Blundell. *Magnetism in Condensed Matter*. Oxford University Press, 2001.

[4] A. Landé. "Über den anomalen Zeemaneffekt (teil i)". In: *Zeitschrift für Physik* 5.4 (1921), pp. 231–241.

[5] A. Abragam and B. Bleaney. *Electron paramagnetic resonance of transition ions*. Clarendon Press, 1970.

[6] D. J. Newman and B. Ng. *Crystal field handbook*. Vol. 43. Cambridge University Press Cambridge, 2000.

[7] I. Ryabov. "On the generation of operator equivalents and the calculation of their matrix elements". In: *Journal of Magnetic Resonance* 140.1 (1999), pp. 141–145.

[8] S. Altshuler and B. Kozyrev. *Electron Paramagnetic Resonance of Compounds of Elements of Intermediate Groups*. Originally published in Russian in 1961. New York: Academic Press, 1964.

[9] S. J. Blundell and K. M. Blundell. *Concepts in Thermal Physics*. Oxford University Press, 2009.

[10] C. Kittel and P. McEuen. *Introduction to solid state physics*. John Wiley & Sons, 2018.

[11] A. Kitaev. "Anyons in an exactly solved model and beyond". In: *Annals of Physics* 321.1 (2006), pp. 2–111.

[12] L. Néel. "Antiferromagnetism and ferrimagnetism". In: *Proceedings of the Physical Society. Section A* 65.11 (1952), p. 869.

[13] P. Zeeman. "The effect of magnetisation on the nature of light emitted by a substance". In: *Nature* 55.1424 (1897), p. 347.

[14] L. D. Landau and E. M. Lifshitz. *Statistical Physics: Volume 5*. Vol. 5. Elsevier, 2013.

[15] A. Bogdanov, A. Zhuravlev, and U. Rößler. "Spin-flop transition in uniaxial antiferromagnets: Magnetic phases, reorientation effects, and multidomain states". In: *Physical Review B* 75.9 (2007), p. 094425.

[16] L. Néel. "Propriétés magnétiques de l'état métallique et énergie d'interaction entre atomes magnétiques". In: *Annales de Physique*. Vol. 11. 5. 1936, pp. 232–279.

[17] W. Zhang et al. "Spin-flop transition and magnetic phase diagram in $CaCo_2As_2$ revealed by torque measurements". In: *Physical Review B* 92.14 (2015), p. 144416.

[18] H. Kato et al. "Metamagnetic phase transitions in $FeTiO_3$". In: *Journal of the Physical Society of Japan* 51.6 (1982), pp. 1769–1777.

[19] R. Yadav et al. "Kitaev exchange and field-induced quantum spin-liquid states in honeycomb α-$RuCl_3$". In: *Scientific Reports* 6.1 (2016), p. 37925.

[20] A. Banerjee et al. "Excitations in the field-induced quantum spin liquid state of α-$RuCl_3$". In: *NPJ Quantum Materials* 3.1 (2018), p. 8.

[21] R. D. Johnson et al. "Monoclinic crystal structure of α- $RuCl_3$ and the zigzag antiferromagnetic ground state". In: *Physical Review B* 92.23 (2015), p. 235119.

[22] S. Choi et al. "Spin waves and revised crystal structure of honeycomb iridate Na_2IrO_3". In: *Physical Review Letters* 108.12 (2012), p. 127204.

[23] A. Ruiz et al. "Correlated states in β-Li_2IrO_3 driven by applied magnetic fields". In: *Nature Communications* 8.1 (2017), p. 961.

[24] A. Coldea et al. "Cascade of field-induced magnetic transitions in a frustrated antiferromagnetic metal". In: *Physical Review B* 90.2 (2014), p. 020401.

[25] R. Coldea et al. "Quantum criticality in an $Ising$ chain: experimental evidence for emergent E_8 symmetry". In: *Science* 327.5962 (2010), pp. 177–180.

[26] G. Wannier. “Antiferromagnetism. the triangular Ising net”. In: *Physical Review* 79.2 (1950), p. 357.

[27] P. W. Anderson. “Resonating valence bonds: A new kind of insulator?” In: *Materials Research Bulletin* 8.2 (1973), pp. 153–160.

[28] H. Takagi et al. “Concept and realization of Kitaev quantum spin liquids”. In: *Nature Reviews Physics* 1.4 (2019), pp. 264–280.

[29] L. Balents. “Spin liquids in frustrated magnets”. In: *nature* 464.7286 (2010), pp. 199–208.

[30] L. Capriotti, A. E. Trumper, and S. Sorella. “Long-range Néel order in the triangular Heisenberg model”. In: *Physical Review Letters* 82.19 (1999), p. 3899.

[31] S. Yan, D. A. Huse, and S. R. White. “Spin-liquid ground state of the S=1/2 kagome Heisenberg antiferromagnet”. In: *Science* 332.6034 (2011), pp. 1173–1176.

[32] W.-J. Hu et al. “Competing spin-liquid states in the spin-1/2 Heisenberg model on the triangular lattice”. In: *Physical Review B* 92.14 (2015), p. 140403.

[33] G. Jackeli and G. Khaliullin. “Mott insulators in the strong spin-orbit coupling limit: from Heisenberg to a quantum compass and Kitaev models”. In: *Physical Review Letters* 102.1 (2009), p. 017205.

[34] J. Chaloupka, G. Jackeli, and G. Khaliullin. “Kitaev-Heisenberg model on a honeycomb lattice: possible exotic phases in iridium oxides A_2IrO_3”. In: *Physical Review Letters* 105.2 (2010), p. 027204.

[35] J. G. Rau, E. K.-H. Lee, and H.-Y. Kee. “Spin-orbit physics giving rise to novel phases in correlated systems: Iridates and related materials”. In: *Annual Review of Condensed Matter Physics* 7 (2016), pp. 195–221.

[36] J. Chaloupka, G. Jackeli, and G. Khaliullin. “Zigzag magnetic order in the iridium oxide Na_2IrO_3”. In: *Physical Review Letters* 110.9 (2013), p. 097204.

[37] X. Liu et al. “Long-range magnetic ordering in Na_2IrO_3”. In: *Physical Review B* 83.22 (2011), p. 220403.

[38] S. Williams et al. “Incommensurate counterrotating magnetic order stabilized by Kitaev interactions in the layered honeycomb α- Li_2IrO_3”. In: *Physical Review B* 93.19 (2016), p. 195158.

[39] K. Plumb et al. “α-$RuCl_3$: A spin-orbit assisted Mott insulator on a honeycomb lattice”. In: *Physical Review B* 90.4 (2014), p. 041112.

[40] Y. Singh et al. “Relevance of the Heisenberg-Kitaev model for the honeycomb lattice iridates A_2IrO_3”. In: *Physical Review Letters* 108.12 (2012), p. 127203.

[41] J. G. Rau, E. K.-H. Lee, and H.-Y. Kee. “Generic spin model for the honeycomb iridates beyond the Kitaev limit”. In: *Physical Review Letters* 112.7 (2014), p. 077204.

[42] A. Banerjee et al. “Neutron scattering in the proximate quantum spin liquid α-$RuCl_3$”. In: *Science* 356.6342 (2017), pp. 1055–1059.

[43] E. K.-H. Lee and Y. B. Kim. “Theory of magnetic phase diagrams in hyperhoneycomb and harmonic-honeycomb iridates”. In: *Physical Review B* 91.6 (2015), p. 064407.

[44] S. Mandal and N. Surendran. “Exactly solvable Kitaev model in three dimensions”. In: *Physical Review B* 79.2 (2009), p. 024426.

[45] I. Kimchi, J. G. Analytis, and A. Vishwanath. "Three-dimensional quantum spin liquids in models of harmonic-honeycomb iridates and phase diagram in an infinite-D approximation". In: *Physical Review B* 90.20 (2014), p. 205126.

[46] K. A. Modic et al. "Realization of a three-dimensional spin-anisotropic harmonic honeycomb iridate". In: *Nature Communications* 5.1 (2014), p. 4203.

[47] A. Biffin et al. "Unconventional magnetic order on the hyperhoneycomb Kitaev lattice in β-Li_2IrO_3: Full solution via magnetic resonant x-ray diffraction". In: *Physical Review B* 90.20 (2014), p. 205116.

[48] T. Takayama et al. "Hyperhoneycomb Iridate β-Li_2IrO_3 as a Platform for Kitaev Magnetism". In: *Physical Review Letters* 114.7 (2015), p. 077202.

[49] A. Biffin et al. "Noncoplanar and Counterrotating Incommensurate Magnetic Order Stabilized by Kitaev Interactions in γ-Li_2IrO_3". In: *Physical Review Letters* 113.19 (2014), p. 197201.

[50] S.-H. Jang et al. "Antiferromagnetic Kitaev interaction in f-electron based honeycomb magnets". In: *Physical Review B* 99.24 (2019), p. 241106.

[51] S.-H. Jang et al. "Computational design of f-electron Kitaev magnets: Honeycomb and hyperhoneycomb compounds A_2PrO_3 (A=alkali metals)". In: *Physical Review Materials* 4.10 (2020), p. 104420.

[52] J. Kanamori. "Theory of the magnetic properties of ferrous and cobaltous oxides, I". In: *Progress of Theoretical Physics* 17.2 (1957), pp. 177–196.

3 Experimental Methods

Contents

3.1 Linear Magnetometry 21
3.1.1 Overview 21
3.1.2 Vibrating Sample Magnetometry 22
3.1.3 Pulsed-Field Extraction Magnetometry 23
3.2 Torque Magnetometry 25
3.2.1 Overview 25
3.2.2 Theory 25
3.2.3 Experimental Approach 27
3.2.4 Example: Uniaxial Paramagnet 30
3.3 Heat Capacity 32
3.3.1 Overview 32
3.3.2 AC Calorimetry 35
3.4 X-ray Diffraction Crystallography 37
3.4.1 Overview 37
3.4.2 Experimental Details 39

3.1 Linear Magnetometry

3.1.1 Overview

Magnetometry, measuring the magnetisation of a sample, is ubiquitous in condensed matter physics to study magnetism. In this thesis it is referred to as *linear* magnetometry to distinguish it from torque magnetometry which is discussed later.

Most experimental methods for measuring magnetisation are based on Faraday's Law

[1]

$$\varepsilon = -\frac{d\Phi}{dt} = -\frac{d}{dt}\iint_{\Sigma} \boldsymbol{B}(t) \cdot \boldsymbol{dS} \tag{3.1}$$

which states that a time-varying magnetic field through a loop will induce an electromotive force around the loop. If this loop is broken, this can be measured as a voltage across the terminals. The magnetic flux through a coil will have contributions from any "background" magnetic field, and a contribution from the sample magnetisation. Different ways of measuring magnetisation usually involve generating a time-varying sample contribution to the field and measuring the induced ε.

There are a number of common methods for measuring magnetisation in samples at low temperatures and in high magnetic fields, including vibrating sample magnetometry, pulsed-field extraction magnetometry, SQUID magnetometry, and gradient-field torque magnetometry. Of these, two were used in this thesis, and these are explained in more depth in the following section.

3.1.2 Vibrating Sample Magnetometry

One method of measuring magnetisation, particularly in DC magnetic fields, is Vibrating Sample Magnetometry (VSM). In order to generate a time-varying magnetic field from the sample, an AC motor moves the sample through the pickup coil. This generates an AC magnetic field at the same frequency, which is picked up with a lock-in amplifier. This can be shown mathematically as the pickup voltage on the coil

$$V = -\frac{d\Phi}{dt} \tag{3.2}$$

$$= -\frac{d\Phi}{dz}\frac{dz}{dt} \tag{3.3}$$

If the sample is approximated as a point-dipole and $z = A\cos\omega t$ with oscillation amplitude A and frequency ω

$$V = AC\omega m_z \sin\omega t \tag{3.4}$$

with sample total moment written as the integrated magnetisation:

$$m_z = \iiint_V \boldsymbol{M} \cdot \hat{\boldsymbol{z}} dV \tag{3.5}$$

and coupling constant C which will depend on coil geometry and is typically determined by calibration. This is important as over a large temperature range the coil will deform, and so C will be temperature dependent. This pickup voltage is therefore linear in the magnetic moment, and the scaling factors are calibrated out.

The proportionality of this sensitivity to frequency ω means that higher sensitivity experiments can be performed by increasing the oscillation frequency. The trade-off with increasing ω is largely increased mechanical stress. For example, in the Quantum Design PPMS VSM used in this thesis, the system is run at $40\,\mathrm{Hz}$, with an oscillation amplitude of $2\,\mathrm{mm}$. In this system the sample and holder experience a peak acceleration of $\sim 13g$ where g is the acceleration under gravity on earth's surface. This provides a substantial mechanical stress on various components of the experiment. As this acceleration scales proportional to the square of the frequency, small increases in sensitivity increase the stress dramatically.

3.1.3 Pulsed-Field Extraction Magnetometry

Compared to DC magnets, pulsed fields allow access to much higher magnetic fields. The largest accessible non-destructive pulsed field reaches $100\,\mathrm{T}$, compared to the largest DC magnetic field of $45\,\mathrm{T}$. In pulsed magnetic fields, the short pulse time makes VSM unsuitable. A common approach is pulsed-field extraction magnetometry which uses the time-variation of the pulsed field itself to generate the time-varying magnetisation.

The operating principle involves a solenoid containing the magnetic material. The magnetic field inside the coil can be written as the sum of applied (auxiliary) magnetic field $\boldsymbol{H}$ and magnetisation $\boldsymbol{M}$

$$\boldsymbol{B}(t) = \mu_0 \left(\boldsymbol{H}(t) + \boldsymbol{M}(t)\right) \tag{3.6}$$

the total voltage over the solenoid is summed over each of the coils, which is treated

as an integral over the length l of the solenoid:

$$V(t) = -\frac{d}{dt}\int dl \overbrace{\iint_{\Sigma} \boldsymbol{B}(t)\cdot\boldsymbol{dS}}^{\Phi} \tag{3.7}$$

$$= -\frac{d}{dt}\iiint_{V} B_z(t)dV \tag{3.8}$$

$$= -\frac{d}{dt}\iiint_{V} \mu_0 H(t)dV - \frac{d}{dt}\iiint_{V} \mu_0 M_z(t)dV \tag{3.9}$$

where the magnetic field and solenoid axis are taken to be parallel to the z axis. The voltage can then be written as a time varying background

$$V_0(t) := -\frac{d}{dt}\iiint_{V} \mu_0 H(t)dV \tag{3.10}$$

and a sample-dependent term, assuming that the coil and sample geometry are time-independent,

$$V_s(t) := -\iiint_{V} \mu_0 \frac{dM_z}{dt}dV \tag{3.11}$$

$$= -\iiint_{V} \mu_0 \frac{dM_z}{dH}\frac{dH}{dt}dV \tag{3.12}$$

The experimental approach involves measuring an empty coil to determine $V_0(t)$, and a coil with the sample under the same conditions. This can then be subtracted to give $V_st)$. If the magnetisation is assumed to be approximately uniform throughout the sample, this gives $\frac{dM_z}{dt}$ which is then integrated to give the sample magnetisation. Typically, there is an unknown scaling factor on this determined value, dependent on coil geometry, sample geometry, and filling factor. This can be brought into absolute units by measuring the same material in a much smaller DC field using another technique such as VSM or SQUID magnetometry to scale the units.

As is shown in (3.12), the pickup signal is proportional to $\frac{dM}{dH}$, so the technique is particularly sensitive to sharp changes in the magnetisation such as first-order magnetic phase transitions. The signal is also proportional to $\frac{dH}{dt}$, so the technique is especially suited for fast-pulse magnets - such as the Helmholtz-Zentrum Dresden-Rossendorf $34\,\mathrm{ms}$, $65\,\mathrm{T}$ pulsed field magnet, used later in this thesis.

3.2 Torque Magnetometry

3.2.1 Overview

An alternative technique to linear magnetometry is torque magnetometry. Like magnetisation, torque probes a first derivative of the free energy, so it is sensitive to phase transitions. A particular advantage of torque magnetometry is that very small single crystals can be measured, well below the sensitivity of magnetisation measurements [2]. This permits experiments to be performed on materials for which large single crystals cannot be grown. This technique is used throughout the thesis as the primary experimental tool to study magnetism. These measurements are performed with field sweeps, temperature sweeps, and angle sweeps with the sample mounted on a rotator probe.

As I will show in the following section, torque magnetometry probes components of magnetisation orthogonal to the magnetic field. As such the technique is complementary to magnetometry techniques which probe the component parallel to the field, such as VSM or extraction-coil magnetometry.

3.2.2 Theory

The two equivalent formulations of magnetic torque commonly quoted in literature are $\boldsymbol{\tau} = \boldsymbol{m} \times \boldsymbol{B}$ [3] and $\tau = -\dfrac{\partial F}{\partial \alpha}$ [4] for some free energy F and angle α. The equivalence of these two is straightforward to prove and is included here for completeness, including a generalisation for non-uniform magnetic fields.

Consider the system of a crystal as a free energy $F(\boldsymbol{B}(\boldsymbol{r}))$, which is a function of the (non-uniform) magnetic field $\boldsymbol{B}(\boldsymbol{r})$ at the crystal's position $\boldsymbol{r}$. If the crystal is free to rotate around some vector $\boldsymbol{n}$, the (scalar) torque is defined to be the negative gradient of free energy with respect to the rotation angle $\alpha' = -\alpha$ i.e. $\tau = -\dfrac{\partial F}{\partial \alpha} = \dfrac{\partial F}{\partial \alpha'}$, where α' is the rotation of the magnetic field in the sample frame of reference. Note the change of sign is because the magnetic field in the sample frame rotates in the opposite direction to the sample in the lab frame,

$$\tau_{\boldsymbol{n}} = \left.\frac{\partial}{\partial \alpha'}\right|_0 F(R_{\boldsymbol{n}}^{\alpha'} \boldsymbol{B}(R_{\boldsymbol{n}}^{\alpha'} \boldsymbol{r})) \tag{3.13}$$

where $R^{\alpha'}\boldsymbol{n}$ is a matrix applying a rotation of angle α' around $\boldsymbol{n}$. This can be written to first order in α' using the generator matrices of rotations as

$$R_{\boldsymbol{n}}^{\alpha'} = \exp(\alpha' \tilde{R}_{\boldsymbol{n}}) \tag{3.14}$$

$$\left.\frac{\partial}{\partial \alpha'}\right|_0 R_{\boldsymbol{n}}^{\alpha'}\boldsymbol{u} = \tilde{R}_{\boldsymbol{n}}\boldsymbol{u} = \boldsymbol{n} \times \boldsymbol{u} \tag{3.15}$$

If this is inserted into (3.13)

$$\tau_{\boldsymbol{n}} = \left.\frac{\partial}{\partial \alpha'}\right|_0 F(R_{\boldsymbol{n}}^{\alpha'}\boldsymbol{B}(R_{\boldsymbol{n}}^{\alpha'}\boldsymbol{r})) \tag{3.16}$$

$$= \nabla_{\boldsymbol{B}} F \cdot \tilde{R}_{\boldsymbol{n}}\boldsymbol{B} + \nabla_{\boldsymbol{B}} F \cdot \left.\frac{\partial}{\partial \alpha'}\right|_0 \boldsymbol{B}(R_{\boldsymbol{n}}^{\alpha'}\boldsymbol{r}) \tag{3.17}$$

$$= \nabla_{\boldsymbol{B}} F \cdot (\boldsymbol{n} \times \boldsymbol{B}) + (\nabla_{\boldsymbol{B}} F \cdot \nabla)\boldsymbol{B} \cdot (\boldsymbol{n} \times \boldsymbol{r}) \tag{3.18}$$

using the standard results:

$$\frac{\partial}{\partial \phi} f(\boldsymbol{r}) = \nabla f \cdot \frac{\partial}{\partial \phi}\boldsymbol{r} \tag{3.19}$$

$$\boldsymbol{a} \cdot \frac{\partial}{\partial \phi}\boldsymbol{B}(\boldsymbol{r}) = (\boldsymbol{a} \cdot \nabla)\boldsymbol{B} \cdot \frac{\partial}{\partial \phi}\boldsymbol{r} \tag{3.20}$$

Both terms in (3.18) are a vector triple product, and are constant under cyclic permutation, allowing the expression to be rewritten

$$\tau_{\boldsymbol{n}} = \boldsymbol{n} \cdot [\boldsymbol{B} \times \nabla_{\boldsymbol{B}} F + \boldsymbol{r} \times (\nabla_{\boldsymbol{B}} F \cdot \nabla)\boldsymbol{B}] \tag{3.21}$$

$$= \boldsymbol{n} \cdot [\boldsymbol{B} \times \nabla_{\boldsymbol{B}} F + \boldsymbol{r} \times \nabla(\nabla_{\boldsymbol{B}} F \cdot \boldsymbol{B})] \tag{3.22}$$

Inserting the definition of magnetisation $\boldsymbol{m} = -\nabla_{\boldsymbol{B}} F$, this gives the definition of vector torque

$$\tau_{\boldsymbol{n}} = \boldsymbol{n} \cdot \boldsymbol{\tau} \tag{3.23}$$

$$\boldsymbol{\tau} = \boldsymbol{m} \times \boldsymbol{B} + \nabla(\boldsymbol{m} \cdot \boldsymbol{B}) \times \boldsymbol{r} \tag{3.24}$$

In a uniform field, the second term is zero, such that $\boldsymbol{\tau} = \boldsymbol{m} \times \boldsymbol{B}$, and torque magnetometry probes the component of magnetisation perpendicular to the magnetic field. As has been shown here, this is proportional to the derivative of energy with angle, so it is a direct measure of magnetic anisotropy. This makes it a particularly useful technique

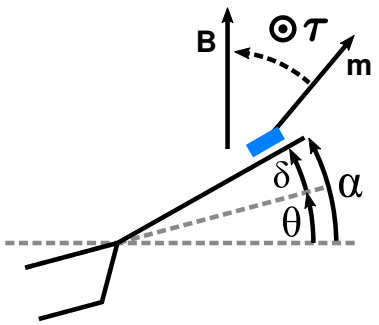


Figure 3.1: Schematic view of torque cantilever defining angles in (3.25). The dashed arrow shows the direction the lever tends to move.

for measuring anisotropic magnetic samples, where the isotropic magnetisation, which the technique is not sensitive to, may be much larger.

The existence of the second term in this expression $\nabla(\boldsymbol{m}\cdot\boldsymbol{B})\times\boldsymbol{r}$ allows for the operation of the gradient-field torque magnetometer [3]. This technique uses a large magnetic field gradient to measure $\nabla(\boldsymbol{m}\cdot\boldsymbol{B})\times\boldsymbol{r}$, sensitive to $\boldsymbol{m}\cdot\boldsymbol{B}$. This can allow the linear magnetisation and magnetic torque to be determined for the same sample.

3.2.3 Experimental Approach

Figure 3.1 shows a schematic view of the experimental setup, the total rotation angle of the sample is split into the equilibrium part θ and deflection δ. Such that $\alpha=\theta+\delta$. The experiment is performed by mounting a crystal on a cantilever, with an equilibrium angle θ from the horizontal. A vertical magnetic field $\boldsymbol{B}=B\boldsymbol{z}$ is applied to the apparatus, which can be placed in a cryogenic system for temperature control. The mechanical system can be analysed by writing the energy to leading order as:

$$E=K\delta^2+F_m(\alpha) \tag{3.25}$$

where F_m is the magnetic energy of the sample. Here, the contribution from the mass of the sample has been neglected.

If the deflection angle δ is small, the magnetic energy can be expanded around $\delta=0$

$$F_m(\alpha)=F_m(\theta)+\frac{\partial F_m}{\partial\alpha}\bigg|_\theta\delta+\frac{1}{2!}\frac{\partial^2F_m}{\partial\alpha^2}\bigg|_\theta\delta^2+\mathcal{O}(\delta^3) \tag{3.26}$$

$$=F_m(\theta)-\tau(\theta)\delta\quad+\kappa(\theta)\delta^2\qquad+\mathcal{O}(\delta^3) \tag{3.27}$$

where τ is the magnetic torque on the sample, and κ is the second derivative of energy with angle, which is sometimes called the *magnetotropic* coefficient [5]. This means the energy of the sample-lever system can be written as a simple harmonic oscillator

$$E \approx \tau(\theta)\delta + K'(\theta)\delta^2 \tag{3.28}$$

$$\approx K'(\delta - \delta_0)^2 \tag{3.29}$$

with effective stiffness $K'(\theta) = \kappa(\theta) + K$ and equilibrium deflection $\delta_0 = \dfrac{\tau}{2K'}$, which can each be measured experimentally. Conventional torque magnetometry, used in this thesis, measures the change in deflection angle δ_0. This is linear in magnetic torque when $|\kappa| \ll K$. The two standard methods for measuring this deflection angle are *piezoresistive* and *capacitive* cantilever torque magnetometry. An alternative technique is torque-differential magnetometry (TDM) [5, 6], which also measures the change in resonant frequency of the oscillator, sensitive to changes in κ. An advantage of this technique over conventional torque magnetometry is that for fields along high-symmetry axes, torque is frequently symmetry constrained to zero. The second derivative of free energy does not have the same problem along such axes.

Piezoresistive torque cantilevers [7] (piezocantilevers) were developed for scanning probe microscopy techniques [8] such as atomic force microscopy [9], meaning that they are available commercially. In a piezoresistive lever, (Fig. 3.2**a**), the "legs" at the base of the cantilever which allow it to bend are coated in a layer of a piezoresistive material, such as silicon, which shows a change in resistance when mechanical strain is applied [10]. This change in resistance is typically measured using a Wheatstone half-bridge, as shown in Figure 3.2**b)**. This circuit measures the difference in resistance between the lever and an identical dummy lever with no sample (lower half of image Fig. 3.2**a**), allowing the variability of resistance with temperature and/or magnetic field to be minimised. Typically this is measured with a lock-in amplifier.

These piezocantilever measurements are beneficial for their extremely high sensitivity, due primarily to their low stiffness. They are therefore able to measure very small moments from small single crystals. They are however challenging to mount on, especially for crystals which are not plate-like, where the orientation desired to be measured in is

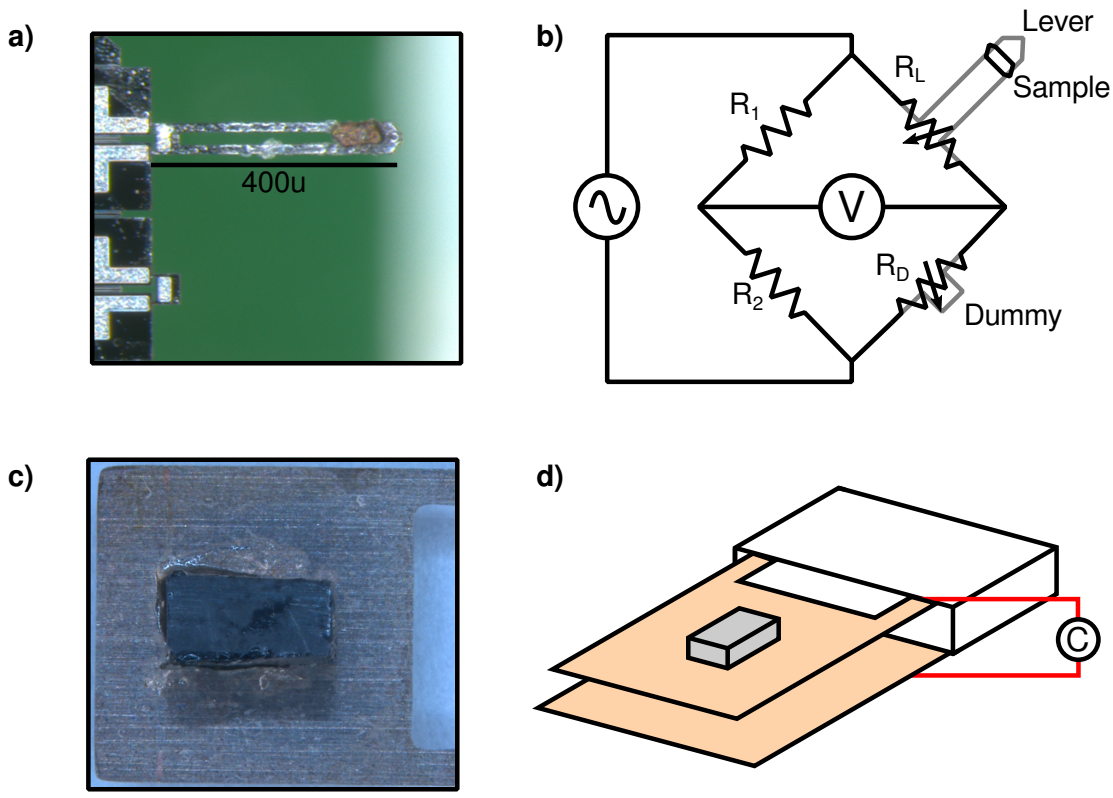


Figure 3.2: **a)** Photograph and **b)** schematic view of piezocantilever torque magnetometer, showing measurement electronics. **c)** Photograph and **d)** schematic view of capacitive cantilever torque magnetometer.

the in-plane, out-of-plane orientation. Additionally, they are fragile, and strong torques caused by large anisotropy in high magnetic fields can cause them to break.

Figure 3.2**c, d)** show an alternative design using a capacitive torque cantilever. This setup works by using the fact that the capacitance of a parallel-plate capacitor depends on the distance between the plates. The sensitivity of the capacitive levers is proportional to the area of the lever and the length of the legs, so are typically larger than piezocantilever measurements. This is beneficial when large crystals need to be mounted, and means specialised mounts can allow crystals to be mounted in orientations which would be challenging on a smaller lever.

In practice, these considerations make capacitive levers a good choice for crystals $\sim 1\mathrm{mm}$ in length, while piezoresistive levers can be made more flexible and thus more sensitive, making them good choices for smaller samples and smaller torques. As is shown later in this thesis, piezocantilever torque magnetometry can be performed on

magnetic single crystal samples down to thin plates with diameters $< 50\mu\mathrm{m}$, too small for many other techniques. This makes it a particularly effective technique for novel materials, which frequently cannot be synthesised as large crystals. Additionally, torque magnetometry directly probes the magnetic anisotropy of the sample, making it especially useful for studies of anisotropy.

3.2.4 Example: Uniaxial Paramagnet

In the simple case of a uniaxial crystal, a paramagnet can be described well in low fields by a susceptibility such that $\boldsymbol{m} = \chi \boldsymbol{B}$, where the susceptibility tensor has the uniaxial form

$$\chi = \begin{pmatrix} \chi_\perp & 0 & 0 \\ 0 & \chi_\perp & 0 \\ 0 & 0 & \chi_\parallel \end{pmatrix} \tag{3.30}$$

When the magnetic field is rotated around the sample such that

$$\boldsymbol{B} = B\left(-\sin\theta\,\boldsymbol{x} + \cos\theta\,\boldsymbol{z}\right) \tag{3.31}$$

producing a magnetisation in the sample

$$\begin{aligned} \boldsymbol{m} &= \chi \boldsymbol{B} && (3.32)\\ &= B\left(-\chi_\perp \sin\theta\,\boldsymbol{x} + \chi_\parallel \cos\theta\,\boldsymbol{z}\right) && (3.33) \end{aligned}$$

which produces a torque around the $\boldsymbol{y}$ axis

$$\begin{aligned} \boldsymbol{\tau} &= \boldsymbol{m} \times \boldsymbol{B} && (3.34)\\ &= \frac{1}{2} B^2 \left(\chi_\perp - \chi_\parallel\right) \sin 2\theta\, \mathbf{y} && (3.35)\\ \tau_y &= \frac{1}{2} B^2 \left(\chi_\perp - \chi_\parallel\right) \sin 2\theta && (3.36) \end{aligned}$$

The magnetic energy can be written

$$F_m = \frac{1}{4} B^2 \left(\chi_\perp - \chi_\parallel\right) \cos 2\theta \tag{3.37}$$

The angular dependence of both of these values is plotted in Figure 3.3 for the easy-axis $\chi_\parallel > \chi_\perp$ and easy-plane $\chi_\parallel < \chi_\perp$ cases. Note that these can be distinguished by the sign of the signal.

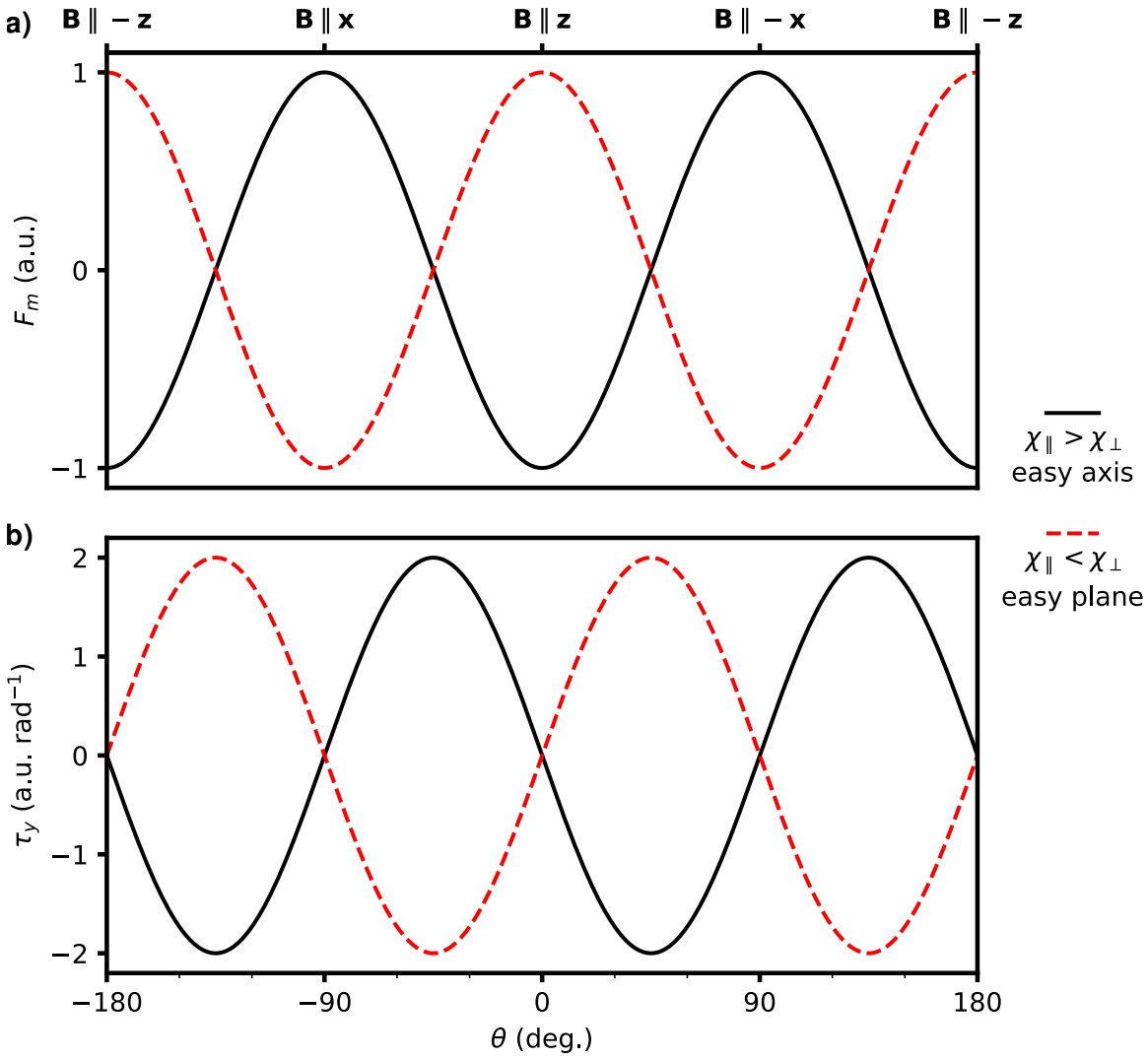


Figure 3.3: Calculated angular dependence of **a)** energy and **b)** torque for uniaxial paramagnet using (3.37) and (3.36) respectively.

A particularly informative feature in the magnetic torque are locations of zero torque $\tau(\theta) = 0$, and the gradient $\frac{\partial \tau}{\partial \theta}$ through the zeros. These zero-torque locations are equilibria, where energy is a maximum or minimum in angle. These two cases can be distinguished by the sign of the gradient. At a stable equilibrium, $\frac{\partial^2 F_m}{\partial \theta^2} > 0$ and $\frac{\partial \tau}{\partial \theta} < 0$. As such the sign of the gradient of torque through zero shows that the system is in a stable equilibrium. Experimentally determining absolute units for the torque can be very challenging, especially as the samples being measured are often too small to accurately determine the mass, however calibrating the sign of the torque simply requires measuring

a sample of a well characterised paramagnet. In this example of a uniaxial paramagnet for instance, the sign of the toque can reveal the order of susceptibilities $\chi_{\parallel}$, $\chi_{\perp}$.

If the susceptibilities in the material change, for instance as the material orders into an antiferromagnet, this will then be seen as a sharp anomaly in magnetic torque, making the technique useful for identifying the onset of magnetic order.

3.3 Heat Capacity

3.3.1 Overview

Heat capacity is a measure of how a material responds to thermal energy. Heat capacity is defined as the amount of heat δQ needed to increase the temperature by an infinitesimal temperature δT [11]

$$C = \lim_{\delta T \to 0} \frac{\delta Q}{\delta T} \tag{3.38}$$

The first law of thermodynamics defines the amount of heat in terms of the change in internal energy of the system

$$dU = dQ + dW \tag{3.39}$$

where the work term includes magnetic contributions

$$dU = dQ - PdV - \mu_0 \boldsymbol{M} \cdot \boldsymbol{dH} \tag{3.40}$$

where $PdV \approx 0$ because the experiments are performed in vacuum.

The most suitable heat capacity to define is the one which is measured experimentally: the heat capacity at constant field

$$C_H = \left(\frac{\partial Q}{\partial T} \right)_{\boldsymbol{H}} \tag{3.41}$$

The utility of this parameter can be best seen by including the second law of thermodynamics[11], which defines entropy S of the system:

$$dQ = TdS \tag{3.42}$$

such that heat capacity can be redefined as

$$C_H = T\left(\frac{\partial S}{\partial T}\right)_{\boldsymbol{H}} \tag{3.43}$$

By introducing the Helmhotz free energy $F = U - TS$, S can be written as

$$S = -\frac{dF}{dT} \tag{3.44}$$

and the heat capacity can be written as

$$C_H = -T\left(\frac{\partial^2 F}{\partial T^2}\right)_{\boldsymbol{H}} \tag{3.45}$$

This is particularly useful as a measure in the region of phase transitions where F is approximated as the Landau free energy $\mathcal{F}$, which depends on the order parameters of the phase transition [12]

$$\mathcal{F} = \mathcal{F}_0 + \Delta\mathcal{F}(\eta_0, \eta_1, \dots) \tag{3.46}$$

This treatment with many order parameters adds complexity and is not necessary to outline the effect on heat capacity at a phase transition. For the sake of simplicity a single order parameter η will be used for the remainder of this section. The entropy then can be written in terms of this Landau free energy

$$S - S_0 = \Delta S = -\frac{d\mathcal{F}}{dT} = -\frac{d\mathcal{F}}{d\eta}\frac{d\eta}{dT} \tag{3.47}$$

where ΔS is the contribution to entropy from the order parameter-dependent part of the free energy.

While the free energy is continuous at the phase transition, it is not analytic. The order of a phase transition is defined at the derivative of the Landau free energy where there is a discontinuity. In the case of a temperature-driven phase transition, there is a discontinuity in

$$\frac{d^n\mathcal{F}}{dT^n} \tag{3.48}$$

such that a 1$^{\text{st}}$order phase transition will have a discontinuity in S and a latent heat $\lambda = T_c\delta S$ needed to bring the system above the transition, where δS is the size of the

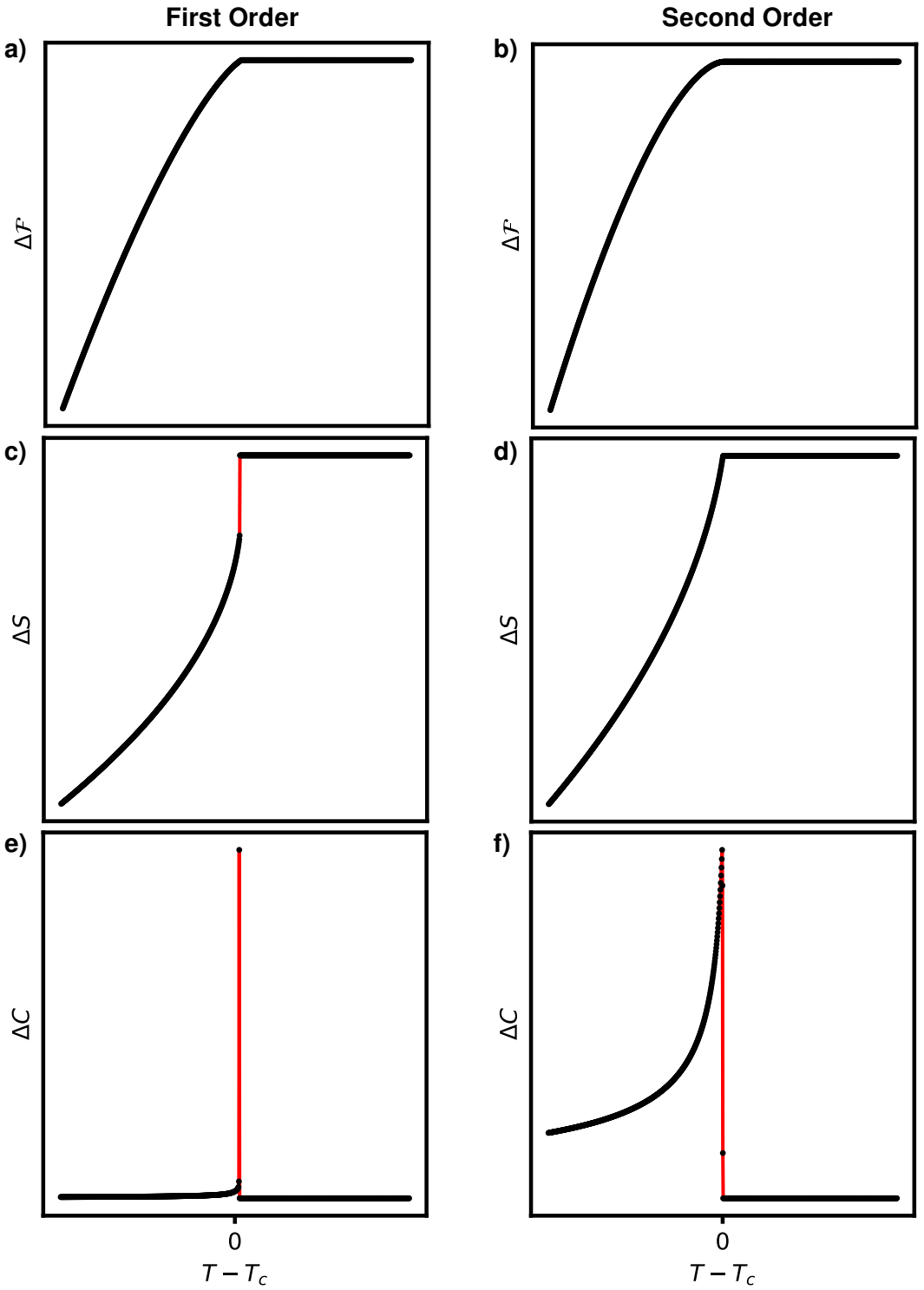


Figure 3.4: Temperature dependence of **a, b)** Landau free energy, **c, d)** entropy, and **e, f)** heat capacity in the vicinity of **a, c, e)** first-order and **b, d, f)** second-order phase transitions.

discontinuity in S. A 2ndorder phase transition will be continuous in S with no latent heat $\lambda = 0$ but have a discontinuity in C. This allows heat capacity to identify phase transitions, and to differentiate between these two classes of phase transitions, which can provide information about the symmetry of any order parameters involved in the transition [13].

For a simple model of phrase transitions, with Landau free energy

$$\Delta\mathcal{F}(\eta) = \frac{T - T_c}{T_c}\eta^2 + b\eta^4 + \eta^6 \tag{3.49}$$

$b < 0$ will show a first-order phase transition at T_c and $b > 0$ will show a second order phase transition at T_c. A comparison of $\Delta\mathcal{F}$, ΔS, and δC for these two models is shown in Figure 3.4, showing the difference in form of the heat capacities in both cases.

There are two common methods for measuring heat capacity. One is relaxation-time calorimetry [14], which involves providing a pulse of power to warm the sample weakly coupled to a bath, and measuring the time it takes to cool the sample to the bath temperature. For a given power output, by measuring the peak temperature, the thermal conductivity K between the sample and bath can be determined. The relaxation time constant is then $\tau = \frac{C}{K}$, giving the heat capacity in absolute units. Instead, this thesis uses the AC calorimetry method, which is introduced in more depth in the following section.

3.3.2 AC Calorimetry

The experimental technique used to measure heat capacity in this thesis is AC calorimetry. This involves exciting a sample with a oscillating current, and measuring the size of the ensuing temperature oscillations. The primary advantage of this method is the lower thermal isolation needed for the sample, compared to other methods. Instead, a relatively short thermal relaxation time is an advantage as is allows faster measurement taking. The analysis in this section comes from the original Sullivan and Seidel paper which first discussed this technique [15].

Consider the simple experimental model shown in Figure 3.5, of a sample coupled to a heater, thermometer, and bath by thermal conductances K_H, K_T, K_B respectively. An AC current through the heater generates an oscillating power output $P(t) = P_0 \cos\omega t + \frac{1}{2}P_0$, with frequency ω.

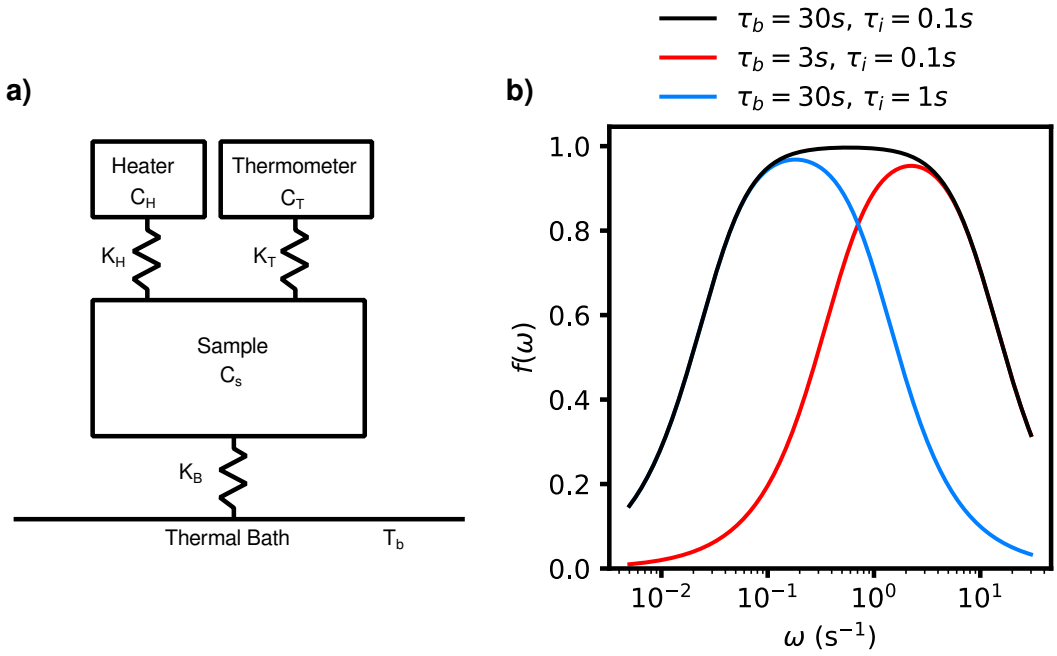


Figure 3.5: **a)** Schematic showing simple model for AC heat capacity probe with thermal conductances K_H, K_B, K_T. **b)** Calculated frequency response curves for various relaxation time parameters, as defined in (3.53).

The equilibrium solution for the measured temperature T on the thermometer is

$$T(t) = T_0 + \tilde{T}\cos(\omega t - \alpha) \tag{3.50}$$

with DC component $T_0 = T_b + \frac{P_0}{K_b}$, limiting the base temperature experimentally available, and oscillating component

$$\tilde{T} \approx \frac{P_0}{2\omega C} f(\omega) \tag{3.51}$$

with total heat capacity $C = C_H + C_T + C_s$ [15]. If characteristic time constants are defined

$$\tau_T = \frac{C_T}{K_T} \tag{3.52a}$$

$$\tau_H = \frac{C_H}{K_H} \tag{3.52b}$$

$$\tau_i^2 = \tau_T^2 + \tau_H^2 \tag{3.52c}$$

$$\tau_b = \frac{C}{K_b} \tag{3.52d}$$

then the frequency response function is approximately

$$f(\omega) \approx \left(1 + \omega^2\tau_i^2 + \frac{1}{\omega^2\tau_b^2}\right)^{-1/2} \tag{3.53}$$

In the case of $\tau_i \ll \tau_b$, this frequency response function has a flat plateau in frequency where $f(\omega) \approx 1$. This can be seen in Figure 3.5. Practically, the various time constants are not straightforward to measure for a given experimental setup. One simple approach is to measure the frequency dependence of $\tilde{T}$ and fit it to the functional form of (3.51), giving the optimal frequency ω_{opt} to perform the experiment at the centre of the plateau region, which is typically assumed to be $f(\omega_{\text{opt}}) \approx 1$, but can also be taken from the fit if $\tau_i \ll \tau_b$ does not hold. P_0 is straightforward to determine experimentally by measuring the voltage on the heater resistor element during the experiment. Given these, in this approximation C can be determined in absolute units without calibration. This total heat capacity includes a sample contribution and an *addenda* from the apparatus, this can be subtracted by measuring the same apparatus under same conditions without the sample to measure the addenda C_{ad}. Additional experimental considerations such as the effect of finite sample thermal conductivity require a more careful treatment [15], one effect of such considerations is that the optimal frequency response $f(\omega_{\text{opt}})$ can differ significantly from 1. This makes the AC technique ineffective in practice of accurately determining C in absolute units.

3.4 X-ray Diffraction Crystallography

3.4.1 Overview

X-ray crystallography is used throughout this thesis for crystal characterisation and structural determination in novel materials. These crystal structure results are not the primary focus of this thesis, so this section presents an overview of the X-ray diffractometry technique.

In diffraction, i.e. elastic scattering, the incoming photon has energy E, and wave vector $\boldsymbol{k}$ and the scattered photon has energy $E' = E$ and wave vector $\boldsymbol{k}'$. The scattering wave vector can then be written $\boldsymbol{Q} = \boldsymbol{k}' - \boldsymbol{k}$. The scattering rate from some potential $V(\boldsymbol{r})$ can be determined from Fermi's golden rule [16]

$$\Gamma(\boldsymbol{k}', \boldsymbol{k}) = \frac{2\pi}{\hbar} \left|\langle \boldsymbol{k}' | \, V \, | \boldsymbol{k} \rangle\right|^2 \delta(E' - E) \tag{3.54}$$

with matrix element

$$\langle \boldsymbol{k}' | \, V \, | \boldsymbol{k} \rangle = \frac{1}{\text{Vol}} \int_{\text{Vol}} e^{i\boldsymbol{k}\cdot\boldsymbol{r}} V(\boldsymbol{r}) e^{-i\boldsymbol{k}'\cdot\boldsymbol{r}} d^3\boldsymbol{r} \tag{3.55}$$

$$= \frac{1}{\text{Vol}} \int_{\text{Vol}} e^{-i\boldsymbol{Q}\cdot\boldsymbol{r}} V(\boldsymbol{r}) d^3\boldsymbol{r} \tag{3.56}$$

where Vol is the volume of the sample, and is needed to normalise the value. This amplitude can be thought of as the Fourier transform of the scattering potential $V(\boldsymbol{r})$. In a crystal, the X-rays are scattering off of electrons which are localised to ions on a periodic Bravais lattice. Because of this, the X-rays are scattering off a periodic potential. The scattering potential can be written in terms of the individual ion contributions as

$$V(\boldsymbol{r}) = \sum_{\boldsymbol{u}} \sum_{j} V_j(\boldsymbol{r} - \boldsymbol{R}_j - \boldsymbol{u}) \tag{3.57}$$

$$= \sum_{\boldsymbol{u}} \delta(\boldsymbol{r} - \boldsymbol{u}) * \sum_{j} \delta(\boldsymbol{r} - \boldsymbol{R}_j) * V_j(\boldsymbol{r}) \tag{3.58}$$

where $*$ represents a convolution, $\boldsymbol{u}$ indexes all primitive lattice vectors, and j indexes all of the atomic sites in the structural unit cell. Because of this, the convolution theorem allows the matrix element to be rewritten as

$$\langle \boldsymbol{k}' | \, V \, | \boldsymbol{k} \rangle = \left[\frac{1}{\text{Vol}} \sum_{\boldsymbol{u}} e^{-i\boldsymbol{Q}\cdot\boldsymbol{u}} \right] \sum_{j} e^{-i\boldsymbol{Q}\cdot\boldsymbol{R}_j} \int_{\text{Vol}} V_j(\boldsymbol{r'}) e^{-i\boldsymbol{Q}\cdot\boldsymbol{r'}} \boldsymbol{dr'} \tag{3.59}$$

The first term in this expression is a (non-divergent) constant if $\boldsymbol{Q}$ is a reciprocal lattice vector, and zero otherwise. This is known as the Laue condition, and positions where it is satisfied are known as Bragg peaks. This allows a scattering form factor to be defined as

$$S(\boldsymbol{Q}) \coloneqq \sum_{j} e^{-i\boldsymbol{Q}\cdot\boldsymbol{R}_j} \int_{\text{Vol}} V_j(\boldsymbol{r'}) e^{-i\boldsymbol{Q}\cdot\boldsymbol{r'}} \boldsymbol{dr'} \tag{3.60}$$

$$= \sum_{j} e^{-i\boldsymbol{Q}\cdot\boldsymbol{R}_j} f_j(\boldsymbol{Q}) \tag{3.61}$$

where the atomic form factor has been inserted:

$$f_j(\boldsymbol{Q}) \coloneqq \int_{\text{Vol}} V_j(\boldsymbol{r'}) e^{-i\boldsymbol{Q}\cdot\boldsymbol{r'}} \boldsymbol{dr'} \tag{3.62}$$

$$\propto \int_{\text{Vol}} \langle \rho(\boldsymbol{r'}) \rangle \, e^{-i\boldsymbol{Q}\cdot\boldsymbol{r'}} \boldsymbol{dr'} \tag{3.63}$$

as in X-ray scattering, the scattering potential is proportional to the electron density $\rho(\boldsymbol{r'})$. The scattering intensity is then proportional to the square of the amplitude:

$$I(\boldsymbol{Q}) \propto \left|\langle \boldsymbol{k}' | \, V \, | \boldsymbol{k} \rangle\right|^2 \propto |S(\boldsymbol{Q})|^2 \tag{3.64}$$

Experimentally, by finding the $\boldsymbol{Q}$ vectors where reflections occur, the lattice constants can be determined. Higher space group symmetries cause systematic absences, that is $\boldsymbol{Q}$ vectors where the Laue condition is fulfilled but $S(\boldsymbol{Q}) = 0$, this allows the Laue class of a crystal to be determined. Finally, by fitting the intensities of the observed peaks to those predicted from theory, a full crystal structure can be refined.

In practice, there are a number of further considerations which much be made to accurately refine these parameters. One important example comes from the fact that in finite temperature, atoms throughout the crystal will vary in position from their equilibrium position. This will produce an incoherent scattering background, and reduce the magnitude of the coherent scattering intensities. The physics of this can be captured in Debye-Waller factors [17, 18] which can be estimated from anisotropic displacement parameters by assuming a Gaussian probability distribution function [19].

3.4.2 Experimental Details

All X-ray crystallography experiments reported in this thesis were performed on an Mo-source Oxford Diffraction Supernova diffractometer. In this apparatus, X-rays are produced by a molybdenum X-ray tube, producing a collimated beam of monochromatic X-rays with wavelength $\lambda = 0.707$Å. X-rays are detected by a CCD area detector.

In this set-up, the incoming beam $\boldsymbol{k}$ is fixed, as is the detector, so a small solid angle of scattered X-rays can be detected. As this is measuring diffraction, $|\boldsymbol{k}'| = |\boldsymbol{k}|$, so all of the possible scattered $\boldsymbol{Q}$ vectors lie on an Ewald sphere [20], and the detection solid angle is simply a region of this sphere. By rotating the crystal on a goniometer, Bragg peaks can be brought onto this region of the Ewald sphere where they can be detected.

By keeping track of the sample orientation throughout the experiment, the scattering wave vectors where reflections are detected can be transformed into the sample frame. A fitting procedure can then determine the highest symmetry lattice which indexes the observed peaks. In order to accurately determine intensities of individual peaks, longer experiments can measure the scattering intensity over a very large volume of the space of

accessible $\boldsymbol{Q}$ vectors. Intensities can be determined by integrating over a small region around individual Bragg peaks. In this thesis, refining the structure from these intensities is done with the FULLPROF [21] analysis software.

Air and moisture sensitive samples are able to be measured without exposure to air by sealing the sample in inert gas or vacuum in a borosilicate glass capillary. This is done by first attaching the sample with paraffin to the outside of a $400\,\mu\mathrm{m}$ rectangular capillary in inert gas in a glove box. This is then placed in a $500\,\mu\mathrm{m}$ cylindrical capillary which may be evacuated and is then sealed by flame. As borosilicate glass is non-crystalline, it does not contribute coherent scattering to the measurement. The additional, and inevitably anisotropic, absorption and incoherent scattering from the capillary cannot be corrected, and so will reduce the accuracy of determined reflection intensities.

References

[1] A. W. Poyser. *Magnetism and electricity: A manual for students in advanced classes*. Longmans, Green, & Company, 1892.

[2] K. A. Modic et al. “Realization of a three-dimensional spin-anisotropic harmonic honeycomb iridate”. In: *Nature Communications* 5.1 (2014), p. 4203.

[3] A. McCollam et al. “High sensitivity magnetometer for measuring the isotropic and anisotropic magnetisation of small samples”. In: *Review of Scientific Instruments* 82.5 (2011), p. 053909.

[4] W. Zhang et al. “Spin-flop transition and magnetic phase diagram in $CaCo_2As_2$ revealed by torque measurements”. In: *Physical Review B* 92.14 (2015), p. 144416.

[5] K. A. Modic et al. “Resonant torsion magnetometry in anisotropic quantum materials”. In: *Nature Communications* 9.1 (2018), pp. 1–8.

[6] A. Kamra et al. “Theoretical model for torque differential magnetometry of single-domain magnets”. In: *Physical Review B* 89.18 (2014), p. 184406.

[7] E. Ohmichi and T. Osada. “Torque magnetometry in pulsed magnetic fields with use of a commercial microcantilever”. In: *Review of Scientific Instruments* 73.8 (2002), pp. 3022–3026.

[8] H. Takahashi, K. Ando, and Y. Shirakawabe. “Self-sensing piezoresistive cantilever and its magnetic force microscopy applications”. In: *Ultramicroscopy* 91.1-4 (2002), pp. 63–72.

[9] F. Ohnesorge and G. Binnig. “True atomic resolution by atomic force microscopy through repulsive and attractive forces”. In: *Science* 260.5113 (1993), pp. 1451–1456.

[10] Y. Kanda. “Piezoresistance effect of silicon”. In: *Sensors and Actuators A: Physical* 28.2 (1991), pp. 83–91.

[11] S. J. Blundell and K. M. Blundell. *Concepts in Thermal Physics*. Oxford University Press, 2009.

[12] L. D. Landau and E. M. Lifshitz. *Statistical Physics: Volume 5*. Vol. 5. Elsevier, 2013.

[13] M. Dresselhaus and G. Dresselhaus. *Applications of group theory to the physics of solids*. MIT Lecture Notes. 2002. URL: https://web.mit.edu/course/6/6.734j/www/group-full02.pdf.

[14] R. Bachmann et al. "Heat capacity measurements on small samples at low temperatures". In: *Review of Scientific Instruments* 43.2 (1972), pp. 205–214.

[15] P. F. Sullivan and G. Seidel. "Steady-state, AC-temperature calorimetry". In: *Physical Review* 173.3 (1968), p. 679.

[16] S. H. Simon. *The Oxford solid state basics*. OUP Oxford, 2013.

[17] P. Debye. "Interferenz von röntgenstrahlen und wärmebewegung". In: *Annalen der Physik* 348.1 (1913), pp. 49–92.

[18] I. Waller. "Zur frage der einwirkung der wärmebewegung auf die interferenz von röntgenstrahlen". In: *Zeitschrift für Physik* 17.1 (1923), pp. 398–408.

[19] K. Trueblood et al. "Atomic dispacement parameter nomenclature. Report of a subcommittee on atomic displacement parameter nomenclature". In: *Acta Crystallographica Section A: Foundations of Crystallography* 52.5 (1996), pp. 770–781.

[20] P. Ewald. "Introduction to the dynamical theory of X-ray diffraction". In: *Acta Crystallographica Section A: Crystal Physics, Diffraction, Theoretical and General Crystallography* 25.1 (1969), pp. 103–108.

[21] J. Rodríguez-Carvajal. "FullProf". In: *CEA/Saclay, France* 1045 (2001), pp. 132–146.

4

General Optimisation Algorithm to Find Classical Magnetic Ground States

Contents

4.1 Introduction 43
4.2 Example: Phase diagram of an Ising-like antiferromagnet on a square lattice for general orientation of magnetic field. 45
4.3 General formalism for multi-sublattice magnetic systems 51
4.4 Riemannian Optimisation Algorithm 55

Abstract *A number of methods exist to determine the ground state magnetic order of interacting spins on periodic lattices. This chapter illustrates the method used in this thesis for the case of an Ising-like antiferromagnet on a square lattice, for general orientation of applied magnetic field, where the magnetic structure is not collinear. This is followed by the general formalisation of the approach for the case of magnetic systems of many sublattices, with arbitrary bilinear exchange.*

4.1 Introduction

In order to make predictions of physical properties such as magnetic torque and linear magnetisation, calculations of magnetic structure using a gradient descent algorithm are performed in this thesis. This allowed development of a classical understanding of the pseudo-spin model of the materials which are discussed later. This approach treats spins as classical vectors and allows calculations to be performed much faster than quantum spin models such as exact-diagonalisation, which is intractable for many three-dimensional systems. A classical, three-dimensional pseudospin model is particularly useful when

the system orders, and classical models are good approximations [1, 2].

The Hamiltonian for a collection of interacting spins in some applied magnetic field $\boldsymbol{B}$ can be written as

$$\mathcal{H} = \sum_{i\alpha\beta ij} J_{ij}^{\alpha\beta} S_i^{\alpha} S_j^{\beta} - \sum_{i\alpha\beta} g_i^{\alpha\beta} B^{\alpha} S_i^{\beta} \tag{4.1}$$

$$= \sum_{ij} \boldsymbol{S}_i^T \mathbb{J}_{ij} \boldsymbol{S}_j \quad - \sum_{i} \boldsymbol{B}^T \mathbb{G}_i \boldsymbol{S}_i \tag{4.2}$$

where $\mathbb{J}_{ij}$ is the exchange tensor between sites i and j and $\boldsymbol{S}_i^T$ is the transpose of fixed-length vector spin at site i. $\mathbb{G}_i$ with elements $g_i^{\alpha\beta}$ is the g-factor at site i in units of μ_B. The classical ground state is the set of spins $\psi_0 = \{\boldsymbol{S}_i\}$ that minimises $\mathcal{H}$, under the condition that all spins have a fixed length s_i:

$$|\boldsymbol{S}_i| = s_i \; \forall i \tag{4.3}$$

Finding this ground state is fundamentally an optimisation problem in which the energy of the system is minimised over the state space. Numerical solutions to these problems are well studied, in physics as well as computer science. A number of algorithms exist to solve these, such as *branch and bound*, *simulated annealing*, and *gradient descent*.

An approach to finding the exact solution in zero field is the Luttinger-Tisza method [3], which works by replacing the strong condition (4.3) with the so-called weak condition

$$\sum_i |\boldsymbol{S}_i|^2 - s_i^2 = 0 \tag{4.4}$$

which is necessary but insufficient for the validity of (4.3). The Hamiltonian can be exactly solved under this condition using a Lagrange multiplier method [4]. If the solution also satisfies the strong condition then it is the true ground state.

A commonly used numerical method for solving these problems in physics is *simulated annealing* [5]. This iterative solution involves considering the current state $\boldsymbol{x}_n$ with energy E and some 'neighbouring' state $\boldsymbol{x}_n^*$ with energy E^*. The state is updated to this new value with probability $P(E, E^*, T)$ which is commonly

$$P(E, E^*, T) = \begin{cases} 1 & \text{if } E^* < E \\ \exp \frac{E - E^*}{T} & \text{otherwise} \end{cases} \tag{4.5}$$

where T is a 'temperature' parameter which decreases over time. This algorithm provably converges if the cooling schedule is sufficiently slow, however it is challenging to determine the ideal cooling rate *a priori*.

A different method, used in this thesis, is based on *gradient descent* (GD). GD works by adjusting the state in the direction which locally minimises the energy. This method reliably and efficiently finds *local* minima in energy, but some care is needed to find *global* minima. A more in-depth explanation of the algorithm is in a later section.

4.2 Example: Phase diagram of an Ising-like antiferromagnet on a square lattice for general orientation of magnetic field.

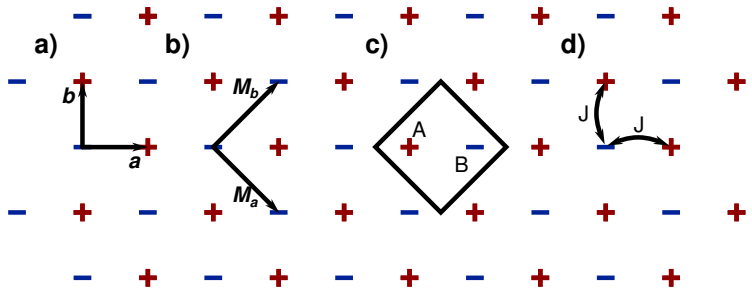


Figure 4.1: Schematic diagram showing a Néel order antiferromagnet on a square lattice. Red plus '+' symbols indicate spins along the $+\boldsymbol{z}$ axis, out of the page. Blue minus '-' symbols indicate spins along the $-\boldsymbol{z}$ axis, into the page. Overlaid diagrams show **a)** primitive lattice vectors $\boldsymbol{a}$, $\boldsymbol{b}$, **b)** magnetic unit cell lattice vectors $\boldsymbol{M_a}$, $\boldsymbol{M_b}$, **c)** magnetic unit cell outline with labelled sublattices A and B, and **d)** nearest-neighbour exchange path J.

Numerical mean field calculations of magnetic structures are particularly useful when considering systems with many exchange terms, or with applied magnetic fields along non-symmetry directions. In order to demonstrate their utility, I will use the example of a square lattice antiferromagnet with nearest-neighbour anisotropic XXZ exchange. A schematic diagram of such a lattice can be seen in Figure 4.1, which shows the primitive lattice vectors $\boldsymbol{a}$ and $\boldsymbol{b}$.

In this system, the total energy can be written as

$$\mathcal{H} = \frac{1}{2}\sum_{i,j} J\left(S_i^x S_j^x + S_i^y S_j^y + \Delta S_i^z S_j^z\right) - \sum_i g\mu_B \boldsymbol{B}\cdot\boldsymbol{S}_i \tag{4.6}$$

where the half prefactor is to correct for double counting of bonds, $J > 0$ parametrises the antiferromagnetic exchange, and Δ allows for exchange anisotropy. In this example $\Delta > 1$ indicates easy-axis Ising-type anisotropy.

The energy on a bond can be minimized by having the adjacent spins be antiparallel and collinear with the Ising $\boldsymbol{z}$ axis, such that the bond energy is $-\Delta JS^2$. On the square lattice, this can be satisfied for every bond by adopting a Néel order, such that adjacent spins are all always antiparallel, shown as alternating $+$ and $-$ symbols on Figure 4.1. Because this structure minimises the energy on every bond, it must be the ground state when $\boldsymbol{B} = 0$.

The magnetic unit cell vectors are

$$\begin{pmatrix} \boldsymbol{M_a} \\ \boldsymbol{M_b} \end{pmatrix} = \begin{pmatrix} 1 & -1 \\ 1 & 1 \end{pmatrix} \begin{pmatrix} \boldsymbol{a} \\ \boldsymbol{b} \end{pmatrix} \tag{4.7}$$

with

$$\det \begin{vmatrix} 1 & -1 \\ 1 & 1 \end{vmatrix} = 2 \tag{4.8}$$

showing that there are two primitive lattice points per magnetic unit cell. As such, the magnetic unit cell volume (in this case, area) is twice as large as the primitive unit cell volume. These magnetic unit cell vectors can be seen in Figure 4.1**b**, the outline of the unit cell can be seen in Figure 4.1**c**, with the two magnetic sublattices labelled A and B.

In order to understand how the spin orientations vary with applied magnetic field in this system, it is assumed that the magnetic unit cell does not change with applied magnetic field. The mean field energy per magnetic unit cell (Eqn. 4.6) can then be rewitten in terms of the spin orientations of the two sublattices $\boldsymbol{S}_A$ and $\boldsymbol{S}_B$

$$\frac{\mathcal{H}}{N} = nJ\left(S_A^x S_B^x + S_A^y S_B^y + \Delta S_A^z S_B^z\right) - g\mu_B \boldsymbol{B} \cdot (\boldsymbol{S}_A + \boldsymbol{S}_B) \tag{4.9}$$

where $n = 4$ is the number of nearest-neighbours on each site, and N is the total number of magnetic unit cells in the crystal. In this simple case, constructing the Hamiltonian as a function of sublattice spins is straightforward by inspection. In the most general case with longer range interactions and arbitrary numbers of sublattices the formalism is non-trivial and this is discussed in detail in Section 4.3.

One interesting feature of this system is that it undergoes a spin-flop transition when $\Delta > 1$, this is a metamagnetic phase transition which occurs when a sufficiently strong field is applied along the Ising $\boldsymbol{z}$ axis. The zero-field ground state has spins along the $\boldsymbol{z}$ axis, so when a field is applied the Zeeman energy

$$E_{\mathrm{Z}} = -\frac{1}{2} g \mu_B \boldsymbol{B} \cdot (\boldsymbol{S}_A + \boldsymbol{S}_B) \tag{4.10}$$

does not decrease with a magnetic field along $\boldsymbol{z}$. The spins are also not able to cant towards the field as they would if the field was applied in the xy plane. Determining the field at which this occurs, and the field dependence of the magnetisation can be done analytically and is demonstrated in many textbooks on the subject [6]. In this model, the spin-flop field B_{SF} is found to be

$$\mu_B g B_{\mathrm{SF}} = SnJ\sqrt{\Delta^2 - 1} \tag{4.11}$$

where a spin-flop occurs for all values of $\Delta > 1$. At this field, the magnetisation changes discontinuously from 0 at $B < B_{\mathrm{SF}}$ to a finite value at $B > B_{\mathrm{SF}}$.

However, the question of how the system behaves for non-axial fields, some arbitrary angle away from the $\boldsymbol{z}$ axis, cannot be answered so clearly analytically. For this reason, it is useful to develop numerical methods for solving the problem. A natural approach is an iterative algorithm called gradient descent. This algorithm works by starting from a state and finding the direction in which the spins can be adjusted that decreases the energy the most. This is repeated until a minimum in energy is found with satisfactory precision.

In this example, Equation 4.9 can be differentiated to give

$$\frac{1}{N} \nabla_{\boldsymbol{S}_A} \mathcal{H} = nJ \begin{pmatrix} S_B^x \\ S_B^y \\ \Delta S_B^z \end{pmatrix} - g \mu_B \boldsymbol{B} \tag{4.12}$$

which can be computed, then the sublattice spin $\boldsymbol{S}_A$ adjusted along the $-\nabla_{\boldsymbol{S}_A} \mathcal{H}$ direction, such that the energy decrease is maximised. Unfortunately, this runs into the problem that the magnitude of the spins $|\boldsymbol{S}_A|$ are unconstrained. For instance, in the Néel order

ground state with no field

$$\begin{aligned} \boldsymbol{S}_A &= \quad S\hat{z} \\ \boldsymbol{S}_B &= -S\hat{z} \\ \frac{1}{N}\nabla_{\boldsymbol{S}_A}\mathcal{H} &= -\Delta n J S\hat{z} \end{aligned}$$

so adjusting $\boldsymbol{S}_A$ by $-\gamma\nabla_{\boldsymbol{S}_A}\mathcal{H}$ with small $\gamma > 0$ will increase the magnitude of $|\boldsymbol{S}_A|$

$$|\boldsymbol{S}_A - \gamma\nabla_{\boldsymbol{S}_A}\mathcal{H}| = |\boldsymbol{S}_A| - \gamma\boldsymbol{S}_A \cdot \nabla_{\boldsymbol{S}_A}\mathcal{H} + \mathcal{O}(\gamma^2) \tag{4.13}$$

To solve this problem, I note that in the limit of small step size $\gamma \ll 1$, $|\boldsymbol{S}_A|$ will not change if $\boldsymbol{S}_A \cdot \nabla_{\boldsymbol{S}_A}\mathcal{H} = 0$. This means that the sublattice spins will be rotated in the plane containing the spin vector and the gradient $\nabla_{\boldsymbol{S}_A}\mathcal{H}$. I approach the formalism for this in a later section, but in summary this treats the condition $|\boldsymbol{S}_A| = S$ as a spherical manifold $\mathcal{M}$, and the adjustments to the state occur in the tangent space of this manifold $T_{\boldsymbol{p}}\mathcal{M}$.

In order to keep the step direction in this plane, I project the energy minimising vector $-\nabla_{\boldsymbol{S}_A}\mathcal{H}$ into the plane and use that as the step direction, and then normalise the new vector again to avoid accumulation of $\mathcal{O}(\gamma^2)$ errors.

$$\boldsymbol{S}_{A,n+1} = \mathrm{proj}_S\left[\boldsymbol{S}_{A,n} - \gamma\,\mathrm{proj}_T\,\nabla_{\boldsymbol{S}_A}\mathcal{H}\right] \tag{4.14}$$

where proj_S indicates the projection onto a sphere with radius S and proj_T indicates projection into the plane normal to $\boldsymbol{S}_A$. This can then be iterated for each spin until an energy minimum is found. Section 4.4 formalises this approach and derives a generalisation of the above expression.

Table 4.1: Calculation parameters for square-lattice XXZ antiferromagnet using definitions in Equation 4.9

n	4
S	½
g	2
J	$1\,\mathrm{meV}$
Δ	$\sqrt{2}$

This calculation was performed with the parameters in Table 4.1. From these, one expects a spin-flop transition to occur at $\mu_B B_{\mathrm{SF}} = 1\mathrm{meV}$ or $B_{\mathrm{SF}} \approx 17.28\mathrm{T}$ and

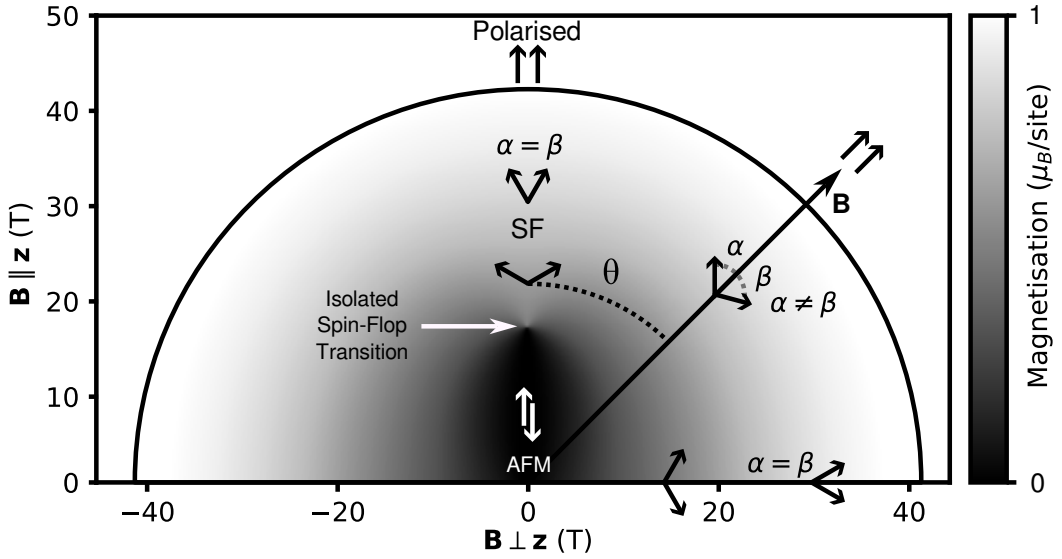


Figure 4.2: Phase diagram showing magnetisation per site for magnetic fields in the xz plane up to $50\,\mathrm{T}$, for an Ising type XXZ antiferromagnet with calculation parameters found in Table 4.1. Shading shows magnetisation projected onto the magnetic field direction as described in the text. Overlaid arrows show alignment of sublattice spins at various magnetic fields. θ is angle between the magnetic field and the Ising $\boldsymbol{z}$ axis. α, β are the angles sublattice spins make with the magnetic field direction. Circular black boundary shows second order phase transition from canted antiferromagnet to polarised phase. For special directions $\boldsymbol{B} \parallel \boldsymbol{z}$, $\boldsymbol{B} \perp \boldsymbol{z}$ $\alpha = \beta$ for general field orientation $\alpha \neq \beta$.

polarisation to occur at $\mu_B B_\mathrm{P} = 2.414\mathrm{meV}$ or $B_\mathrm{P} \approx 41.71\mathrm{T}$. The results of these calculations can be seen in Figure 4.3. Fig. 4.3**a)** shows the evolution of magnetisation against magnetic field for field orientations parallel and perpendicular to the $\boldsymbol{z}$ axis. For fields perpendicular to $\boldsymbol{z}$, the magnetisation increases linearly in field from $0\mu_B$ at $0\,\mathrm{T}$ to $1\mu_B$ at $41.7(1)\,\mathrm{T}$. For fields parallel to $\boldsymbol{z}$, the magnetisation remains at $0\mu_B$ between $0 \rightarrow 17.3(1)\mathrm{T}$, and then discontinuously joins the $\boldsymbol{B} \perp \boldsymbol{z}$ curve at higher fields.

Figure 4.2 shows how the projection of magnetisation onto the magnetic field direction

$$\boldsymbol{M} \cdot \frac{\boldsymbol{B}}{|\boldsymbol{B}|} \tag{4.15}$$

varies as as the magnetic field vector $\boldsymbol{B}$ varies in the xz plane. This shows a spin-flop transition at the isolated point $\boldsymbol{B} = B_\mathrm{SF}\boldsymbol{z}$, such that if the magnetic field is applied directly along the $\boldsymbol{z}$ axis, there is a phase transition, and discontinuous change in magnetisation at $|\boldsymbol{B}| = B_\mathrm{SF}$. This also shows that for off-axis fields, there is no phase transition, but instead a smooth crossover between the two regimes. It show that the spin orientations

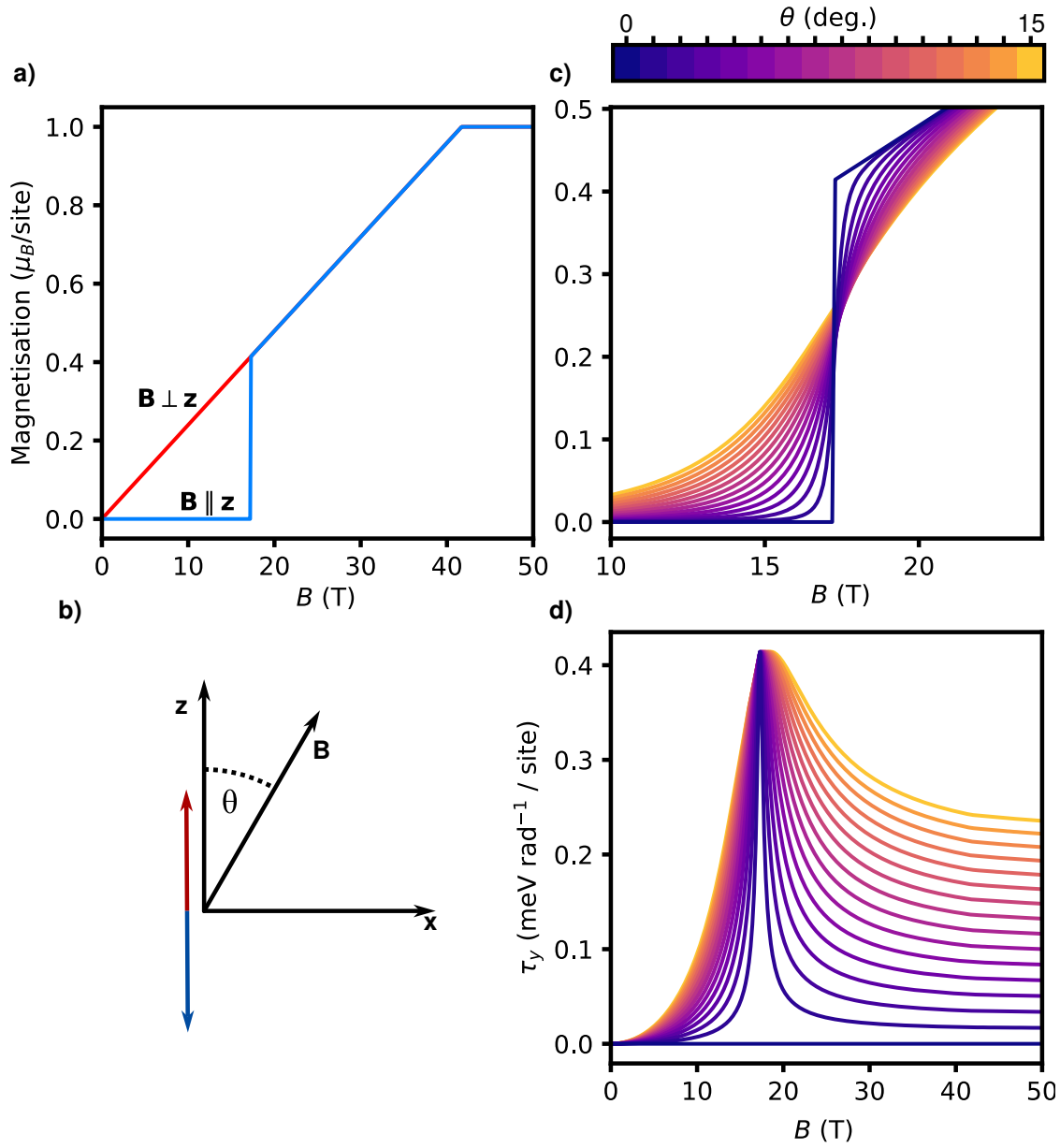


Figure 4.3: a) Evolution of magnetisation versus magnetic field for field aligned along (cyan) and perpendicular to (red) the Ising axis of an XXZ antiferromagnet on a square lattice. **b)** Schematic diagram showing axes arrangement and definition of angles in the rest of the figure. Angle θ is measured from the Ising z axis towards the xy-plane. **c)** shows evolution of magnetisation around the spin-flop field for angles between $0° \leq \theta \leq 15°$ and fields $10\text{T} \leq B \leq 25\text{T}$. **d)** shows evolution of magnetic torque with magnetic field for angles between $0° \leq \theta \leq 15°$ and fields $0\text{T} \leq B \leq 50\text{T}$. Calculation parameters are found in Table 4.1.

which minimise the free energy take different angles with the magnetic field $\alpha \neq \beta$ except in the special cases of axial fields $\theta = 0$, $\theta = \frac{\pi}{2}$, highlighting why this calculation is challenging to do analytically. For all field orientations, the system polarises at the same field $|\boldsymbol{B}| = B_{\mathrm{P}} \approx 41.71\mathrm{T}$, which is in all cases a continuous phase transition.

Fig. 4.3**b-d)** show the effect of off-axis fields on this system. Fig. 4.3**b)** shows how the angle θ is defined in this setup: measuring an angle from the $\boldsymbol{z}$ axis, towards the xy plane. At zero-field the spins are aligned parallel to the $\boldsymbol{z}$ axis. Fig. 4.3**c)** shows how magnetisation against field curves for θ between 0° and 15°. At $\theta = 0^\circ$ the field is exactly along axis and the $\boldsymbol{B} \parallel \boldsymbol{z}$ curve discussed above is recovered. As the field gets further off axis, the discontinuity at $|\boldsymbol{B}| = B_{\mathrm{SF}}$ is immediately replaced by a smooth crossover between the low and high-field regimes. At higher values of θ, the crossover becomes less sharp. Fig. 4.3**d)** shows how magnetic torque, taken around the $\boldsymbol{y} = \boldsymbol{z} \times \boldsymbol{x}$ axis shown in Fig. 4.3**b)**, evolves with applied magnetic field at different values of θ. At $\theta = 0^\circ$ the field is exactly along the $\boldsymbol{z}$ axis, and the torque is constrained by symmetry to be exactly 0 at all fields. For small values of θ, there is a sharp peak in torque around the spin-flop field. As θ increases, the peak becomes broader, and increases slightly in field. At the polarisation field B_{P}, the magnetisation changes slope at all angles θ, indicating a continuous phase transition. There is no anomaly in torque at B_{P} at any angle θ. These results reproduce what is expected theoretically [7, 8] has been seen before experimentally [9].

4.3 General formalism for multi-sublattice magnetic systems

The previous section outlines the ground state determination method for the case of two sublattices in the magnetic unit cell and nearest-neighbour exchange. This is appropriate for many simple systems. This section demonstrates the appropriate formalism for multi-sublattice systems with exchanges beyond nearest-neighbours.

The general form of the a spin Hamiltonian with exchange and Zeeman terms is

$$\mathcal{H} = \sum_{\alpha\beta ij} J_{ij}^{\alpha\beta} S_i^{\alpha} S_j^{\beta} - \sum_{i\alpha\beta} g_i^{\alpha\beta} B^{\alpha} S_i^{\beta} \tag{4.16}$$

$$= \sum_{ij} \boldsymbol{S}_i^T \mathbb{J}_{ij} \boldsymbol{S}_j \; - \sum_{i} \boldsymbol{B}^T \mathbb{G}_i \boldsymbol{S}_i \tag{4.17}$$

allowing for all bilinear exchange terms $J_{ij}^{\alpha\beta}$ and anisotropic g-factors $g_i^{\alpha\beta}$. This form of the Hamiltonian requires indexing over all sites in the crystal. These sites however exist on a Bravis lattice with symmetry constraints which are hard to evaluate in this indexed form. An equivalent formalism for the Hamiltonian is to make this explicit, by summing over the sites in each primitive unit cell, and the lattice points in the crystal. This gives

$$\mathcal{H} = \sum_{\alpha\beta ij\boldsymbol{uv}} J_{ij\boldsymbol{uv}}^{\alpha\beta} S_{i\boldsymbol{u}}^{\alpha} S_{j\boldsymbol{v}}^{\beta} - \sum_{\alpha\beta i\boldsymbol{u}} g_i^{\alpha\beta} B^{\alpha} S_{\boldsymbol{u}}^{\beta} \tag{4.18}$$

where i, j index over the sites in the unit cell and $\boldsymbol{u}, \boldsymbol{v}$ index over the lattice vectors in the crystal. Additionally, the value of the Hamiltonian must be invariant under the symmetry operations of the crystal, including translations by lattice vectors. In other words, it must be invariant under the transformation:

$$\boldsymbol{S}_{i\boldsymbol{u}} \rightarrow \boldsymbol{S}_{i\boldsymbol{u}+\boldsymbol{t}} \tag{4.19}$$

where $\boldsymbol{t}$ is a lattice vector. This constrains the exchange parameters, allowing them to be rewritten:

$$J_{ij\boldsymbol{u},\boldsymbol{u}+\boldsymbol{t}} \rightarrow J_{ij\boldsymbol{t}} \tag{4.20}$$

So including only the unique terms allowed by translational symmetry of the lattice:

$$\mathcal{H} = \sum_{\alpha\beta ij\boldsymbol{ut}} J_{ij\boldsymbol{t}}^{\alpha\beta} S_{i\boldsymbol{u}}^{\alpha} S_{j\boldsymbol{u}+\boldsymbol{t}}^{\beta} - \sum_{\alpha\beta i\boldsymbol{u}} g_i^{\alpha\beta} B^{\alpha} S_{i\boldsymbol{u}}^{\beta} \tag{4.21}$$

The exchange part of the Hamiltonian can then be fully specified by a set of exchange parameters (nearest-neighbour, next-nearest neighbour, and so on).

In order to convert the Hamiltonian into a sum over sublattices, a magnetic unit cell needs to be assumed. This means that the spins $S_{i\boldsymbol{u}}$ and $S_{i\boldsymbol{v}}$ at the same site index i,

for two different lattice vectors $\boldsymbol{u}$, $\boldsymbol{v}$, are equivalent if $\boldsymbol{u}$ and $\boldsymbol{v}$ differ by a *magnetic* lattice vector. Formally:

$$\boldsymbol{S}_{i\boldsymbol{u}} \equiv \boldsymbol{S}_{i\boldsymbol{v}} \quad \text{if } \exists \boldsymbol{m} \in \mathbb{M} : \boldsymbol{u} = \boldsymbol{v} + \boldsymbol{m} \tag{4.22}$$

where $\mathbb{M}$ is the vector space of all magnetic lattice vectors.

This means that the lattice vectors $\boldsymbol{u}$, $\boldsymbol{v}$ can be treated as equivalent if they differ by a magnetic lattice vector. This is the same as performing the algebra in the quotient space $V/\mathbb{M}$, where V is the vector space of primitive lattice vectors. It is worth noting that $\mathbb{M}$ is a vector subspace of V. A useful operator to define is the equivalence class of a vector in V

$$[\boldsymbol{u}] \coloneqq \{\boldsymbol{u} + \boldsymbol{m} \mid \forall \boldsymbol{m} \in \mathbb{M}\} \tag{4.23}$$

which is the set of all primitive lattice vectors which are equivalent under the magnetic unit cell.

To put it simply, by imposing a magnetic unit cell $\mathbb{M}$, two spins $\boldsymbol{S}_{i\boldsymbol{u}}$ and $\boldsymbol{S}_{i\boldsymbol{v}}$ at the same site index i, for two different primitive lattice vectors $\boldsymbol{u}$, $\boldsymbol{v}$, are equivalent if $[\boldsymbol{u}] = [\boldsymbol{v}]$. The set of equivalence classes here can be understood as the set of primitive lattice points in each magnetic unit cell. If there is only one site per primitive cell, then the equivalence classes are just the sublattices. If there is more than one site per primitive cell, the sublattices can be indexed by $i, [\boldsymbol{u}]$, and the number of sublattices is equal to the number of sites per primitive unit cell $\times$ the number of primitive lattice points per magnetic cell.

Because of this imposed symmetry, the spin at site $i, \boldsymbol{u}$ can be rewritten

$$\boldsymbol{S}_{i\boldsymbol{u}} \to \boldsymbol{S}_{i[\boldsymbol{u}]} \tag{4.24}$$

and the Hamiltonian can be rewritten as

$$\mathcal{H} = \sum_{\alpha\beta ij\boldsymbol{ut}} J_{ij\boldsymbol{t}}^{\alpha\beta} S_{i[\boldsymbol{u}]}^{\alpha} S_{j[\boldsymbol{u}+\boldsymbol{t}]}^{\beta} - \sum_{\alpha\beta i\boldsymbol{u}} g_i^{\alpha\beta} B^{\alpha} S_{i[\boldsymbol{u}]}^{\beta} \tag{4.25}$$

This still sums over all of the sites in the crystal, but the sum can be simplified by noting that for a finite size magnetic unit cell, there are a finite number of equivalence classes.

The sum is taken over the magnetic unit cells, and the sites per magnetic unit cell

$$\mathcal{H} = \sum_{\boldsymbol{m}\in\mathbb{M}} \sum_{\alpha\beta ij\boldsymbol{pt}} J_{ij\boldsymbol{t}}^{\alpha\beta} S_{i[\boldsymbol{p}+\boldsymbol{m}]}^{\alpha} S_{j[\boldsymbol{p}+\boldsymbol{m}+\boldsymbol{t}]}^{\beta} - \sum_{\boldsymbol{m}\in\mathbb{M}} \sum_{\alpha\beta i\boldsymbol{p}} g_i^{\alpha\beta} B^{\alpha} S_{i[\boldsymbol{p}+\boldsymbol{m}]}^{\beta} \tag{4.26}$$

$$= N \left(\sum_{\alpha\beta ij\boldsymbol{pt}} J_{ij\boldsymbol{t}}^{\alpha\beta} S_{i[\boldsymbol{p}]}^{\alpha} S_{j[\boldsymbol{p}+\boldsymbol{t}]}^{\beta} - \sum_{\alpha\beta i\boldsymbol{p}} g_i^{\alpha\beta} B^{\alpha} S_{i[\boldsymbol{p}]}^{\beta} \right) \tag{4.27}$$

where the first sum over is taken over all magnetic unit cells in the crystal $\boldsymbol{m} \in \mathbb{M}$, N is the number of magnetic unit cells in the crystal and the sum over $\boldsymbol{p}$ is over the primitive lattice points per magnetic unit cell (the equivalence classes of $V/\mathbb{M}$). The above uses the property of the equivalence classes that $[\boldsymbol{p}+\boldsymbol{m}] = [\boldsymbol{p}] \;\; \forall \boldsymbol{m} \in \mathbb{M}$.

Here, the factor of N can be safely removed by transforming $N\mathcal{H} \to \mathcal{H}$, such that

$$\mathcal{H} = \sum_{\alpha\beta ij\boldsymbol{pt}} J_{ij\boldsymbol{t}}^{\alpha\beta} S_{i[\boldsymbol{p}]}^{\alpha} S_{j[\boldsymbol{p}+\boldsymbol{t}]}^{\beta} - \sum_{\alpha\beta i\boldsymbol{p}} g_i^{\alpha\beta} B^{\alpha} S_{i[\boldsymbol{p}]}^{\beta} \tag{4.28}$$

The final hurdle to solve is the sum over $\boldsymbol{t}$, which still sums over all primitive lattice points. This is easily resolved as in the calculation, only a small number of interaction terms $J_{ij\boldsymbol{t}}^{\alpha\beta}$ are non-zero. This allows the sum to run over all non-zero interactions which have been defined (nearest-neighbour, next-nearest-neighbour, etc.), which is likely to be small in any real-world application, except for dipolar coupled systems which are not the focus of this thesis.

For the sake of completeness, the classical Hamiltonian can be rewritten in terms of the exchange interaction between the sublattices by defining

$$\widetilde{J}_{i[\boldsymbol{p}],j[\boldsymbol{r}]}^{\alpha\beta} \coloneqq \sum_{\boldsymbol{m}\in\mathbb{M}} J_{ij(\boldsymbol{r}-\boldsymbol{p}+\boldsymbol{m})}^{\alpha\beta} \tag{4.29}$$

such that

$$\mathcal{H} = \sum_{\alpha\beta i[\boldsymbol{p}]j[\boldsymbol{r}]} \widetilde{J}_{i[\boldsymbol{p}],j[\boldsymbol{r}]}^{\alpha\beta} S_{i[\boldsymbol{p}]}^{\alpha} S_{j[\boldsymbol{r}]}^{\beta} - \sum_{\alpha\beta i[\boldsymbol{p}]} g_i^{\alpha\beta} B^{\alpha} S_{i[\boldsymbol{p}]}^{\beta} \tag{4.30}$$

where $i[\boldsymbol{p}], j[\boldsymbol{r}]$ sum pairwise over the sublattices. This is the same form as Equation 4.9 in the example, and provides a good starting point for numerically solving these problems. The following section formalises a method for numerically minimising the mean field energy for Hamiltonians of this form.

The effect of applying a finite size magnetic unit cell is that only a subset of magnetic propagation vectors $\boldsymbol{q}$ are allowed, such that

$$\boldsymbol{q} \cdot \boldsymbol{m} \in \mathbb{Z} \quad \forall \boldsymbol{m} \in \mathbb{M} \tag{4.31}$$

This 'rationalisation' of k-space is the standard consequence of applying periodic boundary conditions to a crystal. It should be noted that incommensurate magnetic structures have irrational propagation vectors, so can never be solved with this method.

As the choice of magnetic unit cell $\mathbb{M}$ limits the solutions that can be found, it must be chosen from either prior theoretical work or empirical evidence of the propagation vector such as neutron diffraction experiments.

4.4 Riemannian Optimisation Algorithm

This section formalises a method for solving optimisation problems where the state space is not a vector space. This is needed for finding the ground state magnetic Hamiltonians of the form

$$\mathcal{H} = \sum_{\alpha\beta ij} \widetilde{J}_{ij}^{\alpha\beta} S_i^\alpha S_j^\beta - \sum_{\alpha\beta i} g_i^{\alpha\beta} B^\alpha S_i^\beta + \sum_i A_i(\boldsymbol{S}_i) \tag{4.32}$$

$$= \sum_{ij} \boldsymbol{S}_i^T \mathbb{J}_{ij} \boldsymbol{S}_j \; - \sum_i \boldsymbol{B}^T \mathbb{G}_i \boldsymbol{S}_i + \sum_i A_i(\boldsymbol{S}_i) \tag{4.33}$$

where $A_i(\boldsymbol{S}_i)$ parametrises local anisotropy on site i, some complex anisotropy terms are discussed in Chapter 7.

These have the constraint that the sublattice spin vectors have a fixed magnitude i.e.

$$|\boldsymbol{S}_i| = s_i \forall i \tag{4.34}$$

As such, the space of allowed $\boldsymbol{S}_i$ do not form a vector space. Fortunately, as each spin is constrained to be a vector with a fixed length, it is equivalent to saying that each $\boldsymbol{S}_i$ is a point on a sphere of radius s_i. This forms a differentiable Riemannian manifold over which some optimisation algorithms such as gradient descent can be generalised as shown below.

Traditionally, gradient descent is an algorithm for finding the local minimum of a scalar, differentiable, function F over a vector space

$$F : \mathbb{R}^d \to \mathbb{R} \tag{4.35}$$

The principle of the algorithm comes from defining the gradient operator ∇F such that its inner product with some vector direction $\boldsymbol{v}$

$$\langle \nabla F, \boldsymbol{v} \rangle \coloneqq dF(\boldsymbol{v}) \tag{4.36}$$

the derivative of F along $\boldsymbol{v}$. This is equivalent to the more commonly used definition

$$\nabla F \coloneqq \sum_i \frac{\partial F}{\partial x_i} \hat{\boldsymbol{e}}_i \tag{4.37}$$

where $\hat{\boldsymbol{e}}_i$ is the i^{th}unit basis vector of the vector space, and $\frac{\partial F}{\partial x_i}$ is the partial derivative of F with respect to the coordinate x_i.

For a small step $\boldsymbol{\delta}$, the change in F is maximised when the step is parallel to the gradient ∇F. This prompts the iterative solution

$$\boldsymbol{x}_{n+1} = \boldsymbol{x}_n - \gamma \nabla F(\boldsymbol{x}_n) \tag{4.38}$$

where γ is a learning rate, and is a free parameter.

In order to include the constant length spins constraint (Eqn. 4.3), modifications have to be made to the standard gradient descent algorithm. One option is to use a penalty method, which involves adding some smooth term to the Hamiltonian to penalise moving away from the constraint. In this case one could add the penalty term:

$$P = \sum_i \eta(|\boldsymbol{S}_i| - 1)^2 \tag{4.39}$$

where $\eta > 0$ is a free parameter. This would add a cost to the optimiser to violate the constraint, so it will stay approximately satisfied.

Another solution, with has been implemented for this project, is to consider the constrained state space Ψ as a Riemannian manifold, described below. The gradient descent algorithm can be generalised to apply to any Riemannian manifold, not just the Euclidean geometry $\mathbb{R}^d$ shown above [10–12]. In this form the algorithm is sometimes known as *Riemannian Optimisation*. However, some of the steps which are trivial in the Euclidean case are not trivial in the general case.

A Riemannian manifold is a smooth, differentiable manifold whose tangent spaces have an inner product, which varies smoothly across the manifold. The tangent space

$T_p\mathcal{M}$ of a differentiable manifold $\mathcal{M}$ at p is the vector space spanned by the tangent vectors of all of the curves at p on $\mathcal{M}$. If $\mathcal{M}$ can be embedded in an ambient Euclidean space, this can be easily visualised as the (hyper-)plane spanned by the tangent vectors as in Figure 4.4**a)**.

In this case, F is instead a differentiable, scalar function over the manifold $\mathcal{M}$

$$F : \mathcal{M} \rightarrow \mathbb{R} \tag{4.40}$$

This allows the gradient ∇F to be defined again such that

$$\langle \nabla F, \boldsymbol{v} \rangle = dF(\boldsymbol{v}) \tag{4.41}$$

is the derivative of F along $\boldsymbol{v}$. It should be noted that the vectors $\boldsymbol{v}$ and ∇F are now elements of the tangent space $T_p\mathcal{M}$. Clearly, a step along the vector ∇F will maximise the change in F, so the approach of gradient descent will work. However, unlike in the Euclidean case, the tangent space and the manifold have very different geometry. A tangent vector on $T_p\mathcal{M}$ can be mapped to $\mathcal{M}$ by the *exponential map*:

$$\exp_p : T_p\mathcal{M} \rightarrow \mathcal{M} \tag{4.42}$$

In some cases, this map may be computationally expensive to evaluate. Overall this gives the iteration step for gradient descent on an arbitrary Riemannian manifold:

$$p_{n+1} = \exp_{p_n}(-\gamma \nabla F) \tag{4.43}$$

Applying this to the geometry of the problem in magnetism is straightforward. A point ψ on the overall space Ψ is a collection of N spins $\boldsymbol{S}_i$, which are constrained to be unit vectors. So each spin is a point on a sphere, that is a point on the S^2 spherical manifold. The overall space Ψ is therefore the product manifold

$$\Psi = \underbrace{\mathrm{S}^2 \times \mathrm{S}^2 \times ... \times \mathrm{S}^2}_{N \text{ times}} \tag{4.44}$$

and is easily visualised as N independent coordinates on a sphere. Formally:

$$\psi = (s^1, \ldots, s^N) \in \Psi \tag{4.45}$$

$$s^i \in S^2 \tag{4.46}$$

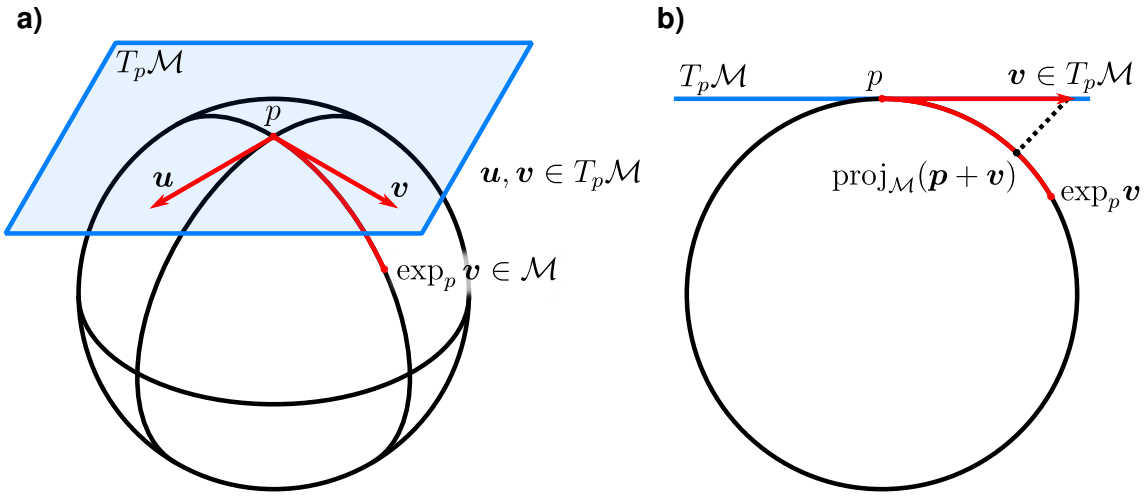


Figure 4.4: Schematic showing some properties of the spherical S^2 manifold $\mathcal{M}$. **a)** shows $\mathcal{M}$ embedded in ambient Euclidean space $\mathbb{R}^3$. At a point p on $\mathcal{M}$, the tangent space $T_p\mathcal{M}$ is visualised as a plane tangent to the sphere at p. Orthogonal unit vectors $\boldsymbol{u}$, $\boldsymbol{v}$ which span $T_p\mathcal{M}$ are shown as red arrows. The exponential map $\exp_p \boldsymbol{v}$ is shown as a red line along the sphere. **b)** shows a cross section of the sphere including $\boldsymbol{v}$ and the origin. The projection operator $\mathrm{proj}_{\mathcal{M}}$ is shown as a black dashed line. Note that p is written without bold when treated as a point on $\mathcal{M}$, and as bold $\boldsymbol{p}$ when treated as a vector in the ambient Euclidean space.

The tangent space of a product manifold $X \times Y$ is the product of the tangent spaces of the individual manifolds [10]:

$$T_{(x,y)}(X \times Y) = T_x X \times T_y Y \tag{4.47}$$

The exponential map has a similar relationship [10]:

$$\exp^{X\times Y}_{(x,y)} = (\exp^X_x, \exp^Y_y) \tag{4.48}$$

This means that the update step with N spins can be divided into N update steps each on a sphere:

$$\psi_{n+1} = (\dots, s^i_{n+1}, \dots) = \exp^{\Psi}_{p_n}(-\gamma \nabla_\Psi F) \tag{4.49}$$

$$= (\dots, \exp^{S_i}_{s^i_n}(-\gamma \nabla_{S_i} F), \dots) \tag{4.50}$$

$$\therefore s^i_{n+1} = \exp^{S_i}_{s^i_n}(-\gamma \nabla_{S_i} F) \tag{4.51}$$

Thankfully, the spherical geometry allows this to be computed without much trouble. Figure 4.4**a,b)** show how the exponential map of the d-sphere S^d can be cheaply

approximated by projecting the first order approximation of the map, the point on the tangent (hyper-)plane, back onto the sphere:

$$\exp_{\boldsymbol{p}}(\boldsymbol{u}) = \boldsymbol{p}\cos|\boldsymbol{u}| + \frac{\boldsymbol{u}}{|\boldsymbol{u}|}\sin|\boldsymbol{u}| \tag{4.52}$$

$$\approx \mathrm{proj}_S(\boldsymbol{p}+\boldsymbol{u}) = \frac{\boldsymbol{p}+\boldsymbol{u}}{|\boldsymbol{p}+\boldsymbol{u}|} = \exp_{\boldsymbol{p}}\left(\frac{\arctan(|\boldsymbol{u}|)}{|\boldsymbol{u}|}\boldsymbol{u}\right) \tag{4.53}$$

The effect of the approximation is to slightly lower the learning rate while the path along which the state is adjusted is unchanged.

By embedding the sphere in $\mathbb{R}^3$, the coordinate of the point on the sphere can be stored as x, y, z components. The tangent space T_pS^2 is the plane $\boldsymbol{v}\cdot\boldsymbol{p}=0$, and is a 2-dimensional vector subspace of the ambient $\mathbb{R}^3$. This allows for a very simple method for computing the gradient from the unconstrained Hamiltonian $\tilde{\mathcal{H}} : \mathbb{R}^3 \to \mathbb{R}$. The unconstrained gradient $\nabla\tilde{\mathcal{H}} \in \mathbb{R}^3$ can be computed cheaply and projected into the tangent plane to give the gradient of the constrained Hamiltonian:

$$\nabla\mathcal{H}|_{\boldsymbol{p}} = \mathrm{proj}_{T_{\boldsymbol{p}}S}\,\nabla\tilde{\mathcal{H}} = \nabla\tilde{\mathcal{H}} - (\nabla\tilde{\mathcal{H}}\cdot\boldsymbol{p})\boldsymbol{p} \tag{4.54}$$

This gives the final expression for the iteration step in the gradient descent algorithm on the sphere as

$$\boldsymbol{x}_{n+1} = \mathrm{proj}_S\left(\boldsymbol{x}_n - \gamma\nabla\mathcal{H}\right) \tag{4.55}$$

$$= \mathrm{proj}_S\left(\boldsymbol{x}_n - \gamma\ \mathrm{proj}_T\,\nabla\tilde{\mathcal{H}}\right) \tag{4.56}$$

$$= \frac{\boldsymbol{x}_n - \gamma(\nabla\tilde{\mathcal{H}} - (\nabla\tilde{\mathcal{H}}\cdot\boldsymbol{x}_n)\boldsymbol{x}_n)}{\left|\boldsymbol{x}_n - \gamma(\nabla\tilde{\mathcal{H}} - (\nabla\tilde{\mathcal{H}}\cdot\boldsymbol{x}_n)\boldsymbol{x}_n)\right|} \tag{4.57}$$

where S represents the sphere, and $T = T_{\boldsymbol{x}_n}S^2$ is the tangent space of the sphere at $\boldsymbol{x}_n$. This is the generalised form of the expression found in the example (Equation 4.14). In the implementation of the algorithm used in this thesis, γ is chosen to keep the maximum angle a spin rotates below a threshold, which starts at $0.05\mathrm{rad}$, and is decreased until a specified precision is reached.

Numerically this can be computed with double precision floating point arithmetic very quickly, as it contains only linear operations, with the exception of the square-root

in the magnitude. The final ingredient is the gradient of the unconstrained Hamiltonian with respect to an individual spin. Analytically this is

$$\nabla_{\boldsymbol{S}_i}\tilde{\mathcal{H}} = \sum_{j\neq i}\mathbb{J}_{ij}\boldsymbol{S}_j + (\mathbb{J}_{ii}+\mathbb{J}_{ii}^T)\boldsymbol{S}_i - \mathbb{G}_i\boldsymbol{B} + \nabla_{\boldsymbol{S}_i}A_i(\boldsymbol{S}_i) \tag{4.58}$$

where the term $\mathbb{J}_{ii}+\mathbb{J}_{ii}^T$ captures exchange interactions between two different sites in the same sublattice. For instance, on the square lattice example, a next-nearest-neighbour interactions would couple the A and B sublattices to themselves. The term $\nabla_{\boldsymbol{S}_i}A_i(\boldsymbol{S}_i)$ captures single-ion anisotropy such as a $-DS_z^2$ term.

The time complexity of an algorithm is defined as the leading order scaling of the execution time as the size of the input grows, in the limit of large input size. For finding local minima this algorithm has a time complexity of $\mathcal{O}(N^2)$, quadratic in the number of spins and equal to the time complexity of computing the gradient of the Hamiltonian. To find global minima in energy, the initial point $\boldsymbol{x}_0$ can be guessed at many points across $\mathcal{M}$. However, in the case of magnetism, the number of points needed to cover the manifold scales exponentially in the number of spins in the calculation. With an overall time complexity of $\mathcal{O}(N^2b^N)$, where the branching factor b depends on the exact form of Hamiltonian. In examples with only one local minima $b=1$ the scaling is very efficient, but examples with many local minima in energy are pathological for this algorithm.

In this case, Riemannian optimisation is a significant improvement over penalty methods in that is ensures that the constraint is satisfied exactly, without sacrificing speed. Compared to simulated annealing, it has the advantage of robustly determining local minima in energy, which is useful for tracking the evolution and stability of domains, and for visualising the evolution of the state when there are degenerate ground states. On the other hand, simulated annealing is able to efficiently find approximate global minima in energy, while gradient descent is exceptionally poor at the task for large numbers of spins and many local minima in energy. In such a case, a hybrid approach could work by using simulated annealing to produce an anstaz to seed the gradient descent algorithm, however in all cases in this thesis this was not required.

This algorithm is similar to variations of gradient descent used in many popular mean-field calculation programs. For example, SPINW's [13] `optmagsteep` method

rotates spins towards the local mean-field, similar to gradient descent. However, the precise formulation used in this thesis means that it provably converges on a local minimum in energy [10].

I used the principles outlined in this chapter to develop the Python library `qafm`, able to numerically find local and global minima in the mean-field energy with and without magnetic field applied. This can be performed on arbitrary crystal structures and commensurate magnetic unit cells, and is able to verify if given exchange tensors are symmetry allowed. This is used in later chapters to understand theoretically the response of different systems to magnetic fields at the mean-field level.

References

[1] J. G. Rau, E. K.-H. Lee, and H.-Y. Kee. "Generic spin model for the honeycomb iridates beyond the Kitaev limit". In: *Physical Review Letters* 112.7 (2014), p. 077204.

[2] E. K.-H. Lee and Y. B. Kim. "Theory of magnetic phase diagrams in hyperhoneycomb and harmonic-honeycomb iridates". In: *Physical Review B* 91.6 (2015), p. 064407.

[3] J. Luttinger and L. Tisza. "Theory of dipole interaction in crystals". In: *Physical Review* 70.11-12 (1946), p. 954.

[4] D. Lyons and T. Kaplan. "Method for determining ground-state spin configurations". In: *Physical Review* 120.5 (1960), p. 1580.

[5] S. Kirkpatrick, C. D. Gelatt Jr, and M. P. Vecchi. "Optimization by simulated annealing". In: *Science* 220.4598 (1983), pp. 671–680.

[6] S. Blundell. *Magnetism in Condensed Matter*. Oxford University Press, 2001.

[7] H. Rohrer and H. Thomas. "Phase transitions in the uniaxial antiferromagnet". In: *Journal of Applied Physics* 40.3 (1969), pp. 1025–1027.

[8] A. Bogdanov, A. Zhuravlev, and U. Rößler. "Spin-flop transition in uniaxial antiferromagnets: Magnetic phases, reorientation effects, and multidomain states". In: *Physical Review B* 75.9 (2007), p. 094425.

[9] W. Zhang et al. "Spin-flop transition and magnetic phase diagram in $CaCo_2As_2$ revealed by torque measurements". In: *Physical Review B* 92.14 (2015), p. 144416.

[10] P.-A. Absil, R. Mahony, and R. Sepulchre. *Optimization algorithms on matrix manifolds*. Princeton University Press, 2009.

[11] H. Sato. *Riemannian optimization and its applications*. Springer, 2021.

[12] H. Sato and T. Iwai. "A new, globally convergent Riemannian conjugate gradient method". In: *Optimization* 64.4 (2015), pp. 1011–1031.

[13] S. Toth and B. Lake. "Linear spin wave theory for single-Q incommensurate magnetic structures". In: *Journal of Physics: Condensed Matter* 27.16 (2015), p. 166002.

5

Canted antiferromagnetic magnetic order in honeycomb α-Na_2PrO_3 revealed by single crystal torque measurements

Contents

5.1 Introduction **64**
5.2 Crystal Structure **65**
5.3 Single Ion Physics **70**
5.4 Previous Reports **73**
5.5 DC Field Torque Magnetometry up to 4T **73**
5.6 Magnetic Structure **79**
5.7 Exchange Parameters and Models **83**
5.8 Powder Magnetisation in Pulsed Field up to 60T **91**
5.9 DC Field Torque Magnetometry up to 35T **93**
5.10 Conclusions **97**

Abstract *The honeycomb antiferromagnet α-Na_2PrO_3 has recently attracted interest as a candidate to display unconventional magnetic behaviour from bond-dependent Kitaev interactions between $4f$ Pr^{4+} ($j_{eff} = 1/2$) moments, complementary to much explored honeycomb iridates and α-$RuCl_3$. Recently, single crystals have been synthesised with no evidence for stacking faults or site mixing, and show a sharp transition to long-range magnetic order at low temperatures, consistent with previously reported powder measurements. Using highly-sensitive piezocantilever torque measurements on untwinned single-grain crystals I observe strongly contrasting angular dependence of the torque in three orthogonal crystallographic planes, which can be naturally explained by a non-collinear, canted magnetic structure and I propose a minimal anisotropic exchange model to explain its stability, compatible with the crystal structure symmetry. I also report torque measurements up to 35T, revealing a spin-flop transition consistent with the minimal model, and observe non-monotonic field dependence of crossover between spin-flop and paramagnetic phases.*

5.1 Introduction

In the Kitaev model [1] on a honeycomb lattice, spin ½ moments interact with their nearest neighbours by Ising interactions along mutually orthogonal directions for the three bonds meeting at each site in a honeycomb. This model is interesting in that it is exactly solvable, with a quantum spin liquid ground state and exotic excitations, very different from the conventional spin-waves of ordered magnets. Strong spin-orbit coupling is needed in order for a system to host these bond-dependent interactions, this has meant that $4d$ and $5d$ electron systems have been proposed candidates for Kitaev physics [2–4]. Generalisations beyond this simple model include the Heisenberg-Kitaev (HK) model, which has been used to describe the exotic magnetic phases observed in the layered honeycomb iridates [5, 6]. A further generalisation included the symmetry allowed "symmetric off-diagonal exchange" Γ, which was used to try to explain the ground states and excitations in some of these honeycomb materials, and revealed a complex magnetic phase diagram, including a finite region of parameter space for a quantum spin liquid (QSL) phase around the exactly solvable pure-Kitaev limit [7]. Magnetic honeycomb materials have had significant theoretical interest due to their rich phase diagram. Much of this work has been in the context of the honeycomb iridates [8].

Honeycomb α-Na_2PrO_3 , with networks of edge-sharing PrO_6 octahedra was recently theoretically predicted to host strong antiferromagnetic Kitaev interactions [9], making it a promising candidate for unconventional magnetism. Studies on powder samples of the material confirm antiferromagnetic order at low temperature [10], but reported inelastic neutron scattering data do not find clear evidence of strong Kitaev interactions.

In this section, I report single-crystal X-ray structure studies, a detailed mapping of torque magnetometry with respect to field orientation up to $4\,\mathrm{T}$ consistent with a non-collinear, canted antiferromagnetic structure, torque magnetometry up to $35\,\mathrm{T}$ revealing a spin-flop transition, and powder magnetometry up to $65\,\mathrm{T}$. Finally, I suggest a minimal anisotropic exchange model which stabilises the proposed magnetic structure, is quantitatively consistent with the angular-dependent torque data in three orthogonal

planes, and predicts a spin-flop transition for field applied parallel to the $\boldsymbol{c}^*$ axis, as is seen experimentally.

5.2 Crystal Structure

Samples of α-Na_2PrO_3 were synthesised by Ryutaro Okuma at the University of Oxford. The polycrystalline samples grown contained many platelet samples with diameters $\sim 80\,\mu\mathrm{m}$. Due to the air sensitivity of the samples, they were synthesised, handled, and selected in an inert gas atmosphere, and sealed by flame in an evacuated borosilicate-glass capillary. In order to determine the crystal structure of α-Na_2PrO_3 , X-ray diffraction was performed at room temperature on single crystal samples of the material with an Mo-source Oxford Diffraction Supernova diffractometer. These measurements were performed with the sample remaining in an evacuated capillary to prevent degradation during data collection. The detailed structure was refined using FULLPROF [11] analysis software, the results of this refinement are summarised in Table 5.1 and Table 5.2, which shows a summary of the structural parameters and atomic fractional coordinates of the material's ions in the monoclinic setting. Figure 5.2 shows a comparison between observed and calculated peak intensities, the small disagreement of a few points at large $|F|^2$ is likely caused by uncorrected absorption from the glass capillary.

Figure 5.1**a, b)** show a comparison between the experimentally observed single-crystal diffraction pattern and calculated Bragg peak intensities for the $0kl$ reciprocal lattice plane, for a representative, untwinned, plate-like sample of $\approx 80\,\mu\mathrm{m}$ diameter. The crystal structure parameters used in the calculation are those in Table 5.1. X-ray diffraction reveals an overall $C2/c$ space group, with two honeycomb networks of edge-sharing PrO_6 octahedra per unit cell separated by layers of Na^+ions in a hexagonal lattice, in approximate agreement with previously reported structural studies on powders of α-Na_2PrO_3 [12]. A key difference observed in single crystal data is a significant different in parameters c and γ, which in powder data are reported as $c = 11.749(2)$ Å, $\gamma = 110.09(1)^\circ$. This difference can be attributed to the fact that powder structure is sensitive primarily to inter-plane distance $c\sin\gamma$, this inter-plane distance agrees very closely with the data observed in single crystals. The structural refinement of this single

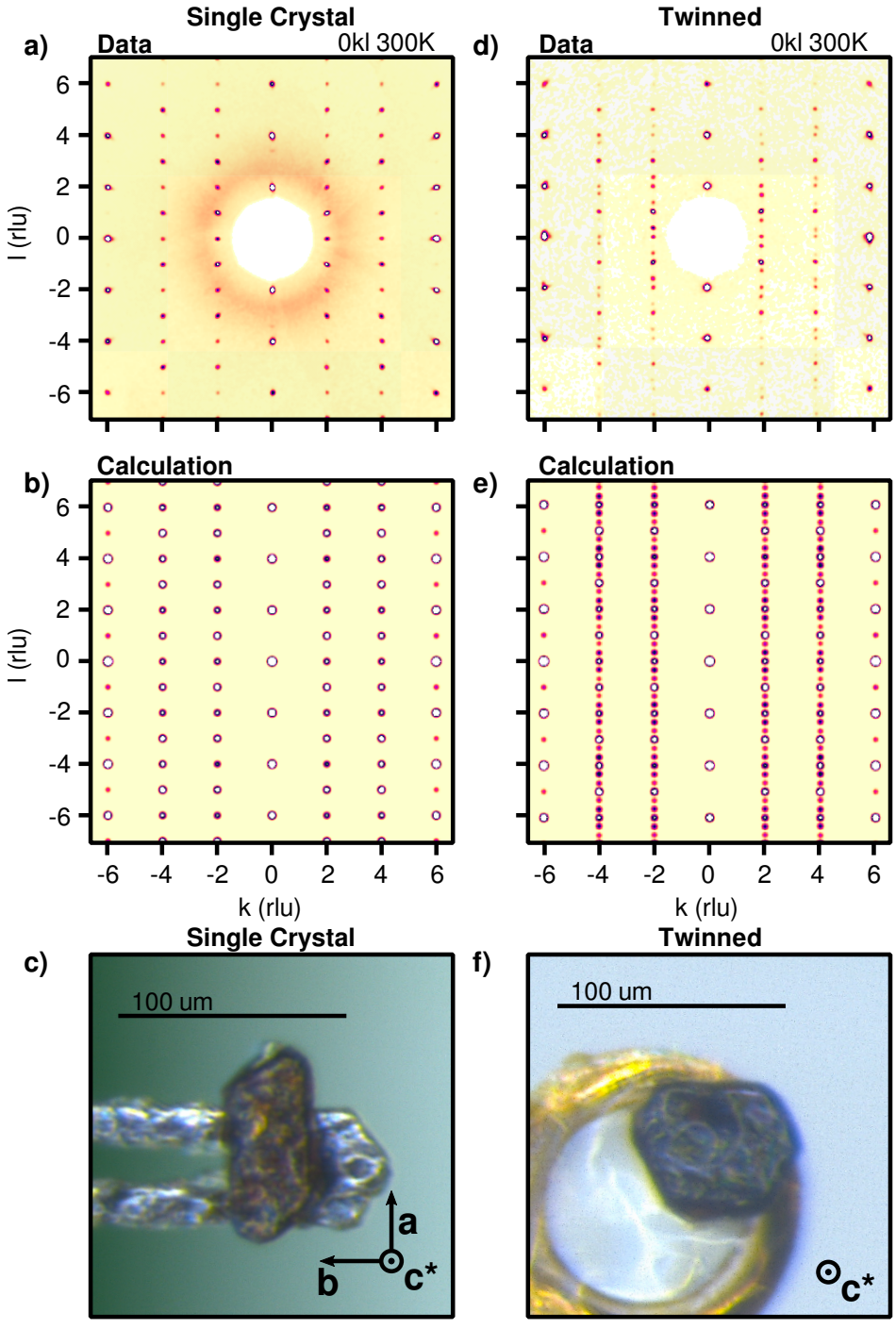


Figure 5.1: a, b) Single crystal, **d, e)** twinned crystal X-ray diffraction pattern in the $0kl$ reciprocal lattice plane. **a, d)** show experimental data measured at 300 K, **b, e)** show calculated Bragg peak intensities. Both colour-maps are on a log scale. **c, f)** show photographs of untwinned single crystal and crystal with twins rotated $\pm 120^\circ$ around the $\boldsymbol{c}^*$ axis respectively. Calculations are for crystal structure with parameters in Table 5.1.

Table 5.1: Refined structural parameters of α-Na_2PrO_3 space group $C2/c$ in conventional monoclinic setting with 2-fold axis $\parallel$ $\boldsymbol{b}$ and an inversion centre at the origin. Isotropic thermal displacement parameter U_{iso} has units (10^{-3}Å^2). Anisotropic displacement parameters can be found in Table 5.2. Error estimates from FULLPROF [11] refinement in parentheses.

Space group: $C2/c$ (15)					
Z = 8					
Cell parameters:					
a, b, c (Å)		5.957(2)	10.332(2)	11.20(2)	
α, β, γ (°)		90	90	100.39(2)	
Volume (Å^3)		678.0(4)			
Atomic fractional coordinates:					
Atom	Wyckoff Site	Site Symmetry	x	y	z	U_{iso}
$Pr^{4+}(1)$	4e	2	0	0.24901(7)	0.25	6.0(4)
$Pr^{4+}(2)$	4e	2	0	0.58174(7)	0.25	5.4(4)
$Na^{+}(1)$	4e	2	0.5	0.4162(5)	0.25	5(3)
$Na^{+}(2)$	8f	1	0.7367(7)	0.4214(4)	0.0001(4)	14(2)
$Na^{+}(3)$	4c	$\bar{1}$	0.25	0.25	0	15(3)
$O^{2-}(1)$	8f	1	0.8560(12)	0.0975(7)	0.3601(7)	9.2(18)
$O^{2-}(2)$	8f	1	0.6472(11)	0.2323(7)	0.1433(6)	7.7(14)
$O^{2-}(3)$	8f	1	0.0980(11)	0.4158(6)	0.1431(6)	7.3(14)

Table 5.2: Anisotropic displacement parameters of α-Na_2PrO_3 in units of 10^{-3}Å^2 in conventional monoclinic setting. Atom labels are the same as in Table 5.1. Error estimates from FULLPROF [11] refinement in parentheses.

Atom	U_{11}	U_{22}	U_{33}	U_{12}	U_{13}	U_{23}
$Pr^{4+}(1)$	5.9(4)	4.8(4)	7.3(4)	0	1.0(3)	0
$Pr^{4+}(2)$	4.9(4)	4.5(4)	6.9(4)	0	0.9(3)	0
$Na^{+}(1)$	1(2)	2(2)	12(3)	0	1(2)	0
$Na^{+}(2)$	15(2)	18(2)	10(2)	3.3(19)	-0.6(17)	-2(2)
$Na^{+}(3)$	17(3)	15(3)	14(3)	1(3)	5(3)	6(3)

crystal data showed no evidence of the atomic site-mixing reported in powder samples [10, 12]. The C centring results in a $h + k = 2n(n \in \mathbb{Z})$ selection rule, which can be seen in Fig. 5.1**a, b)** as systematic absences at odd k. The broad rings of scattering intensity at small scattering wave-vector $|\boldsymbol{Q}|$ is attributed to scattering from the amorphous glass capillaries. The refined crystal structure can be seen in Figure 5.3, where the two inequivalent Pr^{4+}sites are coloured different shades of blue. This shows the layer stacking of the two honeycomb layers.

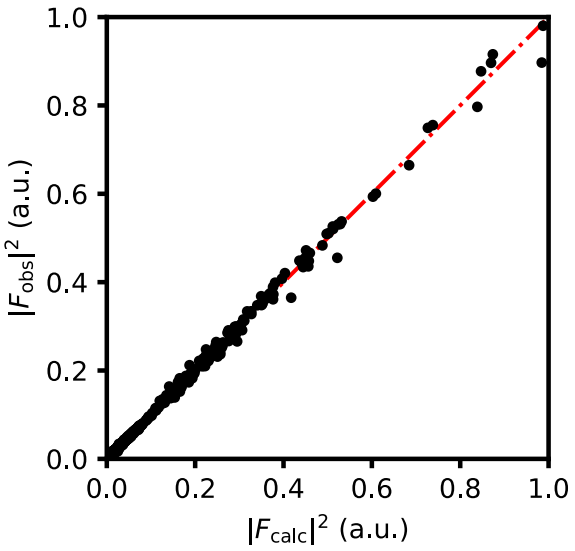


Figure 5.2: Observed vs calculated Bragg peak intensities where dashed line shows 1:1 agreement. Calculated Bragg peak intensities using FULLPROF [11] with parameters in Table 5.1.

Untwinned single crystals of α-Na_2PrO_3 could be identified by their sample morphology, shown Fig. 5.1**c)**. Samples grew as natural plate-like elongated hexagons, with three pairs of equal length and parallel sides. In the standard morphology, the $\boldsymbol{c}^*$ axis is parallel to the plate normal, the $\boldsymbol{a}$ direction within the plate could be identified as parallel to the long edges in the crystal. The largest untwinned single crystals were $\approx 120\mu m$ on their long edge. Most samples grown were $\approx 10\mu m$ thick.

In addition to untwinned single crystals, batches of α-Na_2PrO_3 consistently contained twinned samples. Commonly these contained twins rotated $\pm 120^\circ$ around the $\boldsymbol{c}^*$ axis. This effect can be seen in the X-ray diffraction data as additional reflections on the $(0kl)$ families of Bragg peaks at $l = n \pm 1/3$ $(n \in \mathbb{Z})$ as observed in Figure 5.1**d,e)** which shows a comparison between experimental twinned single-crystal diffraction pattern and calculated Bragg peak intensities for a twinned sample with equal weight twins rotated $\pm 120^\circ$ around the $\boldsymbol{c}^*$ axis. The crystal structure parameters used in the calculation are those in Table 5.1. These twinned crystals could be identified by their morphology, as they would grow in a much more symmetric hexagonal plate shape than the untwinned sample. A comparison between twinned and untwinned crystal morphologies can be seen in Fig 5.1**c,f)**. All torque measurements reported in this chapter were performed on untwinned single crystals of α-Na_2PrO_3 .

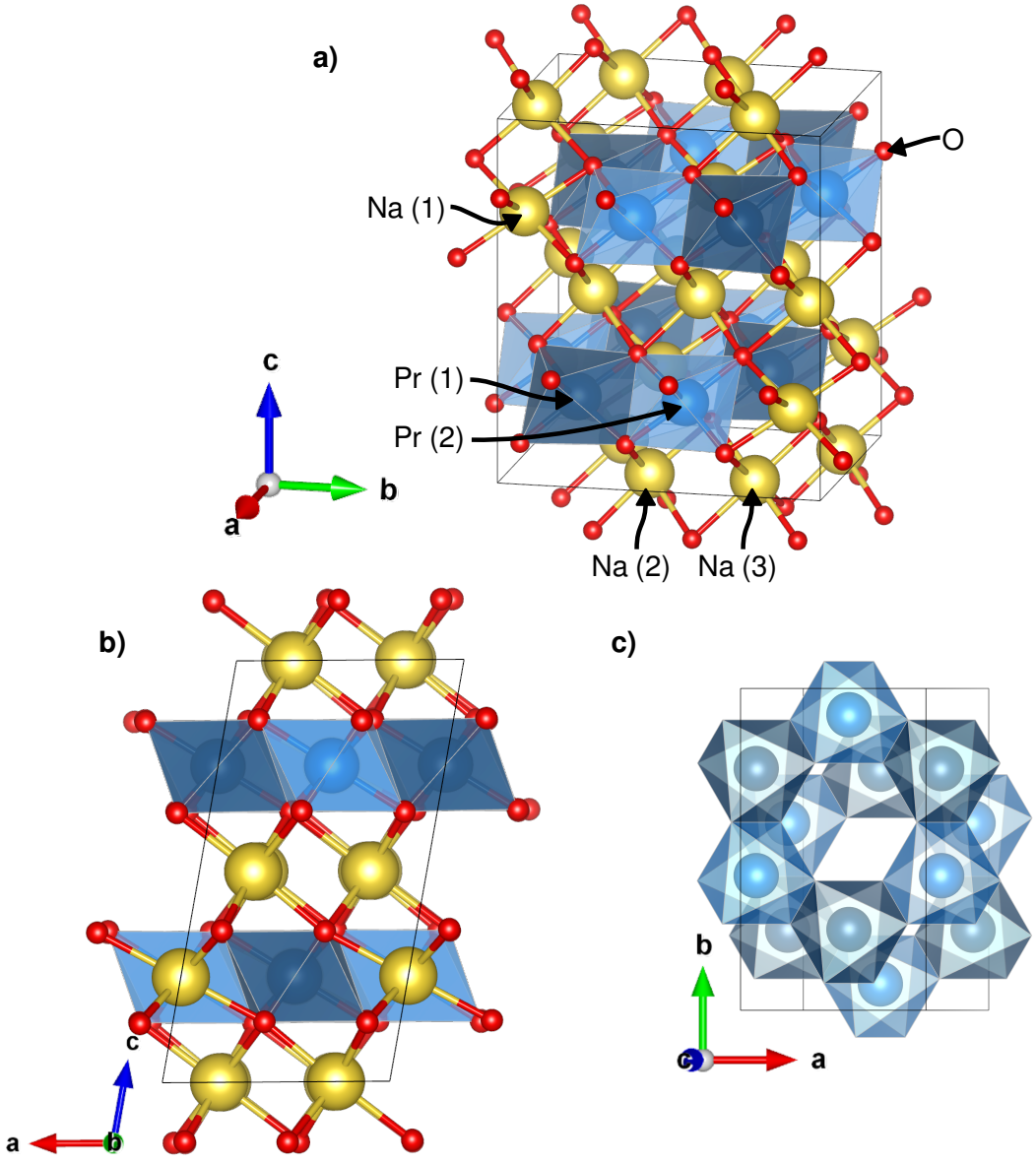


Figure 5.3: Model showing the crystal structure of α-Na_2PrO_3 in the monoclinic setting. Light and dark blue spheres indicate the two structurally inequivalent Pr^{4+}ions, yellow spheres indicate Na^{+}ions, red spheres indicate O^{2-}ions. The thin lines show the outline of the monoclinic structural unit cell, while the red, green, and blue triad of arrows shows directions of the monoclinic lattice vectors $\boldsymbol{a}, \boldsymbol{b}, \boldsymbol{c}$. **a)** Shows isometric view, **b)** shows projection into $\boldsymbol{ac}$ plane, **c)** shows only Pr^{4+}ions projected into honeycomb $\boldsymbol{ab}$ plane.

α-Na_2PrO_3 is structurally very similar to other layered honeycomb materials such as Na_2IrO_3 [13], α-Li_2IrO_3 [14], and α-$RuCl_3$ [15]. All three materials display rods of diffuse scattering intensity along the layer stacking direction, attributed to layer stacking faults [16]. Surprisingly, the majority of untwinned samples of α-Na_2PrO_3 showed no diffuse rods of scattering, or other evidence of stacking faults. This is interesting as the honeycomb Pr^{4+}layers are separated by a hexagonal layer of Na^{+}ions, similar to α-Li_2IrO_3 , and so dislocations of the honeycomb layers in the $\boldsymbol{ab}$ plane might be expected as observed in [13–15]. This is unlike the case of powder samples of α-Na_2PrO_3 , which do show evidence of stacking faults [10], and site mixing [12]. The apparent much lower rate of stacking faults in untwinned single crystals of α-Na_2PrO_3 compared to similar materials suggests a very high degree of structural ordering of the layers. This may be related to the different layer stacking in α-Na_2PrO_3 , with two layers per unit cell interlocked with an offset along $\boldsymbol{b}$, perhaps providing a higher energy of interlayer bonding to ensure stacking faults are less frequent.

An interesting structural motif in α-Na_2PrO_3 is that the fractional spacing between the $Pr^{4+}(1)$ and $Pr^{4+}(2)$ sites along the $\boldsymbol{b}$ axis $d_1 \approx 0.3327(2) \approx 1/3$. Similarly, the distance between the $Na^{+}(2)$ and $Na^{+}(3)$ along the $\boldsymbol{b}$ axis $d_2 \approx 0.3286(4) \approx 1/3$, a similar pattern exists for the O^{2-}sites. The consequence of this is a systematic weakness in the intensity of reflections at $k = 6n (n \in \mathbb{Z})$ (l odd) and $k = 6n + 3 (n \in \mathbb{Z})$ (l even). This can be clearly seen in the X-ray diffraction data in Fig. 5.1.

5.3 Single Ion Physics

The magnetic ions in α-Na_2PrO_3 are Kramers $4f^1$ Pr^{4+}ions, with a Hund's rules ground state of $L = 3$, $S = 1/2$, ^2F. Spin-orbit coupling is described by the Hamiltonian

$$\hat{\mathcal{H}}_{\text{SO}} = \lambda \hat{\boldsymbol{L}} \cdot \hat{\boldsymbol{S}} \tag{5.1}$$

over this 14-fold degenerate manifold of states. Here, $\lambda > 0$ because the shell is less than half full. This can then be diagonalised, coupling the L and S states together into $J = |L - S|, |L - S| + 1, ..., L + S$ states. In these ions, this splits the ^2F manifold into a $^2F_{5/2}$ sextet with energy -2λ and a $^2F_{7/2}$ octet at $\frac{3}{2}\lambda$, which form the free-ion energy levels of Pr^{4+}ions.

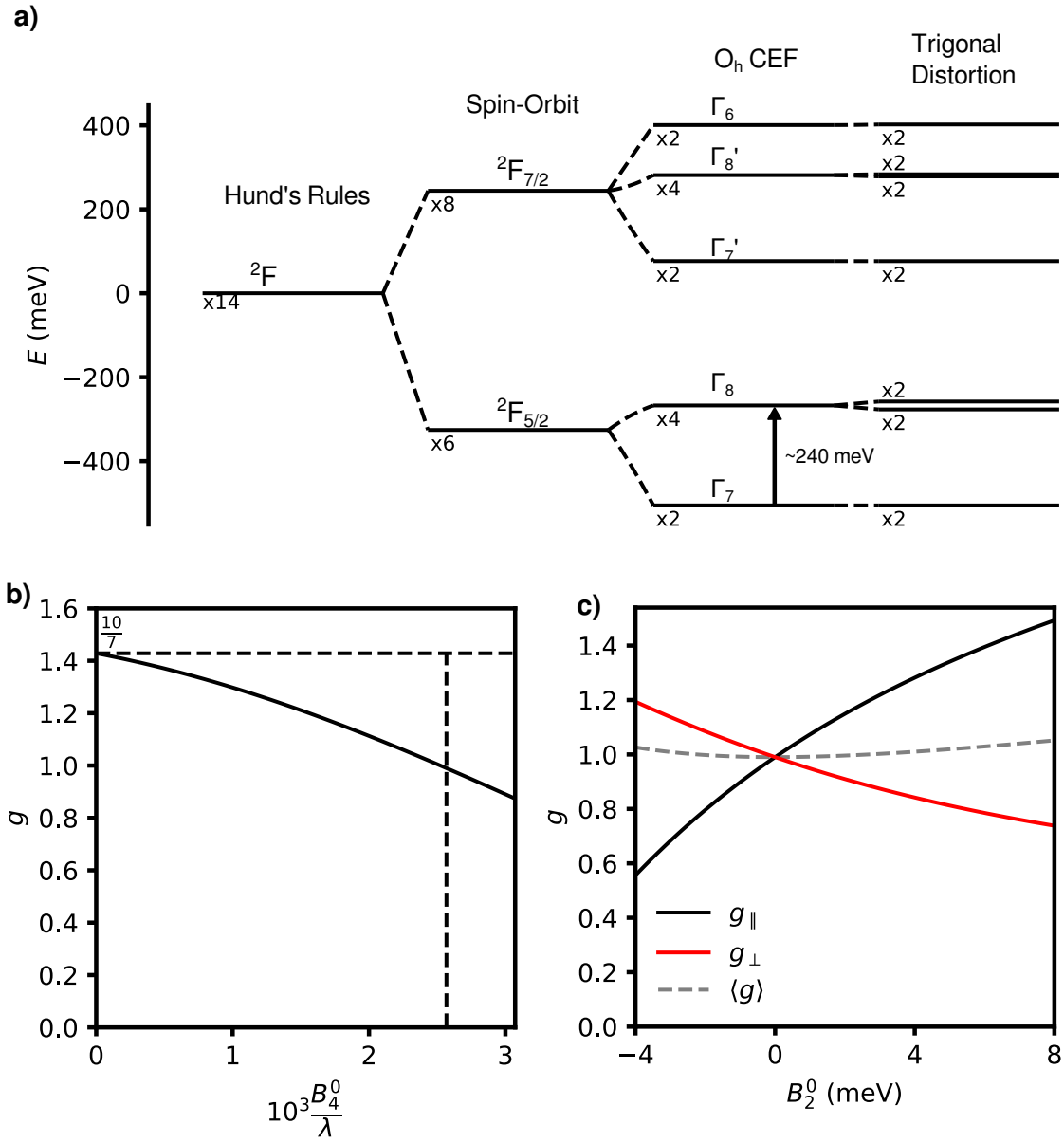


Figure 5.4: a) Schematic diagram showing the level splitting of an isolated Pr^{4+} ion in the presence of spin-orbit coupling, octahedral cubic O_h crystal field environment, and trigonal distortion. Labels on states show good quantum numbers for those levels, and degeneracy of that manifold of states. **b)** Dependence of isotropic g on the cubic octahedral crystal field parameter B_4^0, vertical line marks nominal value of $B_4^0 \approx 2.5 \times 10^{-3}\lambda$ used in the panel **a)** and discussed in the text. **c)** For B_4^0 fixed at this value, dependence of anisotropic g factors on the trigonal distortion parameter B_2^0 ($g_\parallel$ along $\boldsymbol{c}^*$, $g_\perp$ in $\boldsymbol{ab}$ plane, $\langle g \rangle$ powder average).

In a crystal, the effect of the crystal-electric field (CEF) also has to be considered. In α-Na_2PrO_3 , the Pr^{4+}ions are in an octahedral environment of oxygens. If this octahedron is treated as cubic, the octahedral crystal field Hamiltonian $\hat{\mathcal{H}}_{\text{OCF}}$ can be written in terms of Stevens operators O_k^q [17, 18].

$$\hat{\mathcal{H}}_{\text{OCF}} = B_4^0(O_4^0 + 5O_4^4) + B_6^0(O_6^0 - 21O_6^4) \tag{5.2}$$

where for $Pr^{4+}$the ratio between the two cubic crystal field parameters $B_6^0 \approx -0.004B_4^0$ [19]. The ${}^2F_{5/2}$ free-ion sextet is split into a Γ_7 doublet ground state and a Γ_8 quartet excited state [9], where the multiplets are labelled by the irreducible representation they transform as in the O_h point group. This ground state doublet is a Kramers pair and can be treated as a pseudospin with an effective spin of $1/2$, as illustrated in Fig. 5.4. The transition energy between the ground state and the excited quartet is measured directly at $E \approx 240\,\text{meV}$ by low $|\boldsymbol{Q}|$ inelastic neutron scattering [10]. The ${}^2F_{7/2}$ manifold will split into three multiplets as ${}^2F_{7/2} = \Gamma_6 \oplus \Gamma_7 \oplus \Gamma_8$ in order of increasing energy [9, 19] as illustrated in Fig. 5.4. If this cubic octahedral field is treated as a perturbation on the spin-orbit ground state i.e. $\lambda \gg B_4^0$, then the g-factor of the ground state doublet is exactly $\frac{10}{7}$ [20]. As the strength of spin-orbit coupling is made weaker, or equivalently the value of B_4^0 is made larger, this value of g decreases, as shown in Fig. 5.4**b)**. The value of B_4^0 is fixed to $B_4^0 \approx 0.42\,\text{meV}$ to reproduce the $\approx 240\,\text{meV}$ transition to the Γ_8 multiplet [10]. With this value fixed, a spin-orbit coupling of $\lambda \approx 160\,\text{meV}$ reproduces the $g = 0.98$ powder average observed in temperature-dependent magnetic susceptibility measurements [10], extracted from a fit to Curie-Weiss behaviour discussed in the following section. This value of λ is somewhat larger, but close to, a previously proposed free-ion value of $\lambda \approx 110\,\text{meV}$ [21].

Additional distortions of this crystal field split the quartets into doublets, but the ground state doublet is protected by Kramers degeneracy so cannot split further. For example, a symmetry allowed trigonal distortion of the form

$$\hat{\mathcal{H}}_{\text{trig}} = B_2^0 O_2^0 \tag{5.3}$$

will split both quartets, as is illustrated in Figure 5.4**a)**. Additionally, this will break the cubic symmetry and introduce single-ion anisotropy in the g-factor. The effect of this can

be seen in Fig. 5.4**c)**, which shows how a non-zero value of B_2^0 will split $g_\parallel$, measured along the $\boldsymbol{c}^*$ trigonal axis, from $g_\perp$ measured in the $\boldsymbol{ab}$ honeycomb plane. Note that the powder average $\langle g \rangle$ is not very sensitive to this value.

5.4 Previous Reports

Previously published studies on powder samples of α-Na_2PrO_3 reported structure, calorimetry, magnetometry, neutron diffraction, and inelastic neutron scattering [10, 12].

Reported field-cooled (FC) and zero-field-cooled (ZFC) temperature dependent susceptibility show a sharp anomaly at $T_N \approx 4.6\,\mathrm{K}$[10], where FC and ZFC data diverge. The strong suppression of ZFC susceptibility is indicative of dominant antiferromagnetic order, however the large enhancement in the field-cooled susceptibility alongside magnetic order suggests that a ferromagnetic component is also present in the magnetic structure. Neutron scattering at low temperatures did not observe any magnetic Bragg peaks beyond the nuclear scattering Bragg peaks. This is suggestive of a $\boldsymbol{q} = 0$ magnetic structure.

The published calorimetry data shows a cusp-like anomaly in magnetic entropy at the Néel temperature T_N [10]. This is suggestive of a second-order phase transition, which in turn indicates that any magnetic basis vectors involved in the order are described by the same irreducible representation of the paramagnetic space group [22].

5.5 DC Field Torque Magnetometry up to 4T

In order to explore the magnetic anisotropy in α-Na_2PrO_3 , I performed piezocantilever torque magnetometry measurements on $\approx 80\,\mu\mathrm{m}$ single crystals. All torque measurements reported in this section were performed untwinned single crystals of α-Na_2PrO_3 , confirmed by X-ray diffraction measurements.

Figure 5.5 shows an overview of the observed temperature and angular dependent torque measurements in the $\boldsymbol{ac}$ plane between $100\,\mathrm{K}$ and $2\,\mathrm{K}$, measured at fixed applied field magnitude of $\mu_0 H = 4\,\mathrm{T}$. At high temperatures, these measurements show an overall sinusoidal shape, with a stable equilibrium near $\mu_0 \boldsymbol{H} \parallel \boldsymbol{a}$ and an unstable

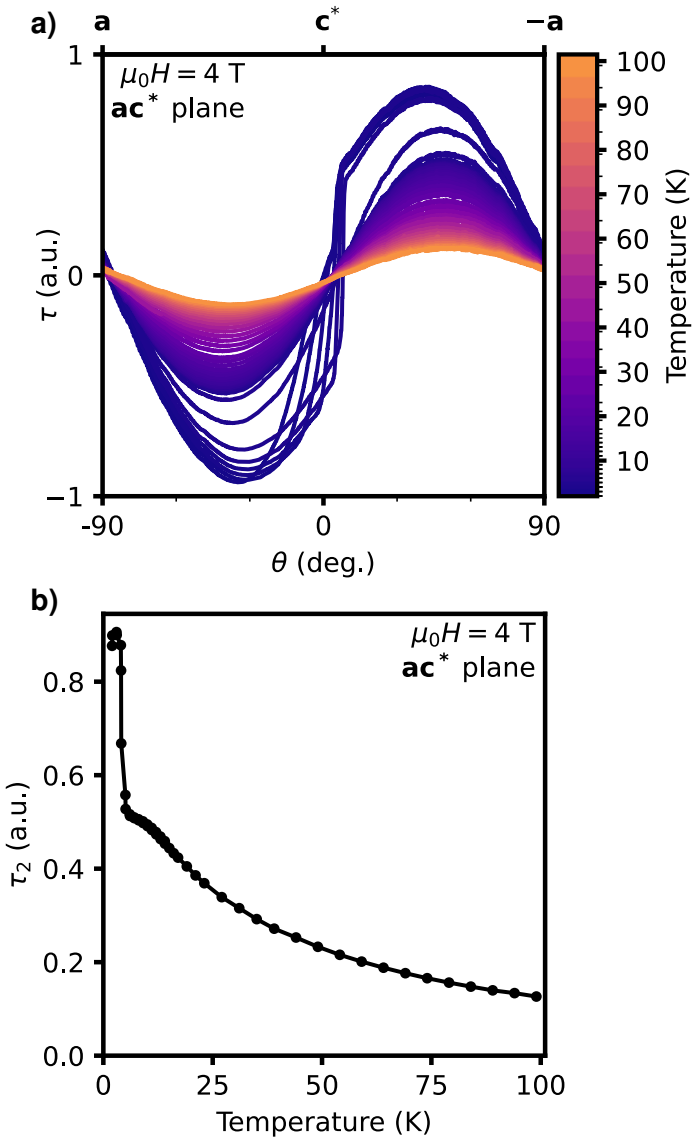


Figure 5.5: a) Angular dependence of magnetic torque in α-Na_2PrO_3 with a 4 T applied field rotated in the crystallographic $\boldsymbol{ac}$ plane and temperatures between 2 K and 100 K shown in colour between blue and yellow. **b)** Fitted amplitude of torque curves in **a)** against temperature between 2 K and 100 K with an applied field of $\mu_0 H = 4$ T. Top labels indicate field is parallel to specified crystallographic axis.

equilibrium near $\mu_0 \boldsymbol{H} \parallel \boldsymbol{c}^*$. This overall shape is consistent with the sinusoidal torque profile expected in a uniaxial paramagnetic sample [23, 24] (See Chapter 3.2):

$$\tau(\theta, T) = -\tau_2(T) \sin 2\theta \tag{5.4a}$$

$$= -\frac{1}{2} B^2 \left(\chi_{\parallel}(T) - \chi_{\perp}(T) \right) \sin 2\theta \tag{5.4b}$$

where $\chi_{\parallel}$ is the susceptibility measured parallel to the $\boldsymbol{c}^*$ out-of-plane direction and $\chi_{\perp}$ is the in-plane susceptibility. The angle θ is measured relative to the crystal $\boldsymbol{c}^*$ axis.

This suggests an order of susceptibilities

$$\chi_{\parallel} < \chi_{\perp} \tag{5.5}$$

in disagreement with the proposed values of the g-factors in [10]. This can be explained as the proposed values come from a fit of crystal-field parameters to temperature-dependant susceptibility of powder samples of α-Na_2PrO_3 . In a powder, given the number of free parameters this is under-constrained and not very sensitive to the anisotropy present. This torque data presented should be able to provide an additional constraint to the fitted CEF parameters.

These torque data are fitted to Eqn. (5.4a) and the fitted temperature-dependent amplitude $\tau_2(T)$ can be seen in Fig. 5.5**b)**. This shows that above $10\,\mathrm{K}$ the torque decreases monotonically with temperature. There is a sharp anomaly in this torque amplitude at the Néel temperature $T_N \approx 4.6\,\mathrm{K}$, below which the torque amplitude rapidly increases upon further cooling.

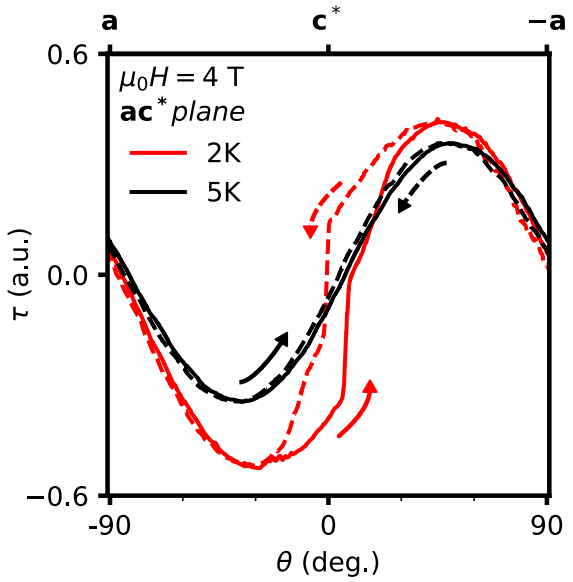


Figure 5.6: Angular dependence of magnetic torque in α-Na_2PrO_3 with a $4\,\mathrm{T}$ applied field rotated in the crystallographic $\boldsymbol{ac}$ plane at $2\,\mathrm{K}$ and $5\,\mathrm{K}$. Overlaid arrows show the sense in which data points were collected. Top labels indicate field is parallel to specified crystallographic axis.

In the low-temperature regime $T < T_N$ the torque profile is no longer fit well by the sinusoidal profile (5.4a). This can be seen most clearly in Figure 5.6 which shows

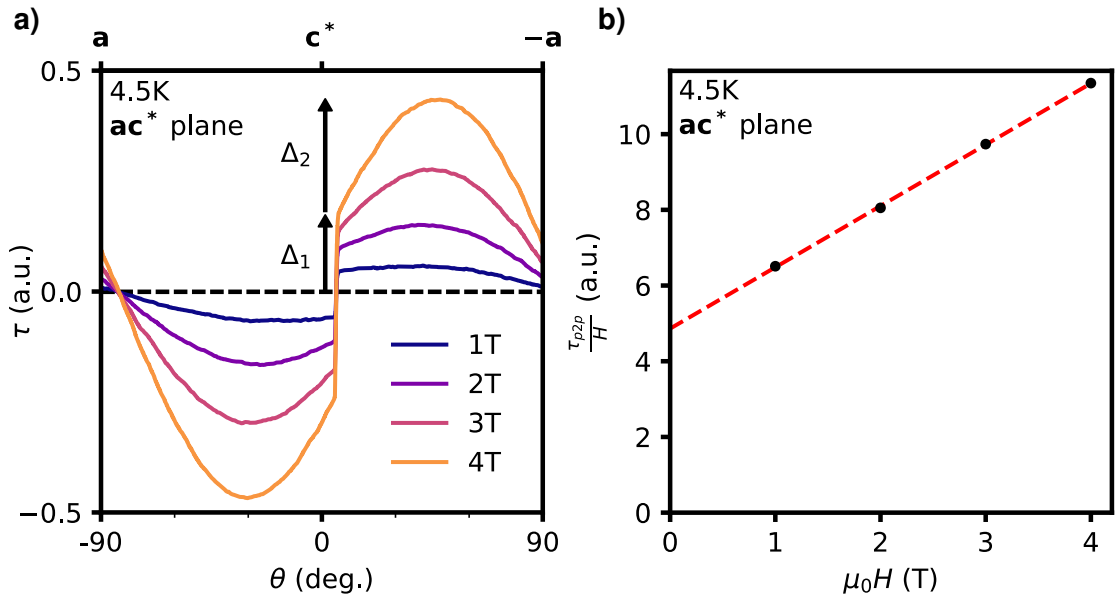


Figure 5.7: a) Angular dependence of magnetic torque in α-Na_2PrO_3 at $4.5\,\mathrm{K}$ for applied field between $1\,\mathrm{T}$ and $4\,\mathrm{T}$ rotated in the $\boldsymbol{ac}$ plane. Top labels indicate field is parallel to specified crystallographic axis. **b)** Peak to peak torque bandwidth τ_{p2p} divided by field strength H as a function of field, fitted to linear behaviour (dashed line).

a comparison between measured angle dependence of torque just above the transition at $5\,\mathrm{K}$ (black) and well below the transition at $2\,\mathrm{K}$ (red). Both rotation directions are shown, clockwise (θ increasing) as a solid line, anticlockwise (θ decreasing) as a dashed line. Above the transition the torque is sinusoidal, with the unstable equilibrium near the $\boldsymbol{c}^*$ direction, as discussed above. In this high-temperature case, the clockwise and anti-clockwise torque curves are the approximately the same, except for a small ($\sim 1^\circ$) shift in θ caused by backlash in the rotator probe. Below the transition, two main features are observed; There is significant hysteresis between the clockwise and anticlockwise rotations, and a sharp jump in torque is observed as the field crosses the $\boldsymbol{c}^*$ axis when the projection of the field onto the $\boldsymbol{a}$ axis changes sign. It should be noted that the width of the hysteresis varies significantly between samples and is larger for lower temperatures. The fact that these two effects onset sharply for $T < T_N$ is suggestive that both are associated with magnetic order.

Figure 5.7 **a)** shows the field and angular dependence of torque curves in the $\boldsymbol{ac}$ plane at $4.5\,\mathrm{K}$ between $1\,\mathrm{T}$ and $4\,\mathrm{T}$. This temperature was chosen as just below the transition the observed jump is particularly sharp and the hysteresis does not complicate the shape of

the data. These data show that there are two contributions to the bandwidth of the torque, the half-height of the torque jump Δ_1 and remaining half-height of the bandwidth Δ_2. I find that $\Delta_1 \sim H$ and $\Delta_2 \sim H^2$, suggesting that the two contributions have different origins, although both are associated with magnetic order. This scaling can be seen in the field dependence of the peak-to-peak bandwidth, visible in Fig. 5.7**b)** where $\frac{\tau_{p2p}}{H}$ is plotted against $\mu_0 H$. In a paramagnet where (5.4b) is valid, this should scale as H, with zero intercept. Instead, a linear fit to the data shows a significant non-zero intercept indicating that up to $4\,\mathrm{T}$ the torque bandwidth has the approximate form

$$\tau_{p2p}(H) = A_1 H + A_2 H^2 \tag{5.6}$$

To further explore the anisotropy of α-Na_2PrO_3 , the magnetic torque was measured in the other two orthogonal crystal planes $\boldsymbol{ab}$ and $\boldsymbol{bc}^*$. The air sensitivity of the sample, and the need for them to be exposed to atmosphere to mount them meant that remounting the same sample in these orientations was not possible. Instead, new samples were mounted. This means that, unlike in the other systems discussed in this thesis, the units of torque between different orientations are not comparable.

Figure 5.8 shows torque magnetometry data measured in the $\boldsymbol{ab}$ plane, on the sample photographed in panel **a)**. In order to mount the sample in this orientation, the sample was mounted to the side of the lever, attached by a small amount of chilled vacuum grease. Precisely aligning the $\boldsymbol{a}$ axis in this case is difficult as the orientation in the rotation plane cannot be seen during mounting. The $\phi = 0$ rotation position is nominally the $\boldsymbol{H} \parallel \boldsymbol{b}$ orientation, and is tentatively placed within 5 degrees of this.

Figure 5.8**b)** shows the angular dependence of magnetic torque measured at $\mu_0 H = 4\,\mathrm{T}$ and temperatures below and above T_N at $4.5\,\mathrm{K}$ and $8\,\mathrm{K}$ respectively. The high temperature data (black) shows a very small torque signal and no observable hysteresis. Overall at $8\,\mathrm{K}$, $\mu_0 \boldsymbol{H} \parallel \boldsymbol{b}$ is the stable equilibrium and $\mu_0 \boldsymbol{H} \parallel \boldsymbol{a}$ is the unstable equilibrium. This is attributed to a small difference in susceptibilities between the directions, caused by g-factor anisotropy $g_a < g_b$, symmetry allowed by the monoclinic structure. Below T_N (red), the torque signal is much bigger, with a clear jump in torque when the projection of the field along the $\boldsymbol{a}$ direction $\boldsymbol{H} \cdot \boldsymbol{a}$ changes sign, that is, the field crosses the $\boldsymbol{b}$ axis. A

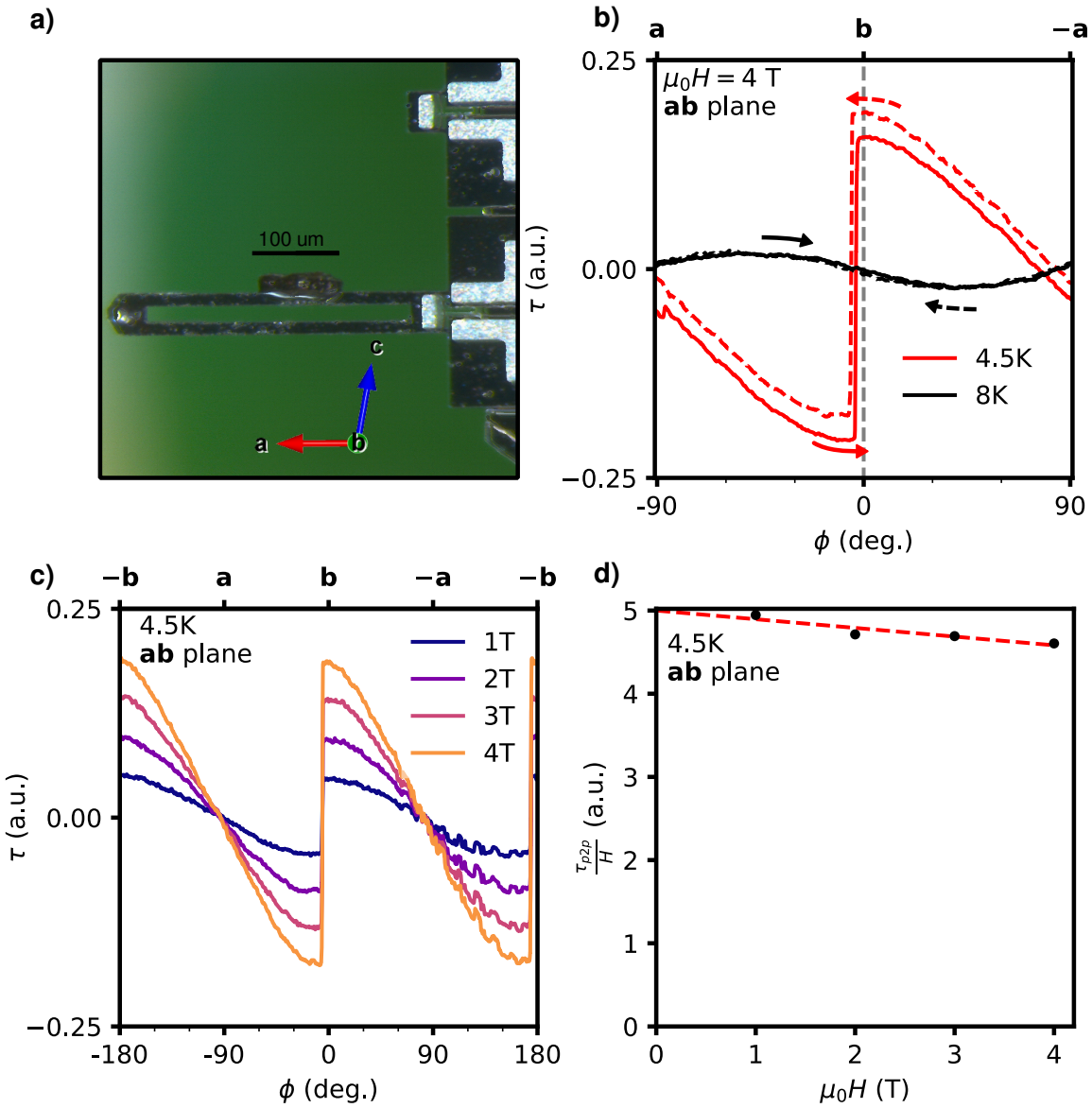


Figure 5.8: a) Photograph of mounted sample, overlaid triad of arrows shows crystallographic axes. **b)** Angular dependence of magnetic torque in α-Na_2PrO_3 with a $4\,\mathrm{T}$ applied field rotated in the crystallographic $\boldsymbol{ab}$ plane at $4.5\,\mathrm{K}$ and $8\,\mathrm{K}$. **c)** Angular dependence of magnetic torque in α-Na_2PrO_3 with applied field up to $4\,\mathrm{T}$ rotated in the crystallographic $\boldsymbol{ab}$ plane at $4.5\,\mathrm{K}$. Overlaid arrows show the sense in which data points were collected. Top labels indicate field is parallel to specified crystallographic axis. Angle ϕ is measured from the $\boldsymbol{b}$ axis. **d)** Peak to peak torque bandwidth τ_{p2p} divided by field strength H as a function of field, fitted to linear behaviour (dashed line).

small amount of hysteresis can also be seen, such that for anti-clockwise rotations the torque is more positive than for clockwise rotations, as seen above in the $\boldsymbol{ac}$ plane. This indicates that the material feels a torque opposing the rotation in field, and is dissipating energy, attributed to an energy cost of domain reorientation.

Figure 5.8**c)** shows the field and angular dependence of magnetic torque measured below the transition at $4.5\,\mathrm{K}$ up to $\mu_0 H = 4\,\mathrm{T}$. The same features are seen at all fields measured, with larger torque signals at higher fields. The peak-to-peak torque bandwidth τ_{p2p} can be seen in Fig. 5.8**d)**, showing that $\frac{\tau_{p2p}}{H}$ is approximately constant, demonstrating that the size of the jump is almost linear in magnetic field, as was seen in the $\boldsymbol{ac}$ plane. A small negative gradient in the linear fit is attributed to the small difference in g-factors between the two orientations, as seen in panel **b)**, causing a difference in differential susceptibility.

The final orientation to consider is the $\boldsymbol{bc}^*$ plane. The angular and temperature dependence of the magnetic torque in this plane in shown in Figure 5.9 **a)**. This shows an overall torque profile such that there is a stable equilibrium with field parallel to the $\boldsymbol{H} \parallel \boldsymbol{b}$ axis and an unstable equilibrium with field parallel to the $\boldsymbol{H} \parallel \boldsymbol{c}^*$ axis. The torque amplitudes were fitted to (5.4a), and the temperature dependence of the amplitude parameter $\tau_2(T)$ is shown in Fig. 5.9**b)**. This shows a broad peak centred at approximately $10\,\mathrm{K}$, and an anomaly at T_N, where the clockwise and anti-clockwise curves diverge. There are no jumps seen in the angular dependence of the torque, and a $\sin 2\theta$ dependence is seen at all temperatures.

5.6 Magnetic Structure

These results can be naturally explained by a minimal model with predominant antiferromagnetism along the $\boldsymbol{c}^*$ direction and a small ferromagnetic moment along the $\boldsymbol{a}$ axis. This would have a time-reversed magnetic domain with a ferromagnetic moment along the $-\boldsymbol{a}$ axis. An applied field with a non-zero projection along the $\boldsymbol{a}$ axis can select which magnetic domain is populated, so when this projection changes sign there is a jump in torque.

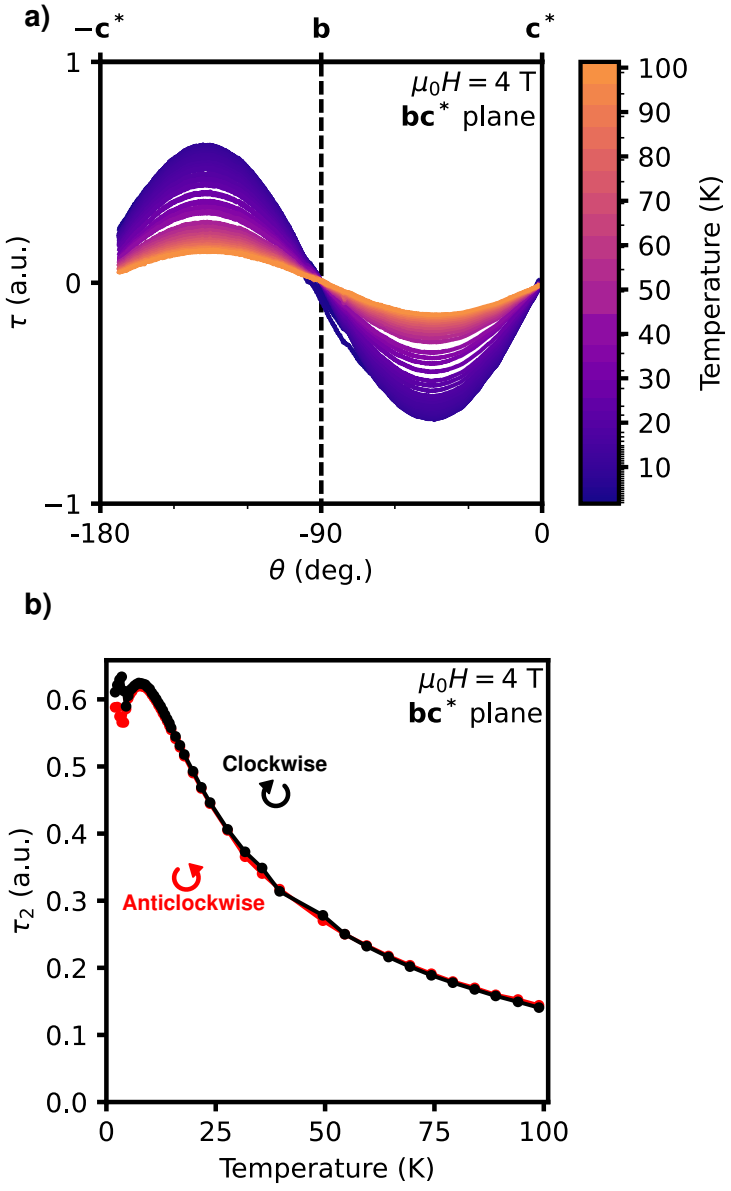


Figure 5.9: a) Angular dependence of magnetic torque in α-Na_2PrO_3 with a $4\,\mathrm{T}$ applied field between rotated in the $\boldsymbol{bc}^*$ plane between 2 and $100\,\mathrm{K}$. Top labels indicate field is parallel to specified crystallographic axis. **b)** Temperature dependence of fitted torque amplitude τ_2 in (5.4a), with angle θ measured relative to $\boldsymbol{c}^*$.

In the low-field limit, the ferromagnetic contribution to the torque can be calculated by considering the net magnetic moment as fixed in magnitude with value $\pm M$ along $\boldsymbol{a}$ for the two magnetic domains. In this case the energy is

$$E = -\boldsymbol{M} \cdot \boldsymbol{B} \tag{5.7a}$$

$$= \mp M B_x \tag{5.7b}$$

$$= \mp M B \sin\theta \tag{5.7c}$$

where θ is the angle measured from the $\boldsymbol{c}^*$ axis, and $\mp$ refer to the two magnetic domains.

The torque is then the derivative with angle

$$\tau_y = -\frac{\partial E}{\partial \theta} \tag{5.8a}$$

$$= \pm M B \cos\theta \tag{5.8b}$$

For $\sin\theta > 0$ the lower energy domain has $E = -MB\sin\theta$, for $\sin\theta < 0$ the lower energy domain has $E = +MB\sin\theta$, such that the overall energy can be written

$$E = -MB\sin\theta\,\mathrm{sign}(\sin\theta) \tag{5.9}$$

$$\tau_y = MB\cos\theta\,\mathrm{sign}(\sin\theta) \tag{5.10}$$

with a jump from $-MB$ to MB at $\theta = 0$. This can explain the linear A_1 term in (5.6), the quadratic A_2 term will come from the difference in differential susceptibility between the $\boldsymbol{c}^*$ and $\boldsymbol{a}$ directions, as in a uniaxial antiferromagnet.

To find a magnetic structure which fits this minimal description, the $\boldsymbol{q} = 0$ irreducible representations of the paramagnetic space group were considered. This is obtained from the structural space group augmented time-reversal symmetry Θ, i.e. $\Theta \otimes C2/c$. The $\boldsymbol{q} = 0$ structures have the same translational symmetry as the structural lattice, as well at the 2-fold rotation around $\boldsymbol{b}$, the c glide plane, and time-reversal, so there are 8 symmetry operations and 8 irreps. This group has irreps $\Gamma_n^{\pm}$, and $m\Gamma_n^{\pm}$ with characters under time reversal $\chi^{(\Gamma_n^{\pm})}(\Theta) = +1$,$\chi^{(m\Gamma_n^{\pm})}(\Theta) = -1$ respectively, and all other characters the same as the associated $\Gamma_n^{\pm}$ irrep of the $C2/c$ structural space group [25]. Only the $m\Gamma_n^{\pm}$ irreps have magnetic basis vectors, which must change sign under time reversal. These irreps and their magnetic basis vectors are tabulated in Table 5.3. Here the unprimed basis

vectors refer to the $Pr^{4+}(1)$ sites, and the primed basis vectors refer to the $Pr^{4+}(2)$ sites. F refers to ferromagnetic alignment of spins of the same sublattice between layers, while A refers to antiferromagnetism of spins on the same sublattice in adjacent layers.

Table 5.3: Irreducible representations (irreps) and associated magnetic basis vectors for $\boldsymbol{q} = 0$ magnetic structures, obtained from ISODISTORT [26].

Irrep	Magnetic Basis Vector
$m\Gamma_1^-$	A_y, A'_y
$m\Gamma_1^+$	F_y, F'_y
$m\Gamma_2^-$	A_x, A_z, A'_x, A'_z
$m\Gamma_2^+$	F_x, F_z,F'_x, F'_z

Previously reported calorimetry data [10] found that entropy was continuous through the transition. This is a signature of a continuous (second-order) phase transition, which in turn suggests that the magnetic order just below T_N should be described by a single irreducible representation of the high-temperature paramagnetic space group. In order to have a ferromagnetic moment along the $\boldsymbol{a}$ axis, an (F_x, F'_x) contribution is needed, described by the $m\Gamma_2^+$ irrep. In order to include the dominant antiferromagnetism along the $\boldsymbol{c}^*$ axis, an additional contribution is needed of the form $(F_z - F'_z)$. It should be noted that there is no symmetry requirement here that the ferromagnetic moment is exactly parallel to the $\boldsymbol{a}$ axis, the moments can be rotated by any angle in the $\boldsymbol{ac}$ plane and the structure will be described by the $m\Gamma_2^+$ irrep. A model of this magnetic structure can be seen in Figure 5.10.

One puzzling feature is that in this structure, with dominant antiferromagnetism along the $\boldsymbol{c}^*$ axis, one would expect substantial suppression of susceptibility for fields along $\boldsymbol{c}^*$ axis. This should be observed in torque as an enhancement in torque in the $\boldsymbol{bc}^*$ plane. That this is not seen may be because the antiferromagnetic axis is rotated away from the $\boldsymbol{c}^*$ axis. Alternatively this may indicate further complexities of the magnetic structure not captured by this minimal model. Ultimately this can be best investigated by single crystal susceptibility measurements, not currently possible due to the very small available sample size.

An alternative structure to explain dominant antiferromagnetism parallel to the $\boldsymbol{c}^*$ axis, and ferromagnetism parallel to the $\boldsymbol{a}$ axis is the (A_z, A'_z, F_x, F'_x) magnetic structure.

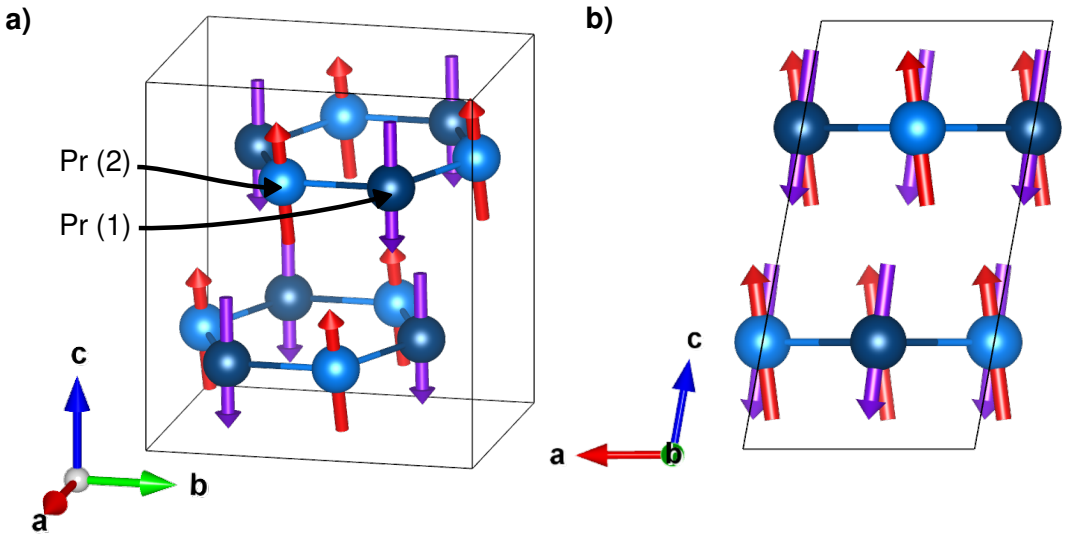


Figure 5.10: Model showing the proposed magnetic structure of α-Na_2PrO_3 in the monoclinic setting. Dark and light blue spheres indicates Pr^{4+}ions on sublattices (1) and (2) respectively. Red and purple arrows show spin orientation sublattices (1) and (2) respectively. The thin lines indicate the outline of the monoclinic structural unit cell, while the red, green, and blue triad of arrows shows directions of monoclinic lattice vectors $\boldsymbol{a}, \boldsymbol{b}, \boldsymbol{c}$. **a)** shows perspective view, **b)** shows projection onto $\boldsymbol{ac}$ plane.

This included magnetic basis vectors in different vectors, so from Landau theory [27] would suggest a first order phase transition at T_N, which is not observed.

As the two Pr^{4+}sites are not symmetry equivalent, there is no symmetry constraint that the moments on the two sites are the same. A ferrimagnetic structure, where these values are different, would naturally have a ferromagnetic and antiferromagnetic component. These components would however be along parallel vectors, for example in the $F_z - \alpha F'_z$ structure, with $\alpha \neq 1$. The antiferromagnetic staggered moment $^1/_2(1+\alpha)\hat{z}$ and the ferromagnetic component $^1/_2(1-\alpha)\hat{z}$ are parallel. This disagrees with the behaviour seen in torque, in which the jumps indicate a net moment along $\pm\boldsymbol{a}$ but the overall sinusoidal behaviour indicates antiferromagnetism along $\boldsymbol{c}^*$, and so the model can be discarded.

5.7 Exchange Parameters and Models

All calculations reported in this section were performed numerically using the `qafm` software I developed for this thesis using the principles outlined in Chapter 4.

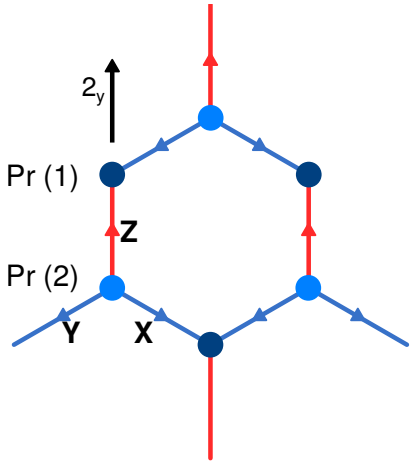


Figure 5.11: Schematic showing honeycomb bonds in the basal plane of α-Na_2PrO_3 . Different colours indicate that bonds/sites are symmetry inequivalent. Labels match those in the text.

A minimal model with only anisotropic bilinear exchange on the honeycomb bonds is able to stabilise the $\boldsymbol{q} = 0$, $(F_z - F'_z) + (F_x + F'_x)$ magnetic structure discussed above.

There are two symmetry inequivalent honeycomb bonds in the α-Na_2PrO_3 structure, labelled as $\mathbf{Z}$, and $\mathbf{X}$ in Figure 5.11. The bonds are labelled with an arrow to indicate nominal bond orientation. The third honeycomb bond in a single layer of α-Na_2PrO_3 , labelled $\mathbf{Y}$, is symmetry equivalent to the $\mathbf{X}$ bond by the 2-fold rotation axis around $\boldsymbol{y}$ labelled 2_y. Here, I am using a Cartesian frame such that $\boldsymbol{x} \parallel \boldsymbol{a}$, $\boldsymbol{y} \parallel \boldsymbol{b}$, $\boldsymbol{z} \parallel \boldsymbol{c}^*$. The $\mathbf{Z}$ bond is along the 2_y rotation axis, and so the exchange matrix is symmetry constrained to the form

$$\mathbf{Z} = \begin{pmatrix} J'_x & 0 & \Gamma' - D' \\ 0 & J'_y & 0 \\ \Gamma' + D' & 0 & J'_z \end{pmatrix} \tag{5.11}$$

where Γ' parametrises symmetric off-diagonal exchange, and D' parametrises a Dzyaloshinskii–Moriya (DM) interaction.

The $\mathbf{X}$ bond is not constrained by symmetry at all, and the tensor is completely general

$$\mathbf{X} = \begin{pmatrix} J''_x & \Gamma''_z + D''_z & \Gamma''_y - D''_y \\ \Gamma''_z - D''_z & J''_y & \Gamma''_x + D''_x \\ \Gamma''_y + D''_y & \Gamma''_x - D''_x & J''_z \end{pmatrix} \tag{5.12}$$

the $\mathbf{Y}$ bond is symmetry equivalent by the 2-fold axis and has value

$$\mathbf{Y} = \begin{pmatrix} J''_x & -\Gamma''_z - D''_z & \Gamma''_y - D''_y \\ -\Gamma''_z + D''_z & J''_y & -\Gamma''_x - D''_x \\ \Gamma''_y + D''_y & -\Gamma''_x + D''_x & J''_z \end{pmatrix} \tag{5.13}$$

in the $\boldsymbol{q} = 0$ structure, with two sublattices in each honeycomb layer (four total), the important parameter is the *effective* interaction between the sublattices, $\mathcal{J} = \mathbf{X} + \mathbf{Y} + \mathbf{Z}$ which evaluates as

$$\mathcal{J} = \mathbf{X} + \mathbf{Y} + \mathbf{Z} \tag{5.14}$$

$$= \begin{pmatrix} J'_x + 2J''_x & 0 & \Gamma' + 2\Gamma''_y - D' - 2D''_y \\ 0 & J'_y + 2J''_y & 0 \\ \Gamma' + 2\Gamma''_y + D' + 2D''_y & 0 & J'_z + 2J''_z \end{pmatrix} \tag{5.15}$$

$$= \begin{pmatrix} J_x & 0 & \Gamma - D \\ 0 & J_y & 0 \\ \Gamma + D & 0 & J_z \end{pmatrix} \tag{5.16}$$

with symmetry allowed off-diagonal terms only in $\mathcal{J}_{xz}$, including DM and symmetric off-diagonal exchange. It's worth noting that if there were a 3-fold symmetry through the Pr^{4+}site, relating all three bonds, then these off-diagonal terms would be symmetry constrained to be zero. It can therefore be concluded that the asymmetry between these bonds will be important to understanding the microscopics of the physics in any future theoretical studies of this system.

A minimal model including only these nearest-neighbour honeycomb bonds, with $J_x = J_y$, $J_z > J_x > 0$, and non-zero D, is able to stabilise the magnetic structure discussed in Section 5.6. This has dominant antiferromagnetism along the $\boldsymbol{c}^*$ axis, caused by the Ising-like antiferromagnetic XXZ exchange terms $J_z > J_x > 0$, and a small canting towards the $\boldsymbol{a}$ axis caused by the DM interaction D. The effect of the Γ term is to rigidly rotate canted spins in the $\boldsymbol{ac}$ plane, but does not change the angle between them. Because of this, it is set to zero in calculations in this section.

Calculations for this model were performed with the parameters found in Table 5.4. The values of J_x, J_z come from [10], the g-factor values are chosen such that the spin-flop transition discussed later matches the experimentally observed value, under the constraint that the powder-averaged g-factor matches the previously determined $g = 0.98$ found in powder susceptibility measurements [10]. These values for g match the order of susceptibilities seen at high temperatures $g_{xy} > g_z$. It is worth noting that the zero-field magnetic structure is insensitive to the values of g. The value of D is fit to match the

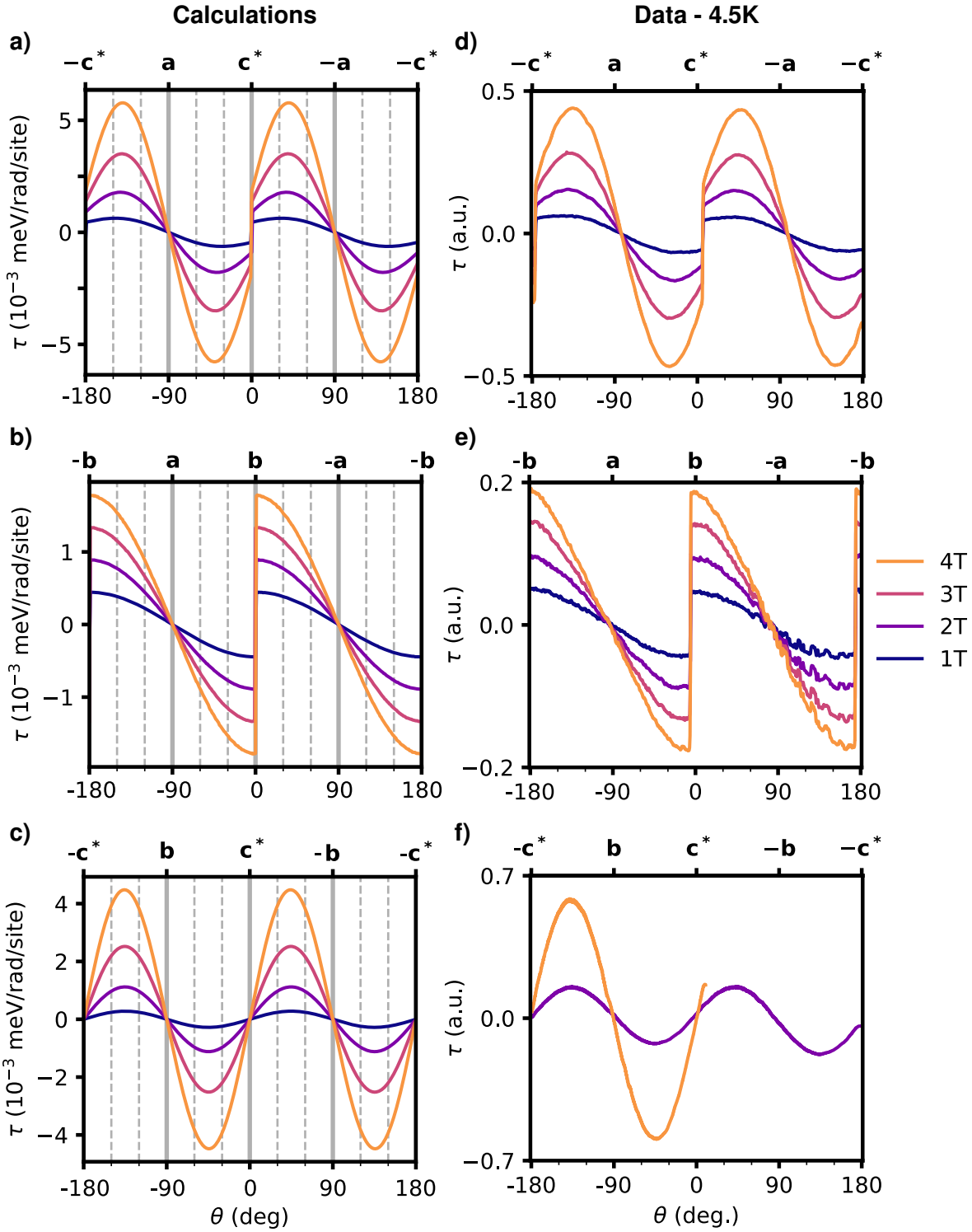


Figure 5.12: a-c) Calculation of angular dependence of magnetic torque for fields between 1 T - 4 T in the crystallographic **a)** ac, **b)** ab, **c)** bc^* planes, using parameters in Table 5.4. **d-f)** Comparison with data at same fields and orientations at 4.5 K in the **d)** ac, **e)** ab, **f)** bc^* planes, reproduced from Section 5.5. Top labels indicate field is parallel to specified crystallographic axis.

Table 5.4: Calculation parameters in a minimal model for α-Na_2PrO_3 as in (5.16)

.	$g_x = g_y = 1.09$	$g_z = 0.80$
	$J_x = J_y = 1.06\text{meV}$	$J_z = 1.22\text{meV}$
	$D = 0.1\text{meV}$	
	$\Gamma = 0$	

ratio A_1/A_2 in (5.6). These values are under-constrained in the absence of absolute units and should be taken as a rough estimate.

Figure 5.12 shows calculated angular dependence of magnetic torque for fields between $1\,\text{T}$ and $4\,\text{T}$. Alongside these calculated torque profiles are the experimentally observed torque profiles at the same magnetic fields, measured at $4.5\,\text{K}$. These show very good qualitative agreement between the calculation and the data, in all orientations measured. All features seen in the data are reproduced, including the field scaling. Fig. 5.12**b)** shows the calculated torque for the honeycomb $\boldsymbol{ab}$ plane. This shows a $\tau_z = MB\cos\theta\,\text{sign}(\sin\theta)$ angular dependence, caused by the magnetic field selecting the domain with a moment along the $\pm\boldsymbol{a}$ axis, so the jump occurs when the field projection along $\boldsymbol{a}$, $\boldsymbol{B}\cdot\boldsymbol{a}$ changes sign. Fig. 5.12**c)** shows the calculated torque for the $\boldsymbol{bc}^*$ plane. This has a sinusoidal behaviour with an overall unstable arrangement with $\boldsymbol{B} \parallel \boldsymbol{c}^*$, caused by the spins aligning along the $\boldsymbol{c}^*$ axis, as in a uniaxial antiferromagnet. Fig. 5.12**a)** shows the angular dependence in the $\boldsymbol{ac}$ plane, revealing a combination of both effects. These features are seen in both calculations and data for all three orthogonal rotation planes.

One interesting feature of this model is that a spin-flop transition is expected for field parallel to the $\boldsymbol{c}^*$ axis, much like in a conventional XXZ model (see Chapter 4). This can be seen in Figure 5.13, which shows field dependence of magnetisation for fields along the $\boldsymbol{a}, \boldsymbol{b}, \boldsymbol{c}^*$ axes. With field parallel to the $\boldsymbol{B} \parallel \boldsymbol{c}^*$ axis, for the model parameters in Table 5.4 a spin-flop transition can be seen at $B_{\text{SF}} \approx 23\,\text{T}$.

Figure 5.14 shows the field phase diagram for this model. The left panel shows the phase diagram for field orientations in the $\boldsymbol{a}, \boldsymbol{c}^*$ plane. The right panel shows the phase diagram for field orientations in the $\boldsymbol{b}, \boldsymbol{c}$ plane. The colour shows the trace of

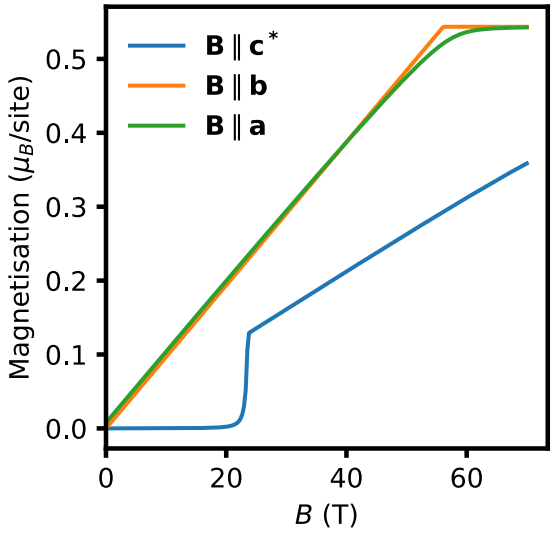


Figure 5.13: Calculated field dependence of single crystal magnetisation for α-Na_2PrO_3 with model parameters given by Table 5.4. Field is applied parallel to the $\boldsymbol{a}$, $\boldsymbol{b}$, $\boldsymbol{c}^*$ crystallographic axes.

the differential susceptibility tensor

$$\chi_{ij} = -\frac{\partial^2 \mathcal{F}}{\partial B_i \partial B_j} \tag{5.17}$$

with free energy $\mathcal{F}$, and magnetic field vector $\boldsymbol{B}$. In Landau theory this is expected to diverge at first-order phase transitions, and have a discontinuity at second-order phase transitions [27]. The extracted phase diagram is shown in panel Fig. 5.14 **b)**, where solid lines indicate sharp phase transitions, and dashed lined indicate smooth crossovers.

For field orientated in the $\boldsymbol{b}, \boldsymbol{c}^*$ plane, close to the $\boldsymbol{b}$ axis, the only phase transition is a continuous phase transition to the paramagnetic field-polarised phase at $\approx 58\,\mathrm{T}$, this phase boundary is connected to the spin-flop transition at field close to $\boldsymbol{c}^*$. The sharp angle this phase boundary makes with the $\boldsymbol{B} \parallel \boldsymbol{c}^*$ axis means that for field sweeps in the $\boldsymbol{b}, \boldsymbol{c}^*$ plane, the phase transition field will vary quickly with angle. There is no further transition to polarisation beyond the spin-flop transition field. This is because the spin-flopped phase only has one domain, the presence of DM interactions selects just one. There is therefore no symmetry breaking between the spin-flop and polarised phases. Instead there is a continuous crossover, as the magnetisation of the material approaches its saturation value asymptomatically. This is in contrast to a spin-flop phase

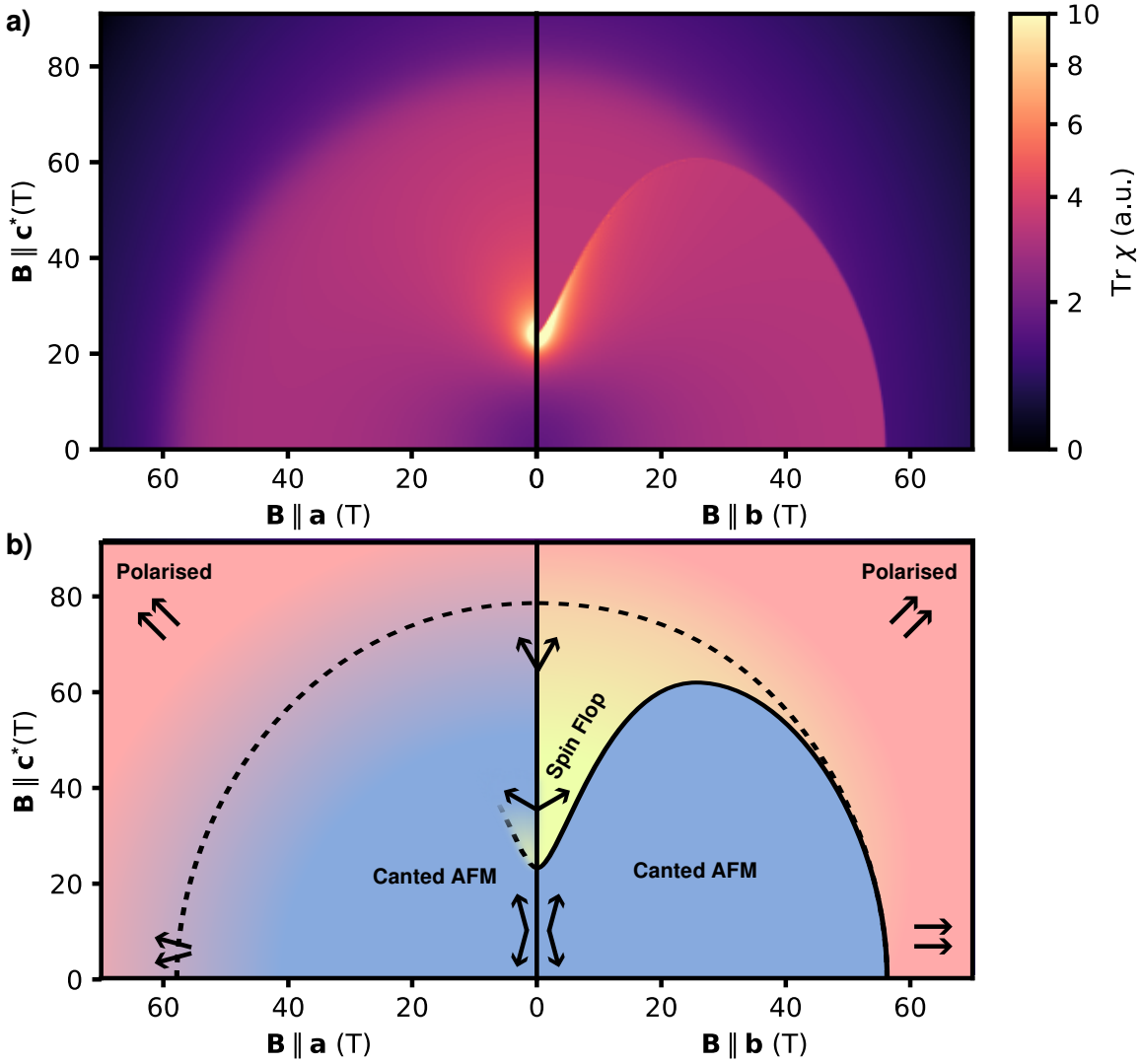


Figure 5.14: Calculated trace of the differential susceptibility tensor (see 5.17) Trχ shown in colour as a function of applied field in the $\boldsymbol{a}$, $\boldsymbol{c}^*$ plane (left panel) and $\boldsymbol{b}$, $\boldsymbol{c}^*$ plane (right panel). **b)** Extracted phase diagram from mean-field calculation for same orientation as **a)**. Coloured regions indicate named phase as described in the text. Dashed lines indicate smooth crossover regions between phases, solid lines indicate sharp phase transitions. Model parameters given by Table 5.4.

without DM, which shows a first-order spin-flop transition at a critical point, with a further continuous transition to polarisation at a higher field.

For field orientated in the $\boldsymbol{a}, \boldsymbol{c}^*$ plane, no phase transition to a polarised phase is seen in any orientation, except for $\boldsymbol{B} \parallel \boldsymbol{c}^*$ exactly which shows a spin-flop transition. This is because a finite field component along $\boldsymbol{a}$ selects one of the two time-reversed domains and so breaks the time-reversal symmetry in the material. There is no phase boundary between the canted antiferromagnet phase with some field component along $\boldsymbol{a}$, and the

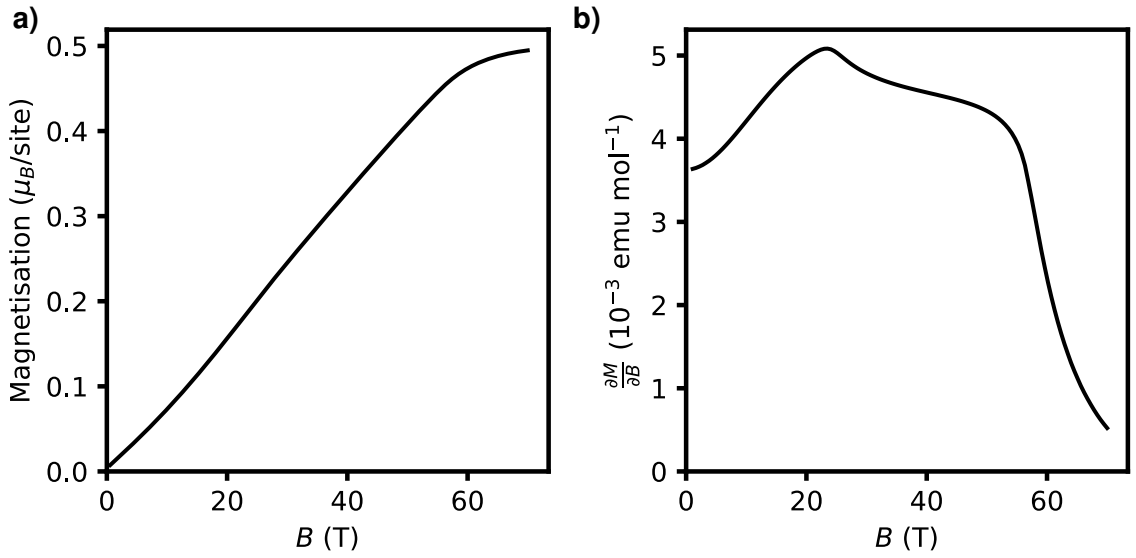


Figure 5.15: Calculated field dependence of powder **a)** magnetisation **b)** differential susceptibility for α-Na_2PrO_3 with model parameters given by Table 5.4. The hump near $24\,\mathrm{T}$ is associated with the spin-flop transition for grains with field along $\boldsymbol{c}^*$.

polarised phase. This case is similar to a ferromagnet, where a finite magnetic field breaks the time-reversal symmetry, so no phase transition is seen between the ordered and paramagnetic phase in finite field, just a smooth crossover.

This spin-flop transition also has an effect on the powder-averaged field dependence of magnetisation, shown in Figure 5.15 **a)** alongside its field gradient in Fig. 5.15 **b)**. The average was estimated by calculating field-dependent magnetisation curves for 256 field orientations evenly distributed over a sphere [28]. This shows an increase in the differential susceptibility, peaking at $24\,\mathrm{T}$, approximately at the spin-flop transition field. The magnetisation quickly flattens off with field at approximately $60\,\mathrm{T}$ upon approaching polarisation. This is not a sharp transition as in the presence of anisotropic g-factors the polarisation field is direction dependent. This shows that powder magnetisation in high magnetic fields is a useful tool for exploring this model.

An alternative minimal model which stabilises the same magnetic structure is the $J, \Gamma > 0$ model on Kitaev axes as has been explored in depth for the case of the honeycomb iridates [7], with an additional unbalanced DM interaction along the $\boldsymbol{b}$ axis. At the mean field level, this is indistinguishable from the XXZ case, as can be seen

by computing the same effective interaction between sublattices. The orthogonal transfer matrix between Kitaev axes and the x, y, z axes defined above can be written

$$P = \begin{pmatrix} -\sqrt{6}/6 & \sqrt{2}/2 & \sqrt{3}/3 \\ -\sqrt{6}/6 & -\sqrt{2}/2 & \sqrt{3}/3 \\ \sqrt{6}/3 & 0 & \sqrt{3}/3 \end{pmatrix} \tag{5.18}$$

The J, K, Γ Hamiltonian can then be written in these coordinates

$$\mathcal{H} = \sum_{\langle i,j \rangle \in \alpha\beta(\gamma)} J\boldsymbol{S}_i \cdot \boldsymbol{S}_j + KS_i^\gamma S_j^\gamma + \Gamma(S_i^\alpha S_j^\beta + S_i^\beta S_j^\alpha) \tag{5.19}$$

where the sum is over the nearest-neighbour bonds. Each bond has an associated Ising axis $\gamma \in \{x, y, z\}$ and $\alpha\beta(\gamma)$ refer to the orthogonal plane to this axis. Such that the exchange tensor for the Kitaev z axis $\mathcal{J}^z$ can be written as

$$\mathcal{J}^z = \begin{pmatrix} J & \Gamma & 0 \\ \Gamma & J & 0 \\ 0 & 0 & J+K \end{pmatrix} \tag{5.20}$$

The effective interaction between sublattices can then be written in the same coordinates as the XXZ Hamiltonian

$$\mathcal{J}' = P^T \left[\mathcal{J}^x + \mathcal{J}^y + \mathcal{J}^z\right] P \tag{5.21}$$

$$= \begin{pmatrix} J+K-\Gamma & 0 & 0 \\ 0 & J+K-\Gamma & 0 \\ 0 & 0 & J+K+2\Gamma \end{pmatrix} \tag{5.22}$$

which with $\Gamma > 0$ is equivalent to an Ising-type XXZ exchange model. In the mean-field limit, these models cannot be distinguished, even in an applied magnetic field, so long as $\boldsymbol{q} = 0$ holds, which is true for a large region of the J, K, Γ parameter space [7]. Beyond this, this model is insensitive to the presence of Kitaev interactions K. Searching for the effects of these terms will require study beyond the mean-field level, such as comparing spin-wave calculations to observed inelastic neutron scattering data.

5.8 Powder Magnetisation in Pulsed Field up to 60T

Attribution note: *Magnetometry measurements reported in this section were performed in collaboration with Matthew Pearce, and Ryutaro Okuma from the University of Oxford, and instrument scientist Yurii Skourski at the HZDR Dresden high-magnetic-field facility.*

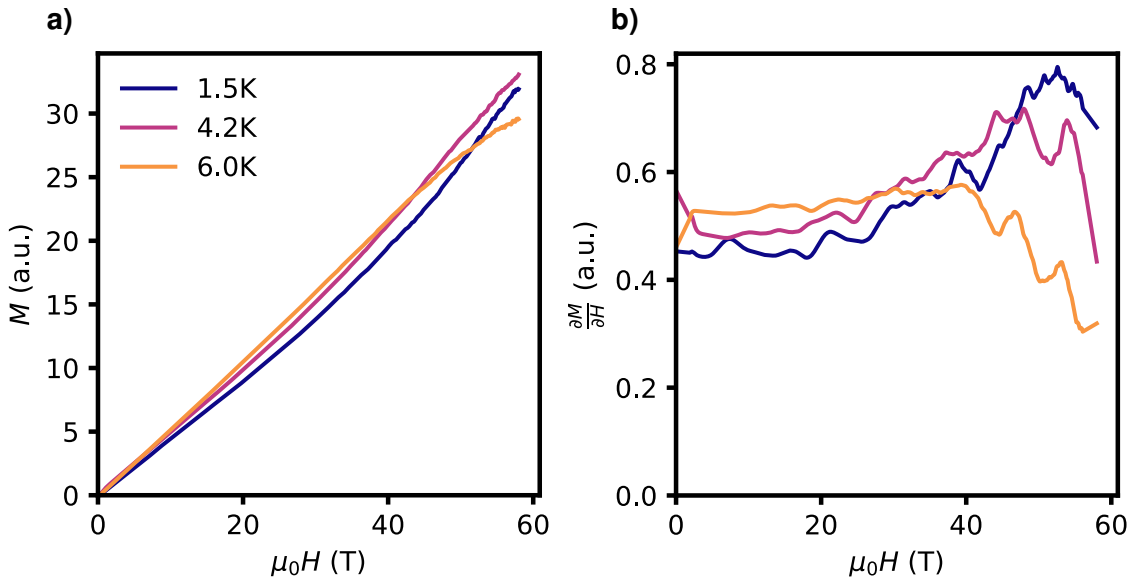


Figure 5.16: Field dependence of **a)** powder magnetisation **b)** its differential susceptibility for α-Na_2PrO_3 between $1.5\,\mathrm{K}$ and $6\,\mathrm{K}$ in pulsed fields up to $60\,\mathrm{T}$.

From the calculations above, it is clear that the situation in α-Na_2PrO_3 could be clarified with magnetisation measurements in large magnetic fields. The largest available single crystals of α-Na_2PrO_3 have a longest edge of $\approx 120\,\mu\mathrm{m}$, and a thickness of $\approx 10\,\mu\mathrm{m}$, too small for single crystal magnetisation. Co-aligning many crystals was considered, but to achieve a suitable filling factor of the extraction coil magnetometer available, several tens of thousands of crystals would need to be simultaneously aligned in a glovebox. Instead, magnetisation was performed on a powder sample of α-Na_2PrO_3 , grown by Rytaro Okuma at the University of Oxford, which could achieve an ideal filling factor of 1.

Figure 5.16 shows the field dependence of magnetisation and its derivative with field for a powder sample of α-Na_2PrO_3 with temperatures below $6\,\mathrm{K}$ and fields up to $60\,\mathrm{T}$. The differentiation is performed with a second-order Savitzky-Golay [29] filter over a window size of $4\,\mathrm{T}$. That is, in a moving window over the data of width $4\,\mathrm{T}$, a quadratic polynomial is fit to the data and the derivative is taken from the slope of the fitted curve at the centre of the window. The data are in arbitrary units. Broadly, this shows at $6\,\mathrm{K}$ a linear dependence of magnetisation with field up to $\approx 45\,\mathrm{T}$, where the magnetisation flattens off, perhaps associated with magnetic saturation. Below the transition, at the

$1.5\,\mathrm{K}$ base temperature, an overall upwards curve is observed in the magnetisation. No flattening of the curve is seen at high field, suggesting that the polarisation field is above the $60\,\mathrm{T}$ maximum available field. No clear anomaly is detected in the differential susceptibility in the region of $25\,\mathrm{T}$, associated with the spin-flop transition, seen in single crystal data (next section), and predicted by calculations of the minimal model (Fig. 5.15). The absence of a clear anomaly near the transition field value in the powder data may be due to a number of factors, such as a preferred orientation of grains with $\boldsymbol{c}^*$ perpendicular to the length of the capsule, a lack of transition caused by increased stacking faults and overall lower sample quality in powder samples of α-Na_2PrO_3 [10, 12], or a more complex Hamiltonian that makes the anomaly less prominent.

5.9 DC Field Torque Magnetometry up to 35T

Attribution note: *Torque magnetometry measurements reported in this section were performed in collaboration with Matthew Pearce and Ryutaro Okuma at the University of Oxford and Alix McCollam, Roos Leenen, and Uli Zeitler at HFML Nijmegen.*

In order to search for the predicted spin-flop transition in α-Na_2PrO_3 , single-crystal piezocantilever torque magnetometry measurements were performed in DC fields up to $35\,\mathrm{T}$. Figure 5.17 shows field sweeps close to the $\boldsymbol{c}^*$ axis, in the $\boldsymbol{ac}$ plane for temperatures between $3\,\mathrm{K}$ and $4.2\,\mathrm{K}$. Below $10\,\mathrm{T}$, these curves lie on top of each other, and the torque is approximately linear in field. This linear relationship matches the behaviour seen at low field previously. At higher fields, a sharp phase transition is seen at all measured temperatures. At lower temperature, the feature becomes sharper and increases in magnetic field. The precise location of the transition field $\mu_0 H_{\mathrm{SF}}$ is extracted by taking the derivative of the signal with field $\frac{\partial \tau}{\partial H}$ Fig. 5.17**b)**. The transition is taken as the centre of the peak in these traces, marked with arrow symbols. At the lowest temperature measured, an additional smaller peak in seen at higher field, just above $20\,\mathrm{T}$, the origin of which is unclear. At low temperatures, a significant hysteresis opens up in the magnetic torque, shown in Fig. 5.17**c)** with the field dependence of torque for two consecutive field sweeps. Below the transition field, the two upsweeps disagree significantly, but above the transition field the curves lie on on top of each other. Between the up and

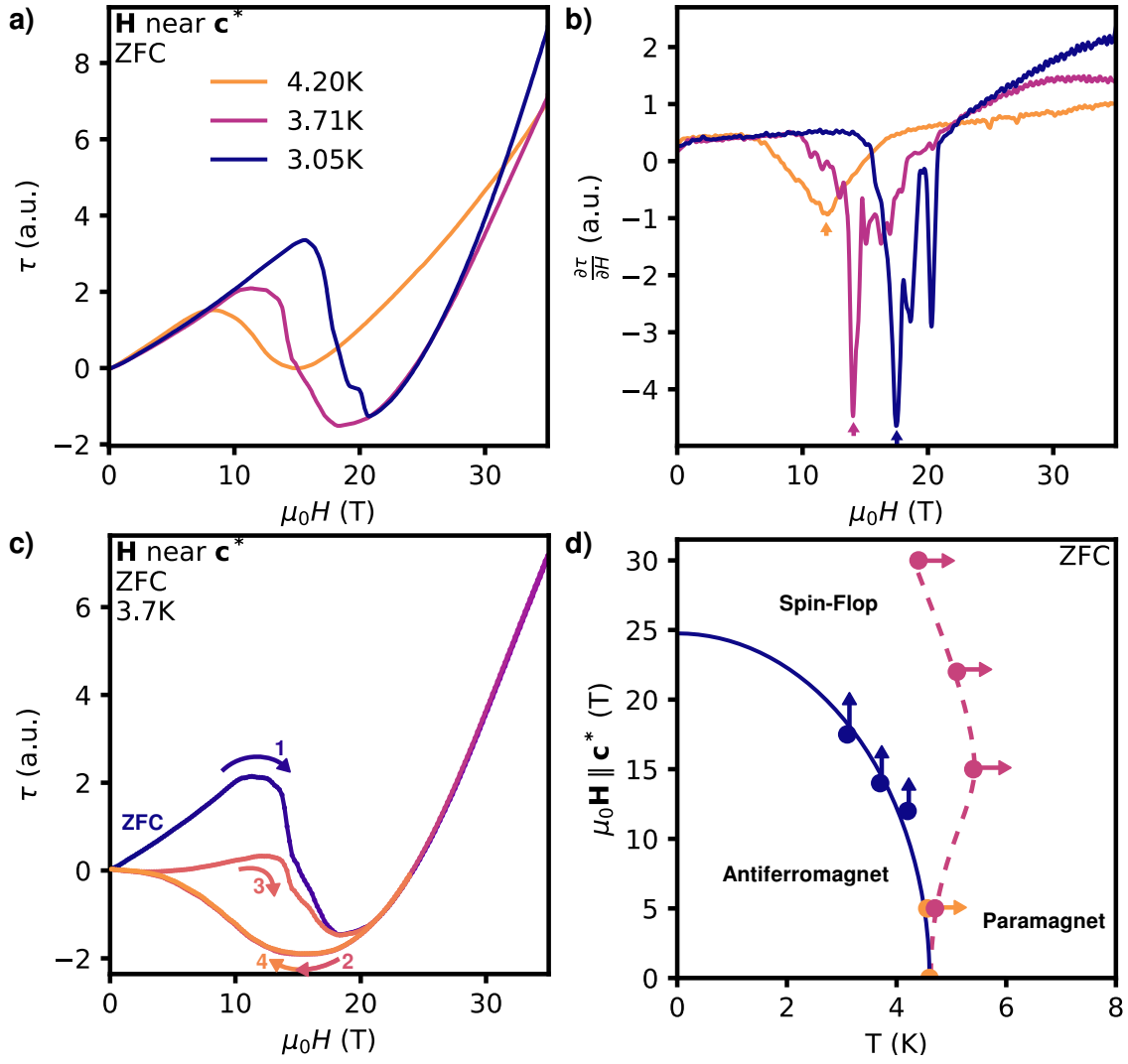


Figure 5.17: Evolution of magnetic torque with applied magnetic field near the $\boldsymbol{c}^*$ axis up to $35\,\mathrm{T}$ for temperatures between $3\,\mathrm{K}$ and $4.2\,\mathrm{K}$. **a)** Raw cantilever voltage, assumed to be proportional to the torque τ_y. **b)** Derivative of the torque with field $\frac{\partial\tau}{\partial H}$. Overlaid arrows indicate nominal transition field. **c)** Hysteresis of magnetic torque for zero-field-cooled upsweep, and subsequent downsweep, upsweep, downsweep. Colour gradient from dark to light shows continuous passage of time, arrows show sweep direction for associated curve, numbers show position in sequence of associate curve. **d)** Extracted low temperature phase diagram showing transitions to spin-flop, paramagnetic, and canted antiferromagnetic phases for fields close to the $\boldsymbol{c}^*$ axis. Lines are guides for the eye, error-bars are smaller than individual point markers. Overlaid arrows show direction in phase space of sweep which determined associated point, (upward arrows indicate field sweep shown in panel **a)**, sideways arrows indicate temperature sweeps discussed later).

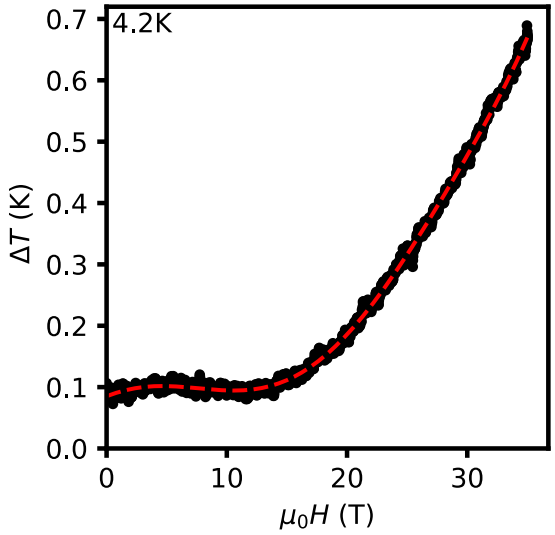


Figure 5.18: Field dependence of thermometer calibration offset measured in bath of liquid helium at $4.2\,\mathrm{K}$.

down sweep directions, hysteresis opens just above the transition field at approximately $20\,\mathrm{T}$, and closes in zero field. Both down sweeps overlap completely. These features are summarised in a phase diagram in Fig. 5.17**d)**.

A possible interpretation for this complex behaviour is as follows. The first and largest peak in $\frac{\partial \tau}{\partial H}$ is the phase transition field, where most of the sample volume transitions to the spin-flop phase. A portion of the sample is trapped in the metastable low-field AFM phase, and gradually collapses into the magnetic spin-flop ground state. The second peak in $\frac{\partial \tau}{\partial H}$, observed at $3\,\mathrm{K}$, may be due to the AFM phase becoming unstable, explaining why it is coincident with the hysteresis opening between up and down sweeps. On the down sweep, the sample remains in the metastable spin-flop phase down to lower field, where is gradually collapses into both domains of the stable AFM phase. On the second upsweep at $3.7\,\mathrm{K}$, both time-reversed domains are populated approximately equally, so the linear contributions to the field dependence of torque cancel out. Above the spin-flop transition there is only one magnetic domain, so there is no hysteresis.

Temperature sweeps in fixed fields were performed to explore the regions of the phase diagram where the phase boundary may be approximately vertical (see Fig. 5.17**d)**). In order to do temperature sweeps in high magnetic fields, the field-dependence of the sample thermometer has to be corrected. This was done by filling the cryostat

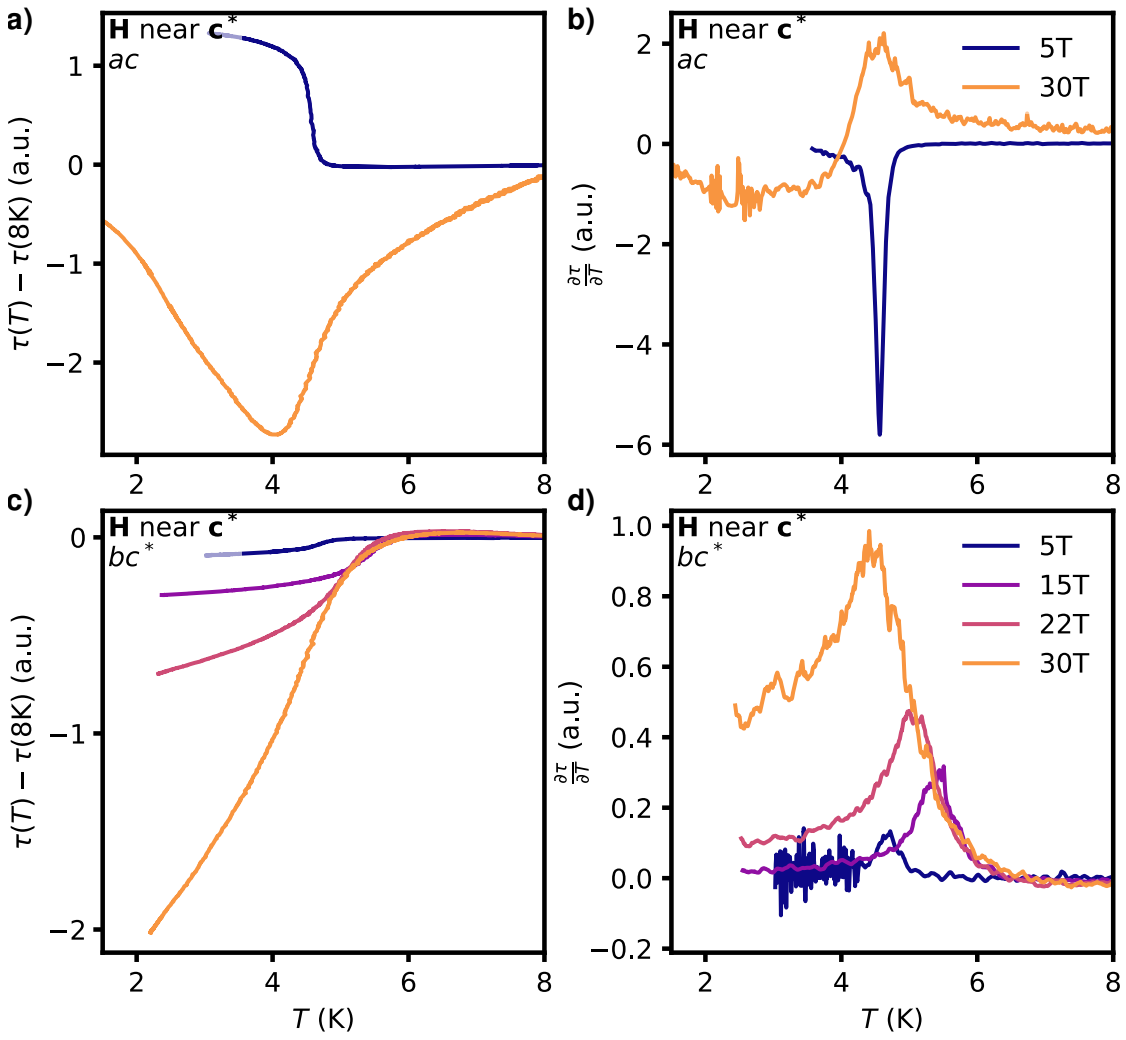


Figure 5.19: Temperature dependence of **a, c)** magnetic torque τ and **b, d)** its derivative $\frac{\partial \tau}{\partial T}$ at an applied field of $5\,\mathrm{T}$ and $30\,\mathrm{T}$ close to the $\boldsymbol{H} \parallel \boldsymbol{c}^*$ direction in the **a, b)** ac^* **c, d)** $\boldsymbol{bc}^*$ planes. Torque curves in **a, c)** are offset by their value at $8\,\mathrm{K}$.

sample volume with liquid helium at ambient pressure to fix the temperature at $4.2\,\mathrm{K}$, the offset from this is measured, and shown in Figure 5.18. This curve is used to correct the measured temperature. While there will be some temperature dependence of this correction factor, the value measured at $4.2\,\mathrm{K}$ is expected to be valid in the region of the phase transition at $4.6\,\mathrm{K}$.

Figure 5.19 shows the measured temperature dependence of magnetic torque measured at $5\,\mathrm{T}$ and $30\,\mathrm{T}$ below $8\,\mathrm{K}$. The right panels show the derivative of this with temperature. Panels **a, b)** show the torque and derive measured in the $\boldsymbol{ac}$ plane, close to $\boldsymbol{c}^*$, within 1° of the jump in torque observed in this plane. At $5\,\mathrm{T}$, this **b)** shows a very sharp peak

at $4.56(1)\,\mathrm{K}$, associated with the onset of magnetic order, this is shown with a yellow point in Fig. 5.17**d)**. At $30\,\mathrm{T}$, a broad peak is seen in torque centred at approximately $4.5(1)\,\mathrm{K}$. The peak observed at high field is the opposite sign than the one seen at low field, indicating that the stability of the system for field $\mu_0\boldsymbol{H} \parallel \boldsymbol{c}^*$ has changed. At low field it was observed that the system was unstable for $\mu_0\boldsymbol{H} \parallel \boldsymbol{c}^*$, so it is an energy maxima. At high field, it appears to be a stable equilibrium. The reason for the broad peak at $4.5(1)\,\mathrm{K}$ may be a smooth crossover from the paramagnetic to the spin-flop phase. Panels **c, d)** show the equivalent measurements made in the bc plane. This shows a broad peak in differential torque at all fields, however the location of the peak in temperature is strongly field dependent, increasing up to $5.4(1)\,\mathrm{K}$ at $15\,\mathrm{T}$. These are plotted as pink points in Fig. 5.17**d)**

It is worth considering that while the two Pr^{4+}sites are symmetry inequivalent, so the spin-flop and paramagnetic phases have the same symmetry. In a more conventional spin-flop phase (example see Chapter 4), there are two spin-flop domains from swapping the spins of the two sites. In this system, there is only one domain because of the inequivalence, the finite value of DM interaction creates an energy gap between these two domains. So as is seen above in calculations, no sharp phase boundary is expected between the spin-flop and paramagnetic phases. The existence of a broad feature in torque may indicating a smooth crossover between these regions of phase space.

5.10 Conclusions

This section primarily reports torque magnetometry experiments on high quality single crystals of α-Na_2PrO_3 up to $35\,\mathrm{T}$. Based on detailed measurements of torque as a function of field orientation in three orthogonal crystallographic planes, a model magnetic structure was proposed with dominant antiferromagnetism along the $\boldsymbol{c}^*$ axis and a small ferromagnetic moment along the $\pm\boldsymbol{a}$ axis. From this, I proposed a minimal anisotropic exchange model compatible with the crystal structure symmetry. Mean-field calculations on this magnetic model with Ising-type XXZ exchange interactions and symmetry allowed Dzyaloshinskii–Moriya interaction on the honeycomb bonds qualitatively reproduce features seen in torque at low temperature up to $4\,\mathrm{T}$ for all three rotation planes measured,

including the field scaling. I show that the magnetic structure can also be explained by a bond anisotropic $J\Gamma$ model with an unbalanced DMI, and that these two models cannot be distinguished at the mean-field level. The experimentally determined order of susceptibilities at high temperatures suggests anisotropic g-factors $g_z < g_{xy}$, in disagreement with previously proposed values from fits to powder susceptibility data. I propose a stronger spin-orbit coupling term λ to reproduce the observed powder average g and trigonal distortion to produce this g-factor anisotropy. High-field toque magnetometry measurements reveal a spin-flop transition for field along the $\boldsymbol{H} \parallel \boldsymbol{c}^*$ axis at $\mu_0 H_{\mathrm{SF}} \approx 17\,\mathrm{T}$ at $3\,\mathrm{K}$. These measurements also reveal significant hysteresis and metastability below this transition. Temperature sweeps in the same orientation reveal a broad peak in torque which may be associated with the expected crossover between paramagnetic and spin-flop regions of the phase diagram. This crossover region has a peculiar field-dependence, with a non-monotonic dependence of the temperature vs field, and maximum temperature of $T \approx 5.4\mathrm{K}$ at $15\,\mathrm{T}$. This is qualitatively similar to the predicted phase boundary in some highly-frustrated systems [30]. The origin of this non-monotonic behaviour is unclear and deserves future study.

In order to better understand the physics of this material, high-field calorimetry measurements would be well placed to trace out the boundary between the paramagnetic and spin-flop regions. Additionally, the exact shape of a heat capacity anomaly could distinguish between smooth crossover and a sharp phase transition between these regions. The same process applied to the canted AFM, spin-flop phase boundary could clarify its shape and low-temperature maximum field, which would help to further constrain theoretical models of this material. Additional single-crystal torque magnetometry measurements at lower temperatures and higher pulsed magnetic fields could reveal if there is an additional phase transition to a polarised phase at much higher fields. If much larger single crystals can be synthesised, single crystal magnetometry measurements could reveal how the magnetic structure is changing between the antiferromagnet and spin-flop phases.

Previous theoretical work on this material predicted dominant antiferromagnetic Kitaev interactions [9]. Mean-field calculations of magnetic structures show that a large

region of the Heisenberg-Kitaev-Γ phase diagram will order as a $\boldsymbol{q} = 0$ antiferromagnetic order with spins-along the $\boldsymbol{c}^*$ axis [7] as is observed experimentally. Inelastic neutron scattering studies on powder samples of α-Na_2PrO_3 did not find evidence for significant Kitaev interactions, and could fit the data instead with a minimal model with XXZ exchange interactions [10]. I have proposed that an extension of this model to include also g-factor anisotropy and DM interactions predicts a canted AFM structure with moments predominantly along $\boldsymbol{c}^*$ canted towards $\pm\boldsymbol{a}$. I show that this model can explain well the observed angular dependence of the torque in three orthogonal crystallographic planes up to $4\,\mathrm{T}$.

This canted antiferromagnetic structure is different from what is observed in other similar materials such as α-$RuCl_3$, α-Li_2IrO_3 , or Na_2IrO_3 and is likely intimately related to the physics of $4f$ Pr^{4+}orbitals. In either case, these experimental results should provide further constraints on theoretical models to understand the nature of exchange interactions and cooperative magnetism of $j_{\text{eff}} = {}^1\!/_2\,Pr^{4+}4f^1$ ions and in Kitaev candidate honeycomb materials more broadly.

References

[1] A. Kitaev. “Anyons in an exactly solved model and beyond”. In: *Annals of Physics* 321.1 (2006), pp. 2–111.

[2] G. Jackeli and G. Khaliullin. “Mott insulators in the strong spin-orbit coupling limit: from Heisenberg to a quantum compass and Kitaev models”. In: *Physical Review Letters* 102.1 (2009), p. 017205.

[3] Y. Motome et al. “Materials design of Kitaev spin liquids beyond the Jackeli–Khaliullin mechanism”. In: *Journal of Physics: Condensed Matter* 32.40 (2020), p. 404001.

[4] H. Takagi et al. “Concept and realization of Kitaev quantum spin liquids”. In: *Nature Reviews Physics* 1.4 (2019), pp. 264–280.

[5] J. Chaloupka, G. Jackeli, and G. Khaliullin. “Kitaev-Heisenberg model on a honeycomb lattice: possible exotic phases in iridium oxides A_2IrO_3”. In: *Physical Review Letters* 105.2 (2010), p. 027204.

[6] Y. Singh et al. “Relevance of the Heisenberg-Kitaev model for the honeycomb lattice iridates A_2IrO_3”. In: *Physical Review Letters* 108.12 (2012), p. 127203.

[7] J. G. Rau, E. K.-H. Lee, and H.-Y. Kee. “Generic spin model for the honeycomb iridates beyond the Kitaev limit”. In: *Physical Review Letters* 112.7 (2014), p. 077204.

[8] V. M. Katukuri et al. “Kitaev interactions between $j = 1/2$ moments in honeycomb Na_2IrO_3 are large and ferromagnetic: insights from ab initio quantum chemistry calculations”. In: *New Journal of Physics* 16.1 (2014), p. 013056.

[9] S.-H. Jang et al. "Antiferromagnetic Kitaev interaction in f-electron based honeycomb magnets". In: *Physical Review B* 99.24 (2019), p. 241106.

[10] M. J. Daum et al. "Collective excitations in the tetravalent lanthanide honeycomb antiferromagnet Na_2PrO_3". In: *Physical Review B* 103.12 (2021), p. L121109.

[11] J. Rodríguez-Carvajal. "FullProf". In: *CEA/Saclay, France* 1045 (2001), pp. 132–146.

[12] Y. Hinatsu and Y. Doi. "Crystal structures and magnetic properties of alkali-metal lanthanide oxides A_2LnO_3 (A= Li, Na; Ln= Ce, Pr, Tb)". In: *Journal of Alloys and Compounds* 418.1-2 (2006), pp. 155–160.

[13] S. Choi et al. "Spin waves and revised crystal structure of honeycomb iridate Na_2IrO_3". In: *Physical Review Letters* 108.12 (2012), p. 127204.

[14] F. Freund et al. "Single crystal growth from separated educts and its application to lithium transition-metal oxides". In: *Scientific Reports* 6.1 (2016), p. 35362.

[15] R. D. Johnson et al. "Monoclinic crystal structure of α- $RuCl_3$ and the zigzag antiferromagnetic ground state". In: *Physical Review B* 92.23 (2015), p. 235119.

[16] S. Hendricks and E. Teller. "X-ray interference in partially ordered layer lattices". In: *The Journal of Chemical Physics* 10.3 (1942), pp. 147–167.

[17] A. Abragam and B. Bleaney. *Electron paramagnetic resonance of transition ions*. Clarendon Press, 1970.

[18] I. Ryabov. "On the generation of operator equivalents and the calculation of their matrix elements". In: *Journal of Magnetic Resonance* 140.1 (1999), pp. 141–145.

[19] S.-H. Jang et al. "Computational design of f-electron Kitaev magnets: Honeycomb and hyperhoneycomb compounds A_2PrO_3 (A=alkali metals)". In: *Physical Review Materials* 4.10 (2020), p. 104420.

[20] E. Harris, J. Mellor, and S. Parke. "Electron paramagnetic resonance of tetravalent praseodymium in zircon". In: *physica status solidi (b)* 122.2 (1984), pp. 757–760.

[21] Y. Hinatsu and N. Edelstein. "Electron paramagnetic resonance spectrum of Pr^{4+} in $BaCeO_3$". In: *Journal of Solid State Chemistry* 112.1 (1994), pp. 53–57.

[22] M. Dresselhaus and G. Dresselhaus. *Applications of group theory to the physics of solids*. MIT Lecture Notes. 2002. URL: https://web.mit.edu/course/6/6.734j/www/group-full02.pdf.

[23] H. Xiao et al. "Angular-dependent torque measurements on $CeCoIn_5$ single crystals". In: *Physical Review B* 73.18 (2006), p. 184511.

[24] W. Zhang et al. "Spin-flop transition and magnetic phase diagram in $CaCo_2As_2$ revealed by torque measurements". In: *Physical Review B* 92.14 (2015), p. 144416.

[25] M. S. Dresselhaus, G. Dresselhaus, and A. Jorio. *Group Theory: Application to the Physics of Condensed Matter*. Springer, 2007.

[26] H. T. Stokes, D. M. Hatch, and B. J. Campbell. *ISODISTORT*. Version 6.11.1. May 26, 2022. URL: iso.byu.edu.

[27] L. D. Landau and E. M. Lifshitz. *Statistical Physics: Volume 5*. Vol. 5. Elsevier, 2013.

[28] D. P. Hardin, T. Michaels, and E. B. Saff. "A comparison of popular point configurations on $\mathbb{S}^2$". In: *arXiv preprint arXiv:1607.04590* (2016).

[29] A. Savitzky and M. J. Golay. “Smoothing and differentiation of data by simplified least squares procedures.” In: *Analytical Chemistry* 36.8 (1964), pp. 1627–1639.

[30] L. Seabra et al. “Phase diagram of the classical Heisenberg antiferromagnet on a triangular lattice in an applied magnetic field”. In: *Physical Review B* 84.21 (2011), p. 214418.

6

Magnetic order and high-field magnetic phase transitions in hyperhoneycomb β-Na_2PrO_3

Contents

6.1 Introduction 104
6.2 Crystal Structure 104
6.3 Single Ion Physics 109
6.4 Heat Capacity 111
6.5 DC Field Torque Magnetometry up to 16T 112
6.6 Magnetic Structure 117
6.7 Candidate Spin Hamiltonians 125
6.7.1 Minimal $J\Gamma\Gamma'$ model 127
6.7.2 $JK\Gamma$ model 135
6.8 Pulsed-Field Torque Magnetometry up to 67T 137
6.9 DC Field Torque Magnetometry up to 35T 147
6.10 Pulsed-Field Magnetisation up to 67T 151
6.11 Discussion/Conclusions 152

Abstract *Unconventional magnetic order and Kitaev quantum spin liquids have been proposed to exist on strongly bond-anisotropic honeycomb lattices, as well as the much rarer hyperhoneycomb lattices with effective spin ½. These have significant experimental and theoretical interest in the case of* $4\mathrm{d}$ *and* $5\mathrm{d}$ *transition metal ions. The theoretical proposal that such physics may occur in the* $4f$ *rare earths has remained experimentally largely unexplored. In this chapter I report crystal structure and magnetic characterisation of the* $4f$ *hyperhoneycomb* β*-*Na_2PrO_3 *using AC calorimetry and single crystal torque magnetometry, which are consistent with the 4 sublattice non-collinear magnetic structure found in neutron diffraction experiments. I explore a proposed minimal model which stabilises this structure, consisting of dominant Heisenberg exchange, frustrated by bond-dependent symmetric off-diagonal exchange. Finally, I report single-crystal torque magnetometry up to* $67\,\mathrm{T}$*, revealing a metamagnetic phase transition for certain field orientations.*

6.1 Introduction

A generalisation of the honeycomb lattice, discussed in Chapter 5, into three dimensions gives the hyperhoneycomb and harmonic honeycomb family of lattices [1], some of which have been realised as polymorphs of Li_2IrO_3. These 3D structures show the same three-fold coordination around each site as the planar honeycomb case, and if they host the same Kitaev exchange interactions on these bonds they can be exactly solved through the same methods [2, 3]. Much like in the honeycomb case discussed previously, more complex models with additional Heisenberg J [3, 4] and symmetric-off-diagonal exchange Γ [5] with only nearest-neighbour interactions were also considered to try to explore the possible physics of hyperhoneycomb and harmonic honeycomb iridates. These revealed a rich phase diagram of exotic magnetic phases depending on the precise balance between the three terms in the model.

A promising candidate material for unconventional magnetism is the hyperhoneycomb β-Na_2PrO_3, which was first synthesised in 1988 [6]. Its promise as a three-fold coordinated $4f$ magnet was first identified in literature only recently [7, 8], where large, antiferromagnetic Kitaev interactions were theoretically predicted.

In this section I report AC-calorimetry, torque magnetometry, and X-ray structural studies of hyperhoneycomb β-Na_2PrO_3, revealing non-collinear magnetic ordering at $T_N = 5.20(2)\,\mathrm{K}$ to a phase stabilised by bond-anisotropic exchange of the symmetric off-diagonal type. I also report torque magnetometry up to $67\,\mathrm{T}$, revealing a metamagnetic phase transition at $26\,\mathrm{T}$ for fields applied close to the crystal $\boldsymbol{a}$ axis.

6.2 Crystal Structure

Samples of β-Na_2PrO_3 were synthesised by Ryutaro Okuma at the University of Oxford. Like its polymorph α-Na_2PrO_3, β-Na_2PrO_3 is very air sensitive so samples were synthesised, handled, and selected in an inert gas atmosphere, and sealed by flame in an evacuated borosilicate-glass capillary. In order to determine the crystal structure of β-Na_2PrO_3, X-ray diffraction was performed at room temperature on $\sim 100\mu\mathrm{m}$ single-crystals with an Oxford Diffraction Supernova diffractometer. These measurements were

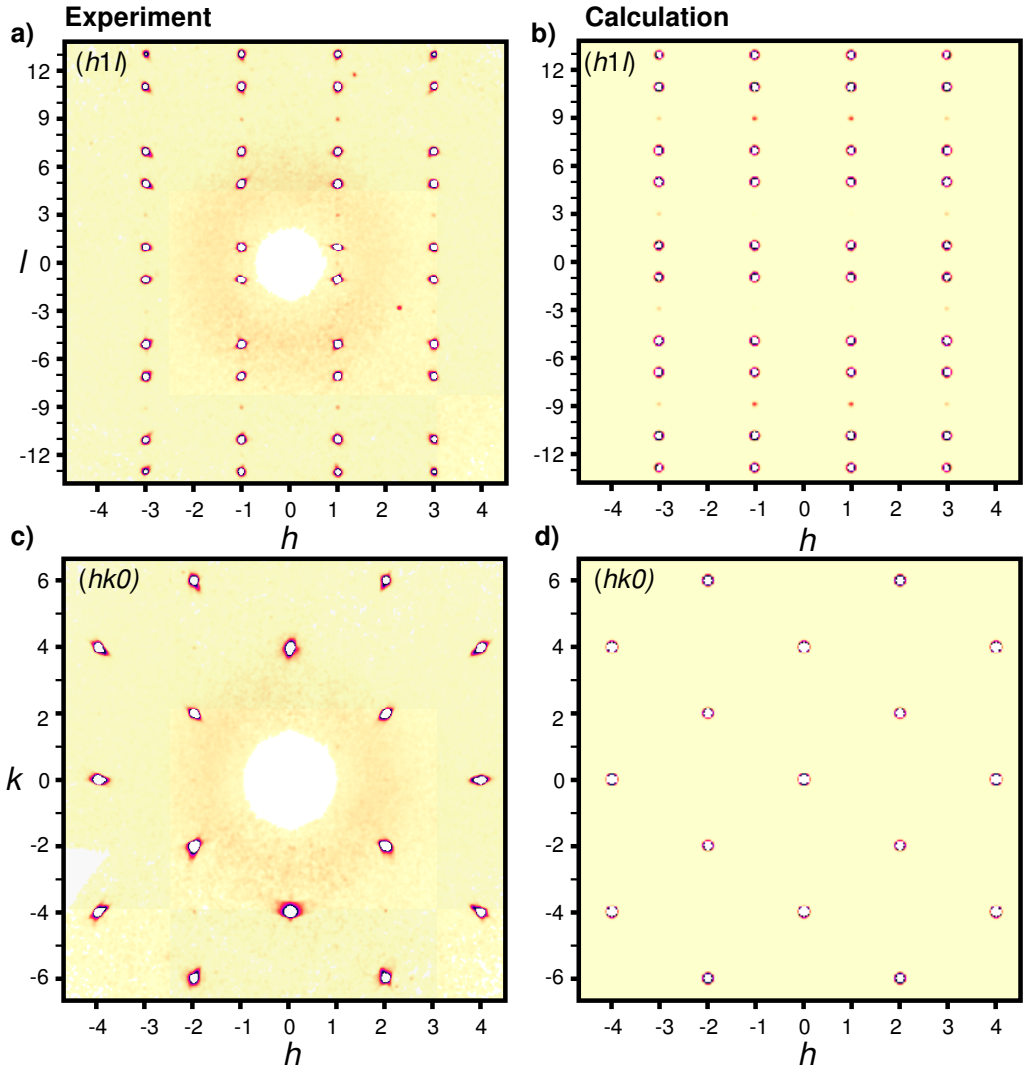


Figure 6.1: Single crystal X-ray diffraction pattern in the **a, b)** $h1l$, **c, d)** $hk0$ reciprocal lattice planes. **a, c)** show experimental data measured at 300 K, **b, d)** show calculated Bragg peak intensities. Both colour-maps are on a log scale.

performed with the sample remaining in the evacuated capillary. The detailed structure was refined using FULLPROF [9] analysis software. The results of this refinement are summarised in Table **??** and Table **??**, which show structural parameters and atomic fractional coordinates of β-Na_2PrO_3 's ions in the orthorhombic setting.

Figure **??** shows a comparison between the experimentally observed diffraction pattern and calculated Bragg peak intensities for the reciprocal lattice planes $(h1l)$, $(hk0)$. The intensities are calculated from the refined atom positions in Table **??**. The $Fddd$

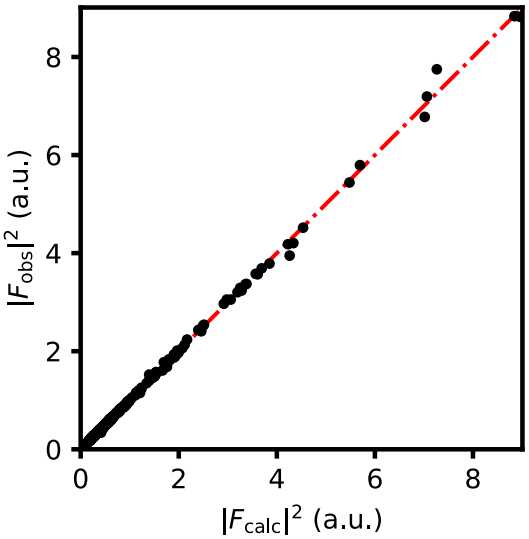


Figure 6.2: Observed vs calculated Bragg peak intensities where dashed line shows 1:1 agreement. Calculated Bragg peak intensities using FULLPROF [9] with parameters in Table **??**.

Table 6.1: Refined structure parameters of β-Na_2PrO_3 in orthorhombic setting with origin choice at $\bar{1}$. Isotropic displacement parameters U_{iso} have units of 10^{-3}Å^2. Anisotropic displacement parameters can be found in Table **??**. Error estimates from FULLPROF [9] refinement in parentheses.

Space group: $Fddd$ (70)						
Z = 16						
Cell parameters:						
a, b, c (Å)			6.759	9.785	20.519	
α, β, γ (°)			90	90	90	
Volume (Å^3)			1357.09			
Atomic fractional coordinates:						
Atom	Wyckoff Site	Site Symmetry	x	y	z	U_{iso}
Pr^{4+}	16g	..2	0.125	0.125	0.70879(2)	5.1(1)
$Na^{+}(1)$	16g	..2	0.125	0.125	0.04634(18)	15.3(16)
$Na^{+}(2)$	16g	..2	0.125	0.125	0.37062(19)	12.3(14)
$O^{2-}(1)$	32h	1	0.3607(9)	0.1021(4)	0.78377(16)	8.6(18)
$O^{2-}(2)$	16e	2..	0.8407(9)	0.125	0.125	9(3)

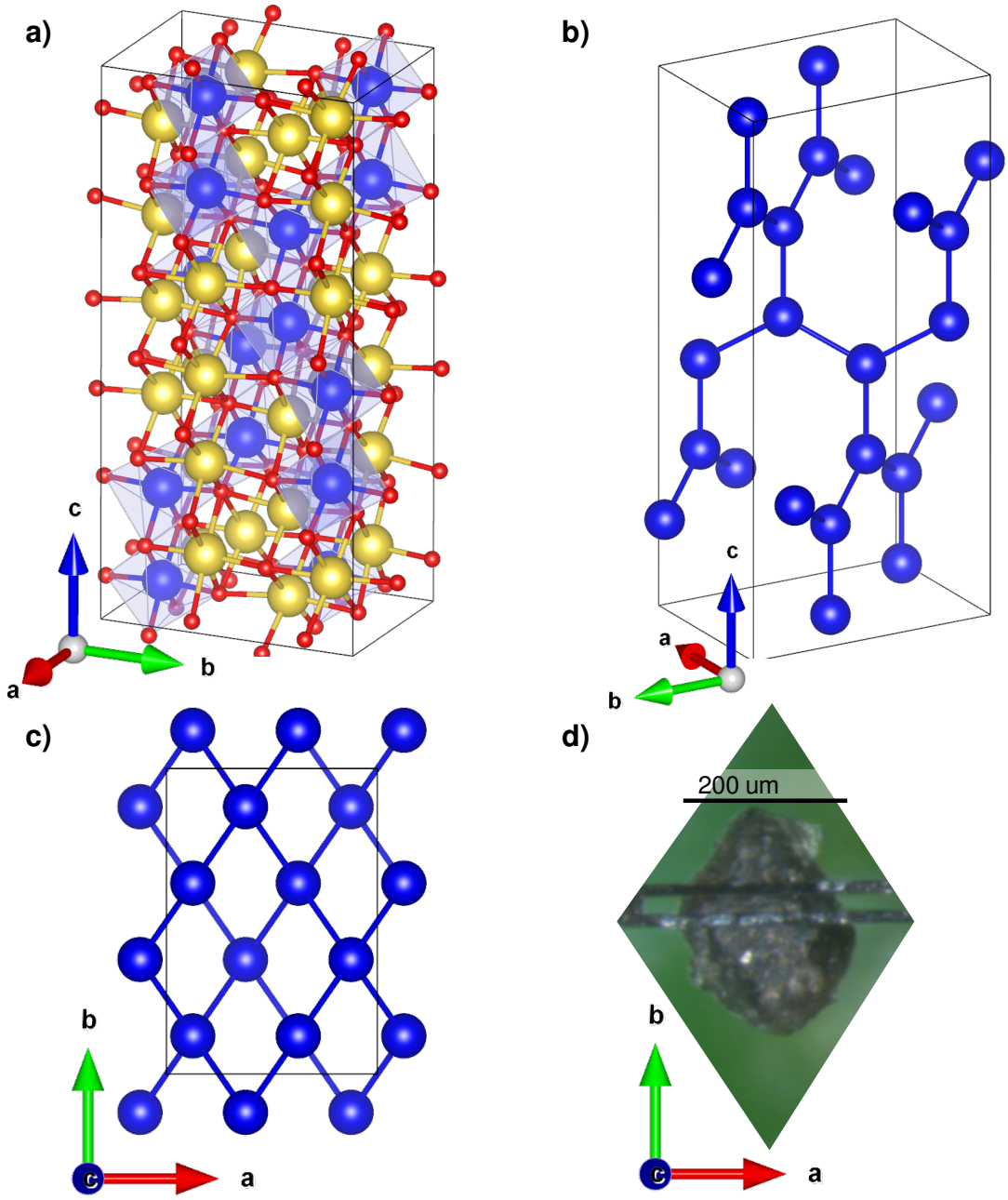


Figure 6.3: Model showing the crystal structure of β-Na_2PrO_3 in the orthorhombic setting. Dark blue spheres indicate Pr^{4+}ions, yellow spheres indicate Na^{+}ions, and red spheres indicate O^{2-} ions. The thin black lines indicate the structural unit cell, while the red, green, and blue triad of arrows shows directions of orthorhombic lattice vectors $\boldsymbol{a}, \boldsymbol{b}, \boldsymbol{c}$. **a)** shows all ions in the structure, **b, c)** show just Pr^{4+}ions to highlight the arrangement of magnetic ions, with **c)** showing the projection onto the $\boldsymbol{ab}$ plane. **d)** shows a microscope photograph of a $\sim 200\,\mu\mathrm{m}$ single crystal of β-Na_2PrO_3 , with crystallographic axes and a scale bar overlaid. The photograph has a diamond-shaped outline to highlight the morphology of the crystal. The additional object visible in the image is a torque piezocantilever, discussed further in Section **??**

Table 6.2: Anisotropic displacement parameters of β-Na_2PrO_3 in units of 10^{-3}Å^2 in the orthorhombic setting. Atom labels are the same as in Table **??**. Error estimates from FULLPROF [9] refinement in parentheses.

Atom	U_{11}	U_{22}	U_{33}	U_{12}	U_{13}	U_{23}
Pr^{4+}	5.9(2)	5.9(2)	3.6(2)	0.7(2)	0	0
$Na^{+}(1)$	11.1(14)	24.0(17)	10.7(16)	1(2)	0	0
$Na^{+}(2)$	16.2(14)	11.6(14)	9.1(14)	-4.3(18)	0	0

space group imposes a number selection rules for scattering. The F centring has the scattering rule h, k, l all odd or all even. The systematic absences due to this selection rule can be seen in the data in the $(h1l)$ plane as no peaks are seen at h even or l even. In the $(hk0)$ plane, there is an additional selection rule $h + k = 4n$ $(n \in \mathbb{Z})$ which is seen in the data. This arises from the diamond glide planes with mirror perpendicular to the $\boldsymbol{c}$ axis, and translation by $\frac{1}{4}(\boldsymbol{a} + \boldsymbol{b})$. Finally, for the family of peaks with h, k, l all odd, the peaks at $l = 6n + 3$ are systematically weak. This is caused by the fact that the $Pr^{4+}$and Na^{+} sites exist in pairs, approximately translated by $\frac{c}{6}$ which causes destructive interference on $l = 6n + 3$ peaks, clearly seen in Fig. **??**. Figure **??** shows a comparison between observed and calculated peak intensities, the small disagreement at large $|F|^2$ is likely caused by uncorrected absorption from the glass capillary the sample was held in to prevent air exposure.

This analysis revealed that β-Na_2PrO_3 has a complex three-dimensional crystal structure, isostructural to hyperhoneycomb β-Li_2IrO_3 [10], with an $Fddd$ space group. This hyperhoneycomb structure contains edge-sharing PrO_6 octahedra containing the Pr^{4+}ion at the centre, arranged to appear locally like a honeycomb structure, but with the bond directions alternating along the $\boldsymbol{c}$-axis. The structure, visualised in Figure **??**, contains zigzag chains of Pr^{4+}ions along the $\boldsymbol{a} + \boldsymbol{b}$ and $\boldsymbol{a} - \boldsymbol{b}$ directions, connected by bonds parallel to the $\boldsymbol{c}$ axis. These chains can be seen in Figure **??c)**. When projected into the $\boldsymbol{ab}$ plane, the chains form a tiling pattern of diamond shapes, with the long axis parallel to $\boldsymbol{b}$ and the short axis parallel to $\boldsymbol{a}$. This shape is reflected in the crystal morphology, visible in Figure **??d)**, as the crystals grow with natural edges parallel to these chains into diamond shapes with the long axis parallel to $\boldsymbol{b}$ and the short axis parallel to $\boldsymbol{a}$. This $Fddd$ space group is in disagreement with the previously reported

lower symmetry $C2/c$ structure [6]. This is due to a mischaracterisation of the material as lower symmetry than the space group observed here.

The primitive unit cell of β-Na_2PrO_3 is triclinic, and contains 4 Pr^{4+}ions, 8 Na^{+} ions, and 12 O^{2-} ions. The primitive cell lattice vectors $\boldsymbol{A}, \boldsymbol{B}, \boldsymbol{C}$ can be written in terms of the centred cell lattice vectors $\boldsymbol{a}, \boldsymbol{b}, \boldsymbol{c}$ as

$$\begin{pmatrix} \boldsymbol{A} \\ \boldsymbol{B} \\ \boldsymbol{C} \end{pmatrix} = \begin{pmatrix} 0 & 1/2 & 1/2 \\ 1/2 & 0 & 1/2 \\ 1/2 & 1/2 & 0 \end{pmatrix} \begin{pmatrix} \boldsymbol{a} \\ \boldsymbol{b} \\ \boldsymbol{c} \end{pmatrix} \tag{6.1}$$

6.3 Single Ion Physics

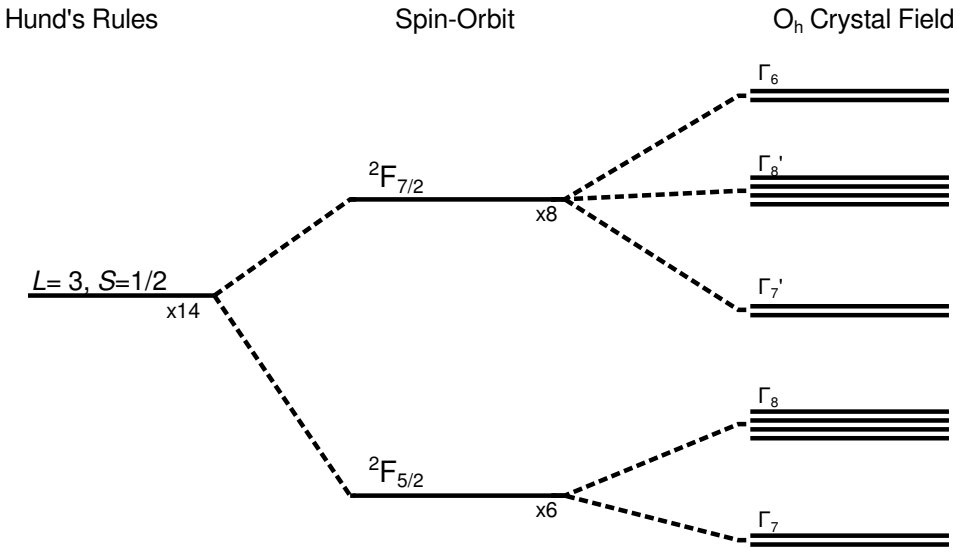


Figure 6.4: Schematic diagram showing level splitting of an isolated Pr^{4+}ion in the presence of spin-orbit coupling and an octahedral cubic O_h crystal field environment. Labels on states show good quantum numbers for those levels.

The magnetic ions in β-Na_2PrO_3 are Kramers $4f^1$ Pr^{4+}ions in an octahedral environment of oxygens, just as in α-Na_2PrO_3 , so up to different values for the strength of the CEF parameters the single-ion physics will be the same as that discussed in Chapter 5. This results in the same energy level spitting diagram shown in Figure **??**, and a $j_{\text{eff}} = 1/2$ ground state.

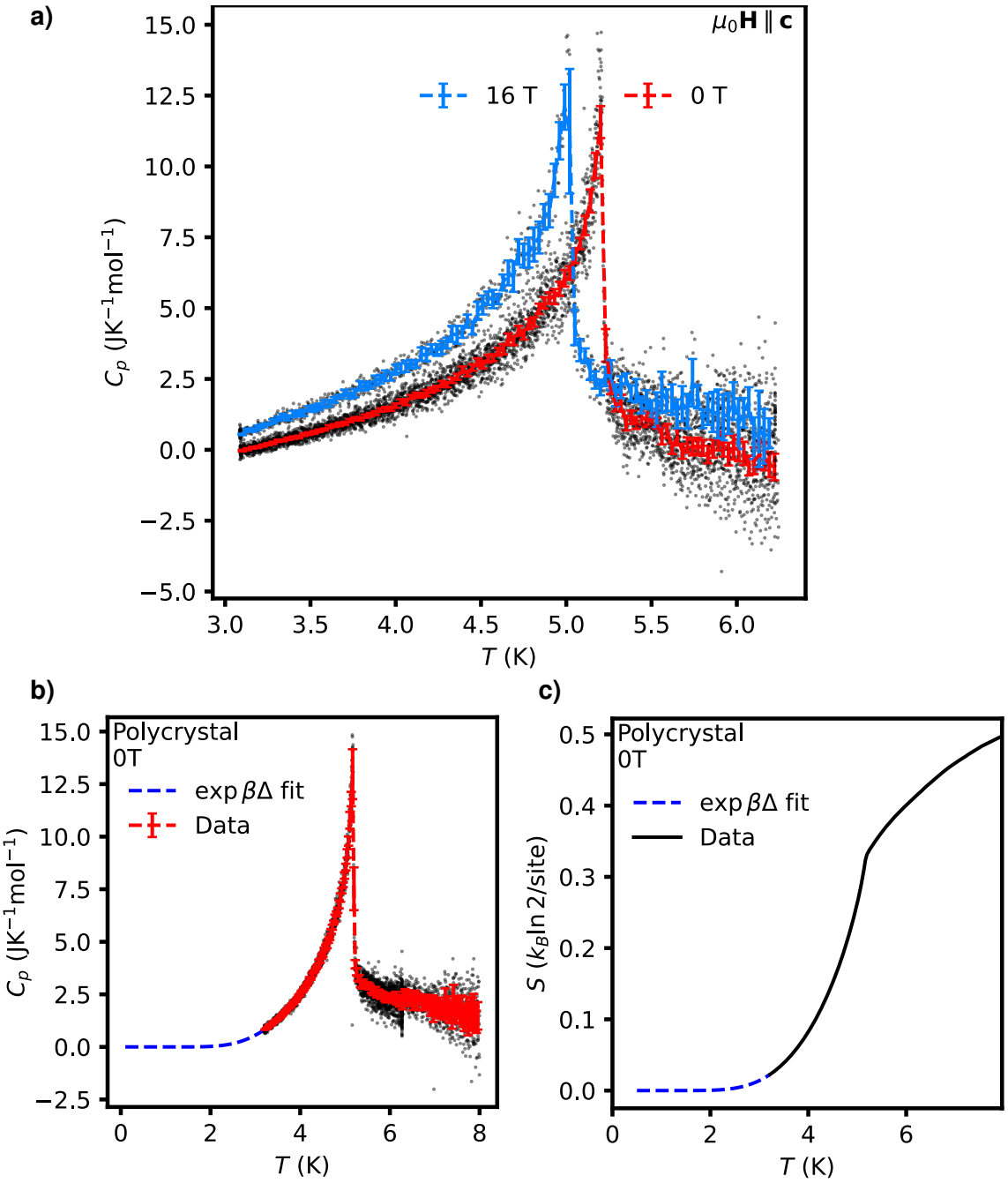


Figure 6.5: **a)** Plot showing evolution of heat capacity of a single crystal of β-Na_2PrO_3 with temperature between 3 K and 6.5 K, with applied magnetic fields along the ***c*** axis $\mu_0 H = 0\,\mathrm{T}$ (red) $\mu_0 H = 16\,\mathrm{T}$ (blue). **b)** Temperature dependence of heat capacity of collection of single crystals. **c)** Temperature dependence of calculated magnetic entropy computed from data in panel **b)**. Data is measured with the AC calorimetry method, and has had an estimate of the addenda background subtracted. Black points show estimated specific heat capacity of a single temperature oscillation, red and blue points show running mean over these points. Error bars indicate 95% confidence interval.

6.4 Heat Capacity

In order to determine if the material orders magnetically at low temperatures, specific heat capacity was measured using the AC method described in Section 3.3. Measurements were first performed on a $0.12(2)\mathrm{mg}$ collection of single crystals in zero-field, revealing a clear peak in heat capacity at $5.2\,\mathrm{K}$, shown in Fig **??b)**. Measurements were then performed on a single crystal of β-Na_2PrO_3 to determine how the transition responded to applied magnetic field, shown Fig. **??a)**. The single-crystal sample was too small to accurately measure the mass on a weighing balance, but by comparing the size of the heat capacity anomaly to that of the multi-crystal sample, the mass could be estimated to $m \approx 0.07\mathrm{mg}$. The sample was mounted with $\boldsymbol{H} \parallel \boldsymbol{c}$, for $0\,\mathrm{T} \leq \mu_0 H \leq 16\,\mathrm{T}$.

Figure **??** shows the evolution of heat capacity with temperature between $2\,\mathrm{K}$ and $6\,\mathrm{K}$. The trace in red shows the evolution of heat capacity C_p with temperature at zero field, revealing a finite peak, with a sharp anomaly at the ordering temperature $T_N = 5.20(2)\,\mathrm{K}$. This is a signature of a second-order phase transition [11], which in turn suggests that the magnetic order just below T_N should be described by a single irreducible representation of the high-temperature paramagnetic space group.

The evolution of specific heat capacity with temperature at the maximum experimentally available field of $\mu_0 H = 16\,\mathrm{T}$ can be seen in the blue curve of Fig. **??a)**. This shows a sharp peak with an anomaly at $5.01(4)\,\mathrm{K}$, suppressed from the zero-field value. The fact that the transition is sharp in a large magnetic field indicates that there is no spontaneous ferromagnetic component to the zero-field magnetic structure, if there were the finite field would break the symmetry and the transition would be a smooth crossover between low and high temperature regimes. The field suppression of the critical ordering temperature is suggestive of antiferromagnetic ordering and is intuitively understood as the fact that the field induces a uniform magnetisation, so less of the moment orders spontaneously in antiferromagnetic structure. Therefore the mean-field energy from ordering is reduced and the critical temperature T_N is reduced.

In order to determine the temperature dependence of magnetic entropy, the heat capacity of the collection of single crystals was fit to a phenomenological form [12]

$$C_{\text{mag}}(T) = AT^n \exp\left(-\frac{\Delta}{k_B T}\right) + C_{\text{bg}} \tag{6.2}$$

with $n = -1$ and the background term C_{bg} was subtracted off. The fitted magnetic gap $\Delta \sim 1\,\text{meV}$ is very sensitive to the value of n used and the temperature fitting window. This is likely an artefact of the small temperature window available. The magnetic entropy was then computed as

$$S_{\text{mag}}(T) = \int_0^T \frac{C_{\text{mag}}(T')}{T'} dT' \tag{6.3}$$

where the fitted $C_{\text{mag}}(T')$ is extrapolated for temperatures below the measurement base temperature, and the measured data itself is used above the base temperature. This computed $S_{\text{mag}}(T)$ is shown in Fig. **??c)**. The high-temperature magnetic entropy produced is $S \approx 0.5 k_B \ln 2$, less than the expected $k_B \ln 2$ value for a $j_{\text{eff}} = 1/2$ paramagnet. This value is also less than the $S \approx 0.76 k_B \ln 2$ value found in α-Na_2PrO_3 [13]. That this may be evidence of strong fluctuations in the ordered state [10] is an interesting prospect, however given the unavailability of an accurate lattice background to subtract, significant uncertainties in the sample mass and low-temperature extrapolation, and the challenge of determining absolute values of heat capacity in the AC calorimetry technique, the uncertainty on the absolute value of this is large, and it should be taken as a rough estimate.

6.5 DC Field Torque Magnetometry up to 16T

In order to explore the magnetic anisotropy in β-Na_2PrO_3 , I performed piezocantilever torque magnetometry measurements on $\sim 200\,\mu\text{m}$ single crystals. Torque measurements reported in this section were performed on the crystal pictured in Fig. **??d)**. Figure **??** shows measured magnetic torque for rotations in the $\boldsymbol{ac}$ and $\boldsymbol{bc}$ planes for temperatures between $2\,\text{K}$ and $100\,\text{K}$. Figure **??a)** shows a waterfall plot of torque against rotation angle in the $\boldsymbol{ac}$ plane, where an angle of 0° implies field parallel to the crystallographic $\boldsymbol{c}$ axis. At all temperatures measured, the torque is fit well by a $\tau = -\tau_2(T) \sin 2\theta$ form, with $\tau_2 > 0$. When the field is approximately parallel to the $\boldsymbol{c}$ axis $\mu_0 \boldsymbol{H} \parallel \boldsymbol{c}$, the torque

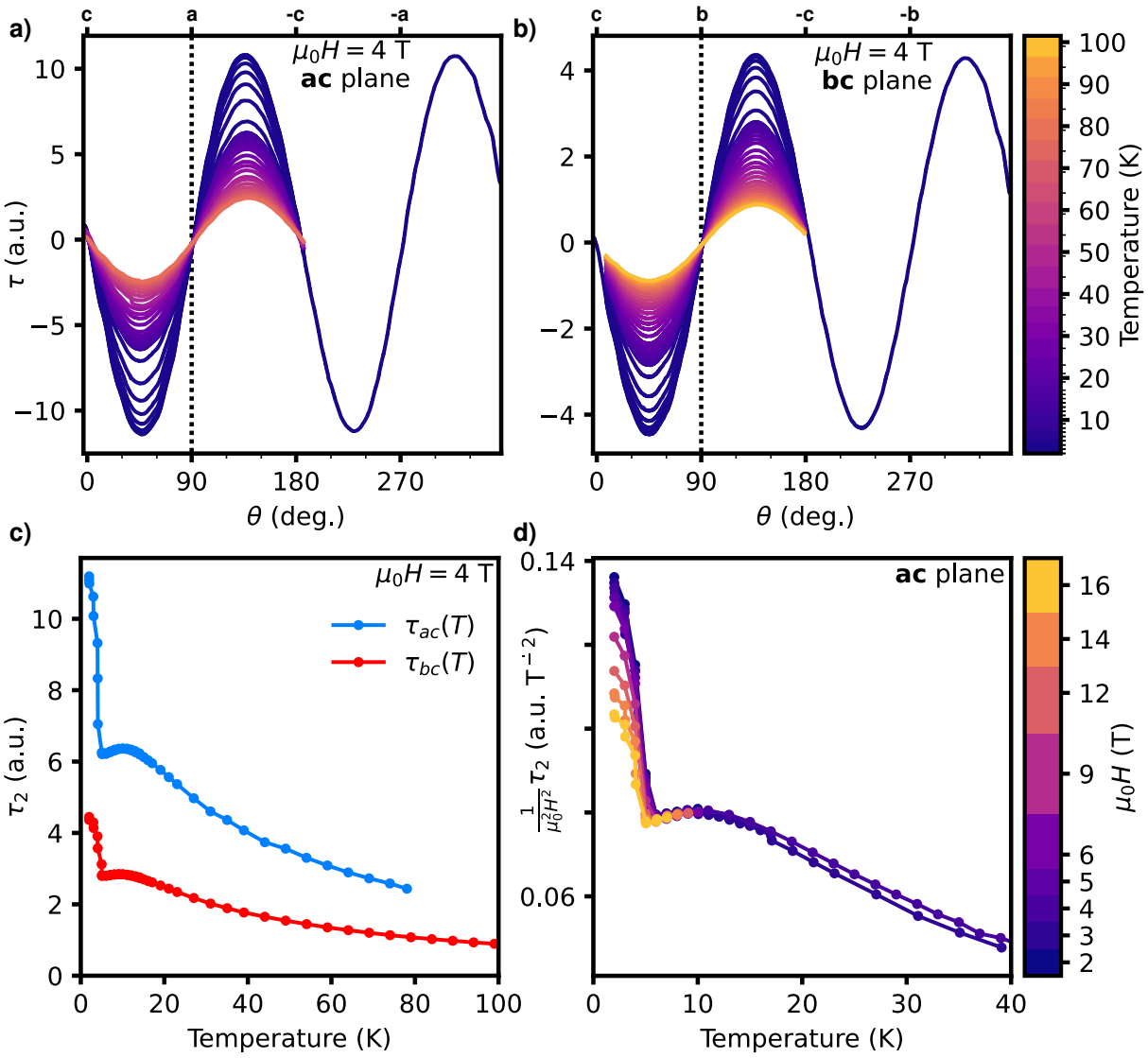


Figure 6.6: a, b) Waterfall plots showing magnetic torque vs rotator angle for temperatures between 2 K and 100 K. Rotations are made in the **a)** $\boldsymbol{ac}$ plane, **b)** $\boldsymbol{bc}$ plane. Dashed vertical lines indicate where field is parallel to the $\boldsymbol{a}$ and $\boldsymbol{b}$ axes respectively. The rotator angle θ is measured from the crystallographic c axis. Top labels indicate angles where the magnetic field direction is aligned parallel to an orthorhombic crystallographic axis. Traces are raw torque piezocantilever voltages in mV. Trace colour indicates temperature, as per colour bar on right of image. **c)** Evolution of fitted torque amplitudes for rotations in the $\boldsymbol{ac}$ and $\boldsymbol{bc}$ planes between 2 K and 100 K. Measurements are made on the same sample so units are comparable. **d)** Evolution of fitted torque amplitudes scaled by $(\mu_0 H)^2$ for rotations in the $\boldsymbol{ac}$ plane between 2 K and 40 K for applied magnetic fields between 2 T and 16 T.

crosses zero with a negative gradient of torque with angle is observed, indicating a stable equilibrium in both the paramagnetic and ordered phases. Conversely, for $\mu_0 \boldsymbol{H} \parallel \boldsymbol{a}$ torque crosses zero with a positive gradient, suggesting that this is an unstable equilibrium. This implies that the susceptibility along the $\boldsymbol{c}$ direction is larger than the susceptibility along the $\boldsymbol{a}$ direction at all temperatures. Figure **??b)** shows torque against rotation angle in the $\boldsymbol{bc}$ plane, where an angle of 0° implies field parallel to the crystallographic $\boldsymbol{c}$ axis. Here the situation is very similar, at all temperatures the torque is fit well by a $\sin 2\theta$ form and the sign of the signal indicates $\mu_0 \boldsymbol{H} \parallel \boldsymbol{c}$ is a stable equilibrium, while $\mu_0 \boldsymbol{H} \parallel \boldsymbol{b}$ is an unstable equilibrium.

At each temperature, torque versus angle curves were fitted to the sinusoidal form

$$\tau(\theta, T) = -\tau_2(T) \sin 2\theta \tag{6.4}$$

where $\tau_2(T) > 0$ indicates a stable equilibrium when $\mu_0 \boldsymbol{H} \parallel \boldsymbol{c}$.

Figure **??c)** shows how these coefficients τ_2 vary with temperature for both orientations. The trace in blue shows the values extracted for the $\boldsymbol{ac}$ plane, while the trace in red shows values for the $\boldsymbol{bc}$ plane. These torque measurements in both planes were performed on the same crystal and the same lever so the units are comparable. In both planes the evolution of this amplitude τ_2 with temperature are qualitatively similar. At high temperatures, above $\sim 20\,\mathrm{K}$ the torque decreases monotonically, as is expected for a Curie-Weiss paramagnet. Here the magnitude of the torque signal is about twice as large in the $\boldsymbol{ac}$ plane as in the $\boldsymbol{bc}$ plane, with the sign of the signal indicating that χ_c is the largest susceptibility. This suggests that the difference in susceptibilities between the $\boldsymbol{c}$ axis and $\boldsymbol{a}$ axis is about twice as large as the difference between the $\boldsymbol{c}$ axis and $\boldsymbol{b}$ axis. From this, the order of susceptibilities can be inferred as

$$\chi_c > \chi_b > \chi_a \tag{6.5}$$

In both orientations there is a broad peak in torque centred at approximately $10\,\mathrm{K}$. Low dimensional systems of weakly coupled chains or planes have been observed to display a broad peak in susceptibility associated with short range magnetic order at a temperature $\tilde{T}$ dependent on the dominant interactions, and an anomaly at a lower

temperature with the onset of long-range order $T_N \ll \tilde{T}$ [14–16]. Whether this could indicate short-range order along the zigzag chains in β-Na_2PrO_3 is an interesting prospect which should be investigated further.

At the Néel temperature, determined from heat capacity as described in Section **??**, $T \simeq 5.2\,\mathrm{K}$, there is a pronounced anomaly in torque. In both orientations, the fitted torque amplitude grows quickly as temperature drops deeper into the ordered phase. This is consistent with a suppression of susceptibility in the $\boldsymbol{a}$ and $\boldsymbol{b}$ directions. The size of the torque anomaly in the $\boldsymbol{ac}$ plane (4.8 a.u.), is much larger than the size of the anomaly in the $\boldsymbol{bc}$ plane (1.6 a.u.), suggesting that the susceptibility is suppressed much more strongly in the $\boldsymbol{a}$ direction than the $\boldsymbol{b}$ direction. This is consistent with an antiferromagnetic structure with spins predominantly along the $\boldsymbol{a}$ axis, but with a finite component also along the $\boldsymbol{b}$ axis.

Figure **??d)** shows how the value of $\frac{\tau_2}{(\mu_0 H)^2}$ varies with temperature for applied fields between $2\,\mathrm{T}$ and $16\,\mathrm{T}$. In the paramagnetic regime, magnetic torque is expected to scale with the field squared $\tau \sim H^2$ [17, 18] (See Chapter 3.2), and indeed the curves $\frac{\tau}{H^2}$ lie on top of each other. This can be seen for all fields measured with temperature $T > 10\,\mathrm{K}$. For temperatures below the transition this relationship holds for small fields up to $6\,\mathrm{T}$. At larger applied fields, the value of $\frac{\tau_2}{(\mu_0 H)^2}$ drops, indicating that the torque is growing slower than H^2. This is further evidence of magnetic order, as the paragenetic torque-field relationship no longer holds.

The most straightforward interpretation of this torque data is a collinear antiferromagnetic order with moments in the $\boldsymbol{ab}$ plane, in-between the $\boldsymbol{a}$ and $\boldsymbol{b}$ axes. To test this torque was measured in the $\boldsymbol{ab}$ plane of the same crystal, so the sample had to be mounted with the lever against the side of the diamond shape visible in the crystal morphology. The absence of a flat face for mounting makes the alignment of this challenging. For this mounting, the lever was aligned parallel to the $\boldsymbol{a} + \boldsymbol{b}$ direction, along the direction of a zigzag chain. The mmm point group of the high-temperature paramagnetic phase means that the torque is required by symmetry to be zero for $\mu_0 \boldsymbol{H} \parallel \boldsymbol{a}$ or $\mu_0 \boldsymbol{H} \parallel \boldsymbol{b}$, as such this can be used to correct any misalignment caused by the mounting difficulties. The $\phi = 0$ position is taken as the angle with $\tau = 0$ at high temperature closest to

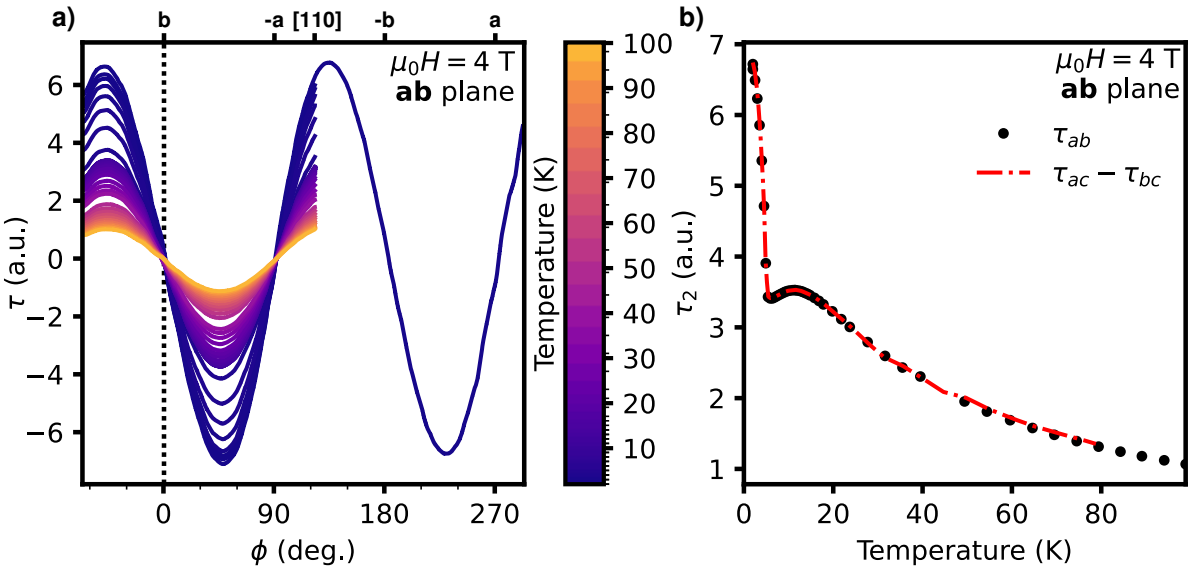


Figure 6.7: a) Waterfall plot showing magnetic torque vs rotator angle for temperatures between 2 K and 100 K for rotations made in the $\boldsymbol{ab}$ plane. The rotator angle ϕ is measured from the crystallographic $\boldsymbol{b}$ axis. Top labels indicate angles where the magnetic field direction is aligned parallel to an orthorhombic crystallographic axis. Traces are raw torque piezocantilever voltages in mV. Trace colour indicates temperature, as per colour bar on right of image. **b)** Evolution of fitted torque amplitudes between 2 K and 100 K. Red overlaid is curve of unscaled $\tau_{ac}(T) - \tau_{bc}(T)$ as described in the text.

the estimated $\boldsymbol{H} \parallel \boldsymbol{b}$ position from crystal geometry. In the measurement reported, the corrected alignment was 8° off the estimated alignment.

Figure **??a)** shows torque versus angle in the $\boldsymbol{ab}$ plane for temperatures between 2 K and 100 K. The angle in plane ϕ is measured from the nominal $\boldsymbol{b}$ axis. Much like in the other orientations, these show an $\tau = -\tau_2 \sin 2\phi$ shape. In the $\boldsymbol{ab}$ plane, the stable equilibrium is near $\mu_0 \boldsymbol{H} \parallel \boldsymbol{b}$ and the unstable equilibrium is near $\mu_0 \boldsymbol{H} \parallel \boldsymbol{a}$, consistent with the order of susceptibilities shown in Eqn. (**??**).

Fig. **??b)** shows the evolution of the fitted torque amplitudes with temperature, showing the same overall shape as seen in both other orientations.

If the torque can be explained simply by anisotropic susceptibilities with principal axes aligned with the crystallographic $\boldsymbol{a}$, $\boldsymbol{b}$, $\boldsymbol{c}$ axes then for small magnetic fields

$$\tau_{2,ab} = -\frac{1}{2} B^2 \left(\chi_b - \chi_a\right) \tag{6.6}$$

$$= \tau_{2,ac} - \tau_{2,bc} \tag{6.7}$$

Overlaid on the data points in red is the curve of $\tau_{ac}(T) - \tau_{bc}(T)$, which agrees qualitatively and quantitatively very well with the measured data points of $\tau_{ab}(T)$. It is worth noting that these data are not scaled to match, but the data was measured on the same sample and lever for all three datasets. The subtracted data is over-plotted with no scaling parameters. This quantitative agreement provides further confirmation of the internal consistency of the dataset. The torque data provides additional confirmation for the non-collinear picture as follows; torque in the $\boldsymbol{ac}$ and $\boldsymbol{bc}$ planes is consistent with suppression of susceptibility along both $\boldsymbol{a}$ and $\boldsymbol{b}$ directions. If the structure was collinear with moments in the $\boldsymbol{ab}$ plane, away from crystallographic axes, one would expect an unstable equilibrium when the field is along the moment axis and susceptibility is close to zero, and a stable equilibrium when the field is normal to this axis. The principal axes of the susceptibility tensor would not be aligned with the crystallographic axes and (**??**) would not hold. However the data in Fig. **??** does not show this. As such, the collinear model can be discarded, and the suppression of susceptibilities along both the $\boldsymbol{a}$ and $\boldsymbol{b}$ directions must be because of a more complex non-collinear magnetic order with the dominant (or full) moment components in the $\boldsymbol{ab}$ plane.

6.6 Magnetic Structure

Together with heat capacity, the torque data reported above provides clear evidence supporting a non-collinear magnetic structure with an ordering temperature of $5.2\,\mathrm{K}$, motivating further research into the magnetic structure.

The magnetic Pr^{4+}sites are at the $16g$ site in the orthorhombic cell, there are four equivalent Pr^{4+}sites in the primitive setting. These are shown in Figure **??a)**, with the four sublattices numbered using the convention developed for β-Li_2IrO_3 [19]. The magnetic basis vectors can be written in terms of the relative orientation of the moments on the Pr^{4+}sites as

$$\begin{pmatrix} \boldsymbol{F} \\ \boldsymbol{A} \\ \boldsymbol{C} \\ \boldsymbol{G} \end{pmatrix} = \frac{1}{4} \begin{pmatrix} +1 & +1 & +1 & +1 \\ +1 & -1 & -1 & +1 \\ +1 & +1 & -1 & -1 \\ +1 & -1 & +1 & -1 \end{pmatrix} \begin{pmatrix} \boldsymbol{\mu}_1 \\ \boldsymbol{\mu}_2 \\ \boldsymbol{\mu}_3 \\ \boldsymbol{\mu}_4 \end{pmatrix} \tag{6.8}$$

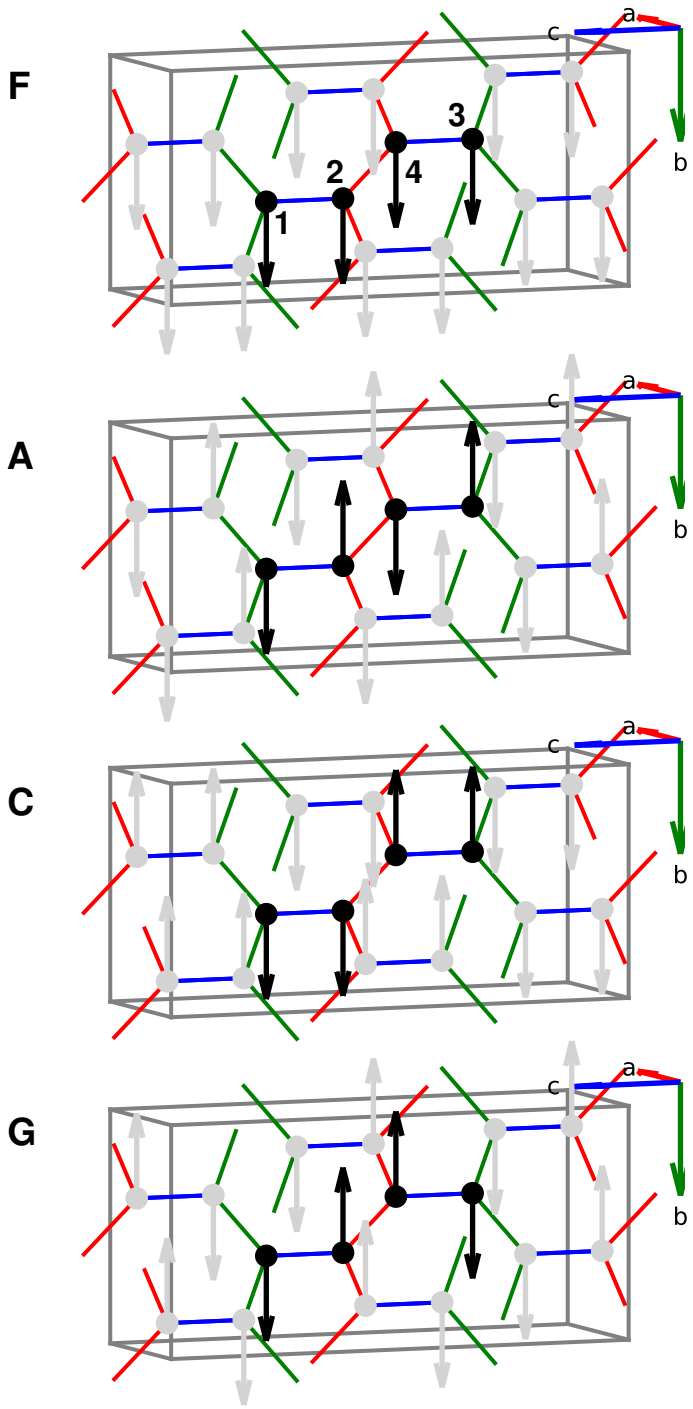


Figure 6.8: Model showing magnetic basis vectors of β-Na_2PrO_3 in the orthorhombic setting. Black and gray circles indicate Pr^{4+}ions, while arrows show local moment for associated Pr^{4+}site. Black circles/arrows show one primitive structural unit cell, same as the primitive magnetic unit cell. Left labels (F, A, C, G) indicate which magnetic basis vector is being shown, as specified in Table **??**, assuming moments polarised along the $\boldsymbol{b}$ axis. Number labels indicate sublattice labels as in [19]. The a, b, c labelled triad of arrows on the right-hand side indicate the conventional structural cell lattice vectors. Red lines between sites indicate $\boldsymbol{a} + \boldsymbol{b}$ chain, green lines indicate $\boldsymbol{a} - \boldsymbol{b}$ chain, blue lines indicate z bonds parallel to $\boldsymbol{c}$ axis.

This is summarised in Table **??**, where +, - symbols indicate a ± 1 entry in the matrix above. These magnetic basis vectors are illustrated in Figure **??**.

Table 6.3: $\boldsymbol{q} = \mathbf{0}$ Magnetic basis vectors for β-Na_2PrO_3 .

	$\boldsymbol{\mu}_1$	$\boldsymbol{\mu}_2$	$\boldsymbol{\mu}_3$	$\boldsymbol{\mu}_4$
F	+	+	+	+
A	+	-	-	+
C	+	+	-	-
G	+	-	+	-

For neutron diffraction, the relevant structure factor for a magnetic reflection at Bragg peak position $\boldsymbol{Q}$ is

$$\boldsymbol{\mathcal{F}}(\boldsymbol{Q}) = f_F \sum_{n=1}^{4} \boldsymbol{\mu}_n e^{i\boldsymbol{Q}\cdot\boldsymbol{r}_n} \tag{6.9}$$

where the sum runs over the sites in the primitive unit cell, and $\boldsymbol{r}_n$ is the position of the n^{th} site [19]. The prefactor $f_F = 1 + e^{i\pi(h+k)} + e^{i\pi(k+k)} + e^{i\pi(k+h)}$ is due to the F-centring of the orthorhombic setting and takes the value

$$f_F = \begin{cases} 4 & \text{if } h,k,l \text{ all even} \\ 4 & \text{if } h,k,l \text{ all odd} \\ 0 & \text{otherwise} \end{cases} \tag{6.10}$$

Each magnetic basis vector has a fixed phase relationship between each site, constraining the structure factors $\boldsymbol{\mathcal{F}}$, and imposing a symmetry constrained extinction ($\boldsymbol{\mathcal{F}} = \mathbf{0}$) on some Bragg peak positions.

Writing the Bragg peak position as

$$\boldsymbol{Q} = h\boldsymbol{a}^* + k\boldsymbol{b}^* + l\boldsymbol{c}^* \tag{6.11}$$

and the position of the Pr^{4+}ions as

$$\boldsymbol{p}_1 = \left(\frac{1}{8}, \frac{1}{8}, -\frac{3}{8} + \delta \right) \tag{6.12a}$$

$$\boldsymbol{p}_2 = \left(\frac{1}{8}, \frac{1}{8}, -\frac{3}{8} - \delta \right) \tag{6.12b}$$

$$\boldsymbol{p}_3 = \left(-\frac{1}{8}, -\frac{1}{8}, \frac{3}{8} - \delta \right) \tag{6.12c}$$

$$\boldsymbol{p}_4 = \left(-\frac{1}{8}, -\frac{1}{8}, \frac{3}{8} + \delta \right) \tag{6.12d}$$

with $\delta = 0.0838(1) \approx \frac{1}{12}$, equivalent to the structure of β-Li_2IrO_3 [10], the explicit structure factors evaluate as

$$\boldsymbol{\mathcal{F}}_F(\boldsymbol{Q}) = \begin{cases} 16\ \boldsymbol{\mu}(-1)^l \cos\xi \cos 2\pi l\delta & \text{if } h,k,l \text{ all even or all odd} \\ 0 & \text{otherwise} \end{cases} \tag{6.13a}$$

$$\boldsymbol{\mathcal{F}}_A(\boldsymbol{Q}) = \begin{cases} 16i\boldsymbol{\mu}(-1)^l \cos\xi \sin 2\pi l\delta & \text{if } h,k,l \text{ all even or all odd} \\ 0 & \text{otherwise} \end{cases} \tag{6.13b}$$

$$\boldsymbol{\mathcal{F}}_C(\boldsymbol{Q}) = \begin{cases} 16i\boldsymbol{\mu}(-1)^l \sin\xi \cos 2\pi l\delta & \text{if } h,k,l \text{ all even or all odd} \\ 0 & \text{otherwise} \end{cases} \tag{6.13c}$$

$$\boldsymbol{\mathcal{F}}_G(\boldsymbol{Q}) = \begin{cases} 16\ \boldsymbol{\mu}(-1)^l \sin\xi \sin 2\pi l\delta & \text{if } h,k,l \text{ all even or all odd} \\ 0 & \text{otherwise} \end{cases} \tag{6.13d}$$

where ξ is defined to be

$$\xi := \frac{\pi}{4}(h+k+l) \tag{6.14}$$

These structure factors create some additional selection rules. Where h,k,l are all even, if $h+k+l = 4n$, where n is an integer $\xi = n\pi$. So $\boldsymbol{\mathcal{F}}_C = 0$, and $\boldsymbol{\mathcal{F}}_G = 0$. In the other case if $h+k+l = 4n+2$ then $\xi = \left(n+\frac{1}{2}\right)\pi$. So $\boldsymbol{\mathcal{F}}_F = 0$, and $\boldsymbol{\mathcal{F}}_A = 0$. Additionally, in β-Na_2PrO_3 $\delta \approx \frac{1}{12}$ (see Table **??**), so at $l = 6p+3$, $\boldsymbol{\mathcal{F}}_F = 0$, $\boldsymbol{\mathcal{F}}_C = 0$ and at $l = 6p$, $\boldsymbol{\mathcal{F}}_A = 0$, $\boldsymbol{\mathcal{F}}_G = 0$. These selection rules are summarised in Table **??**.

Table 6.4: Selection rules for $\boldsymbol{q} = 0$ magnetic basis vectors in β-Na_2PrO_3 .

	F	A	C	G
h, k, l all odd, $l \neq 6p+3$	✓	✓	✓	✓
h, k, l all odd $l = 6p+3$	·	✓	·	✓
h, k, l all even - $h+k+l = 4n$, $l \neq 6p$	✓	✓	·	·
h, k, l all even - $h+k+l = 4n$, $l = 6p$	✓	·	·	·
h, k, l all even - $h+k+l = 4n+2$, $l \neq 6p$	·	·	✓	✓
h, k, l all even - $h+k+l = 4n+2$, $l = 6p$	·	·	✓	·

Attribution note: *β-Na_2PrO_3 powder sample synthesis, powder neutron diffraction measurements, and magnetic structure fits using FULLPROF [9] were performed by Rytaro Okuma at the University of Oxford and reported in [20]. These data are reproduced in this section for completeness.*

Powder neutron diffraction data measured below T_N was reported in [20], showing clear magnetic scattering below T_N. The magnetic peaks are shown by taking the

difference between base temperature ($1.3\,\mathrm{K}$) and well above the transition ($10\,\mathrm{K}$). The use of a centred cell for indexing the peaks can make it less clear what the magnetic unit cell is, given a set of reflections. This is because a larger magnetic cell than the structural primitive cell could still have the translational symmetry of the centred cell, so magnetic reflections would still have integer Miller indices. Table **??** shows a number of expected peaks for $\boldsymbol{q} = 0$ magnetic reflections in β-Na_2PrO_3 , alongside the associated lattice plane spacing.

Table 6.5: Miller indices of expected $\boldsymbol{q} = 0$ magnetic reflections in β-Na_2PrO_3 , and associated lattice plane spacing d for $d \geq 2.9$Å. Tick and crosses in the rightmost three columns indicate whether a particular basis vector could have caused that reflection according to the selection rules in Table **??**

h	k	l	d (Å)	seen?	A	C	G
0	0	2	10.26	✓	·	✓	✓
1	1	1	5.37	✓	✓	✓	✓
0	0	4	5.13	✓	✓	·	·
0	2	0	4.89	✗	·	✓	·
0	2	2	4.42	✓	✓	·	·
1	1	3	4.31	✓	✓	·	✓
0	2	4	3.54	✓	·	✓	✓
0	0	6	3.42	✓	·	✓	·
2	0	0	3.38	✓	·	✓	·
1	1	5	3.30	✓	✓	✓	✓
2	0	2	3.21	✓	✓	·	·
1	3	1	2.91	✓	✓	✓	✓

All of the magnetic reflections detected can be indexed by Miller indices of the primitive structural cell, indicating a $\boldsymbol{q} = 0$ magnetic propagation vector.

The presence or absence of magnetic reflections at different Miller indices can be compared to the selection rules to determine which magnetic basis vectors are present. Of particular interest are the peaks (020), (006), and (200). From the selection rules in Table **??** it can be seen that these reflections are in the h, k, l all even, $h + k + l = 4n + 2$, $l = 6p$ family of peaks, which only have intensity from the C basis vector. The presence of finite intensity on the (006) and (200) peaks indicates that a C basis vector must be present, the zero intensity at (020) means that this must be a C_y component, as this will not contribute to $\boldsymbol{Q} \parallel \boldsymbol{y}$ peaks due to the neutron polarisation factor. There is also finite

intensity at the (004) peak which can have contributions from A and F basis vectors. F can be ruled out as this is a ferromagnetic contribution, and non-zero μ_{tot} would be detected as a ferromagnetic anomaly in susceptibility, and have a clear signature in torque as is seen in α-Na_2PrO_3 and discussed in Chapter 5. This indicates that there is an A_x or A_y contribution, which must come from A_x, as the combination A_y, C_y cannot maintain the fixed lengths of the spin vectors at each site. Together, these observed peaks with these selection rules imply a magnetic structure made up of A_x and C_y magnetic basis vectors.

Table **??** shows the irreducible representations (irreps) for $\boldsymbol{q} = 0$ magnetic structures. The relevant group is $Fddd \otimes \Theta$, where Θ is the time-reversal operator. This group has irreps $\Gamma_n^{\pm}$, and $m\Gamma_n^{\pm}$ with characters under time reversal $\chi^{(\Gamma_n^{\pm})}(\Theta) = +1$,$\chi^{(m\Gamma_n^{\pm})}(\Theta) = -1$ respectively, and all other characters the same as the associated $\Gamma_n^{\pm}$ irrep of the $Fddd$ structural space group [21]. All magnetic basis vectors exist in the $m\Gamma_n^{\pm}$ irreps, as they all change sign under time-reversal.

Table 6.6: Irreducible representations (irreps) and associated magnetic basis vectors for $\boldsymbol{q} = 0$ magnetic structures, obtained from ISODISTORT [22].

Irrep	Basis Vector
$m\Gamma_1^+$	G_z
$m\Gamma_2^+$	F_z
$m\Gamma_3^+$	F_x, G_y
$m\Gamma_4^+$	F_y, G_x
$m\Gamma_1^-$	A_z
$m\Gamma_2^-$	C_z
$m\Gamma_3^-$	A_y, C_x
$m\Gamma_4^-$	A_x, C_y

From this table, it can be seen that the A_x and C_y magnetic basis vectors are members of the same $m\Gamma_4^-$ irrep. The natural interpretation is that these are the only magnetic basis vectors present in the magnetic structure. This is consistent with the behaviour seen in heat-capacity at the transition, discussed in Section **??**, as second order phase transition at T_N suggests that the magnetic ordering will be described by a single irrep.

The time-reversal symmetry operation of the paramagnetic phase maps the magnetic structure $\alpha A_x + \beta C_y$ to $-\alpha A_x - \beta C_y$, so they must have the same energy. These are expected as two magnetic domains. Because A_x and C_y are both basis vectors for the

same $m\Gamma_4^+$ irrep, there are no symmetry operations which change the relative phase between the A_x and C_y components. This phase can be determined from the intensities of reflections where both A_x and C_y states contribute. These peaks are the h, k, l all odd, $l \neq 6p+3$ family, as per Table **??**

The intensity of magnetic scattering of a Bragg peak at (hkl) can be determined from the structure factor as

$$I(\boldsymbol{Q}) = |\boldsymbol{\mathcal{F}}_\perp(\boldsymbol{Q})|^2 \tag{6.15a}$$

$$= \boldsymbol{\mathcal{F}}_\perp(\boldsymbol{Q}) \cdot \boldsymbol{\mathcal{F}}_\perp^*(\boldsymbol{Q}) \tag{6.15b}$$

where $\boldsymbol{\mathcal{F}}_\perp(\boldsymbol{Q})$ is the component of the structure factor normal to the scattering direction $\boldsymbol{Q}$. If the vector moments are taken out of the structure factors

$$\boldsymbol{\mathcal{F}}(\boldsymbol{Q}) = \boldsymbol{\mu}_A \mathcal{F}_A(\boldsymbol{Q}) + \boldsymbol{\mu}_C \mathcal{F}_C(\boldsymbol{Q}) \tag{6.16}$$

then the perpendicular component can be extracted as

$$\boldsymbol{\mathcal{F}}_\perp(\boldsymbol{Q}) = \boldsymbol{\mu}_A^\perp \mathcal{F}_A(\boldsymbol{Q}) + \boldsymbol{\mu}_C^\perp \mathcal{F}_C(\boldsymbol{Q}) \tag{6.17}$$

where

$$\boldsymbol{\mu}_n^\perp = \boldsymbol{\mu}_n - \frac{\boldsymbol{\mu}_n \cdot \boldsymbol{Q}}{\boldsymbol{Q} \cdot \boldsymbol{Q}} \boldsymbol{Q} \tag{6.18}$$

The intensity at $\boldsymbol{Q}$ can then be written

$$\begin{aligned} I(\boldsymbol{Q}) =& \mu_A^2 \left(1 - \frac{(\boldsymbol{\mu}_A \cdot \boldsymbol{Q})^2}{\mu_A^2 Q^2}\right) \left|\mathcal{F}^A\right|^2 \\ &+ \mu_B^2 \left(1 - \frac{(\boldsymbol{\mu}_C \cdot \boldsymbol{Q})^2}{\mu_C^2 Q^2}\right) \left|\mathcal{F}^C\right|^2 \\ &- 2\frac{(\boldsymbol{\mu}_A \cdot \boldsymbol{Q})(\boldsymbol{\mu}_C \cdot \boldsymbol{Q})}{Q^2} \Re\left(\mathcal{F}_A^*(\boldsymbol{Q}) \cdot \mathcal{F}_C(\boldsymbol{Q})\right) \end{aligned} \tag{6.19}$$

where $\Re$ indicates the real part of the expression. The last term is a 'cross' term which is sensitive to the difference between (A_x, C_y) and $(A_x, -C_y)$.

A fit of the powder neutron diffraction data to each of these structures showed that a $(A_x, -C_y)$ structure has good quantitative agreement with the intensities of the observed peaks. The resulting magnetic structure is non-collinear, with spins in each zigzag chain close to the direction of the chain and a large angle between spins in adjacent chains. This structure can be seen in Figure **??**, where the black sites indicate the primitive/magnetic unit cell.

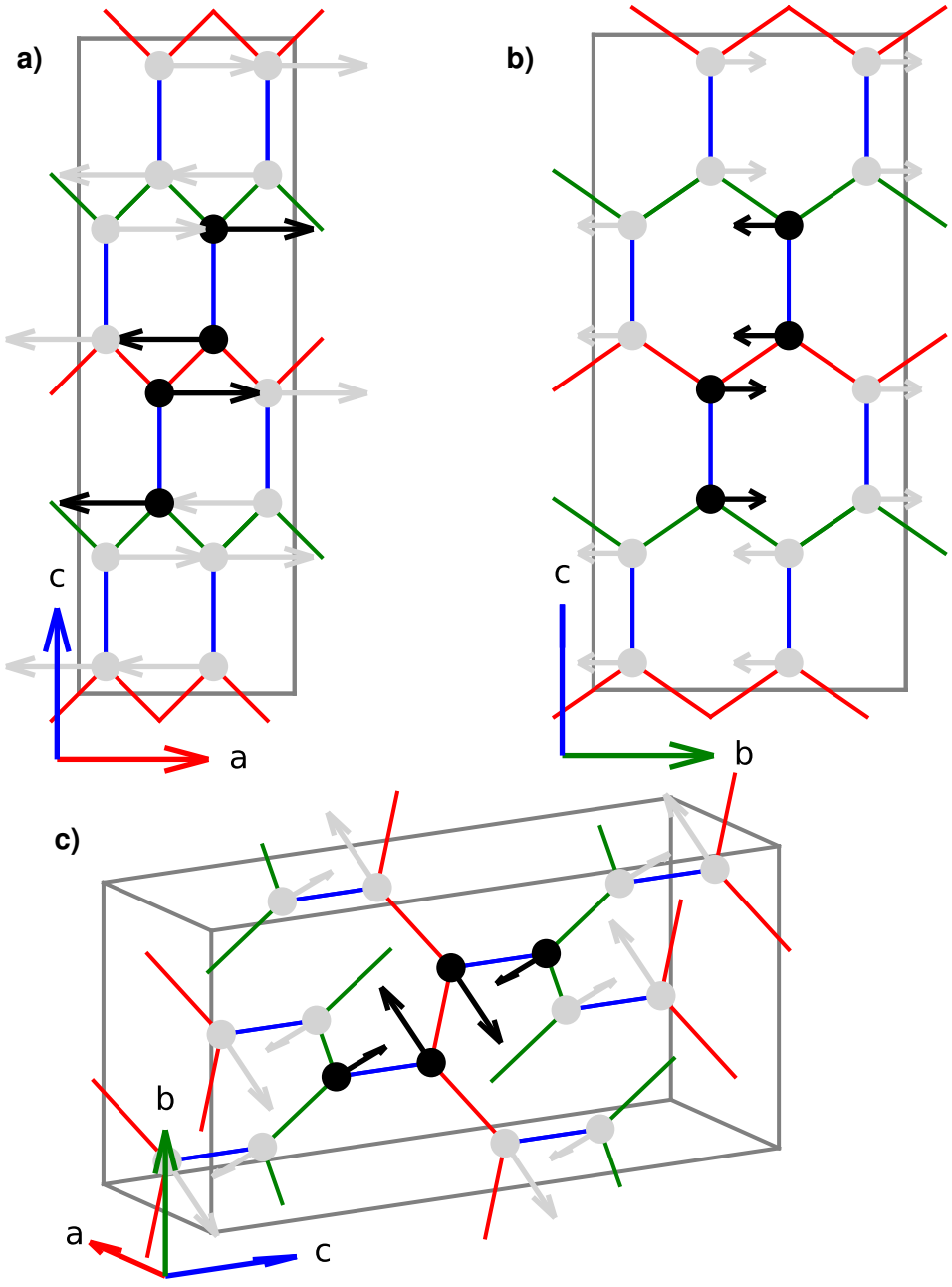


Figure 6.9: 3D model of experimentally observed $A_x, -C_y$ magnetic structure. **a)** is projection onto $\boldsymbol{ac}$ plane, **b)** is projection onto $\boldsymbol{bc}$ plane, **c)** is orthographic projection. Bonds in red show chain along $\boldsymbol{a}+\boldsymbol{b}$ direction, bonds in green show chain along $\boldsymbol{a}-\boldsymbol{b}$ direction, bonds in blue are parallel to the $\boldsymbol{c}$ axis. Sites marked in black show one primitive/magnetic unit cell.

6.7 Candidate Spin Hamiltonians

The magnetic phase diagrams of hyperhoneycomb lattices has been the explored in detail theoretically. The case with nearest-neighbour Kitaev interactions has been solved exactly, with a quantum spin liquid ground state [2], which is expected to have a finite transition temperature [23]. Extensions to this such as the Heisenberg-Kitaev model have also been studied [24]. Another proposed minimal model for hyperhoneycomb is the J-K-Γ model [5]. This includes only nearest-neighbour interactions and has the form

$$\mathcal{H} = \sum_{\langle i,j\rangle \in \alpha\beta(\gamma)} J\boldsymbol{S}_i \cdot \boldsymbol{S}_j + KS_i^\gamma S_j^\gamma \pm \Gamma(S_i^\alpha S_j^\beta + S_i^\beta S_j^\alpha) \tag{6.20}$$

where the sum is over the nearest-neighbour bonds. Each bond has an associated Ising axis $\gamma \in \{x, y, z\}$ and $\alpha\beta(\gamma)$ refer to the orthogonal plane to this axis. In the idealised $Fddd$ crystal structure with all PrO_6 octahedra cubic, the Pr-O-Pr-O superexchange planes have normal axes, called Kitaev axes, which each are a local Ising axis for the associated Pr-Pr bond [5, 25]. These Kitaev axes are mutually orthogonal and can be written in terms of the orthorhombic crystal axes

$$\begin{pmatrix} \hat{\boldsymbol{x}} \\ \hat{\boldsymbol{y}} \\ \hat{\boldsymbol{z}} \end{pmatrix} = \mathcal{R} \begin{pmatrix} \hat{\boldsymbol{a}} \\ \hat{\boldsymbol{b}} \\ \hat{\boldsymbol{c}} \end{pmatrix} = \begin{pmatrix} \frac{-1}{\sqrt{2}} & 0 & \frac{-1}{\sqrt{2}} \\ \frac{-1}{\sqrt{2}} & 0 & \frac{1}{\sqrt{2}} \\ 0 & -1 & 0 \end{pmatrix} \begin{pmatrix} \hat{\boldsymbol{a}} \\ \hat{\boldsymbol{b}} \\ \hat{\boldsymbol{c}} \end{pmatrix} \tag{6.21}$$

The Hamiltonian can also be written in tensor notation

$$\mathcal{H} = \sum_{\langle i,j\rangle \in \gamma, \mu\nu} \mathcal{J}_{\mu\nu}^\gamma S_i^\mu \, S_j^\nu \tag{6.22}$$

such that the Hamiltonian for an individual bond $\mathcal{H}_{i,j}^\gamma = \boldsymbol{S}_i^T \mathcal{J}^\gamma \boldsymbol{S}_i$. For the z-bond, the Hamiltonian $\mathcal{H}_{i,j}^z = J\boldsymbol{S}_i \cdot \boldsymbol{S}_j + KS_i^z S_j^z + \Gamma(S_i^x S_j^y + S_i^y S_j^x)$ exchange tensor can be written in Kitaev axes as

$$\mathcal{J}^z = \begin{pmatrix} J & \Gamma & 0 \\ \Gamma & J & 0 \\ 0 & 0 & J+K \end{pmatrix} \tag{6.23}$$

and in orthorhombic axes this takes the diagonal form

$$\mathcal{R}^T \mathcal{J}^z \mathcal{R} = \begin{pmatrix} J-\Gamma & 0 & 0 \\ 0 & J+K & 0 \\ 0 & 0 & J+\Gamma \end{pmatrix} \tag{6.24}$$

In previous theoretical work [5], the x,y,z bonds were treated as being related by pseudo-symmetry under a 3-fold rotation around the normal to the local honeycomb plane, which contains all three bonds coming from each site. This approximation is reasonable for the idealised $Fddd$ crystal structure with cubic PrO_6 octahedra. However, β-Na_2PrO_3 shows some local distortions which may invalidate this simplification. The important symmetries constraining the nearest-neighbour bonds are a 2-fold axis through the z bonds, which relate the x and y bonds together, and an inversion centre at the x and y bond midpoints. The J, K, Γ parameters on z and x bonds are not required to be the same by symmetry, so the values for an x bond on the $\boldsymbol{a} + \boldsymbol{b}$ chain are written as J', K', Γ' respectively as

$$\mathcal{J}^x = \begin{pmatrix} J' + K' & 0 & 0 \\ 0 & J' & \Gamma' \\ 0 & \Gamma' & J' \end{pmatrix} \tag{6.25}$$

and the y bond on the same zigzag chain is related by a two-fold rotational symmetry around the $(1/8, 1/8, z)$ axis

$$\mathcal{J}^y = \begin{pmatrix} J' & 0 & -\Gamma' \\ 0 & J' + K' & 0 \\ -\Gamma' & 0 & J' \end{pmatrix} \tag{6.26}$$

The previous work on this model found that with $J = J', K = K', \Gamma = \Gamma'$ it could stabilise many different classical magnetic structures including a number of $\boldsymbol{q} = 0$ non-collinear magnetic structures. This section seeks to find a minimal model for the observed magnetic structure, investigating various parts of the $J' = J, K' = K, \Gamma' = \pm\Gamma$ family of Hamiltonians. In all the models discussed in this section, an isotropic g-factor $g = 1$ is used consistent with the value determined from powder susceptibility measurements are high temperatures [20], equal to the powder average value determined for the honeycomb polymorph α-Na_2PrO_3 [13]. Changes in the g-factor will affect the quantitative magnetic fields where features occur but not the qualitative features themselves or the overall phase diagram.

All calculations reported in this section were performed numerically using the `qafm` software I developed for this thesis using the principles outlined in Chapter 4.

6.7.1 Minimal $J\Gamma\Gamma'$ model

A minimal model with $K = 0$ and dominant Heisenberg interactions can stabilise the $A_x, -C_y$ structure found with neutron diffraction as described above [20].

In this model, with values which fit the spin gap and bandwidth of excitations observed in inelastic neutron scattering experiments [20], $J = 1.22\text{meV}$, $K = 0$, $\Gamma = -\Gamma' = -0.27\text{meV}$. This stabilises a $0.99A_x - 0.14C_y$ zero-field magnetic structure, which has a smaller C_y component than the one measured with neutron diffraction, possibly due to interactions not captured in the minimal model.

Figure **??** shows theoretical mean-field calculations of how the magnetic state changes within this minimal model as field is applied along the crystallographic directions. Fig. **??a)** shows how the projection of the magnetic state onto the basis vectors varies as magnetic field increases in the $\boldsymbol{B} \parallel \boldsymbol{a}$ direction. This shows a first order spin-flop phase transition at $g_x B_{\text{SF}} = 14\,\text{T}$. This is a transition between the $\pm(A_x, -C_y)$ low-field ground state to a $(F_x, G_y) \pm (A_y, -C_x)$ spin-flop phase. Note that while $F_x \pm (A_y, -C_x)$ would not be allowed due to the constraint that the moment lengths are fixed, mixing in the G_y term allows the states to coexist. For fields parallel to the crystallographic $\boldsymbol{a}, \boldsymbol{b}, \boldsymbol{c}$ axes, 8 of the 16 total symmetry operations are broken, but the 8 irreps in all three groups have the same magnetic basis vectors as the zero-field group (Tables A.1, A.2, A.3). For fields $\boldsymbol{B} \parallel \boldsymbol{a}$ the magnetic structures $(A_x, -C_y)$ and $(A_y, -C_x)$ are in different irreducible representations and must be separated by a phase transition. At $g_x B_{\text{P}} = 65\,\text{T}$ this canted phase has a continuous phase transition to a near-polarised (F_x, G_y) phase. There is no higher field transition to a pure F_x phase, this is because F_x and G_y are basis vectors of the same $\Gamma_1^+(\boldsymbol{B} \parallel \boldsymbol{a})$ irrep of the paramagnetic group with field applied. This G_y is reduced asymptotically to zero with increasing field above B_{P}.

Fig. **??b, c)** show how the projection of the magnetic state onto the basis vectors varies as magnetic field increases in the $\boldsymbol{B} \parallel \boldsymbol{b}$, $\boldsymbol{B} \parallel \boldsymbol{c}$ directions respectively. In both cases, there is a continuous phase transition to a near-polarised state at $65\,\text{T}$. For field $\boldsymbol{B} \parallel \boldsymbol{b}$, the F_y state mixes with the G_x state in the same $\Gamma_1^+(\boldsymbol{B} \parallel \boldsymbol{b})$ irrep. For field $\boldsymbol{B} \parallel \boldsymbol{c}$, the F_z state has no other magnetic basis vectors in the same $\Gamma_1^+(\boldsymbol{B} \parallel \boldsymbol{c})$ irrep to mix with.

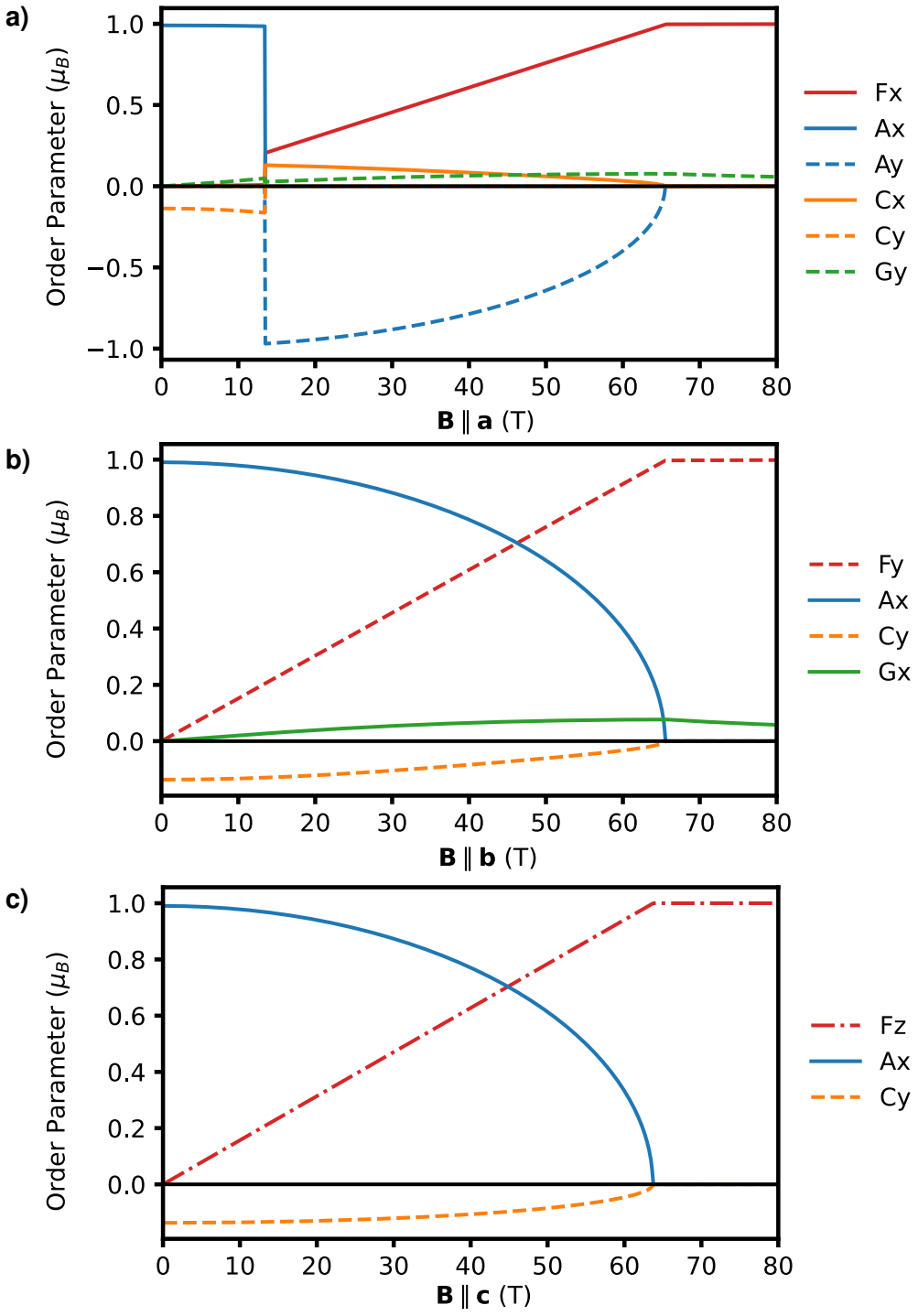


Figure 6.10: Calculated evolution of magnetic order parameters, defined in text, with field up to $B = 80\,\mathrm{T}$ for applied fields in the **a)** ***a***, **b)** ***b***, **c)** ***c*** crystallographic directions. Here, values of $\pm\mu_B$ is fully saturated. Calculation is a mean-field model for $J = 1.22\mathrm{meV}$, $K = 0$, $\Gamma = -\Gamma' = -0.27\mathrm{meV}$ as described in the text.

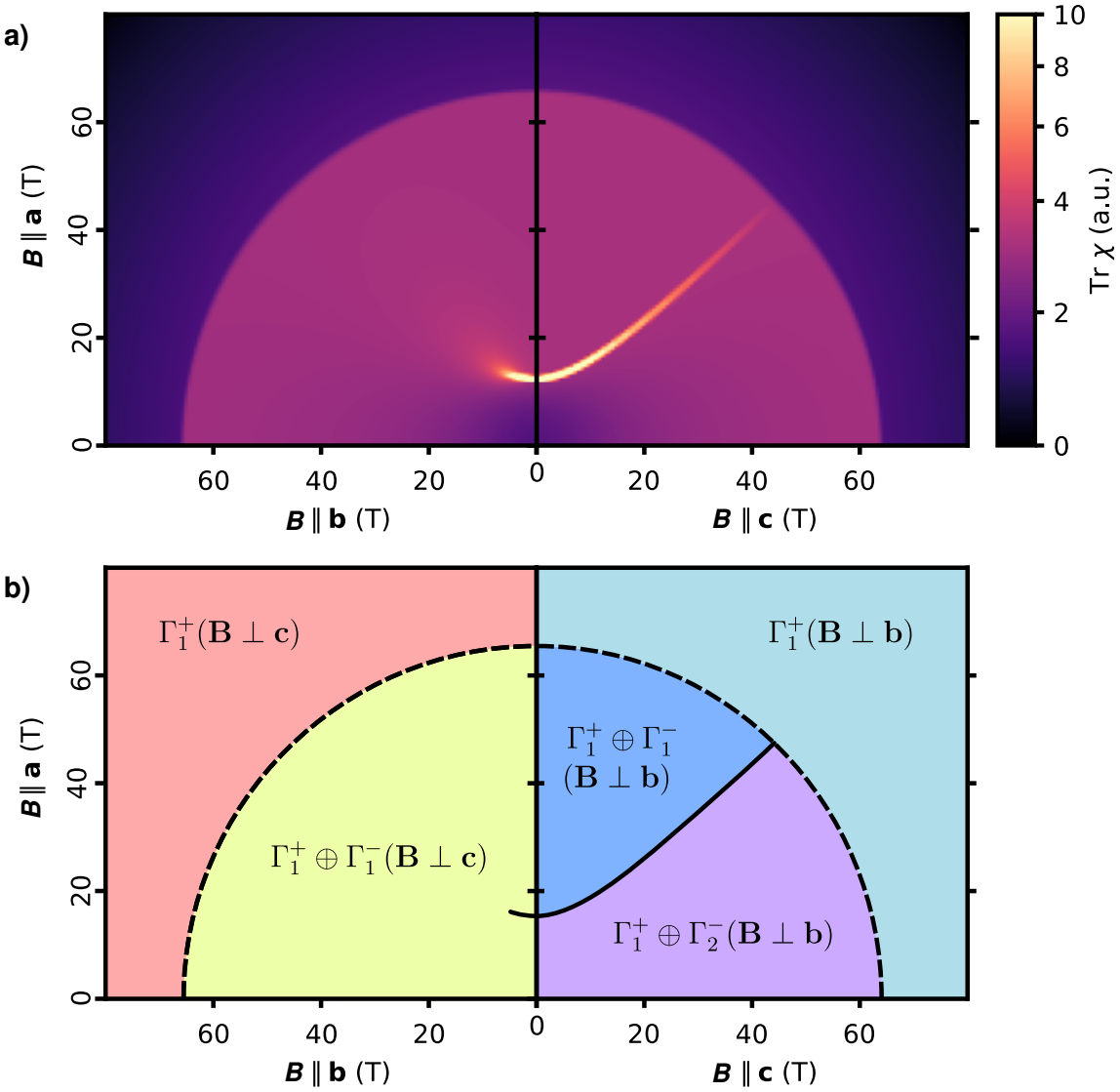


Figure 6.11: a) Calculated trace of the differential susceptibility tensor (see **??**) Trχ as a function of applied field in the $\boldsymbol{a}$, $\boldsymbol{b}$ plane (left panel) and $\boldsymbol{a}$, $\boldsymbol{c}$ plane (right panel).**b)** Extracted phase diagram from mean-field calculation for applied field in the $\boldsymbol{a}$, $\boldsymbol{b}$ plane (left panel) and $\boldsymbol{a}$, $\boldsymbol{c}$ plane (right panel). Coloured regions indicate regions where magnetic state irrep contribution does not change, text overlays show irreducible representation content of magnetic state using irreps for the associated field plane, as in Table **??**. Dashed lines indicate continuous phase transition, solid lines indicate first-order phase transitions. Calculation is a mean-field model for $J = 1.22\mathrm{meV}$, $K = 0, \Gamma = -\Gamma' = -0.27\mathrm{meV}$ as described in the text.

Figure **??** shows the field phase diagram for this model. In Fig. **??a)** the left panel shows the phase diagram for field orientations in the $\boldsymbol{a}, \boldsymbol{b}$ plane. The right panel shows the phase diagram for field orientations in the $\boldsymbol{a}, \boldsymbol{c}$ plane. The colour is derived from the trace of the differential susceptibility tensor

$$\chi_{ij} = -\frac{\partial^2 \mathcal{F}}{\partial B_i \partial B_j} \tag{6.27}$$

with free energy $\mathcal{F}$, and magnetic field vector $\boldsymbol{B}$. In Landau theory this is expected to diverge at first-order phase transitions, and have a discontinuity at second-order phase transitions [11, 26].

For all orientations of fields in the $\boldsymbol{a}, \boldsymbol{b}$ plane, there is a continuous transition to a near-polarised state at $65\,\mathrm{T}$, as is seen in the order parameter sweeps discussed above. This transition field is approximately independent of angle with the isotropic g factor used in the calculation. The effect of an anisotropic g factor will linearly scale the fields along the $\boldsymbol{a}, \boldsymbol{b}, \boldsymbol{c}$ directions, but the phase diagram will remain qualitatively the same. For fields directly along the $\boldsymbol{a}$ direction, there is a first-order spin-flop phase transition, discussed above. This first order transition remains for small angles made to the $\boldsymbol{a}$ axis, however for large enough angles towards $\boldsymbol{b}$ no transition is seen. As such, one can move between the low-field $A_x, -C_y$ and high-field $A_y, -C_x$ regions for fields along $\boldsymbol{a}$, without crossing a phase transition, by first increasing the field along $\boldsymbol{b}$. For fields in the $\boldsymbol{a}, \boldsymbol{c}$ plane, there is also a continuous transition to a near-polarised state at $65\,\mathrm{T}$ which is approximately independent of the field direction. In this case, the first order transition for fields along $\boldsymbol{a}$ is joined by a line of first order transitions to the polarisation phase boundary. As such, there is no way of moving between the $A_x, -C_y$ and $A_y, -C_x$ regions for fields along $\boldsymbol{a}$ without crossing a phase boundary, when field is kept in the $\boldsymbol{a}, \boldsymbol{c}$ plane.

These differences between the two planes can be understood from the symmetry of the crystal. When a magnetic field is applied, the symmetry of the space group is reduced. The symmetry operations which remain are those which leave the magnetic field invariant. For a completely general magnetic field orientation, the only symmetry operations are E, and $\bar{1}$, but for magnetic fields applied parallel to or perpendicular to the crystallographic axes the symmetry is higher than this. Table **??** shows the irreps, character table, and

Table 6.7: Irreducible representations (irreps), character table, and magnetic basis vectors for space group $Fddd$ with applied magnetic field perpendicular to crystallographic axis $\boldsymbol{n} \in \{\boldsymbol{a}, \boldsymbol{b}, \boldsymbol{c}\}$. In character table '+' indicates $\chi = 1$, '-' indicates $\chi = -1$.

	E	$\bar{1}$	$2'_{\boldsymbol{n}}$	$d'_{\boldsymbol{n}}$	$\boldsymbol{n} = \boldsymbol{c}$	$\boldsymbol{n} = \boldsymbol{b}$	$\boldsymbol{n} = \boldsymbol{a}$
$\Gamma_1^+(\boldsymbol{B} \perp \boldsymbol{n})$	+	+	+	+	G_x, G_y, F_x, F_y	F_x, F_z, G_y	G_x, F_y, F_z
$\Gamma_2^+(\boldsymbol{B} \perp \boldsymbol{n})$	+	+	-	-	G_z, F_z	G_x, G_z, F_y	F_x, G_y, G_z
$\Gamma_1^-(\boldsymbol{B} \perp \boldsymbol{n})$	+	-	+	-	A_x, A_y, C_x, C_y	C_x, C_z, A_y	A_x, C_y, C_z
$\Gamma_2^-(\boldsymbol{B} \perp \boldsymbol{n})$	+	-	-	+	A_z, C_z	A_x, A_z, C_y	A_y, A_z, C_x

basis vectors for magnetic fields perpendicular to the crystallographic axes. In all cases for finite magnetic field, the $\Gamma_1^+(\boldsymbol{B} \perp \boldsymbol{n})$ couples linearly to the field, so can be non-zero without crossing a phase boundary. Note that for a completely general orientation of magnetic field, with details in Table A.5, there are only two irreps Γ^+, Γ^- so the only symmetry breaking transition possible is the polarisation transition at high field.

For field in the $\boldsymbol{a}, \boldsymbol{b}$ plane the phase diagram can be seen in the left panel of Fig. **??b)**. Here, $\boldsymbol{n} = \boldsymbol{c}$ and the $A_x, A_y, C_x, C_y \in \Gamma_1^-(\boldsymbol{B} \perp \boldsymbol{c})$ basis vectors are all members of the same irrep, so by applying field in the $\boldsymbol{a}, \boldsymbol{b}$ plane, these can mix without crossing a phase transition in the region marked in light green. In the near-polarised state (pink), the magnetic structure only contains basis vectors in the $\Gamma_1^+(\boldsymbol{B} \perp \boldsymbol{c})$ irrep, which couples to the field. These two regions have different irrep content and so must be separated by a phase transition.

For field in the $\boldsymbol{a}, \boldsymbol{c}$ plane, the phase diagram can be seen in the right panel of Fig. **??b)**. Here, $\boldsymbol{n} = \boldsymbol{b}$ and the basis vectors $A_x, C_y \in \Gamma_2^-(\boldsymbol{B} \perp \boldsymbol{b})$, $A_y, C_x \in \Gamma_1^-(\boldsymbol{B} \perp \boldsymbol{b})$ are members of different irreps. When applying field in the $\boldsymbol{a}, \boldsymbol{c}$ plane, these cannot mix without crossing a phase transition. So this region of the phase digram is separated into a $\Gamma_1^+ \oplus \Gamma_2^-(\boldsymbol{B} \perp \boldsymbol{b})$ region (purple), and a $\Gamma_1^+ \oplus \Gamma_1^-(\boldsymbol{B} \perp \boldsymbol{b})$ region (dark blue). In the near-polarised state (light blue), the magnetic structure only contains basis vectors in the $\Gamma_1^+(\boldsymbol{B} \perp \boldsymbol{b})$ irrep.

Figure **??** shows predicted torque vs field up to $80\,\mathrm{T}$ for fields applied close to the crystallographic $\boldsymbol{a}$, $\boldsymbol{b}$, $\boldsymbol{c}$ axes. The curves are produced by putting the field at $\theta = 5^\circ$ from a nominal crystal axis, in an assumed rotation plane containing the nominal axis and another crystal axis out of $\boldsymbol{a}, \boldsymbol{b}, \boldsymbol{c}$, and calculating the torque projected onto the axis

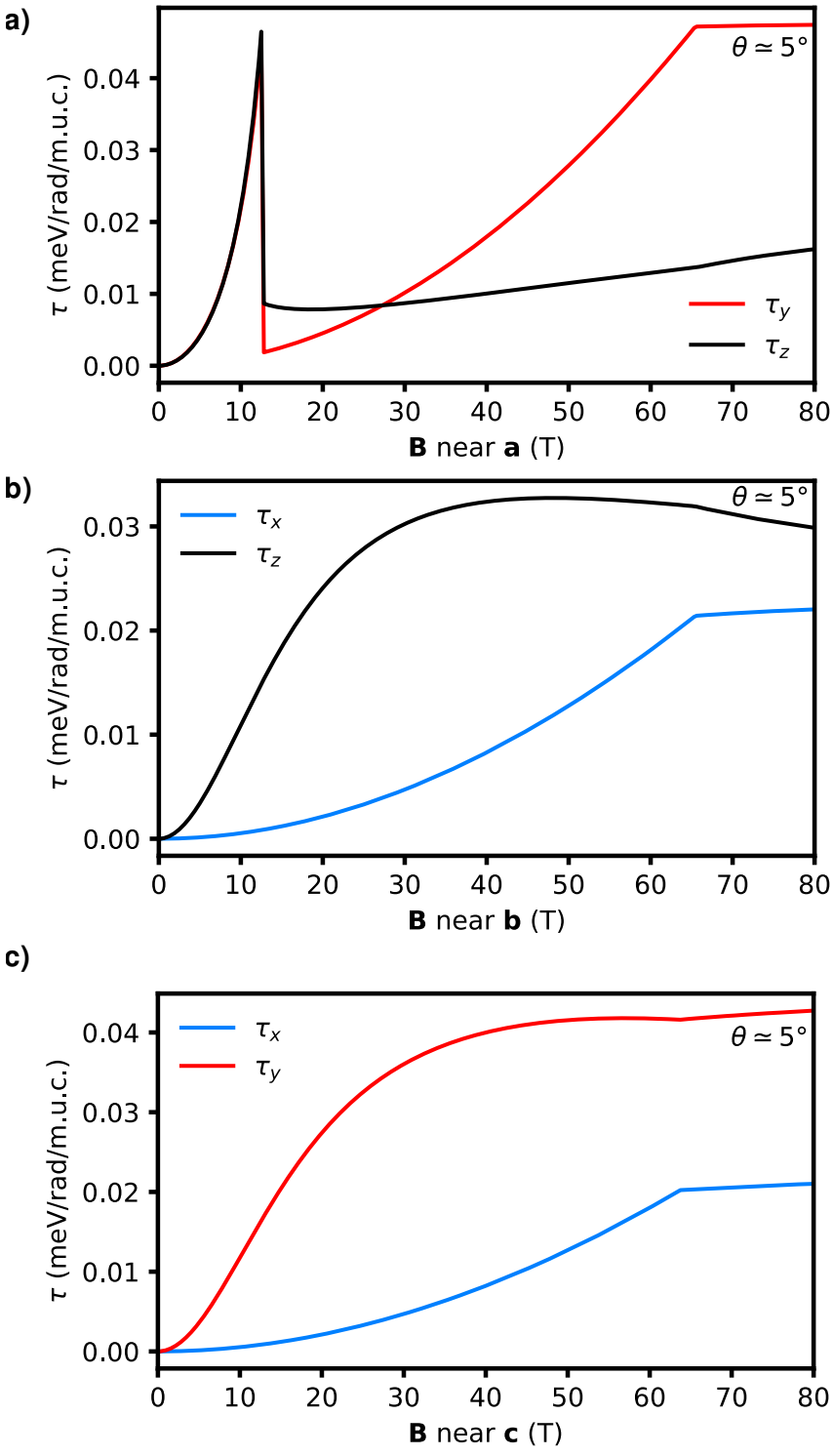


Figure 6.12: Calculated magnetic torque versus field up to $80\,\mathrm{T}$ for fields close to the $\boldsymbol{a}$, $\boldsymbol{b}$, $\boldsymbol{c}$ crystal axes. Torque is projected onto crystallographic axes as described in the text. In **a)**, the field is applied at angle θ away from $\boldsymbol{a}$ towards $\boldsymbol{b}$ for τ_z and towards $\boldsymbol{c}$ for τ_y. Situation is similar for panels **b, c)**. Calculation is a mean-field model for $J = 1.22\mathrm{meV}$, $K = 0, \Gamma = -\Gamma' = -0.27\mathrm{meV}$ as described in the text.

normal to the rotation plane. Both orthogonal rotation planes are considered for each nominal axis. Note that as the rotation angle sign is ambiguous, it is chosen such that the torque remains positive. For instance, Fig. **??a)**, the black trace shows torque projected onto the $\boldsymbol{c}$ axis (τ_z), with field applied 5° from the $\boldsymbol{a}$ axis towards the $\boldsymbol{b}$ axis. This is what would be measured experimentally if the sample was rotated in the $\boldsymbol{ab}$ plane, close to the $\boldsymbol{a}$ axis. For fields near the crystal $\boldsymbol{a}$ axis, both projections of torque show a sharp peak-like feature in torque at the spin-flop field. At high field, only the projection of torque onto the $\boldsymbol{b}$ axis shows a cusp-like anomaly at the polarisation field. With fields near the $\boldsymbol{b}$ axis, a very broad peak can be seen in the $\boldsymbol{c}$ projection of torque, centred at around $40\,\mathrm{T}$, but no clear sharp anomaly, even at the polarisation field. The $\boldsymbol{x}$ projection of torque shows a cusp-like anomaly at the polarisation field. The situation with fields along the $\boldsymbol{c}$ axis is similar, the projection onto the $\boldsymbol{a}$ axis shows a cusp-like transition at the polarisation field, and the projection onto the $\boldsymbol{b}$ axis shows a broad peak centred at $40\,\mathrm{T}$. This indicates no spin-flop transition for field near the $\boldsymbol{c}$ axis.

With these results in mind, if this model were realised experimentally, when rotating in the $\boldsymbol{ac}$ plane one would expect to see a peak-like anomaly in torque at the spin-flop, followed by a cusp-like transition for fields close to the $\boldsymbol{a}$ axis which would become less prominent as the field approached the $\boldsymbol{c}$ axis. When rotating in the $\boldsymbol{ab}$ plane, a peak-like anomaly in torque at the spin-flop transition would be seen, but no anomaly alongside polarisation. Finally, in the $\boldsymbol{bc}$, one would expect a cusp-like anomaly at the transition to polarisation at all angles between $\boldsymbol{b}$ and $\boldsymbol{c}$.

Figure **??a)** shows torque along the $\boldsymbol{a} + \boldsymbol{c}$ direction up to $16\,\mathrm{T}$. The red dashed line shows $\tau \sim B^2$ behaviour. This shows that for torque in the $\boldsymbol{ac}$ plane, magnetic torque is proportional to the field squared at low fields, but at higher fields the torque is growing slower than B^2, qualitatively consistent with the behaviour seen experimentally in Figure **??**. Magnetisation versus field is shown in Fig. **??b)**, this shows an order of susceptibilities at low field

$$\chi_c > \chi_b > \chi_a \tag{6.28}$$

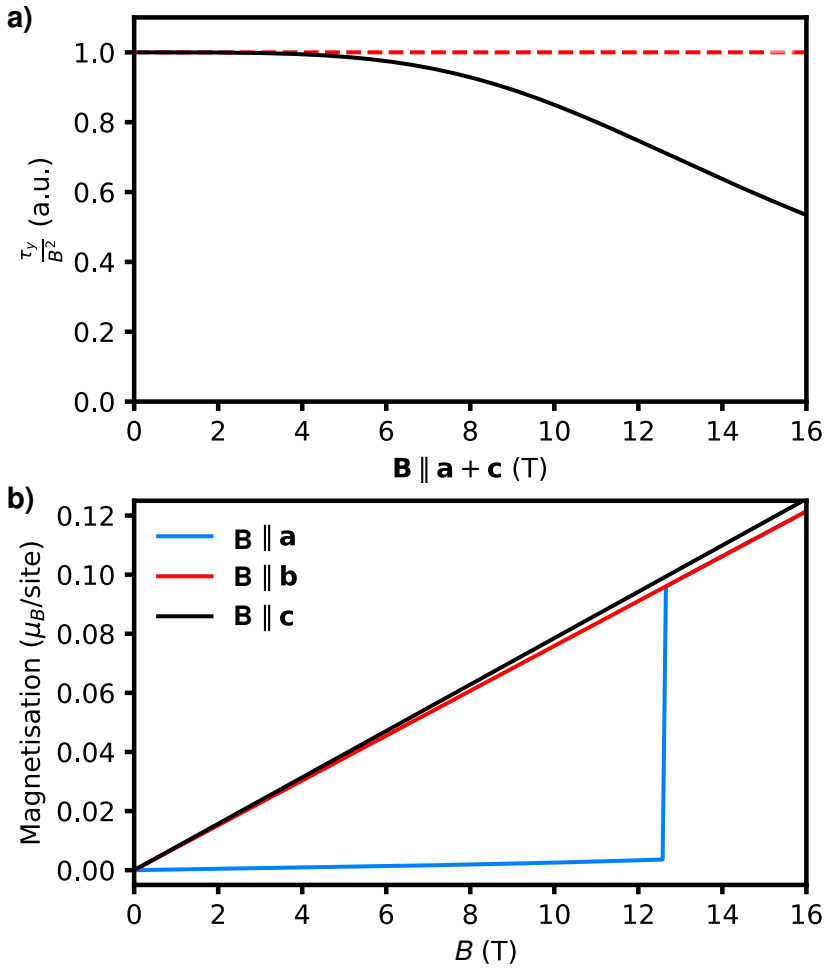


Figure 6.13: a) Calculated field dependence of magnetic torque scaled by square field $\frac{\tau}{B^2}$ up to $16\,\mathrm{T}$ for fields parallel to $\boldsymbol{a}+\boldsymbol{c}$ crystal axes. Torque is projected onto crystallographic $\boldsymbol{b}$ axis. Red dashed line shows $\tau \sim B^2$ behaviour. **b)**) Magnetisation versus field for field parallel to $\boldsymbol{a}$, $\boldsymbol{b}$, $\boldsymbol{c}$ directions up to $16\,\mathrm{T}$. Calculation is a mean-field model for $J = 1.22\mathrm{meV}$, $K = 0$, $\Gamma = -\Gamma' = -0.27\mathrm{meV}$ as described in the text.

consistent with what was observed experimentally, although with χ_b only slightly smaller than χ_c, where the empirical difference observed in torque appears much more significant. The spin-flop field of $12.5\,\mathrm{T}$ is experimentally accessible and would have been observed in in the torque magnetometry measurements discussed above. This, alongside the under-predicted C_y component in the structure, could suggest that the anisotropy in this model is not as strong as in β-Na_2PrO_3 . However, the increase in spin-flop field would also be consistent with anisotropic g-factor along $\boldsymbol{a}$ being less than the powder averaged value of $g \approx 1$. The high temperature torque magnetometry discussed above is consistent with this. It is likely that both effects contribute.

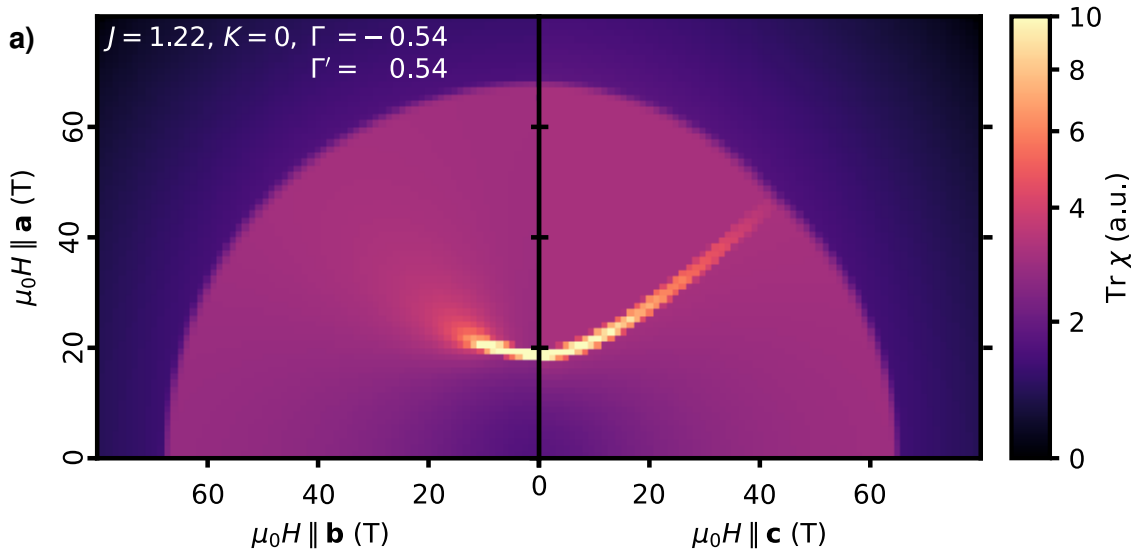


Figure 6.14: a) Calculated trace of the differential susceptibility tensor (see **??**) Trχ as a function of applied field in the $\boldsymbol{a}$, $\boldsymbol{b}$ plane (left panel) and $\boldsymbol{a}$, $\boldsymbol{c}$ plane (right panel). Calculation is a mean-field model for $J = 1.22\text{meV}$, $K = 0$, $\Gamma = -\Gamma' = -0.54\text{meV}$ as described in the text.

The model can be made more anisotropic by increasing by the Γ term, maintaining the $\Gamma = -\Gamma'$ relationship. Figure **??** shows the field phase diagram for a mean-field model with $J = 1.22\text{meV}$, $K = 0$, $\Gamma = -\Gamma' = -0.54\text{meV}$. The consequence is an increase in the spin-flop field, and a longer first order line in the $\boldsymbol{ab}$ plane. The zero-field ground state is $0.97A_x - 0.24C_y$, which has a larger C_y component than the $\Gamma = -0.27\text{meV}$, closer to the experimentally determined value. This model was however discounted in [20] due to disagreement with the observed spin gap in powder inelastic neutron scattering measurements.

6.7.2 $JK\Gamma$ model

By including a large Kitaev term in the model, an $A_x, -C_y$ magnetic structure can be stabilised with $\Gamma = \Gamma'$. For instance, with $J = 1.22\text{meV}$, $K = -1.4\text{meV}$, $\Gamma = \Gamma' = 0.5\text{meV}$, a $0.49A_x - 0.87C_y$ structure is stabilised. This model was found by searching many values of $J, K, \Gamma = \Gamma'$ such that the overall energy scale $\sqrt{J^2 + K^2 + \Gamma^2}$ is constant. This structure with dominant C_y is inconsistent with the dominant A_x structure seen with neutron diffraction.

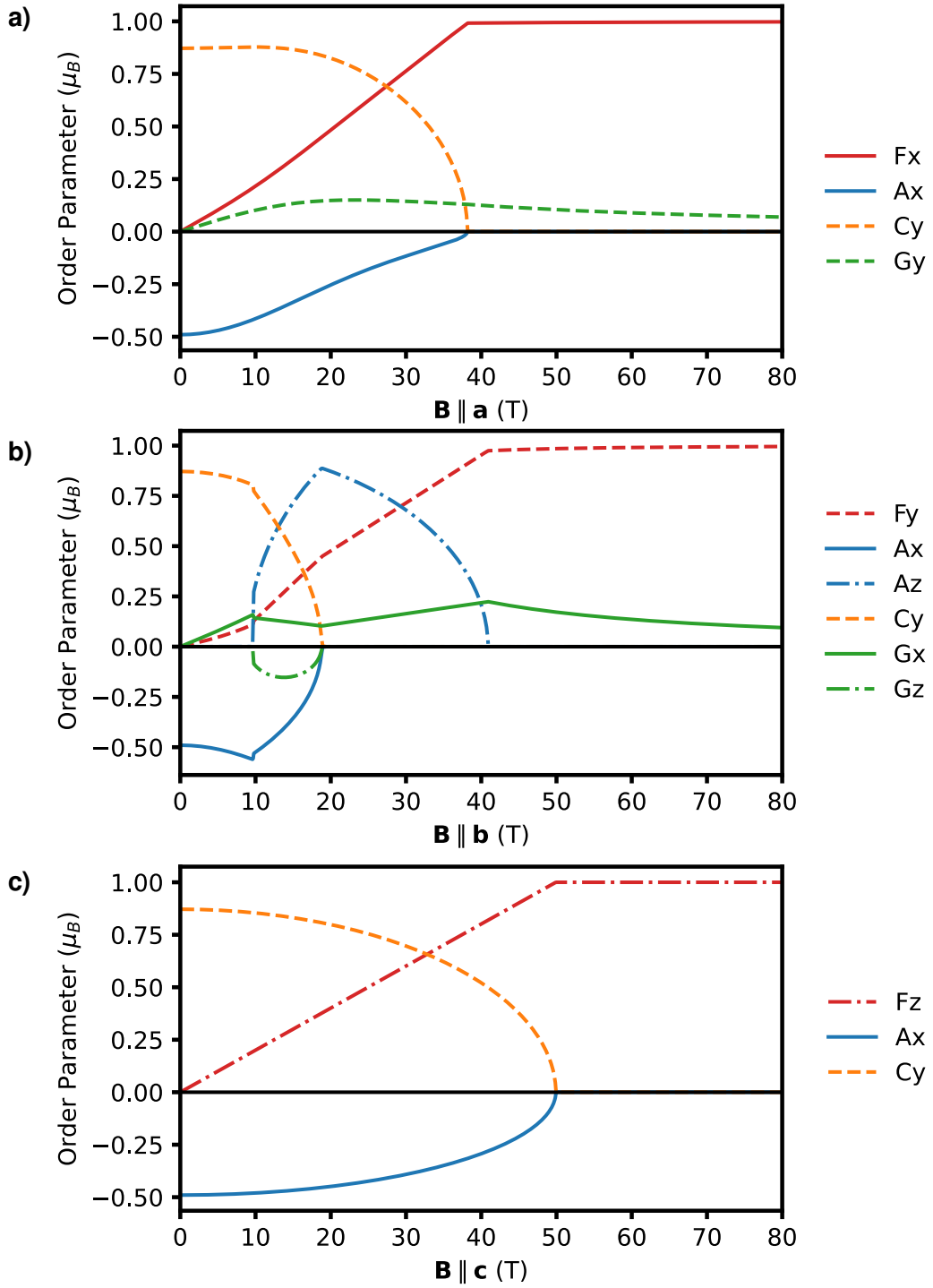


Figure 6.15: Calculated evolution of magnetic order parameters, defined in text, with field up to $B = 65\,\mathrm{T}$ for applied fields in the **a)** ***a***, **b)** ***b***, **c)** ***c*** crystallographic directions. Calculation is a mean-field model for $J = 1.22\mathrm{meV}$, $K = -1.4\mathrm{meV}$, $\Gamma = \Gamma' = 0.5\mathrm{meV}$ as described in the text.

Fig. **??** shows how the projection of the magnetic state onto the basis vectors varies as magnetic field increases in the $\boldsymbol{B} \parallel \boldsymbol{a}, \boldsymbol{b}, \boldsymbol{c}$ directions. This reveals two continuous magnetic phrase transitions along the $\boldsymbol{B} \parallel \boldsymbol{b}$ direction, with a high-field A_z structure, followed by a transition to polarisation at high field. No spin-flop transitions are seen in the $\boldsymbol{a}, \boldsymbol{c}$ directions.

While this model is inconsistent with the observed magnetic structure, and so is not fully explored, it is included to highlight the complexity of the J, K, Γ phase diagram with applied magnetic field.

6.8 Pulsed-Field Torque Magnetometry up to 67T

The presence of magnetic field induced phase transitions along certain crystallographic directions, and their evolution as the field is rotated in different planes, allows these models to be tested by using high-field magnetometry measurements. The presence of magnetic phase transitions will cause anomalies in magnetic torque and magnetisation, which could allow different magnetic phase diagrams and therefore different models, to be distinguished. In order to achieve this, torque magnetometry was performed at high magnetic fields at HZDR Dresden, allowing access to fields larger than $65\,\mathrm{T}$. These were performed using a $150\,\mu\mathrm{m}$ piezoresistive cantilever on a rotator probe. Additional measurements in DC fields up to $35\,\mathrm{T}$ will be presented in the subsequent Section **??**.

Attribution note: *Torque magnetometry measurements reported in this section were performed in collaboration with Matthew Pearce, and Ryutaro Okuma from the University of Oxford, and instrument scientists Toni Helm and Yurii Skourski at the HZDR Dresden high-magnetic-field facility.*

As the zero-field magnetic structure is predominantly antiferromagnetism along the $\boldsymbol{a}$ axis, a metamagnetic phase transition is likely when the magnetic field is applied along the $\boldsymbol{H} \parallel \boldsymbol{a}$ axis, regardless of the details of the model which stabilised the structure. Because of this, initial measurements were performed for fields close to the crystal $\boldsymbol{a}$ axis.

An $\approx 150\mu\mathrm{m}$ long sample was prepared such that the experimental rotation stage would rotate the sample in the $\boldsymbol{ac}$ plane. Here, θ is defined as the angle between the field direction and the $\boldsymbol{a}$ axis, in the $\boldsymbol{ac}$ plane. Initially, the sample was rotated such that the

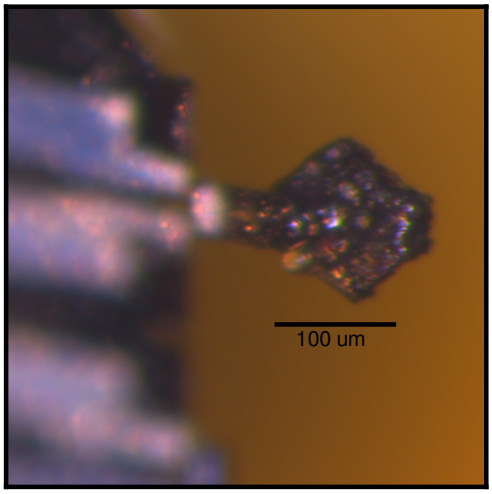


Figure 6.16: Photograph showing mounted β-Na_2PrO_3 crystal on piezoresistive cantilever for rotation in the $\boldsymbol{bc}$ plane. Sample is mounted on a natural growth face with $\boldsymbol{c}$ normal.

field would be applied close to the $\boldsymbol{a}$ axis, and was then rotated until it made a $\theta \simeq -15°$ angle with the axis. In between each field sweep, the sample was rotated by $4.5°$ in the $\boldsymbol{ac}$ plane, such that θ increased. Because of the $\boldsymbol{ac}$ rotation plane, the measured torque is the projection of the full vector torque $\boldsymbol{\tau} = \boldsymbol{M} \times \boldsymbol{B}$ onto the crystal $\boldsymbol{b}$ axis. A photograph of the mounted sample can be seen in Figure **??**, note that the photograph shows the sample in the $\boldsymbol{bc}$ plane, as this image shows the sample morphology most clearly.

Figure **??** shows the evolution of magnetic torque with applied magnetic field up to $67\mathrm{T}$ for fields close to the crystallographic $\boldsymbol{a}$ axis measured at $1.5\,\mathrm{K}$. Fig. **??a)** shows these torque data for $-9° < \theta < 9°$. All of these curves show a peak feature at $\mu_0 H_{\mathrm{SF}} = 26.2(1)\mathrm{T}$. This peak is sharper for fields closer to the $\boldsymbol{a}$ axis, and broadens at the angle made with this axis increases. This behaviour is consistent with a spin-flop transition. The angle θ is defined by taking the sweep with the sharpest peak as $\theta = 0°$, the angle of other sweeps is determined by measuring the angle offset from this point. This is challenging as the angle appears to change when the probe is thermally cycled, as such angles reported here are estimates. Fig. **??b)** shows the up- and down-sweeps for $\theta = 9°$ in yellow and black respectively. In addition to the peak feature attributed to a spin-flop transition, an additional cusp feature, marked with a downward arrow, can be seen in the up-sweep at $\mu_0 H_{\mathrm{P}} = 58.0(1)\,\mathrm{T}$. In the down-sweep, this feature cannot

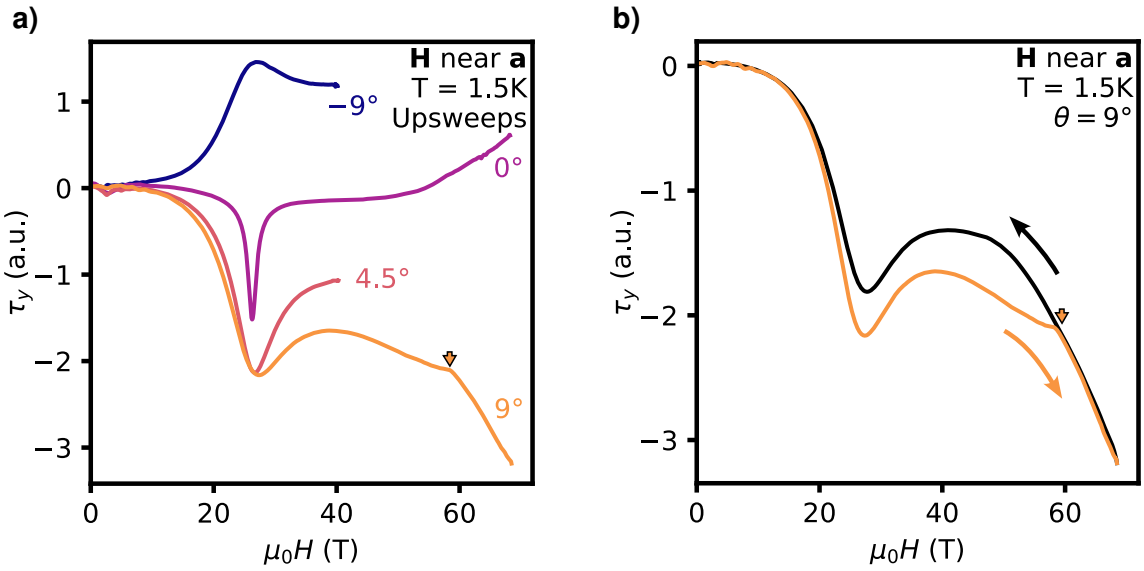


Figure 6.17: Evolution of magnetic torque with applied magnetic field close to the $\boldsymbol{H} \parallel \boldsymbol{a}$ axis for magnetic fields up to 67 T. Angle shown is measured from the nominal $\boldsymbol{a}$ axis towards the $\boldsymbol{c}$ axis. All curves are measured at $T = 1.5$ K. Arrow shows extracted polarisation field for sweep at 9°. **a)** Up-sweeps for angles between $-9°$ and 9°. **b)** Up-sweep in yellow, down-sweep in black.

be seen, instead at this point significant hysteresis opens and closes again at zero-field. I attribute the anomaly at H_P to a polarisation transition.

Figure **??** shows magnetic torque up-sweeps for temperatures between 0.67 K and 4.2 K with applied field close to the $\boldsymbol{a}$ axis. Fig. **??a)** shows these curves for $\theta \simeq 0°$. These show a sharp peak in torque at the spin-flop field for the measured temperatures below 4 K, which appears to be approximately temperature independent. Fig. **??b)** shows these curves for $\theta \simeq 13°$. These show a much broader peak in torque at the spin-flop field for the measured temperatures below 4 K, which appears to be approximately temperature independent. Additionally, these show a cusp feature at higher field. At applied fields above this feature, all temperature curves lie on top of each other. This cusp feature is strongly temperature dependent, consistent with a polarisation transition. From the these torque measurements, a phase diagram is produced, shown in Fig. **??c)**.

Figure **??** shows magnetic torque up-sweeps at 1.5 K for sweeps in the $\boldsymbol{ac}$ plane, rotating from near the $\boldsymbol{a}$ axis towards the $\boldsymbol{c}$ axis for $5° < \theta < 27°$. Fig. **??a)** shows the raw measured torque, while Fig. **??b)** shows the calculated derivative of this signal. For small angles, with the field close to the $\boldsymbol{a}$ axis, the peak in torque associated with the

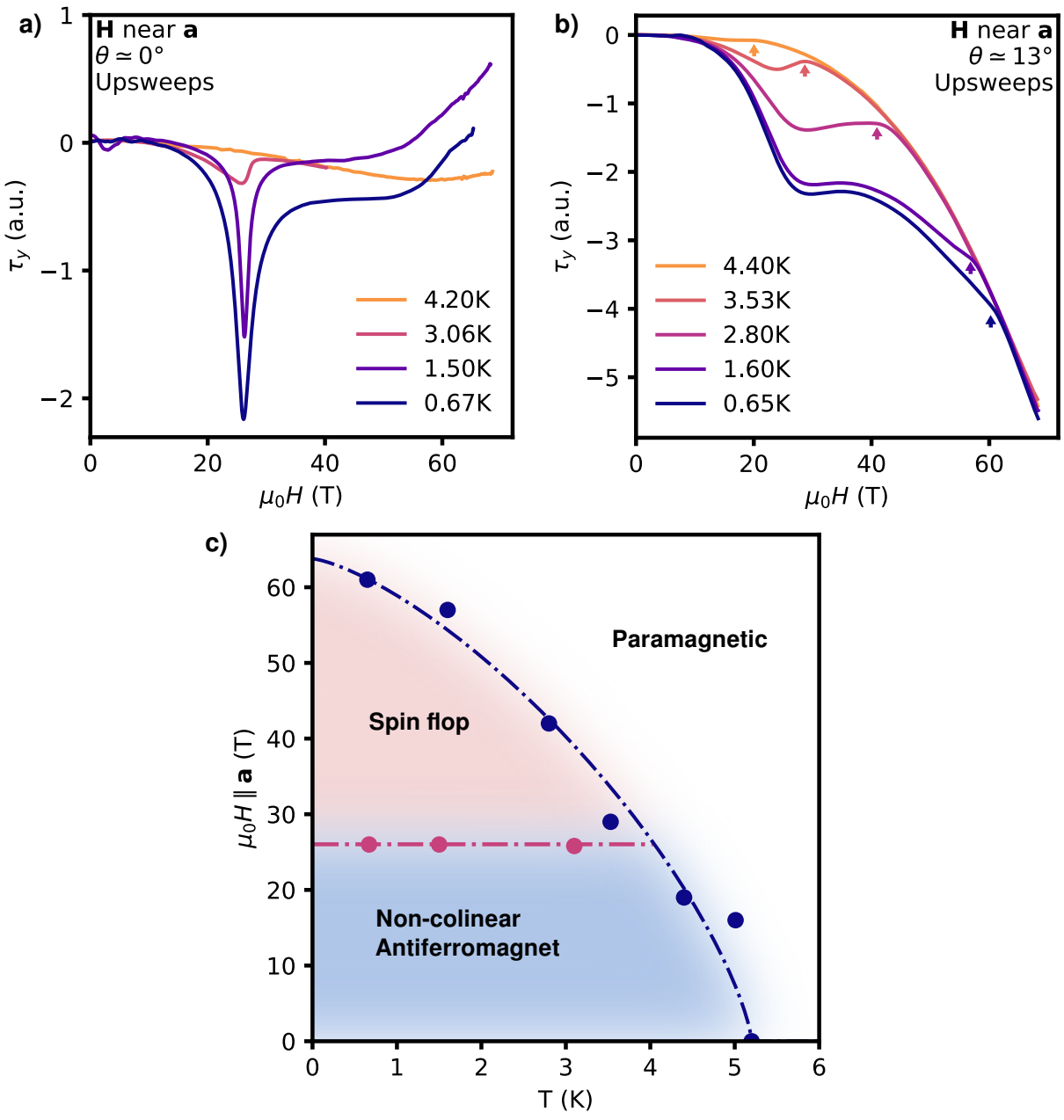


Figure 6.18: Evolution of magnetic torque with applied magnetic field close to the $\boldsymbol{H} \parallel \boldsymbol{a}$ axis for magnetic fields up to $67\,\mathrm{T}$ for temperatures between $0.67\,\mathrm{K}$ and $4.2\,\mathrm{K}$. In **a)** the nominal angle is $\theta = 0°$, in **b)** the nominal angle is $\theta = 9°$. Only up-sweeps are shown. **c)** Extracted low temperature phase diagram showing transitions to spin-flop, paramagnetic, and non-collinear antiferromagnetic phases for fields close to the $\boldsymbol{a}$ axis. Dashed lines are guides for the eye, error-bars are smaller than individual point markers.

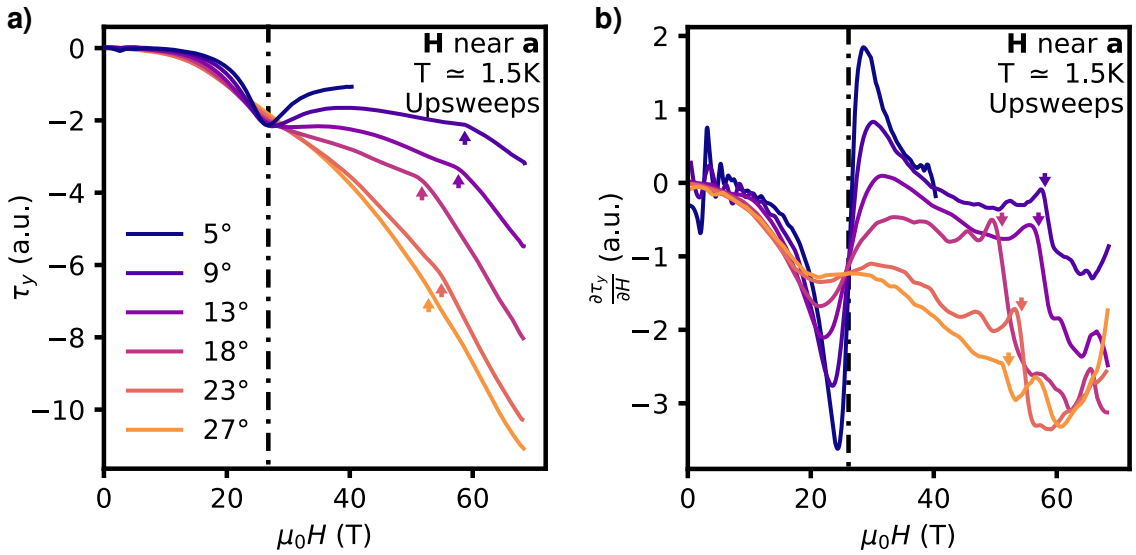


Figure 6.19: Evolution of magnetic torque with applied magnetic fields in the $\boldsymbol{ac}$ plane for up to 67 T. Angle shown is measured from the nominal $\boldsymbol{a}$ axis towards the $\boldsymbol{c}$ axis. All curves are measured at $T \simeq 1.5$ K. Arrows above curves show extracted polarisation field for associated sweep. **a)** shows up-sweep torque for angles between 5° and 27°. **b)** Derivative of torque with field $\frac{\partial \tau}{\partial H}$. Dotted black line shows nominal spin-flop field.

spin-flop field is prominent. This can be seen as a sharp feature in the derivative at the same field. As θ increases, this spin-flop peak becomes broader and smaller. In the largest angle shown of 27°, the spin-flop feature can not be seen in the raw data, but is still visible as a flattening of the derivative at $\mu_0 H \simeq 26$ T. This shows that the field where the feature occurs is independent of rotation angle. The cusp features associated with polarisation can also be seen in these data. These can also be seen as a step-change in the derivative, and are shown with arrows above the data. As angle increases, these appear to decrease in field. It is worth noting though that the high sensitivity of this transition to temperature makes it also sensitive to precise cryogenic conditions in the cryostat during the pulse. There is therefore some uncertainty in the temperature during the pulse, and so also uncertainty in this field. The measured polarisation field drops from 58 T at 9° to 55 T at 23°. At larger angles, the size of this feature drops in magnitude, making it unclear in both the raw torque and the derivative at the largest angle shown of 27°.

To determine the magnetic phase diagram close to the $\boldsymbol{b}$ axis the sample was remounted such that the rotator rotated in the $\boldsymbol{bc}$ plane. The mounted sample can be seen in Figure **??**, with the sample mounted on a flat growth plane normal to the $\boldsymbol{c}$ axis. The sample was

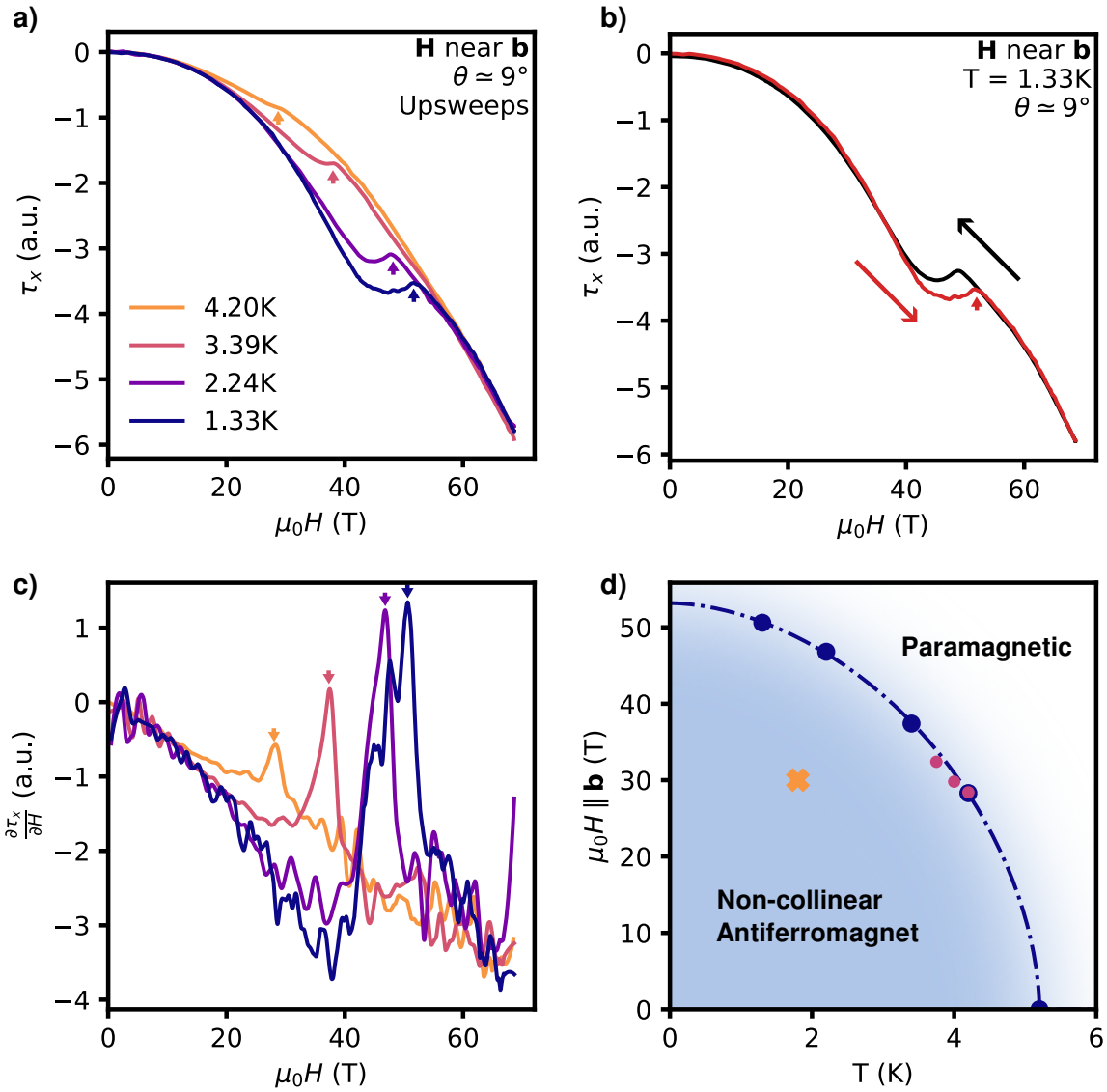


Figure 6.20: Evolution of magnetic torque with applied magnetic field close to the $\boldsymbol{H} \parallel \boldsymbol{b}$ axis for magnetic fields up to 67 T for temperatures between 1.3 K and 4.2 K, with nominal angle against the axis of $\theta = 9°$. In **a)** only up-sweeps are shown, in **b)** up-sweep is shown in red, down-sweep is shown in black. **c)** shows derivative of torque with field for up-sweeps, used to extract polarisation field. Upwards pointing arrows show extracted polarisation field. **d)** Extracted low temperature phase diagram showing transitions to paramagnetic and non-collinear antiferromagnetic phases for fields close to the $\boldsymbol{b}$ axis. Blue circles are extracted features shown from panel **c)**, pink circles are the same features extracted in DC fields, discussed later, yellow cross is feature in $\boldsymbol{ab}$ plane rotation discussed later. Dashed lines are guides for the eye, error-bars are smaller than individual point markers.

then rotated until the field was close to this $\boldsymbol{b}$ axis. These measurements were performed in a ^{4}He flow cryostat, with a base temperature of $\simeq 1.3\,\mathrm{K}$.

Figure **??** shows magnetic torque vs field for field applied close to the crystallographic $\boldsymbol{b}$ axis for temperatures between $1.33\,\mathrm{K}$ and $4.2\,\mathrm{K}$. In all temperatures below the transition, these show a cusp-like feature, with increases in field as the temperature decreases. Fig. **??b)** shows both up and down sweep for the base temperature measurement at $1.33\,\mathrm{K}$. This shows that a hysteresis opens at the cusp feature, much like the cusp feature observed close to the $\boldsymbol{a}$ axis. This feature can be seen clearly as a sharp peak in the differential of torque with field, shown in Fig. **??c)**, this sharp peak allows the field where the feature occurs to be extracted. The strong temperature dependence of this feature, combined with the fact that this is the only feature seen up to $67\,\mathrm{T}$, leads me to attribute this to the transition to the paramagnetic phase. The temperature evolution of the extracted polarisation field allows a phase diagram to be constructed for fields close to the crystal $\boldsymbol{b}$ axis Fig. **??d)**. The dotted line on the phase diagram is a fit to the functional form

$$\left(\frac{H_{\mathrm{P}}(T)}{H_{\mathrm{P}}(0\mathrm{K})}\right)^{\alpha} + \left(\frac{T}{T_c}\right)^{\alpha} = 1 \tag{6.29}$$

and is intended as a guide to the eye. From this fit, the zero-temperature polarisation field is placed in the region of $53\,\mathrm{T}$, and $\alpha \simeq 2$.

The evolution of torque-field dependence as the field is rotated towards the $\boldsymbol{c}$ axis can be seen in Fig. **??**. This shows that as the field is rotated towards the $\boldsymbol{c}$ axis, the observed features in torque broaden and become harder to distinguish from the background. Especially prominent in the $\theta = 23^\circ$ sweep, an additional feature can be seen above $60\,\mathrm{T}$, appearing as a flattening of the torque at high field. This can be seen at steeper angles, although it has a broader onset. The physical origin of this feature is unclear, if it is present close to the $\boldsymbol{b}$ axis, it must be at above the $67\,\mathrm{T}$ maximum field. If this is the case, it would suggest a more complex phase diagram than the one proposed. Despite the uncertainty in the origin and precise location of the feature, the associated anomaly in the derivative of torque can be seen in all the angles shown, including with fields close to the $\boldsymbol{c}$ axis.

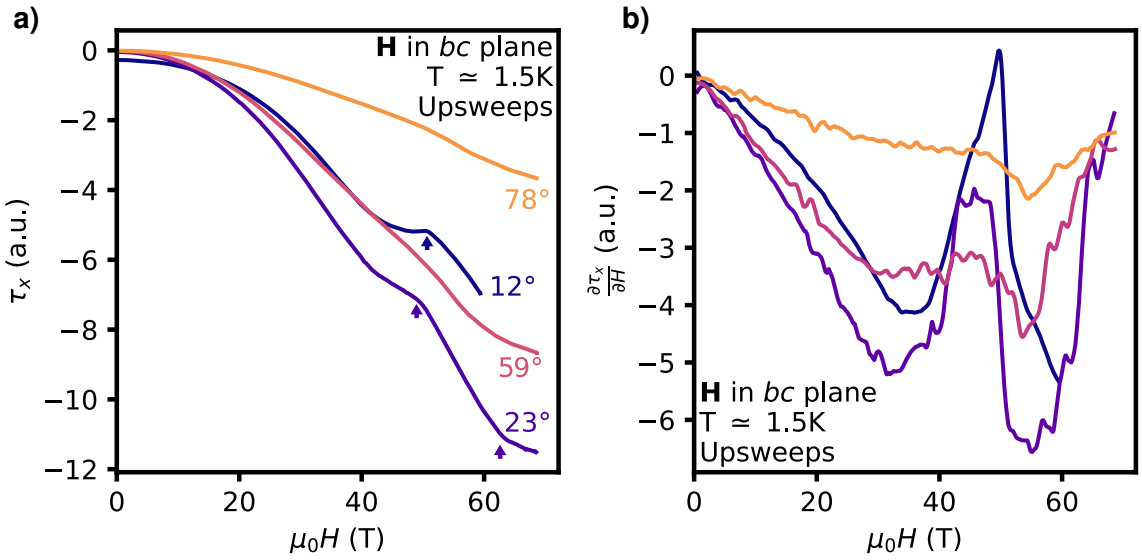


Figure 6.21: Evolution of magnetic torque with applied magnetic fields in the $\boldsymbol{bc}$ plane up to $67\,\mathrm{T}$. Angle shown is measured from the nominal $\boldsymbol{b}$ axis towards the $\boldsymbol{c}$ axis. All data shown were measured at $T \simeq 1.5\,\mathrm{K}$. Arrows under curves show features which are discussed in the text. **a)** shows up-sweep torque for angles between $9°$ and $57°$. **b)** Derivative of torque with field $\frac{\partial \tau_x}{\partial H}$.

The last high-symmetry plane explored with torque is the $\boldsymbol{ab}$ plane. Sample morphology means that precise alignment on a cantilever in this plane is challenging. To overcome this an $\approx 170\mu\mathrm{m}$ long single crystal sample of β-Na_2PrO_3 was mounted on a metal plate with natural growth plane normal to $\boldsymbol{c}$ flush with the plate. This was then placed in a ThermoFisher Dual Beam Focused Ion Beam Scanning Electron Microscope (FIB-SEM). The sample was then cut in the $\boldsymbol{ac}$ plane using the ion beam (FIB) providing a flat surface with the $\boldsymbol{c}$ axis orthogonal to the surface-normal. Figure **??** shows an image of the sample, taken with SEM after this cut, showing clear sample morphology covered by a layer of non-crystalline material. Note especially that the sample is mounted on a flat growth face, measured with X-ray diffraction to be normal to $\boldsymbol{c}$, providing confidence that this alignment is precise. This sample was mounted for torque with the cantilever flush to the cut face, allowing the sample to be rotated in the $\boldsymbol{ab}$ plane.

Figure **??b,c)** show the torque-field dependence and the corresponding derivative for fields close to the $\boldsymbol{a}$ axis. These show a very sharp transition at $26.6(2)\,\mathrm{T}$, matching closely with the spin-flop field measured previously. The higher field behaviour is less clear, but the rapid change in torque, and corresponding peak in $\frac{\partial \tau}{\partial H}$ at approximately

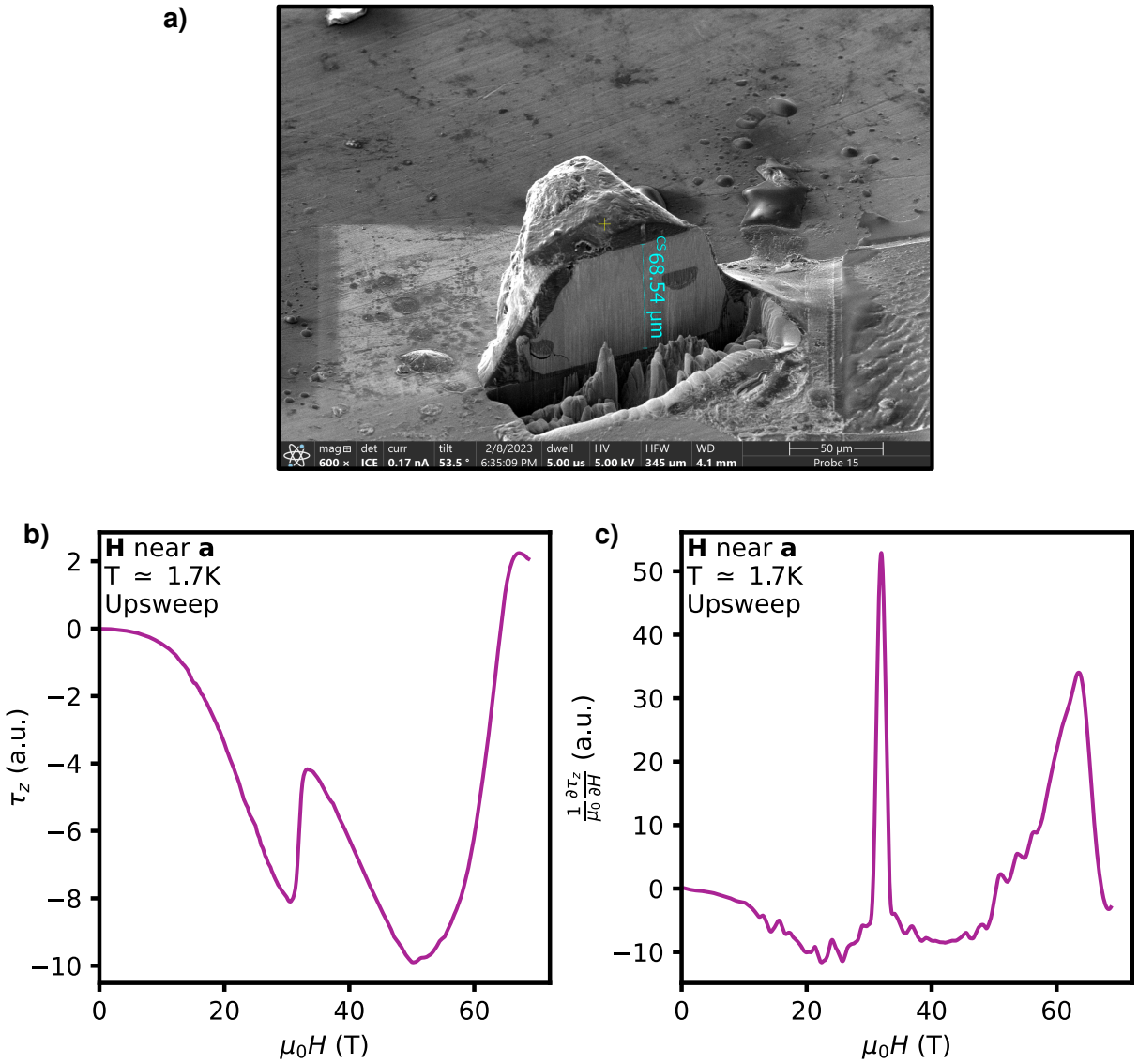


Figure 6.22: a) SEM image showing cut β-Na_2PrO_3 sample using focused ion beam in preparation for torque magnetometry measurements with the sample rotated in $\boldsymbol{ab}$ plane. The cut plane is $\boldsymbol{ac}$, with $\boldsymbol{c}$ axis vertical. **b, c)** Magnetic toque against applied field up to 67 T with field close to the $\boldsymbol{a}$ axis. Torque is projection onto $\boldsymbol{c}$ axis of full vector torque. Showing **b)** raw torque signal, **c)** derivative of torque with field $\frac{\partial \tau_z}{\partial H}$

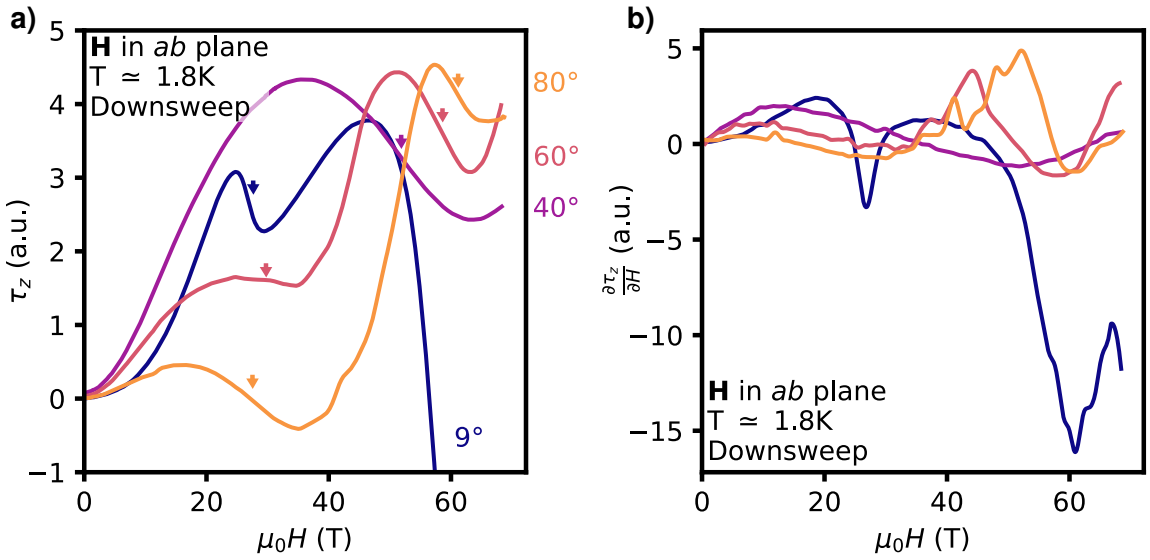


Figure 6.23: Evolution of magnetic torque with applied magnetic fields in the $\boldsymbol{ab}$ plane up to $67\,\mathrm{T}$. Angle shown is measured from the nominal $\boldsymbol{a}$ axis towards the $\boldsymbol{b}$ axis. All curves are measured at $T \simeq 1.5\,\mathrm{K}$. Arrows under curves show features which are discussed in the text. **a)** shows down-sweep torque for angles between $9°$ and $80°$, **b)** derivative of torque with field $\frac{\partial \tau}{\partial H}$.

$\mu_0 H \simeq 62\,\mathrm{T}$ may be associated with the polarisation transition observed in the $\boldsymbol{ac}$ plane torque measurements. The absence of a sharp cusp at polarisation, seen in other orientations, is likely caused by the different projections of the torque vector. In calculations for some models a cusp feature is only expected to be seen in particular projections of the torque, this can be seen in Fig. **??**.

Figure **??** shows the torque vs field and the corresponding derivative for fields applied in the $\boldsymbol{ab}$ plane. The sweep at each angle shows rich behaviour, including low-field peak-trough features in torque even close to the $\boldsymbol{b}$ axis. Arrow markers above the curves show inflection points in the data. Unlike in previous cases in this section, the derivative is not particularly illuminating, as the behaviour is too complex to select individual features of note. For the smallest angle, there is a sharp peak-trough feature associated with the spin-flop, and a drop in torque which may be associated with transition to polarisation. For angles close to the $\boldsymbol{b}$ axis, marked $60°$ and $80°$, there is a peak-trough-peak-trough feature. Close to the $\boldsymbol{a}$ axis, the spin-flop feature is selected as a sharp peak in the derivative of torque, if this is applied to the broad peak seen close to the $\boldsymbol{b}$ axis, it suggests a broad low field feature, marked with an arrow, in the region of $30\,\mathrm{T}$. This feature is

marked in Fig. **?? b)** with a yellow cross symbol. The fact that no feature can be seen in the $\boldsymbol{bc}$ plane measurements is likely caused by one of two scenarios. The anomaly could be only present in the τ_z projection of torque, not the τ_x projection measured in the $\boldsymbol{bc}$ plane. The second possibility is that the feature is related to a projection of field into the $\boldsymbol{a}$ axis, which is zero in the $\boldsymbol{bc}$ plane. Ultimately these scenarios cannot be practically distinguished with torque magnetometry. The high-field inflection point noted with an arrow is in the region of $60\,\mathrm{T}$. The prominence of both features decreases as the field approaches the $\boldsymbol{b}$ axis. At the intermediate angle of 40° there is a large and broad peak-trough feature at around $40\,\mathrm{T}$.

6.9 DC Field Torque Magnetometry up to 35T

A limitation of pulsed magnetic fields is that long magnet cool-down times limit the density of data that can be taken. The data also has a tendency to be noisier than that available in DC fields. In order to better understand the magnetic phase diagram in the $\boldsymbol{ab}$ plane, magnetic torque was measured up to $35\,\mathrm{T}$ in DC fields. These experiments were performed using capacitive cantilever torque magnetometry such that a jig could be used to hold the sample in the $\boldsymbol{ab}$ plane.

Attribution note: *Torque magnetometry measurements reported in this section were performed in collaboration with Matthew Pearce and Ryutaro Okuma at the University of Oxford and Alix McCollam, Roos Leenen, and Uli Zeitler at HFML Nijmegen.*

Figure **??** shows magnetic torque in the $\boldsymbol{ab}$ plane up to $35\,\mathrm{T}$. The top panels show raw cantilever capacitances, proportional to torque, the bottom panels show the derivative of this with field. Each measurement was taken at $4.0\,\mathrm{K}$, the highest temperature which kept all observed transitions below the $35\,\mathrm{T}$ maximum field available. Every torque vs field trace shown in this plane shows a cusp-like transition. Near the $\boldsymbol{a}$ axis, the transition occurs at $21.5(1)\,\mathrm{T}$ and is sharp, consistent with the behaviour seen in pulsed fields at these temperatures. In this section, angle θ is the angle made in the $\boldsymbol{ab}$ plane between the field direction and the crystal $\boldsymbol{a}$ axis. As the field rotates towards the $\boldsymbol{b}$ axis, for $0^\circ < \theta \leq 45^\circ$, the transition remains sharp and the transition field varies strongly with angle, up to $34.9(2)\,\mathrm{T}$ at $\theta = 45^\circ$. Towards the $\boldsymbol{b}$ axis, $45^\circ \leq \theta < 90^\circ$ the

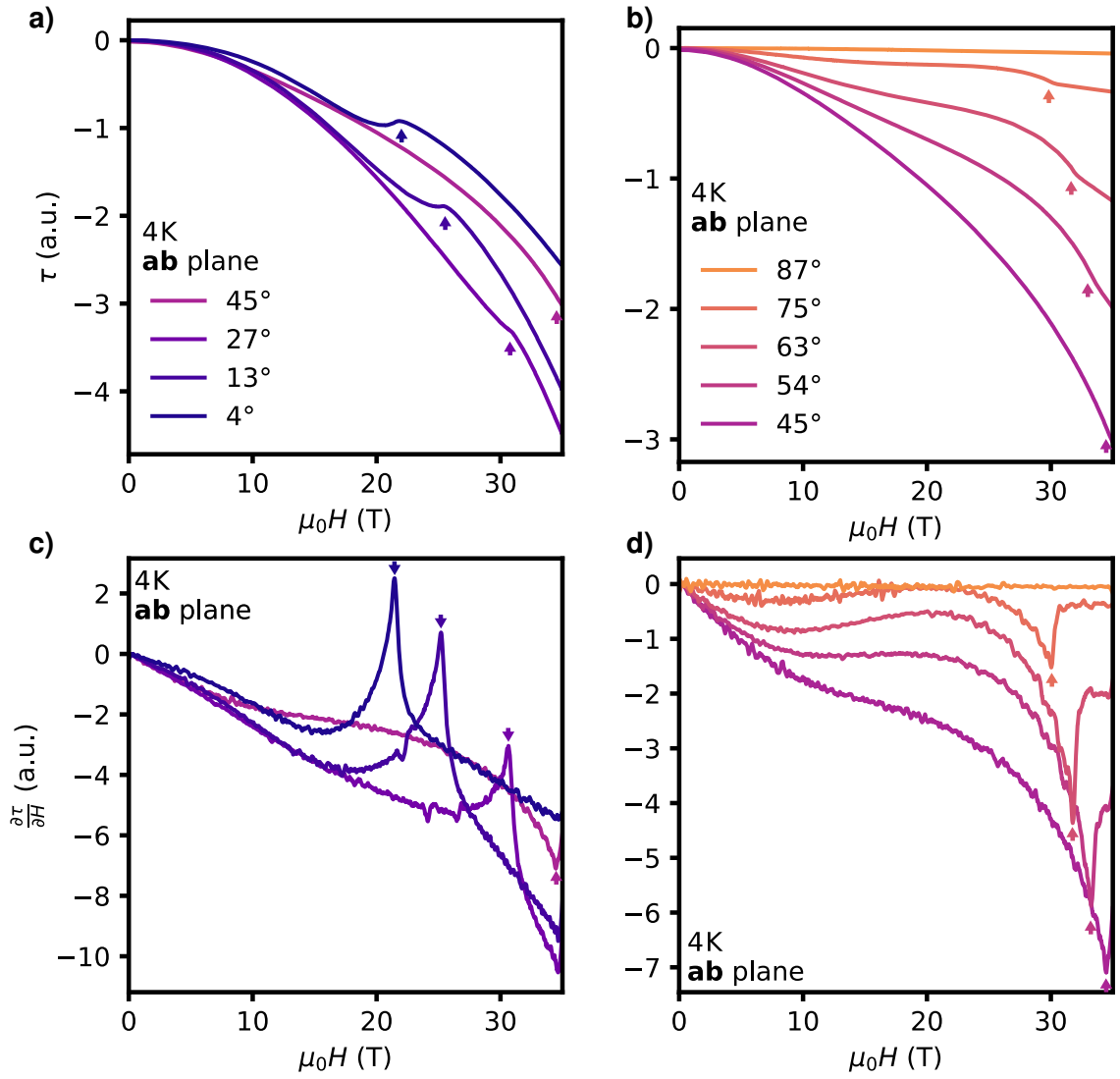


Figure 6.24: Evolution of magnetic torque with applied magnetic fields in the $\boldsymbol{ab}$ plane up to $35\,\mathrm{T}$. Angle shown is measured from the nominal $\boldsymbol{a}$ axis towards the $\boldsymbol{b}$ axis. All curves are measured at $T \simeq 4.0\,\mathrm{K}$. Arrows under curves show features which are discussed in the text. **a, b)** show raw cantilever capacitance, taken to be proportional to torque. **c, d)** show derivative of torque with field $\frac{\partial\tau}{\partial H}$. **a, c)** show data closer to $\boldsymbol{a}$, **b, d)** show data closer to $\boldsymbol{b}$.

anomaly associated with the transition is much less pronounced, although it can still be clearly seen in both raw and derivative plots. Close to the $\boldsymbol{b}$ axis, the transition field is approximately $30.0(2)\,\mathrm{T}$, in agreement with the value determined in pulsed fields at the same temperature of $4\,\mathrm{K}$. This can be seen in the pink circles overlaid on Fig **??d)**. This increases monotonically with angle up to $\theta = 45°$. In addition to the transition, fields near the $\boldsymbol{b}$ axis show a broad peak-trough feature that was also observed in pulsed fields.

Figure **??** shows the derivative of torque with field for all the angles measured.

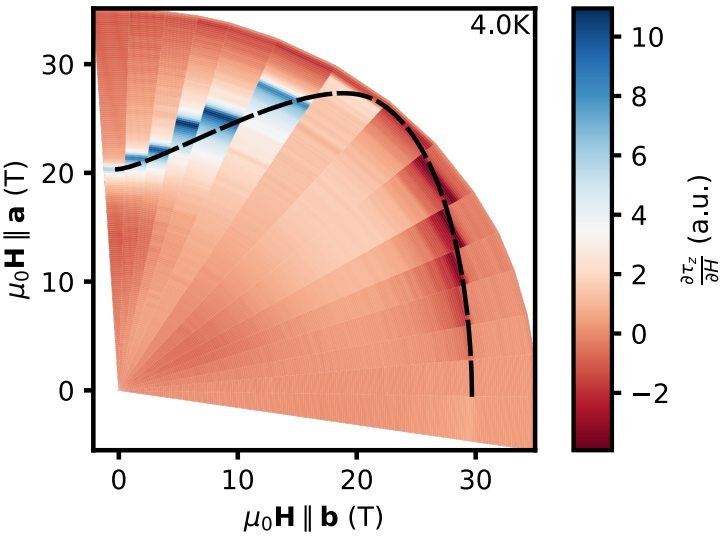


Figure 6.25: Colour plot showing derivative of torque with field $\frac{\partial \tau}{\partial H}$ for fields in the $\boldsymbol{ab}$ plane at $4.0\,\mathrm{K}$. A smooth background is subtracted to highlight sharp features. Dashed line is a guide to the eye.

Overlaid is a guide to the eye, indicating where magnetic phase transitions occur. This shows a suppression of the transition field when the magnetic field is applied close to the $\boldsymbol{a}$ axis. It is important to note that at this temperature, $4.0\,\mathrm{K}$, only one transition is seen when the field is applied along the $\boldsymbol{a}$ axis. One possible interpretation of this suppression is that at low temperatures, there is a phase boundary connecting the spin-flop along $\boldsymbol{a}$ and the polarisation transition in the $\boldsymbol{ab}$ plane. This would be expected if the spin-flop phase magnetic state was in a different irrep to the zero-field $A_x, -C_y$ ground state. These are tabulated in Table **??**, when the magnetic field is in the $\boldsymbol{ab}$ plane, the ground state is in the Γ_1^- irrep, a possible spin-flop structure in a different irrep would be A_z, C_z in the Γ_2^- irrep.

Figure **??** shows evolution of magnetic torque near the $\boldsymbol{a}$ axis with field for temperatures between $1.4\,\mathrm{K}$ and $4.0\,\mathrm{K}$. These show a sharp peak in the derivative at the spin-flop transition. At base temperature, the spin-flop field is $\mu_0 H_{\mathrm{SF}} = 25.5(2)\,\mathrm{T}$, this is slightly lower than the value determined in pulsed-fields, but overall in good agreement. This can be seen in the phase diagram including both sets of data, in Figure **??c)**.

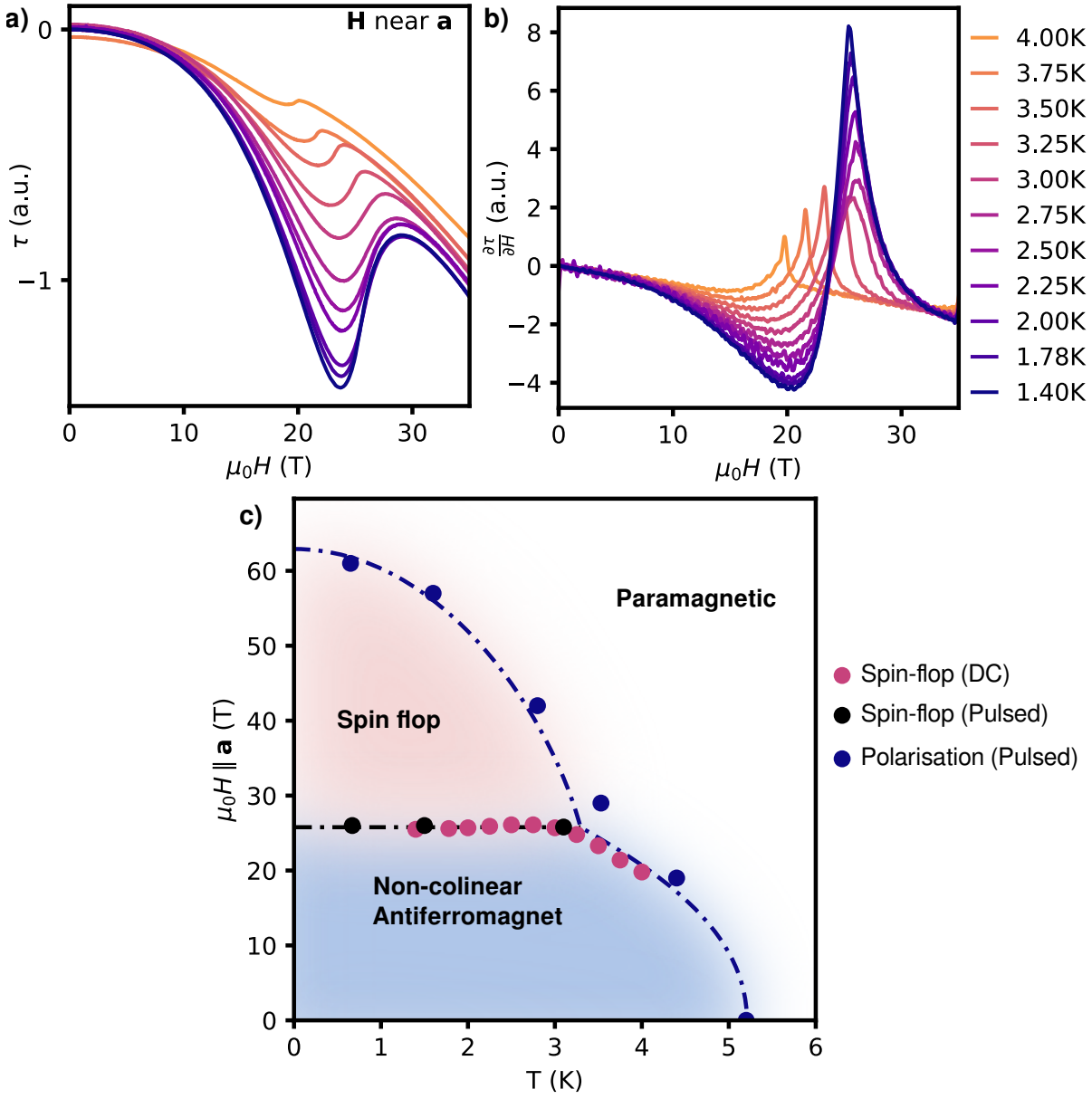


Figure 6.26: Evolution of magnetic torque with applied magnetic field near the $\boldsymbol{a}$ axis up to 35 T for temperatures between 1.4 K and 4.0 K. **a)** shows raw cantilever capacitance, taken to be proportional to torque. **b)** shows derivative of torque with field $\frac{\partial \tau}{\partial H}$. **c)** Extracted low temperature phase diagram showing transitions to spin-flop, paramagnetic, and non-collinear antiferromagnetic phases for fields close to the $\boldsymbol{a}$ axis. Dashed lines are guides for the eye, error-bars are smaller than individual point markers.

6.10 Pulsed-Field Magnetisation up to 67T

Attribution note: *Measurements reported in this section were performed in collaboration with Matthew Pearce, and Ryutaro Okuma from the University of Oxford, and instrument scientist Yurii Skourski at the HZDR Dresden high-magnetic-field facility.*

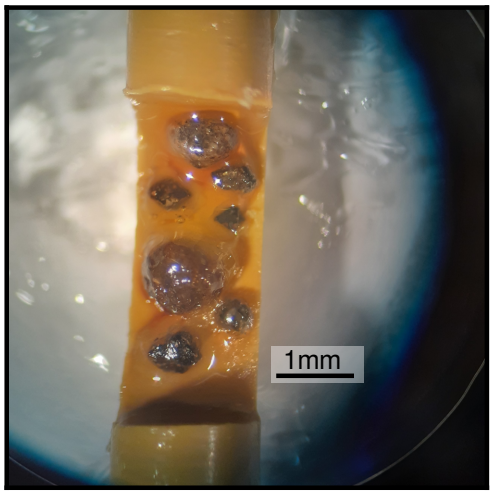


Figure 6.27: Co-aligned β-Na_2PrO_3 crystals for field $\mu_0 \boldsymbol{H} \parallel \boldsymbol{a}$ magnetisation measurements.

In order to understand the high-field magnetic phase transitions observed in β-Na_2PrO_3 , magnetisation measurements were attempted using coil extraction magnetometry up to $67\,\mathrm{T}$. A collection of 7 single-crystals were co-aligned such that field would be applied along the $\boldsymbol{a}$, shown in Figure **??**. The total mass of this collection is estimated at $m \sim 5\,\mathrm{mg}$. In order to allow time for co-alignment without them degrading in air, the samples were coated in paraffin in a glovebox and sealed in vacuum. In the experiment however, no magnetic signal was detected above the experimental noise level. While it is possible that more samples could be co-aligned to fit into the sample space, it is clear that given the small moment a substantially larger amount of material, at least an order of magnitude, would be needed to measure a significant signal. As such, it is unclear if co-aligning crystals is a realistically viable method of achieving a suitable filling factor of the measurement coil with the sample sizes available. If larger samples are able to be grown, or the largest available samples today can be produced more consistently, then this could be reattempted.

6.11 Discussion/Conclusions

This chapter reported on the hyperhoneycomb magnet β-Na_2PrO_3 . I have shown detailed single-crystal structural refinement, and attempted to characterise the magnetic properties of the material for the first time. The material was shown to order at $5.20\,\mathrm{K}$ with AC calorimetry measurements. Single crystal torque magnetometry in low fields suggested non-collinear antiferromagnetic order, with suppression of susceptibilities in the $\boldsymbol{a}$ and $\boldsymbol{b}$ directions. This was confirmed by neutron diffraction measurements, performed by others, which showed an $(A_x, -C_y)$ magnetic ground state. A minimal J, Γ, Γ' model was developed, and the behaviour of this model in magnetic fields was explored using mean-field calculations, showing that a spin-flop transition was expected for fields along the $\boldsymbol{a}$ axis. A symmetry analysis considering what magnetic states could be reached with and without crossing a phase boundary for fields applied in the high symmetry planes showed that this predicted phase boundary was symmetry-protected in the $\boldsymbol{ac}$ plane, giving a clear signature to look for.

The magnetic torque data presented in this chapter shows rich behaviour in all orientations measured. Close to the $\boldsymbol{a}$ axis, a sharp spin-flop phase transition is observed in both pulsed and DC fields. As the field is rotated toward the $\boldsymbol{c}$ axis it broadens rapidly. This is unlike the behaviour expected from the minimal J, Γ, Γ' model, in which a symmetry-protected first-order transition between $(A_x, -C_y)$ and $(A_y, -C_x)$ states is expected. One possible explanation is that the phase boundary between these states is close to the $\boldsymbol{a}$ axis, such that field sweeps only cross it for very small angles against the axis. Substantial broadening of the transition is seen at an angle of $\theta < 5^\circ$, so some effort would be needed to understand why this would be the case in this scenario. An alternative explanation is that the observed anomaly is a transition to a different spin-flop phase in the same irrep, such as A_z or predominant C_y order. In the $\boldsymbol{ab}$ plane, these phases are in different irreps. In the A_z case, this would imply a symmetry protected transition between the zero-field $(A_x, -C_y)$ and spin-flop A_z states.

In the $\boldsymbol{ab}$ plane, the spin-flop along $\boldsymbol{a}$ axis can be seen. Away from the $\boldsymbol{a}$ axis, further features are seen which are not explained by the minimal J, Γ, Γ' model, including

board low-field peak-trough features which are not observed in other orientations. The discrepancy between orientations may be caused by the different projection of torque being measured in each case. Alternatively, the anomaly may only be visible between the $\boldsymbol{b}$ and $\boldsymbol{a}$ axes, not also the $\boldsymbol{b}$ and $\boldsymbol{c}$ axes. These scenarios cannot be distinguished by with the data available, future experimental work with different techniques such as high-field calorimetry could identify which if these possibilities is realised and to understand the origin of the feature.

At $4\,\mathrm{K}$, rotating between the $\boldsymbol{a}$ and $\boldsymbol{b}$ axes shows a sharp transition at all angles. The associated transition field appears to be suppressed close to the $\boldsymbol{a}$ axis, this may be because of a symmetry protected phase boundary between the $(A_x, -C_y)$ and spin-flop A_z states as mentioned above. However, whether or not a sharp boundary remains at low temperatures could not be determined. In the $\boldsymbol{bc}$ plane, close to the $\boldsymbol{b}$ axis, a sharp, temperature dependent feature is seen. This may be associated with a polarisation transition, but other measurements at larger angles to the axis appear to show a further anomaly at even higher field.

The J, K, Γ, Γ' model on a hyperhoneycomb lattice discussed here, and explored in depth elsewhere [5], shows incredibly rich physics, stabilising numerous distinct ground states depending on the parameters used. Many of those ground states themselves have complex phase diagrams in field. Even in this minimal case, the problem of determining model parameters is under-constrained.

The proposed minimal J, Γ, Γ' model, with $J = 1.22\,\mathrm{meV}, \Gamma = -\Gamma' = -0.27\,\mathrm{meV}$, predicts a C_y component to the magnetic structure much smaller than is observed, and a spin-flop field smaller than is determined by torque. These disagreements can be reduced by increasing the value of $|\Gamma|$ in the model, however this causes calculated powder neutron scattering to agree less well with experimentally observed data [20]. Reconciling these different experimental observations will likely require extensions beyond the minimal model.

Given the extensive theoretical and experimental interest in magnetic hyperhoneycomb systems, this material clearly deserves further research. The primary areas of future work should be experimental. Torque magnetometry at higher magnetic fields could elucidate

the second anomaly seen at high fields near the $\boldsymbol{b}$ axis. Additionally, high-field angle dependence below $3\,\mathrm{K}$ in the $\boldsymbol{ab}$ plane could clarify what happens with the phase boundary between $\boldsymbol{a}$ and $\boldsymbol{b}$ at low temperatures, this could in turn help determine the spin-flop phase and therefore narrow down the interactions in the structure. Heat capacity in high magnetic fields could determine which features in torque correspond to true phase transitions. If larger single crystals could be grown, single crystal magnetisation in high magnetic fields could clarify what transitions are happening where. In the long term, single crystal inelastic neutron scattering will likely clarify many of the mysteries of this system.

Previous theoretical work predicted large Kitaev interactions in β-Na_2PrO_3 [8] and in the related honeycomb polymorph α-Na_2PrO_3 [7]. Current data does not support this to be the case here. Future theoretical work could attempt to understand why these interactions are not observed, or what key signatures could be looked for in available experimental techniques. Other productive work would seek to understand better the observed torque data, and to build a model and phase diagram which explains all the transitions and anomalies seen.

References

[1] K. A. Modic et al. “Realization of a three-dimensional spin-anisotropic harmonic honeycomb iridate”. In: *Nature Communications* 5.1 (2014), p. 4203.

[2] S. Mandal and N. Surendran. “Exactly solvable Kitaev model in three dimensions”. In: *Physical Review B* 79.2 (2009), p. 024426.

[3] I. Kimchi, J. G. Analytis, and A. Vishwanath. “Three-dimensional quantum spin liquids in models of harmonic-honeycomb iridates and phase diagram in an infinite-D approximation”. In: *Physical Review B* 90.20 (2014), p. 205126.

[4] E. K.-H. Lee et al. “Heisenberg-Kitaev model on the hyperhoneycomb lattice”. In: *Physical Review B* 89.4 (2014), p. 045117.

[5] E. K.-H. Lee and Y. B. Kim. “Theory of magnetic phase diagrams in hyperhoneycomb and harmonic-honeycomb iridates”. In: *Physical Review B* 91.6 (2015), p. 064407.

[6] R. Wolf and R. Hoppe. “Über Na2PrO3 und Na2TbO3”. In: *Zeitschrift für Anorganische und Allgemeine Chemie* 556.1 (1988), pp. 97–108.

[7] S.-H. Jang et al. “Antiferromagnetic Kitaev interaction in f-electron based honeycomb magnets”. In: *Physical Review B* 99.24 (2019), p. 241106.

[8] S.-H. Jang et al. “Computational design of f-electron Kitaev magnets: Honeycomb and hyperhoneycomb compounds A_2PrO_3 (A=alkali metals)”. In: *Physical Review Materials* 4.10 (2020), p. 104420.

[9] J. Rodríguez-Carvajal. "FullProf". In: *CEA/Saclay, France* 1045 (2001), pp. 132–146.

[10] T. Takayama et al. "Hyperhoneycomb Iridate β-Li_2IrO_3 as a Platform for Kitaev Magnetism". In: *Physical Review Letters* 114.7 (2015), p. 077202.

[11] M. Dresselhaus and G. Dresselhaus. *Applications of group theory to the physics of solids*. MIT Lecture Notes. 2002. URL: https://web.mit.edu/course/6/6.734j/www/group-full02.pdf.

[12] A. Wolter et al. "Field-induced quantum criticality in the Kitaev system α-$RuCl_3$". In: *Physical Review B* 96.4 (2017), p. 041405.

[13] M. J. Daum et al. "Collective excitations in the tetravalent lanthanide honeycomb antiferromagnet Na_2PrO_3". In: *Physical Review B* 103.12 (2021), p. L121109.

[14] L. J. De Jongh and A. R. Miedema. "Experiments on simple magnetic model systems". In: *Advances in Physics* 50.8 (2001), pp. 947–1170.

[15] A. Nakua et al. "Crystal structure, short range and long range magnetic ordering in $CuSb_2O_6$". In: *Journal of Solid State Chemistry* 91.1 (1991), pp. 105–112.

[16] J. Greedan, N. Raju, and I. Davidson. "Long range and short range magnetic order in orthorhombic LiMnO2". In: *Journal of Solid State Chemistry* 128.2 (1997), pp. 209–214.

[17] H. Xiao et al. "Angular-dependent torque measurements on $CeCoIn_5$ single crystals". In: *Physical Review B* 73.18 (2006), p. 184511.

[18] W. Zhang et al. "Spin-flop transition and magnetic phase diagram in $CaCo_2As_2$ revealed by torque measurements". In: *Physical Review B* 92.14 (2015), p. 144416.

[19] A. Biffin et al. "Unconventional magnetic order on the hyperhoneycomb Kitaev lattice in β-Li_2IrO_3: Full solution via magnetic resonant x-ray diffraction". In: *Physical Review B* 90.20 (2014), p. 205116.

[20] R. Okuma et al. "Noncollinear magnetism from frustrated bond-dependent anisotropic exchange on the f-electron hyperhoneycomb lattice β-Na_2PrO_3". In preparation.

[21] M. S. Dresselhaus, G. Dresselhaus, and A. Jorio. *Group Theory: Application to the Physics of Condensed Matter*. Springer, 2007.

[22] H. T. Stokes, D. M. Hatch, and B. J. Campbell. *ISODISTORT*. Version 6.11.1. May 26, 2022. URL: iso.byu.edu.

[23] J. Nasu et al. "Finite-temperature phase transition to a quantum spin liquid in a three-dimensional Kitaev model on a hyperhoneycomb lattice". In: *Physical Review B* 89.11 (2014), p. 115125.

[24] S. Lee et al. "Order-by-disorder and magnetic field response in the Heisenberg-Kitaev model on a hyperhoneycomb lattice". In: *Physical Review B* 89.1 (2014), p. 014424.

[25] G. Jackeli and G. Khaliullin. "Mott insulators in the strong spin-orbit coupling limit: from Heisenberg to a quantum compass and Kitaev models". In: *Physical Review Letters* 102.1 (2009), p. 017205.

[26] L. D. Landau and E. M. Lifshitz. *Statistical Physics: Volume 5*. Vol. 5. Elsevier, 2013.

7

Six-fold clock-anisotropy in honeycomb titanates $CoTiO_3$ and $FeTiO_3$

Contents

7.1 Six-Fold Clock Anisotropy in $CoTiO_3$ 158
7.1.1 Crystal Structure of $CoTiO_3$ 158
7.1.2 Single Ion Physics of Co^{2+}in $CoTiO_3$ 160
7.1.3 Magnetic Structure of $CoTiO_3$ 163
7.1.4 Exchange Interactions and Magnetic Anisotropy 163
7.1.5 Single Crystal Vibrating Sample Magnetometry studies of $CoTiO_3$ 169
7.1.6 Single Crystal Torque Magnetometry Studies of $CoTiO_3$ . . . 172
7.2 Six-Fold Clock Anisotropy in $FeTiO_3$ 184
7.2.1 Single ion physics of Fe^{2+}ions in $FeTiO_3$ 185
7.2.2 Torque magnetometry studies of $FeTiO_3$ 188
7.3 Conclusions 195

Abstract *Recently published neutron scattering experiments have shown that the easy-plane honeycomb cobaltate $CoTiO_3$ shows incredibly rich low temperature physics including a six-fold in-plane anisotropy proposed to originate in bond dependent exchange and quantum zero-point fluctuation mechanism. This chapter reports single-crystal piezocantilever torque magnetometry experiments that aim to directly probe the magnetic anisotropy and test the proposed scenario of in-plane six-fold anisotropy. Measurements are reported for both the easy-plane honeycomb magnet $CoTiO_3$, as well as the isostructural easy-axis magnet $FeTiO_3$. Clear evidence of a six-fold clock anisotropy is observed in both materials.*

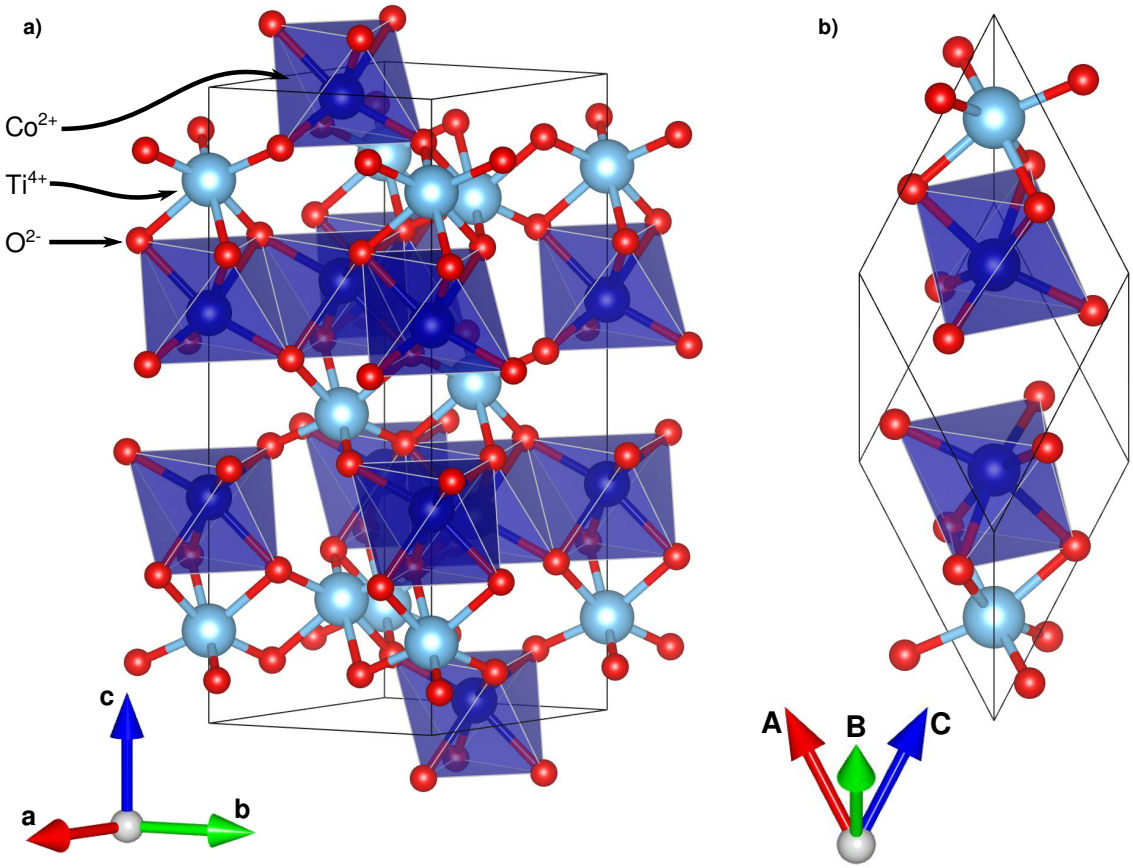


Figure 7.1: Model showing crystal structure of $CoTiO_3$ in the **a)** hexagonal **b)** rhombohedral settings. Dark blue spheres indicate Co^{2+}ions, light blue spheres indicate Ti^{4+} ions, red spheres indicate O^{2-} ions. The thin black lines indicate the structural unit cell in each setting, and the triad of arrows in the bottom left corner of each panel are the associated lattice vectors for that setting.

7.1 Six-Fold Clock Anisotropy in $CoTiO_3$

7.1.1 Crystal Structure of $CoTiO_3$

$CoTiO_3$ has an Ilmenite crystal structure comprised of stacked layers of honeycombs with an $R\bar{3}$ space group. Figure 7.1**a** shows that the layers alternate between containing honeycombs of edge sharing CoO_6 octahedra and edge sharing TiO_6 octahedra. The honeycomb layers are not quite in the $\boldsymbol{a}$, $\boldsymbol{b}$ plane, but the two sites of the honeycomb are displaced relative to one another along the $\boldsymbol{c}$ axis, leading to some buckling of the planes.

Figure 7.1**b** shows an alternative setting for the structure, the rhombohedral setting. This setting is the primitive structural unit cell and contains two Co^{2+}sites, two Ti^{4+}

Table 7.1: Structure parameters of $CoTiO_3$ in standard setting (Domain A in Fig. 7.2)

Space group: $R\bar{3}\,H$ (148)				
Hexagonal setting				
Z = 6				
Cell parameters:				
a, b, c (Å)			5.066	5.066	13.918
α, β, γ (°)			90	90	120
Volume (Å^3)			309.365		
Atomic fractional coordinates:					
Atom	Wyckoff Site	Site Symmetry	x	y	z
Co^{2+}	6c	3	0	0	0.35511
Ti^{4+}	6c	3	0	0	0.14558
O^{2-}	18f	1	0.31623	0.02091	0.24588

sites, and six O^{2-} sites. The hexagonal basis vectors $(\boldsymbol{a}, \boldsymbol{b}, \boldsymbol{c})$ can be written it terms of the primitive vectors $(\boldsymbol{A}, \boldsymbol{B}, \boldsymbol{C})$ as

$$\begin{pmatrix} \boldsymbol{a} \\ \boldsymbol{b} \\ \boldsymbol{c} \end{pmatrix} = \begin{pmatrix} 0 & 1 & -1 \\ -1 & 0 & -1 \\ 1 & 1 & 1 \end{pmatrix} \begin{pmatrix} \boldsymbol{A} \\ \boldsymbol{B} \\ \boldsymbol{C} \end{pmatrix} \tag{7.1}$$

Previous studies have reported the crystal structure to a high quality standard [1, 2]. Table 7.1 shows a summary of the structural parameters and atomic fractional coordinates of the material's ions, with data taken from [1].

In addition, previous reports [3, 4] pointed out commonly occurring twins in single crystals. These are the A domain, with parameters consistent with [1], shown in Table 7.1, and the B domain, which is rotated $180°$ around the (110) axis in the hexagonal setting. This rotation leaves the positions of the $Co^{2+}$and Ti^{4+} ions unchanged, but does change the O^{2-} ion positions. Because of this change in oxygen positions, one can determine which domains are present in a sample through X-ray diffraction. This is possible by finding Bragg peaks where the structure factor changes significantly in magnitude between the two domains. In this case, because the transition metal ion positions are invariant between the domains, this change in structure factor will be large if the contribution from the O^{2-} ions changes sign between the two domains.

Figure 7.2 shows results of calculations of Bragg peak intensities in the $(hk1)$ crystallographic plane for domains A and B. On these are highlighted a trio of peaks whose

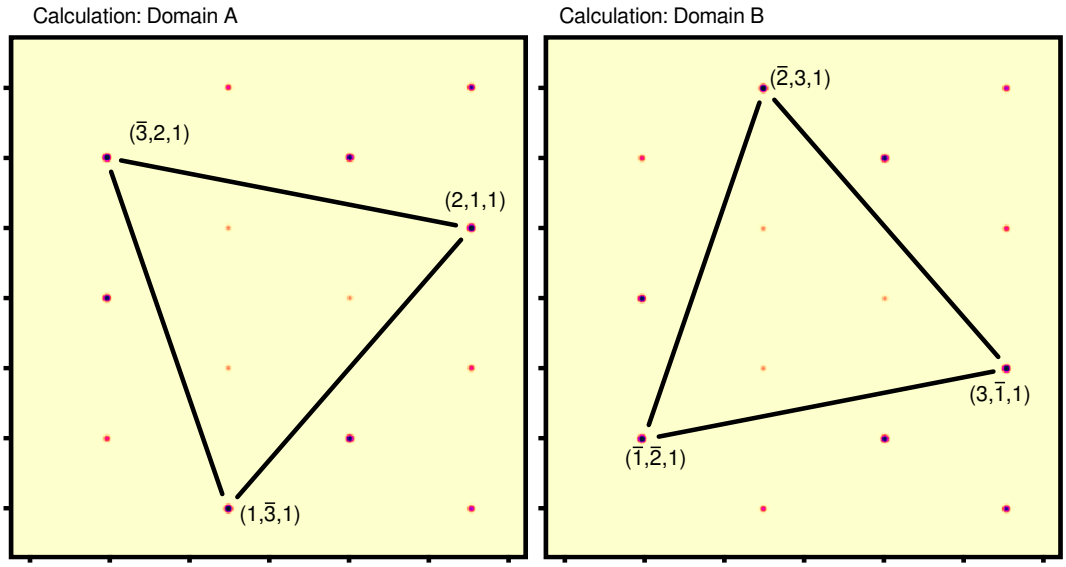


Figure 7.2: Calculated Bragg peak intensities in the $(hk1)$ plane for two structural domains of $CoTiO_3$, related by a 2-fold rotation around (110). Highlighted are trios of peaks which change intensities strongly between the two domains.

intensity varies strongly between the domains. X-ray diffraction was performed at room temperature with an Oxford Diffraction Supernova diffractometer on all $CoTiO_3$ crystals used in this chapter to verify sample quality. By comparing measured Bragg peak intensities to the calculated values, the domain populations can be estimated. Each crystal used for the torque measurements is an untwinned A-domain sample.

7.1.2 Single Ion Physics of Co^{2+}in $CoTiO_3$

The magnetic ions in $CoTiO_3$ are $3d^7$ Co^{2+}ions in an octahedron of oxygen ions, this octahedral crystal environment is trigonally distorted along the $\boldsymbol{c}$ direction. The Hund's rules ground state for this electron configuration is $L = 3$, $S = \frac{3}{2}$. The crystal field Hamiltonian can be written

$$\hat{\mathcal{H}}_{\text{CEF}} = \frac{2}{3} B_4 \left(O_4^0 + 20\sqrt{2} O_4^3 \right) + B_2^0 O_2^0 + B_4^0 O_4^0 \tag{7.2}$$

using the Stevens operators O_n^k in the Cartesian basis with x, y, z along the a^*, b, c axes respectively. $B_4 > 0$ parametrises the octahedral cubic crystal field environment, and the additional terms characterise a trigonal distortion along the $\boldsymbol{c}$ axis. With this, spin-orbit coupling is included to give a single-ion Hamiltonian

$$\hat{\mathcal{H}} = -\lambda \hat{\boldsymbol{L}} \cdot \hat{\boldsymbol{S}} + \hat{\mathcal{H}}_{\text{CEF}} \tag{7.3}$$

where $\lambda > 0$ because the shell is more than half filled.

This can be approached perturbatively by assuming that the octahedral cubic crystal field (OCF)

$$\hat{\mathcal{H}}_{\text{OCF}} = \frac{2}{3} B_4 \left(O_4^0 + 20\sqrt{2} O_4^3 \right) \tag{7.4}$$

is the largest energy scale.

In the $|L_z\rangle$ basis, the OCF gives a ground state T_{1u} triplet at energy $-480B_4$, an excited T_{2u} triplet at $+120B_4$, and a further excited excited A_{2u} singlet at $+600B_4$ [5]. The ground state has basis vectors

$$\left|\widetilde{0}\right\rangle = -\sqrt{\frac{4}{9}} \left|0\right\rangle + \sqrt{\frac{5}{9}} \frac{1}{\sqrt{2}} \left[\left|+3\right\rangle - \left|-3\right\rangle\right] \tag{7.5a}$$

$$\left|\pm\widetilde{1}\right\rangle = \pm\sqrt{\frac{5}{6}} \left|\mp 2\right\rangle + \sqrt{\frac{1}{6}} \left|\pm 1\right\rangle \tag{7.5b}$$

where the states are labelled by the effective angular momentum operator $|l_z\rangle$ with the equivalence relation $\hat{\boldsymbol{L}} \equiv -\frac{3}{2}\hat{\boldsymbol{l}}$, valid on the projected subspace of this triplet of states. The spin-orbit and trigonal distortion terms can then be treated as a perturbation on this ground state manifold.

The spin-orbit coupling operator $\hat{\mathcal{H}}_{\text{SO}} = -\lambda \hat{\boldsymbol{L}} \cdot \hat{\boldsymbol{S}}$ can be rewritten in terms of the effective orbital angular momentum operator $\hat{\mathcal{H}}_{\text{SO}} = \frac{3}{2}\lambda \hat{\boldsymbol{l}} \cdot \hat{\boldsymbol{S}}$. By itself, this couples the spin and orbital parts of the angular momentum into a total effective angular momentum J_{eff}, with values $J_{\text{eff}} = {}^1\!/_2, {}^3\!/_2, {}^5\!/_2$.

The trigonal distortion operator can be written in terms of effective orbital angular momentum operator as $\hat{\mathcal{H}}_{\text{trig}} = \delta \left(\hat{l}_z^2 - \frac{2}{3} \right) = \frac{1}{3}\delta O_2^0$. Acting on the octahedral crystal field $l = 1, S = {}^3\!/_2$ ground state, this splits the 12-fold degenerate manifold into an a 8-fold degenerate $l_z = \pm 1$ manifold of states and a 4-fold degenerate $l_z = 0$ manifold. Acting as on the J_{eff} states from spin-orbit coupling, it mixes the states with same J_{eff}^z, as seen in the level splitting diagram in Figure 7.3. The result is a ground state Kramers doublet with $J_{\text{eff}}^z = \pm {}^1\!/_2$, and the next excited level a $J_{\text{eff}}^z = \pm {}^3\!/_2$ doublet at $\approx 15\,\text{meV}$. These levels are determined by diagonalising the perturbation Hamiltonian, treating the spin-orbit coupling and trigonal distortion at the same level. The effects of each of these terms on the energy levels can be seen in Figure 7.3.

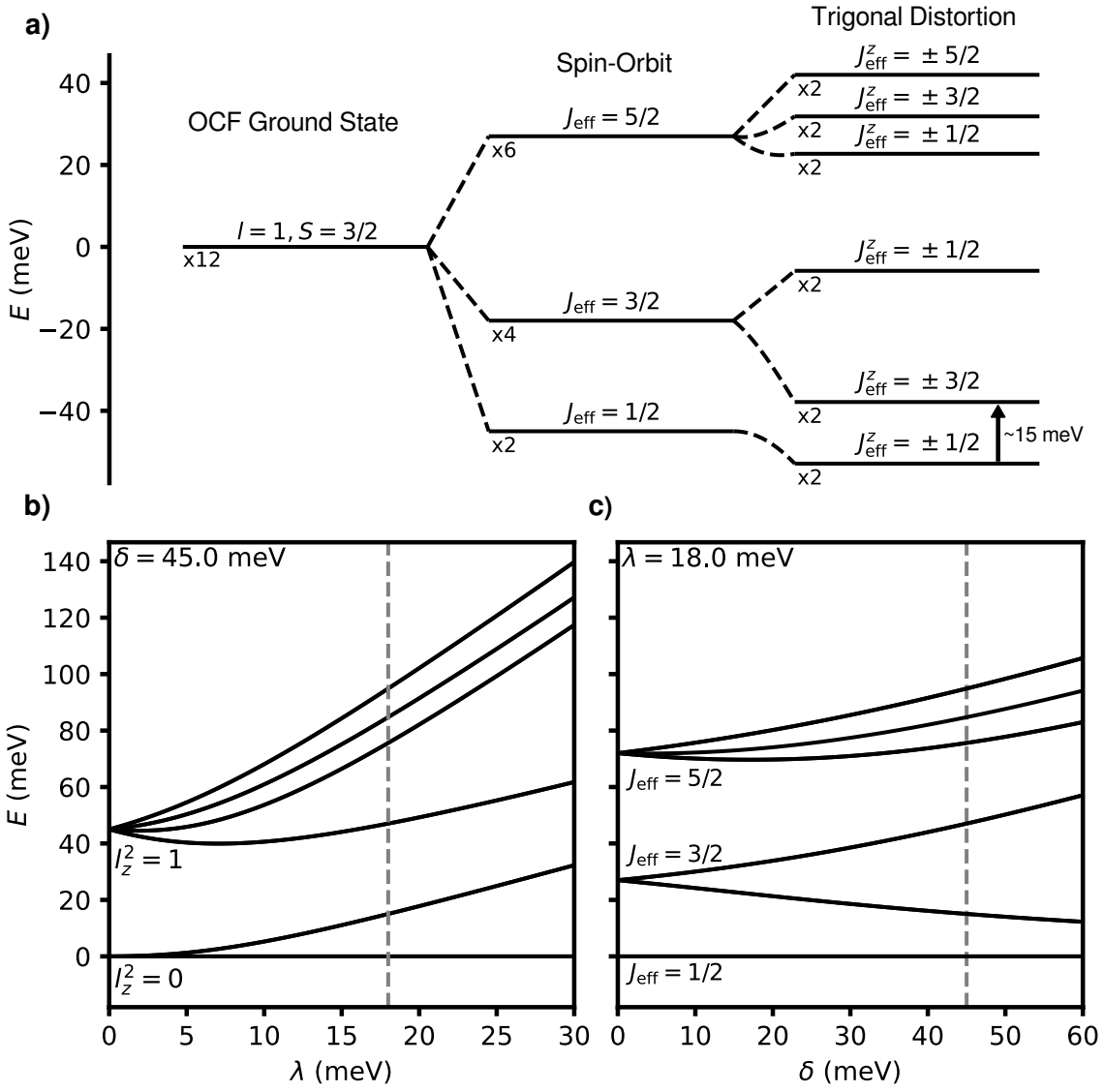


Figure 7.3: a) Schematic diagram showing the level splitting of isolated Co^{2+}ion in an octahedral crystal field in the presence of trigonal distortion and spin-orbit coupling. Labels on states show good quantum numbers for those levels. **b, c)** show evolution of energy levels with spin-orbit coupling strength λ and trigonal distortion strength δ starting from the limit of fixed δ and fixed λ respectively. Vertical lines show values proposed in [4].

The values of λ and δ used were determined by previous reports by fitting the energy levels to an inelastic neutron scattering energy scan [3, 4].

7.1.3 Magnetic Structure of $CoTiO_3$

$CoTiO_3$ has been shown previously to order at $38\,\mathrm{K}$ into an antiferromagnetic arrangement [3, 4, 6–8]. The structure consists of spins ferromagnetically aligned within each honeycomb layer, the layers alternate so that each layer has opposite spin alignment to the previous. The primitive magnetic unit cell has lattice vectors $\boldsymbol{M}_a, \boldsymbol{M}_b, \boldsymbol{M}_c$ which can be written in terms of the structural lattice vectors as

$$\begin{pmatrix} \boldsymbol{M}_a \\ \boldsymbol{M}_b \\ \boldsymbol{M}_c \end{pmatrix} = \begin{pmatrix} 0 & 1 & 1 \\ 1 & 0 & 1 \\ 1 & 1 & 0 \end{pmatrix} \begin{pmatrix} \boldsymbol{A} \\ \boldsymbol{B} \\ \boldsymbol{C} \end{pmatrix} = \frac{1}{3} \begin{pmatrix} 1 & 2 & 2 \\ -2 & -1 & 2 \\ 1 & -1 & 2 \end{pmatrix} \begin{pmatrix} \boldsymbol{a} \\ \boldsymbol{b} \\ \boldsymbol{c} \end{pmatrix} \tag{7.6}$$

The primitive magnetic unit cell is a doubling of the primitive (rhombohedral) structural unit cell. The magnetic cell unit vectors $(\boldsymbol{M}_a, \boldsymbol{M}_b, \boldsymbol{M}_c)$ are rotated relative to $(\boldsymbol{A}, \boldsymbol{B}, \boldsymbol{C})$ by $\frac{\pi}{3}$ around the rhombohedral (111) axis. The cell is also stretched along the same axis, doubling the unit cell volume relative to the primitive structural unit cell. In total there are four Co^{2+}sites in the magnetic unit cell.

Alternatively, Figure 7.4**a)** shows how the magnetic unit cell can be constructed in the hexagonal setting. In this setting, the magnetic unit cell is a simple doubling of the *hexagonal* structural unit cell along the $\boldsymbol{c}$ direction. This doubling occurs because there are three layers per structural unit cell in this setting; the layers alternate in magnetisation so six layers, or two structural cells, are needed for the magnetic structure to repeat.

7.1.4 Exchange Interactions and Magnetic Anisotropy

No single-ion anisotropy is allowed in the ground state, because the ground state doublet is described by an effective $S = 1/2$ and all even polynomials of S_x^2, S_y^2, S_z^2 are constants. The anisotropy effect, an energy preference of spins to point in particular directions over another, must be caused by exchange anisotropy. An inelastic neutron scattering study fit a minimal XXZ exchange model including nearest-neighbour intralayer exchange J_1 and next-nearest-neighbour interlayer Heisenberg exchanges J_4, J_6 [9]. These parameters can be seen in Table 7.2. By using these parameters in a classical model, which is solved

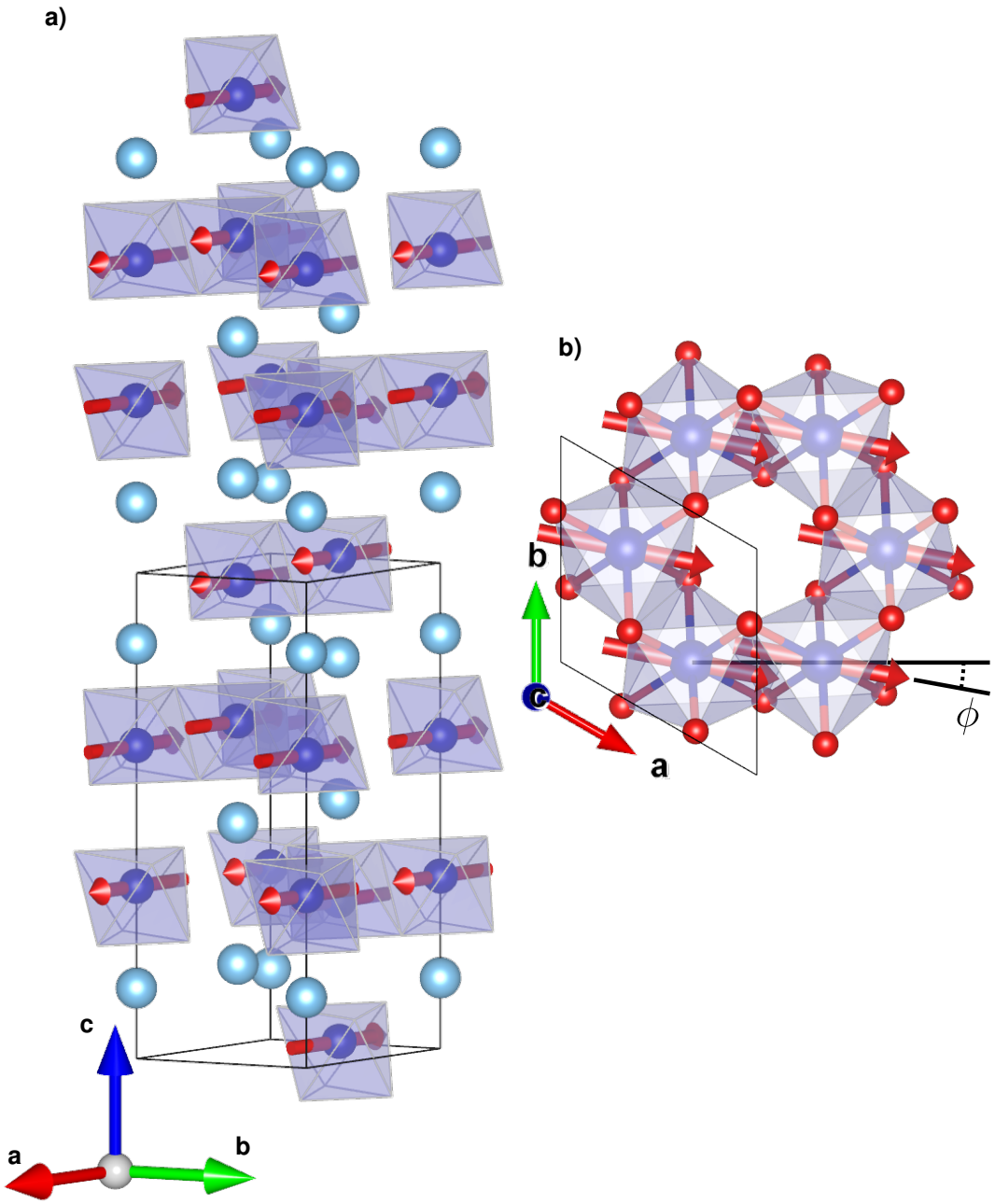


Figure 7.4: a) Model showing magnetic unit cell of $CoTiO_3$ in hexagonal setting. Solid lines indicate the structural unit cell in the hexagonal setting. Arrows overlaid on Co^{2+} ion sites indicate spin alignment at that site. **b)**, projection of single honeycomb layer onto $\boldsymbol{ab}$ plane. Label ϕ shows angle between ordered spin orientation and $\boldsymbol{a}^*$ axis.

as discussed in Chapter 4, the magnetic ground state described above is stabilised up to a spontaneous orientation of spins in the $\boldsymbol{ab}$ plane.

Table 7.2: XXZ exchange parameters in a minimal model for $CoTiO_3$ from [9]

$J_1^x = -4.44\text{meV}$	$J_1^z = 0.0\text{meV}$
$J_4^x = J_4^z = 0.6\text{meV}$	
$J_6^x = J_6^z = 0.6\text{meV}$	

The XXZ Hamiltonian as described has no dependence on the orientation of spins in the $\boldsymbol{ab}$ plane. This is because it has a continuous $U(1)$ symmetry, higher than the discrete $\bar{3}$ point group symmetry of the material. If a $U(1)$ symmetry was realised, one would expect an associated gapless Goldstone mode in the excitation spectrum [10], whereas measurements observe a clear spin-gap [3]. The model developed by Elliot *et.al* [3] lifted this in-plane degeneracy by including a bond-dependent anisotropic exchange term on the nearest-neighbour honeycomb bonds through a parameter η defined such that

$$\eta = J^y - J^x \tag{7.7}$$

in the the local coordinates of the each nearest-neighbour bond. In these coordinates, $\boldsymbol{z}$ is the $\boldsymbol{c}$ axis, $\boldsymbol{x}$ is the projection of the bond direction into the $\boldsymbol{ab}$ plane, and $\boldsymbol{y} = \boldsymbol{z} \times \boldsymbol{x}$. As such the bond's Hamiltonian is written as

$$\hat{\mathcal{H}}_{ij} = J^x S_i^x S_j^x + (J^x + \eta) S_i^y S_j^y + J^z S_i^z S_j^z \tag{7.8}$$

when η is non-zero, it introduced a dependence of the spin-wave spectrum on the azimuthal angle ϕ, defined as the angle between the ordered spin direction and the $\boldsymbol{a}^*$ axis, as seen in Fig.7.4. As a consequence, the zero-point contribution to the ground state energy acquires a dependence on ϕ and discrete spin orientations in-plane are selected, with a 60° periodicity.

The classical, mean field calculation developed in this thesis cannot capture this effect. This can be demonstrated by explicitly computing the effective interaction between sublattices discussed in Chapter 4.

The most general bilinear exchange matrix can be written as

$$\mathcal{J} = \begin{pmatrix} J_x & \Gamma_z + D_z & \Gamma_y - D_y \\ \Gamma_z - D_z & J_y & \Gamma_x + D_x \\ \Gamma_y + D_y & \Gamma_x - D_x & J_z \end{pmatrix} \tag{7.9}$$

where D terms parametrise a Dzyaloshinskii–Moriya (DM) interaction, and Γ terms parametrise symmetric off-diagonal exchange. In this coordinate system, $\boldsymbol{z}$ along the local 3-fold axis, $\boldsymbol{x}$ is the $\boldsymbol{a}^*$ direction, and $\boldsymbol{y} = \boldsymbol{z} \times \boldsymbol{x}$. For each bond not parallel to the $\boldsymbol{z}$ axis, there is another symmetry equivalent bond obtained by a 3_z^+ rotation with exchange matrix

$$\mathcal{J}' = \mathcal{R}_z\left(\frac{2\pi}{3}\right)\mathcal{J}\mathcal{R}_z\left(\frac{-2\pi}{3}\right) \tag{7.10}$$

where $\mathcal{R}_z\left(\pm\frac{2\pi}{3}\right)$ are matrix representations of the the 3-fold rotation about the $\boldsymbol{z}$ axis for spins in these coordinates. This has components given in Table 7.3.

Table 7.3: Symmetry constrained exchange terms for bond obtained by a 3_z^+ rotation.

J'_x	$\frac{1}{4}J_x + \frac{3}{4}J_y + \frac{\sqrt{3}}{2}\Gamma_z$
J'_y	$\frac{3}{4}J_x + \frac{1}{4}J_y - \frac{\sqrt{3}}{2}\Gamma_z$
J'_z	J_z
D'_x	$\frac{1}{2}\left(-D_x - \sqrt{3}D_y\right)$
D'_y	$\frac{1}{2}\left(\sqrt{3}D_x - D_y\right)$
D'_z	D_z
Γ'_x	$\frac{1}{2}\left(-\Gamma_x + \sqrt{3}\Gamma_y\right)$
Γ'_y	$\frac{1}{2}\left(-\sqrt{3}\Gamma_x - \Gamma_y\right)$
Γ'_z	$-\frac{1}{2}\Gamma_z - \frac{\sqrt{3}}{4}J_x + \frac{\sqrt{3}}{4}J_y$

In the magnetic structure of $CoTiO_3$, the spins in the honeycomb plane are all parallel, so the total exchange energy between sites $\boldsymbol{S}_A$ and $\boldsymbol{S}_B$ for these three bonds can be written as the sum

$$\begin{aligned} \mathcal{H} &= \boldsymbol{S}_A^T \mathcal{J} \boldsymbol{S}_B \\ &\quad + \boldsymbol{S}_A^T \mathcal{R}_z\left(\frac{2\pi}{3}\right)\mathcal{J}\mathcal{R}_z\left(-\frac{2\pi}{3}\right)\boldsymbol{S}_B \qquad (7.11a) \\ &\quad + \boldsymbol{S}_A^T \mathcal{R}_z\left(-\frac{2\pi}{3}\right)\mathcal{J}\mathcal{R}_z\left(\frac{2\pi}{3}\right)\boldsymbol{S}_B \\ &= \boldsymbol{S}_A^T \mathcal{J}_T \boldsymbol{S}_B \qquad (7.11b) \end{aligned}$$

where $\mathcal{J}_T$ can be written in terms of the single bond exchange

$$\mathcal{J}_T = 3\begin{pmatrix} \frac{1}{2}(J_x + J_y) & D_z & 0 \\ -D_z & \frac{1}{2}(J_x + J_y) & 0 \\ 0 & 0 & J_z \end{pmatrix} \tag{7.12}$$

The off-diagonal terms show a DM contribution which also cancels. This is because all the bonds with multiplicity of three, such as nearest-neighbour bonds, have an inversion centre at their midpoint so $D_z = 0$ by symmetry. Other bonds with a multiplicity of six, such as next-nearest neighbour, in these the other trio of bonds must have opposite D_z such that the total is zero. The diagonal terms show no dependence on orientation in the $\boldsymbol{ab}$ plane so at the mean field level, no bilinear exchange term can introduce an energy dependence on the alignment of spins in the xy plane.

Calculations of the zero-point contribution to the ground state energy find a clear energy dependence on the spin orientation in the $\boldsymbol{ab}$ plane of the form

$$E(\phi) = \Lambda \cos 6\phi \tag{7.13}$$

where $\Lambda \sim \eta^3$ to leading order [3]. This 6-fold periodicity is a requirement of the $\bar{3}$ point group symmetry of the crystal combined with time reversal. The energy of the system cannot change if the system is transformed under a symmetry operation of the Hamiltonian, for example if all spin operators are reversed.

In the mean field approximation, spin operators are replaced with their expectation values, which in shorthand can be written as $\mathsf{x} := \langle S^x \rangle, \mathsf{y} := \langle S^y \rangle, \mathsf{z} := \langle S^z \rangle$. In order to preserve the 3 point group site symmetry of the Co^{2+}ion, the basis functions must be unchanged under the symmetry operations of that group. Additionally, time reversal maps $\boldsymbol{S} \to -\boldsymbol{S}$, so the basis functions must also be unchanged under inversion. Up to 6$^{\text{th}}$order polynomials of $\mathsf{x}, \mathsf{y}, \mathsf{z}$, this energy is

$$\begin{aligned} E_A(\mathsf{x},\mathsf{y},\mathsf{z}) = {} & A\mathsf{z}^2 + B\mathsf{z}^4 \\ & + C\mathsf{z}(\mathsf{x}^3 - 3\mathsf{x}\mathsf{y}^2) + C'\mathsf{z}(3\mathsf{x}^2\mathsf{y} - \mathsf{y}^3) \\ & + D\mathsf{z}^3(\mathsf{x}^3 - 3\mathsf{x}\mathsf{y}^2) + D'\mathsf{z}^3(3\mathsf{x}^2\mathsf{y} - \mathsf{y}^3) \\ & + E(\mathsf{x}^6 - 15\mathsf{x}^4\mathsf{y}^2 + 15\mathsf{x}^2\mathsf{y}^4 - \mathsf{y}^6) \\ & + E'(6\mathsf{x}^5\mathsf{y} - 20\mathsf{x}^3\mathsf{y}^3 + 6\mathsf{x}\mathsf{y}^5) \end{aligned} \tag{7.14}$$

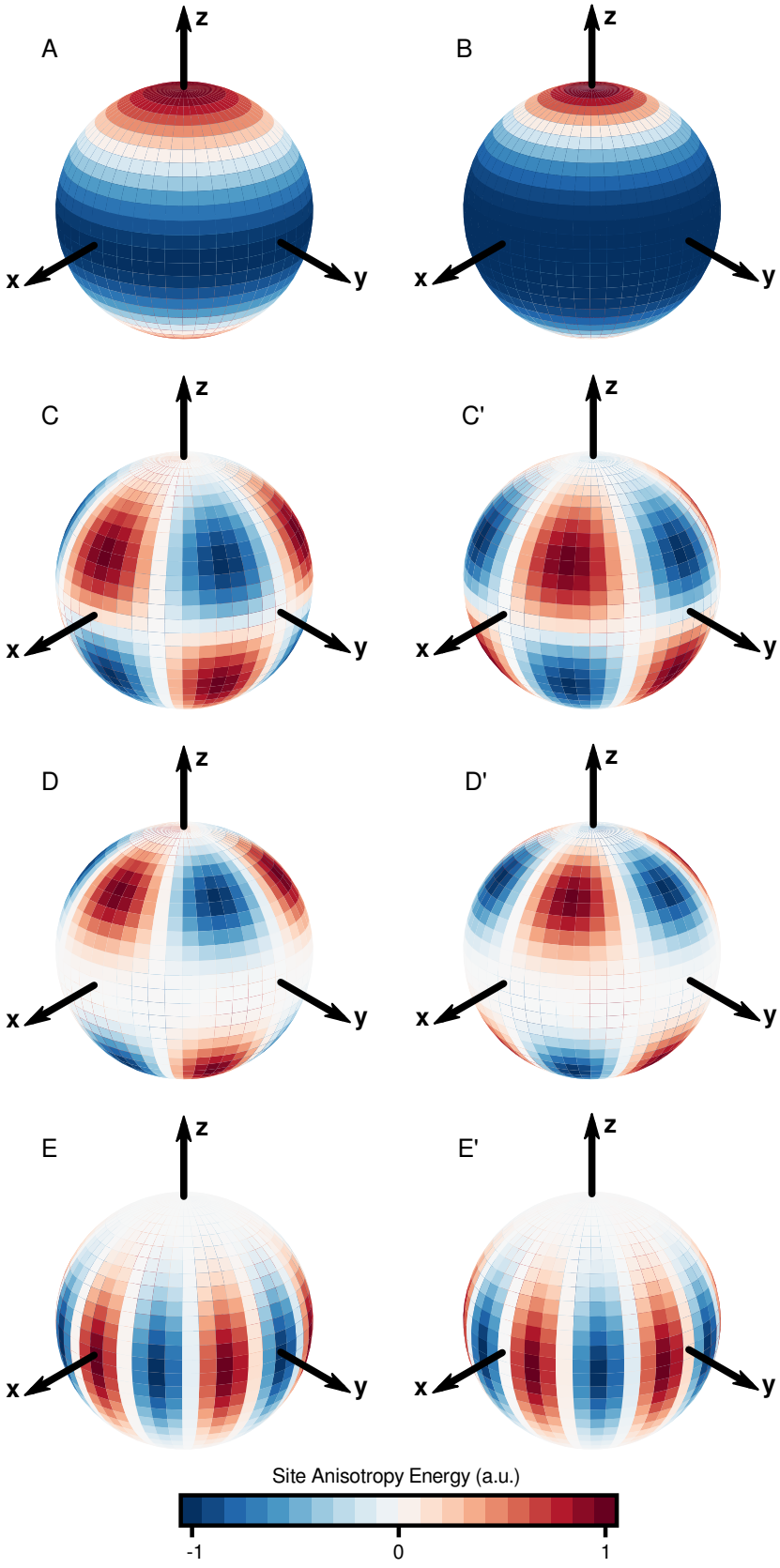


Figure 7.5: Angular dependence of effective site anisotropy energy, top labels indicate the corresponding terms in Eqn. 7.14. Blue colours show negative energies, red areas show positive energies. Here, the z is the projection of the spin onto the crystallographic $\boldsymbol{c}$ axis, x $\parallel$ $\boldsymbol{a}^*$, y $\parallel$ $\boldsymbol{b}$

These functions are plotted over the unit sphere in Figure 7.5, labelled by their coefficient, which shows the negative energies (easy axes) in blue and positive energies (hard axes) in red. For spins in the $\boldsymbol{ab}$ plane $\mathsf{z} = 0$, so only the E and E' functions are non-zero, and the anisotropy energy can be written

$$E_A = \Lambda_0 \sin^6\theta \cos 6(\phi - \phi_6) \tag{7.15a}$$

$$= \Lambda \cos 6(\phi - \phi_6) \tag{7.15b}$$

with ϕ the azimuthal angle measured from the $\boldsymbol{a}^*$ axis, $\tan 6\phi_6 = \dfrac{E'}{E}$, and $|\Lambda| = \sqrt{E^2 + E'^2}$. When $\phi_6 = 0$, $\Lambda > 0$ the easy axes are at $\phi = \frac{\pi}{2} + n\frac{\pi}{3}$ and change to $\phi = n\frac{\pi}{3}$ for $\Lambda < 0$. This behaviour matches that of the quantum-fluctuation induced anisotropy energy in the presence of bond-dependent anisotropy η [3].

It is worth highlighting that the E and E' terms cannot come from single-ion anisotropy in $CoTiO_3$. This is because the quantum form of the single-ion anisotropy terms involves Stevens operators. In order to get the E and E' terms, the $O_6^{\pm 6}$ operators are needed which have the form

$$O_6^{+6} = \frac{1}{2}\left[\hat{L}_+^6 + \hat{L}_-^6\right] \tag{7.16a}$$

$$= \hat{L}_x^6 - 15\hat{L}_x^4\hat{L}_y^2 + 15\hat{L}_x^2\hat{L}_y^4 - \hat{L}_y^6 \tag{7.16b}$$

$$O_6^{-6} = \frac{1}{2i}\left[\hat{L}_+^6 - \hat{L}_-^6\right] \tag{7.16c}$$

$$= 6\hat{L}_x^5\hat{L}_y - 20\hat{L}_x^3\hat{L}_y^3 + 6\hat{L}_x\hat{L}_y^5 \tag{7.16d}$$

These operators give no energy change for Co^{2+}ions. This is because the $L = 3$ quantum state in $Co^{2+}$is made up of d orbital electrons, so the highest order Stevens operator with a non-zero eigenvalue is $O_4^{\pm n}$, where n can be 0, 2, or 4. The anisotropy being modelled originates from interactions; it is not a single-ion effect.

7.1.5 Single Crystal Vibrating Sample Magnetometry studies of $CoTiO_3$

In order to determine the high temperature magnetic properties of $CoTiO_3$, the magnetic susceptibility of single crystals was measured using vibrating sample magnetometry. Figure 7.6**a)** shows the evolution of the magnetic susceptibility between $2\,\mathrm{K}$ and $300\,\mathrm{K}$,

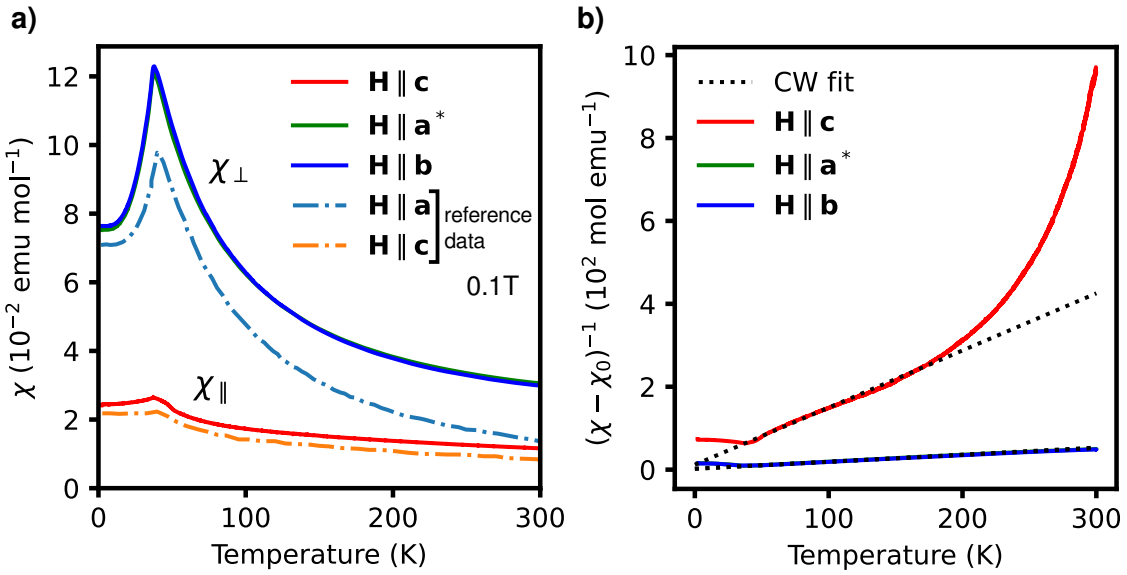


Figure 7.6: Temperature dependence of **a)** susceptibility and **b)** inverse susceptibility in $CoTiO_3$ for orthogonal sample orientations $\boldsymbol{H} \parallel \boldsymbol{a}^*$, $\boldsymbol{H} \parallel \boldsymbol{b}$, $\boldsymbol{H} \parallel \boldsymbol{c}$. In **a)** dot-dash lines show reference data from [6]. In **b)** dotted line shows Curie-Weiss fit.

measured at $0.1\,\mathrm{T}$ for orthogonal field orientations relative to the crystallographic axes. The curves in green and blue show the susceptibility along the $\boldsymbol{a}^*$ and $\boldsymbol{b}$ directions respectively, while the curve in red shows the susceptibility along the $\boldsymbol{c}$ direction. There is a remarkably strong anisotropy between the directions parallel and normal to the $\boldsymbol{c}$ axis, showing an overall easy-plane arrangement. There is a strong suppression of susceptibility for temperatures below $38\,\mathrm{K}$ in the $\boldsymbol{ab}$ plane, while the suppression along the normal direction is much smaller. This confirms that $CoTiO_3$ orders into an antiferromagnet with a Néel temperature of $T_N = 38\,\mathrm{K}$. There is no significant difference in susceptibilities for fields along the two directions in the $\boldsymbol{ab}$ plane across the entire temperature range, suggesting that $CoTiO_3$ behaves very close to uniaxially in its magnetic behaviour, i.e. the anisotropy in the $\boldsymbol{ab}$ plane is very small.

Temperature dependent susceptibility data (Fig. 7.6) can be fitted to a Curie-Weiss relationship

$$\chi = \chi_0 + \frac{C}{T + \theta_{\mathrm{CW}}} \tag{7.17}$$

over the temperature range $50\,\mathrm{K}$-$200\,\mathrm{K}$.

Table 7.4: Fitted Curie-Weiss parameters for $CoTiO_3$ temperature-dependent susceptibility data.

	χ_0 (10^{-2} emu mol^{-1})	θ_{CW} (K)	C (emu Kmol^{-1})	μ_{eff} (μ_B)
$\boldsymbol{H} \parallel \boldsymbol{a}^*$	1.049(4)	13.3(1)	5.98(1)	6.9
$\boldsymbol{H} \parallel \boldsymbol{b}$	0.936(2)	11.9(1)	5.89(1)	6.9
$\boldsymbol{H} \parallel \boldsymbol{c}$	1.056(4)	8.7(2)	0.73(1)	2.4

The fitted parameters can be seen in Table 7.4. These data in some areas agree well with previously published data [6, 7, 11]: the low-temperature shapes of the curves and absolute scale of the susceptibilities, and the strong anisotropy of susceptibilities that is seen at all temperatures. The high-temperature data does not agree well with the previously published results, here a larger value of $\chi_\perp$ is observed than previously reported. This discrepancy is likely caused by a magnetic background from the brass sample holder, which has not been subtracted. Where susceptibility data is used for calibration in later sections, the reference data [6] is used. While this high temperature discrepancy may also account for disagreement between the fitted and published Curie-Weiss parameters [11], if the fitting process is repeated on more recently published data in [6], the fitted moment μ_{eff} agrees relatively well. This data gives $\mu_{\text{eff}} = 2.5\mu_B$, $7.3\mu_B$ along the $\boldsymbol{c}$ and $\boldsymbol{a}$ directions respectively. This is because a background term χ_0 is captured in the fit. The poor fit of Curie-Weiss behaviour at high temperature is expected from the relatively small energy gap of $\approx 15\,\text{meV} \approx 175\,\text{K}$ to the next excited doublet. For temperatures greater than this value, the excited doublet states are populated and the CW treatment fails. A more thorough treatment including all of the energy levels predicted from the level splitting would capture this effect, but as the crystal field parameters and λ have already been established, this is not necessary.

Figure 7.7**a)** shows the evolution of magnetisation with applied magnetic field up to $4\,\text{T}$ for temperatures between $2\,\text{K}$ and $40\,\text{K}$. Above T_N, the relationship is linear. As the temperature falls below the Néel temperature, the linear relationship no longer holds. For fields below $B^* \approx 2.5\,\text{T}$ and temperatures below T_N, the differential susceptibility is suppressed significantly, as can be seen in Fig 7.7**b)**. This effect was reported previously [6], where the peak in $\frac{\partial M}{\partial H}$ at approximately $2.5\,\text{T}$ was labelled B^*. This can be attributed to the in-plane anisotropy proposed previously, as magnetic domains exist in the material

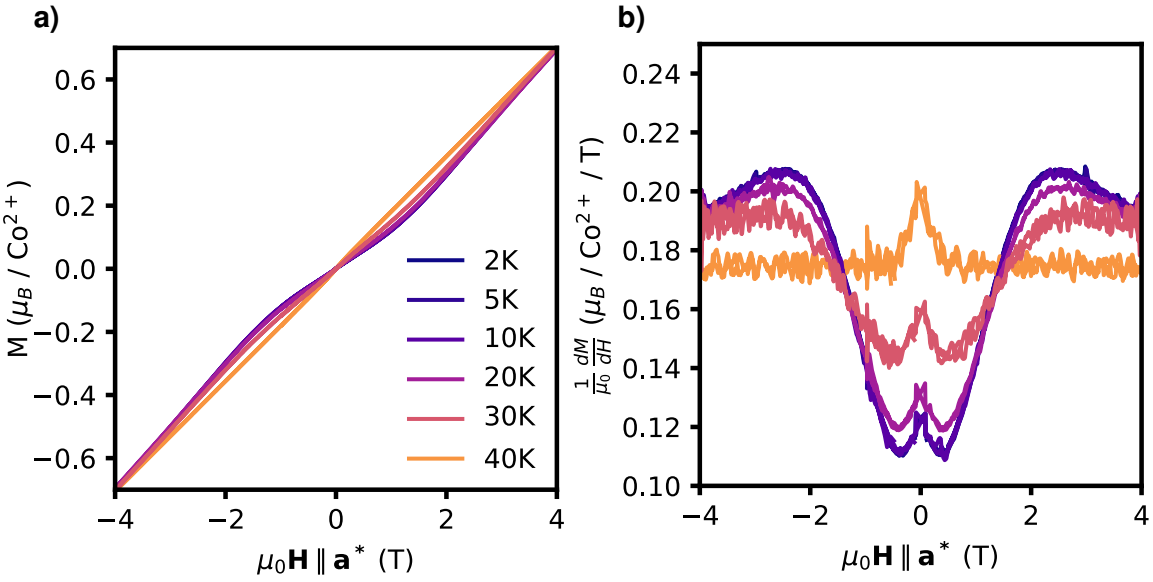


Figure 7.7: Field dependence of **a)** magnetisation **b)** differential susceptibility in $CoTiO_3$ for a range of temperatures from 2K to 40K with $\boldsymbol{H} \parallel \boldsymbol{a}^*$.

at low field, with ordered moments in the $\boldsymbol{ab}$ plane. This suggests that a single domain is selected for fields $\mu_0 H \gg B^*$.

7.1.6 Single Crystal Torque Magnetometry Studies of $CoTiO_3$

As has been discussed in Chapter 3.2, torque magnetometry is a powerful tool for exploring the anisotropy of a material. In this section I discuss how this technique was used to study the in-plane anisotropy of $CoTiO_3$.

While I was able to cut large crystals of $CoTiO_3$ into arbitrary shapes to align the field along the different crystallographic axes for the VSM experiments described above, the size of the cantilevers requires very small single crystals of order $\sim 100\,\mu\mathrm{m}$ to be able to measure torque. To prepare these crystals I crushed small amounts of the larger $CoTiO_3$ crystals in grease. This allowed small crystallites to be collected from the resulting material. As $CoTiO_3$ is a layered material, it preferentially broke between layers, leading to large numbers of plate-like single crystals with a normal vector parallel to $\boldsymbol{c}$. An example of such a crystal can be seen in Figure 7.8**a)**, which shows a plate-like single crystal of $CoTiO_3$ with a diameter of $\sim 100\,\mu\mathrm{m}$, mounted ready for torque measurements in the $\boldsymbol{a}^*\boldsymbol{c}$ plane. This plate-like arrangement made mounting the crystal for torque in the

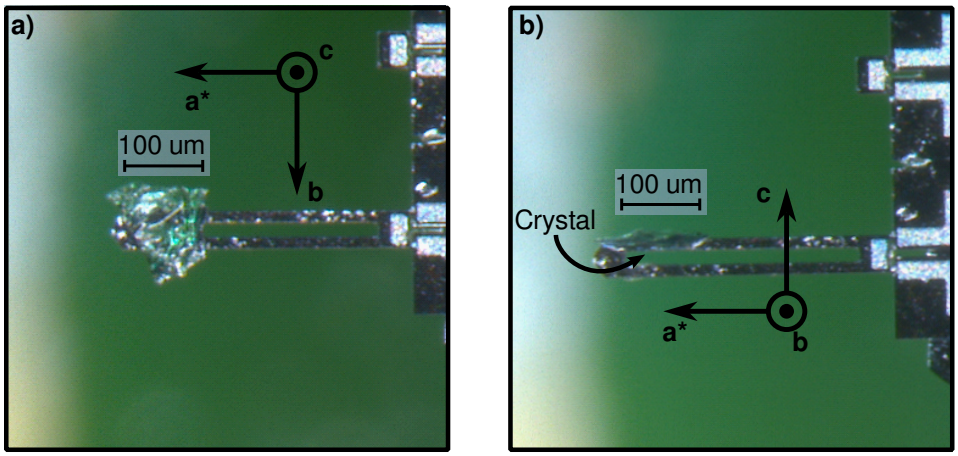


Figure 7.8: Photographs of $CoTiO_3$ single crystals mounted on piezoresistive cantilevers for torque measurements. In **b)** the crystal is attached 'edge on' and is just visible on the top side of the lever.

$\boldsymbol{ab}$ plane much more challenging, as the plane normal $\boldsymbol{c}$ had to be perpendicular to the lever surface normal. In order to measure the crystal in such an orientation, I mounted it on the side of the lever, as seen in Figure 7.8**b)**, supported by a small quantity grease on the surface. This made precise alignment very difficult. In this image, the crystal is seen 'edge-on'. As the in-plane susceptibility is much larger than the out-of-plane susceptibility $\chi_\perp \gg \chi_\parallel$ even at high temperature, subjecting the crystal to a large magnetic field causes a torque on the sample which would tend to improve the alignment of the crystal. That is, the energy is minimised if the field is in the $\boldsymbol{ab}$ plane. This effect was used to improve the crystal alignment in the $\boldsymbol{ab}$ plane by rotating the crystals in a $16\,\mathrm{T}$ field at $300\,\mathrm{K}$, such that the grease was a unfrozen. The crystal was then cooled in field to base temperature.

Unlike in the other systems studies in this thesis, I have been able to normalise the torque signal in $CoTiO_3$ in absolute units. This is because of the availability of high quality published data of anisotropic susceptibilities along different crystal axes in absolute units, as discussed above. Above the Néel temperature, $CoTiO_3$ behaves as a uniaxial paramagnet, so the torque at high temperatures can be calculated from the susceptibility data (Eqn. 3.36) using the susceptibility measured parallel to the $\boldsymbol{c}$ axis

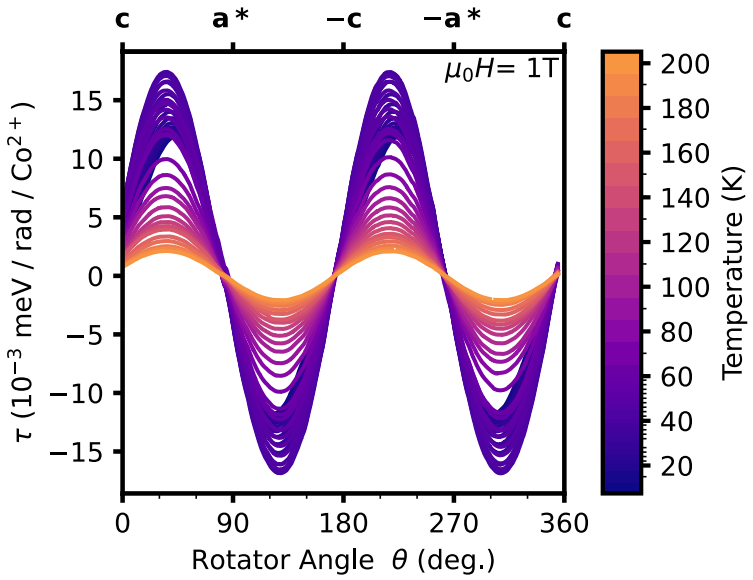


Figure 7.9: a) Waterfall plot showing magnetic torque vs rotator angle for temperatures between 2 K and 200 K in ac plane. Top axis labels indicate angles where the magnetic field direction is aligned parallel to a crystallographic axis. Traces are raw torque piezocantilever voltages converted to absolute units as described in the text.

$\chi_\parallel$, and measured in the $\boldsymbol{ab}$ plane $\chi_\perp$:

$$\tau(\theta, T) = \frac{1}{2} B^2 \left(\chi_\perp(T) - \chi_\parallel(T)\right) \sin 2\theta \tag{7.18a}$$

$$= -\tau_2(T) \sin 2\theta \tag{7.18b}$$

where θ is the angle between the field and the $\boldsymbol{c}$ axis. As the anisotropic susceptibilities are known in absolute units, torque in the $\boldsymbol{a}^*\boldsymbol{c}$ plane can be measured for a large temperature range above the T_N and the results compared to the predicted values to determine the conversion factor between the measured signal and the physical torque, which will capture both the sensitivity of the lever and the mass of the sample.

Figure 7.9 shows measured magnetic torque for rotations in the $\boldsymbol{a}^*\boldsymbol{c}$ plane at 1 T and temperatures between 10 K and 200 K. These show an overall $\sin 2\theta$ dependence, with a positive gradient when fields are parallel to the $\boldsymbol{c}$ axis and a negative gradient when fields are parallel to the $\boldsymbol{a}^*$ axis at all temperatures, indicating a smaller susceptibility in-plane than out of plane. This is in agreement with easy-plane type antiferromagnet model determined from the VSM data reported previously. These piezocantilever voltages, in units of mV were fitted to the form

$$V = -V_0 \sin 2(\theta - \theta_0) \tag{7.19}$$

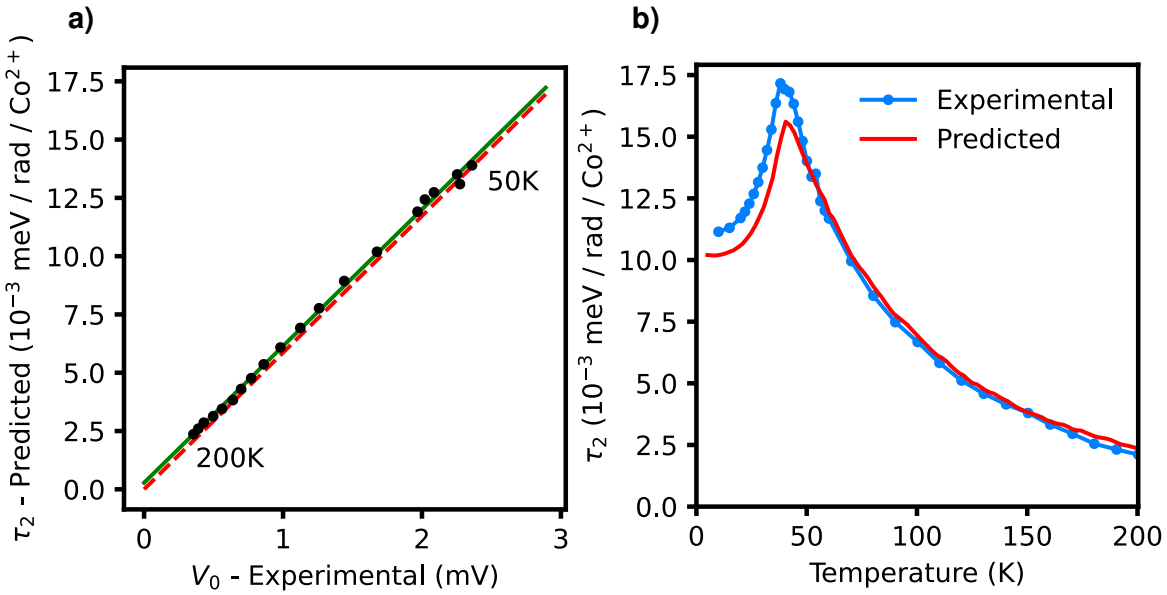


Figure 7.10: **a)** Plot showing fitted torque amplitudes in $\boldsymbol{a^*c}$ plane against predicted torque amplitudes from published susceptibility data [6] with linear fit (green line), and linear fit with zero intercept (red dashed line). **b)** Plot showing evolution of (cyan points) fitted torque amplitudes, (red curve) predicted torque amplitudes from published susceptibility data [6] for rotations in $\boldsymbol{a^*c}$ plane against temperature.

and the values V_0 compared to the predicted values

$$\tau_2(T) = -\frac{1}{2}B^2\left(\chi_\perp(T) - \chi_\parallel(T)\right) \tag{7.20}$$

for temperatures $T > 50\,\mathrm{K}$. Figure 7.10 shows the plot of V_0 vs τ_2 for all temperatures measured, the green line shows a linear fit to these data. The dashed red line shows a line with the same gradient and zero intercept. This calibrated scaling factor comes to

$$\tau = V \cdot 5.938(10) \times 10^{-3}\frac{\mathrm{meV rad^{-1}/Co^{2+}}}{\mathrm{mV}} \tag{7.21}$$

which can be used to calibrate all other measurements on the same sample-lever pair. It should be noted that these samples are too small for their mass to be measured using standard equipment, so this calibration factor is not able to calibrate other samples on the same lever. For this reason, all torque data reported in this chapter has been measured using the same calibrated sample shown in Figure 7.8. Figure 7.10 shows how this calibration was verified by comparing the temperature dependence of the experimentally observed torque amplitudes, scaled by this calibration factor, against the predicted temperature dependence for the paramagnetic phase from (7.20). These

show good agreement over the high temperature region where (7.20) is valid, indicating that this calibration procedure was effective.

Figure 7.11**a)** shows the evolution of magnetic torque with field in the $\boldsymbol{ab}$ plane, measured at the experimental base temperature of $2\,\mathrm{K}$, far below the ordering temperature for this material. These torque profiles show complex behaviour at all fields, unlike the simple $\sin 2\theta$ behaviour seen in the $\boldsymbol{a^*c}$ orientations. Despite the complexity, six peaks and six troughs can be clearly seen in all fields in the $\phi = 0° \rightarrow 360°$ angle range. This suggests a significant contribution from a six-fold energy term, however the signal also contains other components. Some of these will be contributed by the lever background, as the resistance of the bridge will vary slightly with applied magnetic field. Others will be caused by a small projection of the $\boldsymbol{c}$ axis onto the rotation plane, as the anisotropy between the $\boldsymbol{ab}$ plane and the $\boldsymbol{c}$ axis is much stronger than any anisotropy within the $\boldsymbol{ab}$ plane, only a small projection of this axis is needed for the signal to be significant compared to the very small contribution from in-plane anisotropy.

In order to better show the six-fold contribution to the torque signal, I have performed a simple background subtraction by removing low order Fourier components. To do this I fit the signal to the form

$$\tau = C_0 + C_1\phi + \sum_{n=1}^{m} A_n \sin n\phi + B_n \cos n\phi \tag{7.22a}$$

$$= C_0 + C_1\phi + \sum_{n=1}^{m} \tau_n \sin n(\phi - \phi_n) \tag{7.22b}$$

where all A_n, B_n, C_n are free fitting parameters, and $m = 12$ is chosen to be sufficiently large that increasing it does not significantly improve the fit. Here $\tau_n^2 = A_n^2 + B_n^2$, and $\tan n\phi_n = \frac{A_n}{B_n}$. This form is motivated from the experimental design: C_0 is non-zero if the electronic Wheatstone bridge balancing is not perfect. C_1 can account for a linear drift in the lever balancing over the course of the experiment, which occurs as the temperature stability is not ideal. The choice of the Fourier series is because the rotation is a physical rotation of the levers in the magnetic field. Physically, the torque applied to the lever must be periodic in ϕ, unless it is hysteretic. I then take the fitted curve with parameters $n < 5$ as the 'background' to be removed, which is subtracted from the raw signal. Note that

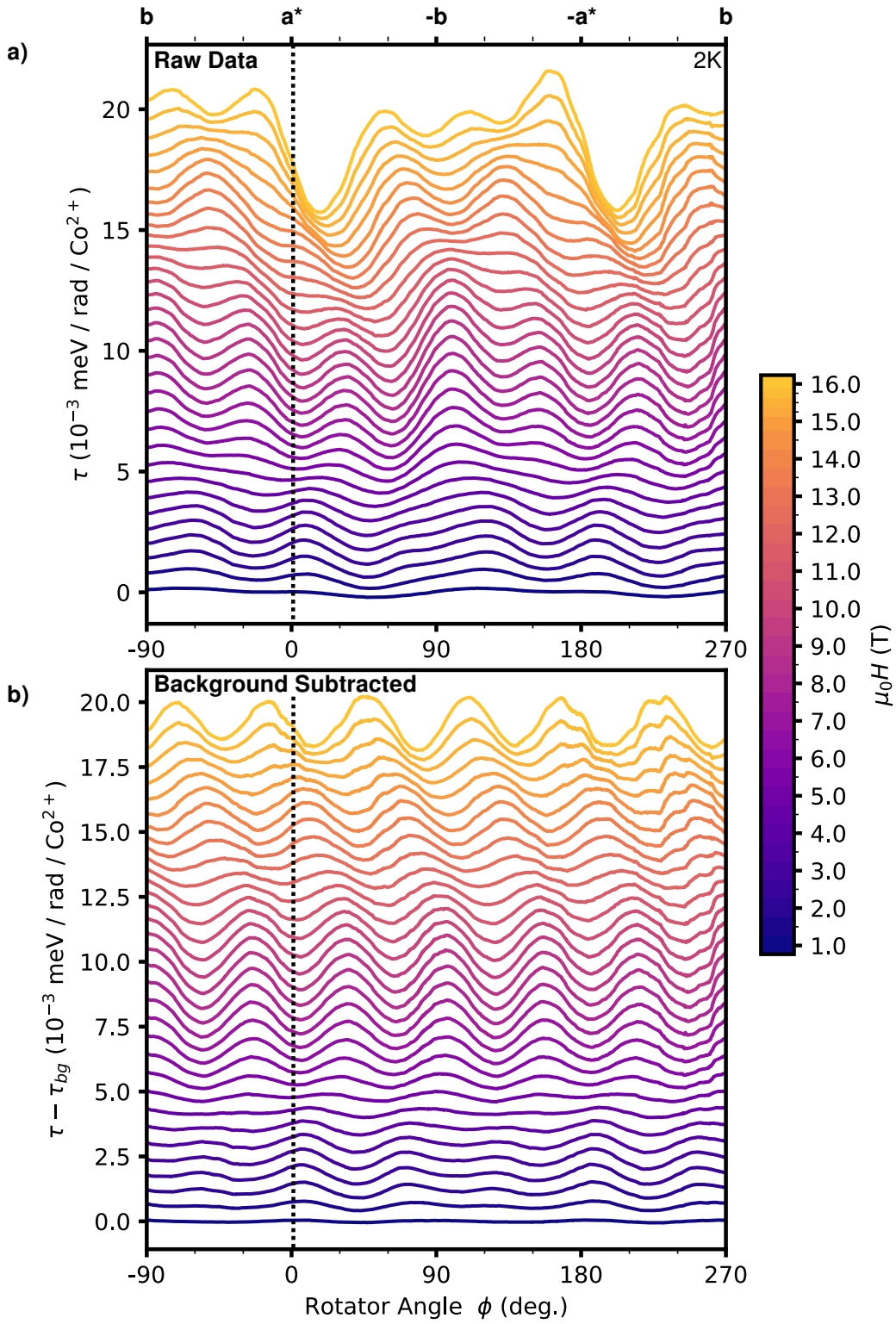


Figure 7.11: Waterfall plot showing magnetic torque vs rotator angle ϕ for applied magnetic fields between 1 T and 16 T in the $\boldsymbol{ab}$ plane, measured at the experimental base temperature of 2 K. **a)** shows raw data, while **b)** shows the same data with background subtracted. ϕ is measured from the nominal $\boldsymbol{a}^*$ axis. Top labels above **a)** indicate angles where the magnetic field direction is aligned parallel to a crystallographic axis. Dashed vertical line corresponds to field along the $\boldsymbol{a}^*$ axis. Traces are torque piezocantilever voltages converted to absolute units as described in the text, and vertically offset between subsequent fields for clarity.

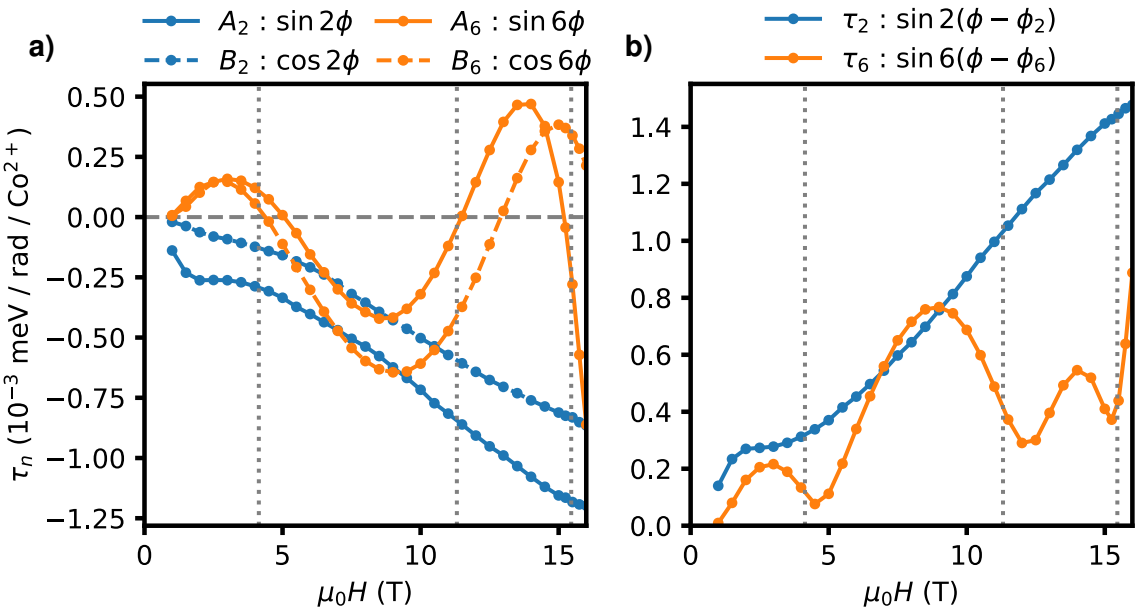


Figure 7.12: Plot showing evolution of fitted components of **a)** Eqn. (7.22a) **b)** Eqn. (7.22b) with applied magnetic field between 1 T and 16 T for torque measurements in the $\boldsymbol{ab}$ plane of $CoTiO_3$ measured at 2 K. Dashed vertical lines indicate fields where τ_6 components are expected to change sign as described in the text.

Fourier components $n = 1, 3, 4$ are very small, but above the noise level, likely coming from non-linearities and background in the lever assembly itself.

Figure 7.11**b)** shows the same signal measured at 2 K with the background subtracted as described above. This shows an overall pattern of a six-fold torque signal, which increases in magnitude as the strength of the applied magnetic field increases from 1 T to 16 T. Additionally the phase and amplitude of the signal is modulated with the magnetic field strength. In order to explore these effects, Figure 7.12 shows the evolution of the fitted parameters in Eqn. (7.22a) as a function of applied magnetic field. This shows that the six-fold components are comparable in magnitude to the two-fold components. Additionally it shows the modulation of the A_6 and B_6 components, which increase in magnitude with applied magnetic field and change sign at approximately equal magnetic fields. This effect can be more clearly seen in Figure 7.13, which shows select torque traces, with background subtracted, by themselves. These clearly show the change in sign of the signal as the applied magnetic field increases.

I have drawn a vertical line at 0° on Figure 7.11**b)** to indicate where the magnetic

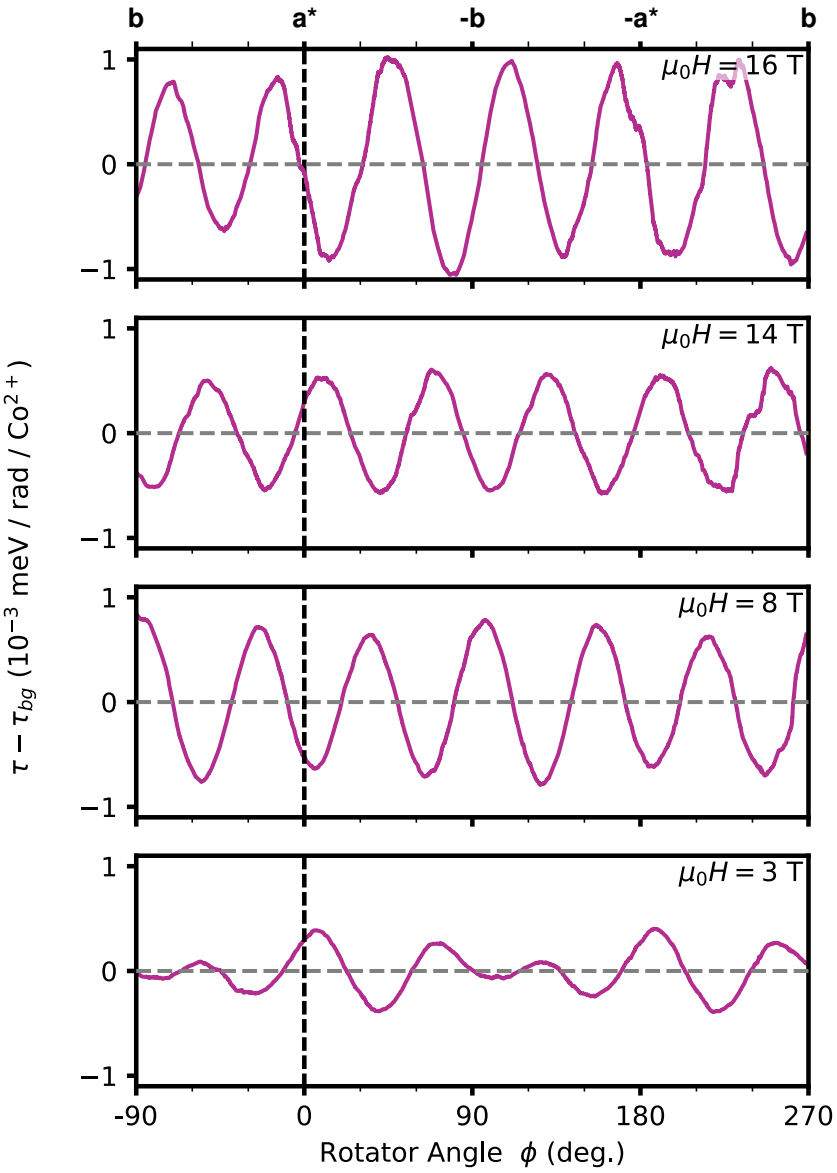


Figure 7.13: Angular dependence of magnetic torque in $\boldsymbol{ab}$ plane for a selection of applied magnetic fields 3, 8, 14, 16 T. All measured at 2 K. Top labels indicate angles where the magnetic field direction is aligned parallel to a crystallographic axis. Vertical dashed line indicates $\boldsymbol{H} \parallel \boldsymbol{a}^*$. Traces are raw torque piezocantilever voltages converted to absolute units and with background subtracted as described in the text.

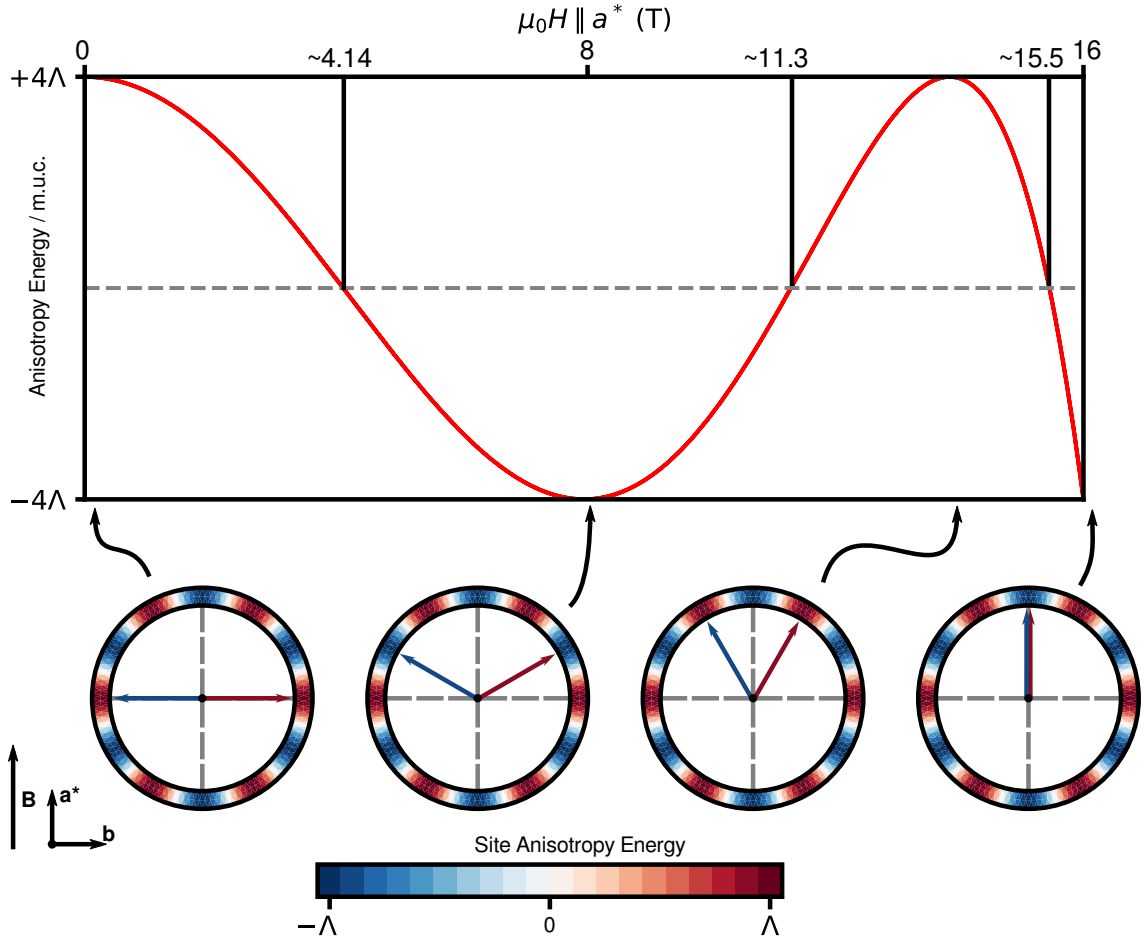


Figure 7.14: Field dependence of calculated total anisotropy energy per magnetic unit cell (Eqn. 7.15) for $\boldsymbol{B} \parallel \boldsymbol{a}^*$ between 0 T and 16 T for the case of $\Lambda < 0$ and $\phi = 0°$. All exchange and g-factor parameters are as in the text (Table 7.2) and $\Lambda < 0$ is assumed to be independent of field strength. Blue/red arrows show the alignment of spins in adjacent layers in the $\boldsymbol{ab}$ plane while colour in the annular region indicates the corresponding local energy environment of the spins.

field is approximately parallel to the $\boldsymbol{a}^*$ axis. This is close to the zeros of the six-fold torque signal. In low fields, below $\approx$ 4 T, the gradient through this point is positive, indicating an unstable equilibrium. At large fields (above $\approx$ 14 T), the gradient is negative indicating a stable equilibrium. At intermediate fields the gradient changes three times, at 4 T, 10 T, and 14 T. The gradient is negative between $\approx$ 4 T and $\approx$ 10 T and positive between $\approx$ 10 T and $\approx$ 14 T.

These changes can be naturally explained by considering the changes in the anisotropy energy as the material becomes magnetised. At the largest field of 16 T in-plane the

magnetisation is almost saturated; the spins are approximately parallel with the magnetic field. An overall stable equilibrium with the field along $\boldsymbol{a}^*$ suggests that the local anisotropy for the spins has a stable equilibrium at the same position. In small magnetic fields below $\approx 4\,\mathrm{T}$ the spins are approximately antiparallel, and orthogonal to the field direction in order to minimise energy. With $\boldsymbol{B} \parallel \boldsymbol{a}^*$, this constrains the spins to be collinear with $\boldsymbol{b}$ ($\perp \boldsymbol{a}^*$). The overall system is in an unstable equilibrium, indicating that spins along this orientation is an energy maximum, determined by the positive torque gradient $\frac{\partial \tau}{\partial \phi} > 0$ when the $\boldsymbol{B} \parallel \boldsymbol{a}^*$ (see Fig. 7.13). The intermediate field behaviour can be understood as caused by the modulations in local energy of the spins as they rotate towards the field. I illustrate this is Figure 7.14, which shows the evolution in the anisotropy energy as field is increased along the $\boldsymbol{a}^*$ direction. With the magnetic field below $\sin 15^\circ \cdot B_{sat}$, the system is in an unstable equilibrium. For $\sin 15^\circ \cdot B_{sat} < B < \sin 45^\circ \cdot B_{sat}$ the system is stable and so on. The numbers on the x-axis indicate the fields when these switches will occur for a saturation field of $16\,\mathrm{T}$. These fields are overlaid as vertical lines on Figure 7.12, which show good agreement with the minima in the fitted amplitudes of the τ_6 components.

From this model and the data in Figure 7.11, I can determine the anisotropy parameters of interest. In particular, at $16\,\mathrm{T}$, the angular dependence of torque can be fit to the form

$$\tau(\phi) = \tau_6 \sin 6(\phi - \phi_6) \tag{7.23}$$

with $\tau_6 = -8.5(2) \times 10^{-4}\ \mathrm{meVrad}^{-1}/\mathrm{Co}^{2+}$ and $\phi_6 \approx +2^\circ$. Note that the absence of mirror planes containing the $\boldsymbol{c}$-axis means that ϕ_6 is not symmetry constrained and could in principle take any value. As the material should be (approximately) fully polarised at this magnetic field strength, this torque should be coming from the full scale of the anisotropy energy

$$E_A = \Lambda \cos 6(\phi - \phi_6) \tag{7.24}$$

$$\implies \tau_6 = 6\Lambda \sin 6(\phi - \phi_6) \tag{7.25}$$

so the local anisotropy energy can be read off simply as $\Lambda = -1.4(1) \times 10^{-4}\ \mathrm{meV}/\mathrm{Co}^{2+}$.

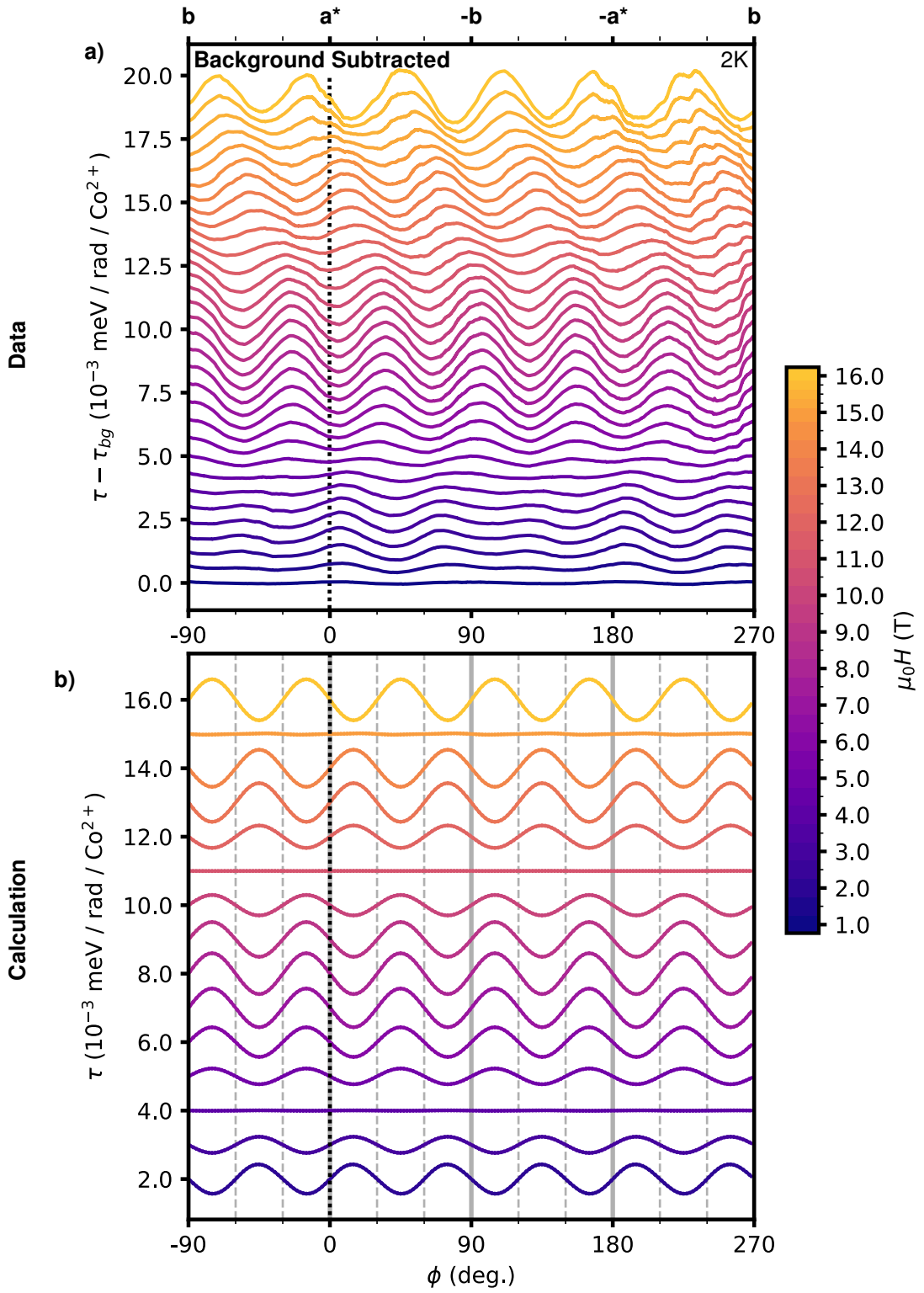


Figure 7.15: a) Reproduced from Figure 7.11 for comparison. **b)** Waterfall plot showing calculated magnetic torque vs rotator angle ϕ for applied magnetic fields between 1 T and 16 T in the $\boldsymbol{ab}$ plane, with ϕ measured from the $\boldsymbol{a}^*$ axis. Top labels above **a)** indicate angles where the magnetic field direction is aligned parallel to a crystallographic axis. Dashed vertical line corresponds to field along the $\boldsymbol{a}^*$ axis. Calculation details are in the text.

The model for a quantum-fluctuation induced six-fold clock anisotropy [3] suggests that at leading order

$$\Lambda = \frac{1}{8} a \eta^3 \tag{7.26}$$

where a is a constant estimated at $a = 6.13(7) \times 10^{-5}\ \mathrm{meV}^{-2}$ and η, defined in Eqn. (7.7), $\approx -1.7\,\mathrm{meV}$, suggesting a value of $\Lambda \cong -3.8 \times 10^{-5}\ \mathrm{meV}$. This is of the same order of magnitude as the value estimated from torque.

Practical considerations with the mounting mean that precisely aligning crystallographic axes within the plane is not possible, so the phase ϕ_6 should not be taken to be a precise offset. However, it is clear from the data that the stable equilibrium is close to the $\boldsymbol{a}^*$ axis and the unstable equilibrium close to the $\boldsymbol{b}$ axis, tentatively placed within 5° of these. In the quantum fluctuations model, the negative $\eta < 0$ favoured spins parallel to the bond direction, which is parallel to $\boldsymbol{a}^*$. Together with the order of magnitude quantitative agreement of the size of the magnetic anisotropy this agreement on the locations of the in-plane easy axes provides strong support for the interpretation that quantum fluctuations are the origin of the anisotropy.

Figure 7.15 shows a numerical calculation for torque in the $\boldsymbol{ab}$ plane for fields between $2\,\mathrm{T}$ and $16\,\mathrm{T}$ with the anisotropy energy taken as above. This calculation captures the modulations in torque strength and phase change with magnetic field strength. The calculation predicts a larger magnitude of torque at small fields than is measured, this is likely a combination of two main factors. It is clear from the suppression of susceptibility in the $\boldsymbol{ab}$ plane that $CoTiO_3$ has magnetic domains which remain in small magnetic fields, the pinning of these domains is not modelled by the calculation and their presence is likely to suppress the energy modulation as the field is rotated. If the anisotropy amplitude Λ originates from zero-point quantum fluctuations, one would expect a variation with field strength. Most straightforwardly the quantum fluctuations would be expected to be suppressed at high field, inconsistent with what is seen experimentally. It should be noted however that the energy scale here is $g\mu_B B \ll J^x$, so quantum fluctuations should still be significant.

Table 7.5: Refined 300 K crystal structure parameters of $FeTiO_3$ from analysis of powder diffraction data in [4].

Space group: $R\bar{3}\,H$ (148)				
Hexagonal setting				
Z = 6				
Cell parameters:				
a, b, c (Å)		5.088	5.088	14.085
α, β, γ (°)		90	90	120
Volume (Å^3)		309.365		
Atomic fractional coordinates:				
Atom	Wyckoff Site	Site Symmetry	x	y	z
Fe^{2+}	$6c$	3	0	0	0.3562(6)
Ti^{4+}	$6c$	3	0	0	0.1469(6)
O^{2-}	$18f$	1	0.3561(13)	0.0397(18)	0.2384(7)

7.2 Six-Fold Clock Anisotropy in $FeTiO_3$

A contrasting case to $CoTiO_3$ is the isostructural material $FeTiO_3$, which has an identical magnetic structure of stacked ferromagnetic layers, where adjacent layers are antiferromagnetically coupled, however $FeTiO_3$ is an easy-axis system, rather than an easy-plane like $CoTiO_3$. The structural parameters of $FeTiO_3$ can be seen in Table 7.5.

$FeTiO_3$ orders at $58\,\mathrm{K}$ as an easy-axis antiferromagnet [12], as can be seen clearly by the susceptibility-temperature curves shown in Figure 7.16. These show nearly isotropic susceptibilities in the high-temperature limit and a sharp peak in susceptibility along the $\boldsymbol{c}$ axis (cyan) at the ordering temperature. Below the Néel temperature, the susceptibility along the $\boldsymbol{c}$ is strongly suppressed while the susceptibility in the $\boldsymbol{ab}$ plane is approximately temperature independent. The magnetic structure of $FeTiO_3$ is identical to that of $CoTiO_3$. Layers of $Fe^{2+}$are ferromagnetically aligned, with alternating layers antiferromagnetic. In $FeTiO_3$, the spins are almost parallel to the $\boldsymbol{c}$ axis, although neutron diffraction studies report a clear experimental signature of a small but finite $\approxeq\ 1.6°$ tilt away from the $\boldsymbol{c}$ axis [13–15].

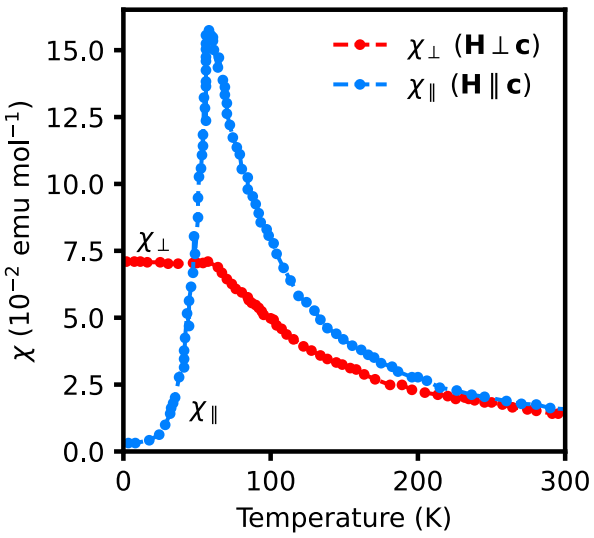


Figure 7.16: Temperature dependence of anisotropic susceptibilities in plane (red) and out of plane (blue) for $FeTiO_3$ between 2 K and 300 K measured in an applied magnetic field of $\mu_0 H = 1.38$ T adapted from [12]

7.2.1 Single ion physics of Fe^{2+}ions in $FeTiO_3$

The magnetic ions in $FeTiO_3$ are $3d^6$ Fe^{2+}ions in an octahedral crystal environment with trigonal distortion. The Hund's rules ground state for this electronic configuration is $L = 2$, $S = 2$. The octahedral crystal field Hamiltonian can be written

$$\hat{\mathcal{H}}_{\text{CEF}} = -\frac{2}{3}B_4\left(O_4^0 + 20\sqrt{2}O_4^3\right) + B_2^0 O_2^0 + B_4^0 O_4^0 \tag{7.27}$$

using the Stevens operators O_n^k in the Cartesian basis with x, y, z along the $\boldsymbol{a}^*, \boldsymbol{b}, \boldsymbol{c}$ axes respectively [5]. $B_4 > 0$ parametrises the octahedral cubic crystal field environment, and the additional terms characterise a trigonal distortion along the $\boldsymbol{c}$ axis. With this, spin-orbit coupling is included to give a single-ion Hamiltonian

$$\hat{\mathcal{H}} = -\lambda \hat{\boldsymbol{L}} \cdot \hat{\boldsymbol{S}} + \hat{\mathcal{H}}_{\text{CEF}} \tag{7.28}$$

where $\lambda > 0$ because the shell is more than half filled.

This can be approached perturbatively by assuming that the cubic octahedral crystal field $\hat{\mathcal{H}}_{\text{OCF}}$ is the largest energy scale in $\hat{\mathcal{H}}$.

In the $|L_z\rangle$ basis, the octahedral field gives a ground state T_{2g} triplet at energy $-48B_4$,

and an excited E_g doublet at $+72B_4$ [5]. The ground state has basis vectors

$$\left|\widetilde{0}\right\rangle = |0\rangle \tag{7.29a}$$

$$\left|\pm\widetilde{1}\right\rangle = \pm\sqrt{\frac{2}{3}}\,|\mp 2\rangle - \sqrt{\frac{1}{3}}\,|\pm 1\rangle \tag{7.29b}$$

where the states are labelled by the effective angular momentum operator $|l_z\rangle$ (z along the trigonal $\boldsymbol{c}$ axis) with the equivalence relation $\hat{\boldsymbol{L}} \equiv -\hat{\boldsymbol{l}}$, valid on the projected subspace of this triplet of states. The spin-orbit and trigonal distortion terms can then be treated as a perturbation on this ground state manifold.

The spin-orbit coupling operator $\hat{\mathcal{H}}_{\text{SO}} = -\lambda\hat{\boldsymbol{L}}\cdot\hat{\boldsymbol{S}}$ can be rewritten in terms of the effective orbital angular momentum operator $\hat{\mathcal{H}}_{\text{SO}} = \lambda\hat{\boldsymbol{l}}\cdot\hat{\boldsymbol{S}}$. By itself, this couples the spin and orbital parts of the angular momentum into a total effective angular momentum J_{eff}, with values $J_{\text{eff}} = 1, 2, 3$.

The trigonal distortion operator can be written in terms of the effective orbital angular momentum operator as $\hat{\mathcal{H}}_{\text{trig}} = \delta\left(\hat{l}_z^2 - \frac{2}{3}\right) = \frac{1}{3}\delta O_2^0$. Acting on the 15-fold degenerate octahedral crystal field $\hat{l} = 1, S = 2$ ground state manifold, this splits the state into an a 10-fold degenerate $\hat{l}_z = \pm 1, S = 2$ manifold and a 5-fold degenerate $l_z = 0, S = 2$ manifold. Acting on the J_{eff} states from spin-orbit coupling, it mixes the states with same J_{eff}^z, as seen in the level splitting diagram in Figure 7.17. The result is a ground state doublet with $J_{\text{eff}}^z = \pm 1$, and the next excited level a $J_{\text{eff}}^z = 0$ singlet. These levels are determined by diagonalising the perturbation Hamiltonian, treating the spin-orbit coupling and trigonal distortion together. The effects of each of these terms on the energy levels can be seen in Figure 7.17.

In the presence of this $\delta < 0$ trigonal distortion, as appears to be the experimental case [4], the ground state is the easy-axis situation $J_{\text{eff}}^z = \pm 1$, with next excited $J_{\text{eff}}^z = 0$ singlet at $3\,\text{meV}$. By applying a small field to split the ground state doublet, the moment along the z axis can be determined as $\mu_z = 4.43\mu_B$. In `qafm`, the classical spin is taken as $J_{\text{eff}} = 1$ with a single-ion anisotropy term $A = -D(J_{\text{eff}}^z)^2$, where $D > 0$ because the system is easy-axis. The energy D can be read off as as the gap between the ground state doublet and excited singlet as $D \approx 3\,\text{meV}$, if the values from [4] are used. This easy-axis situation is confirmed by the metamagnetic spin-flip transition seen at $8\,\text{T}$ for fields along

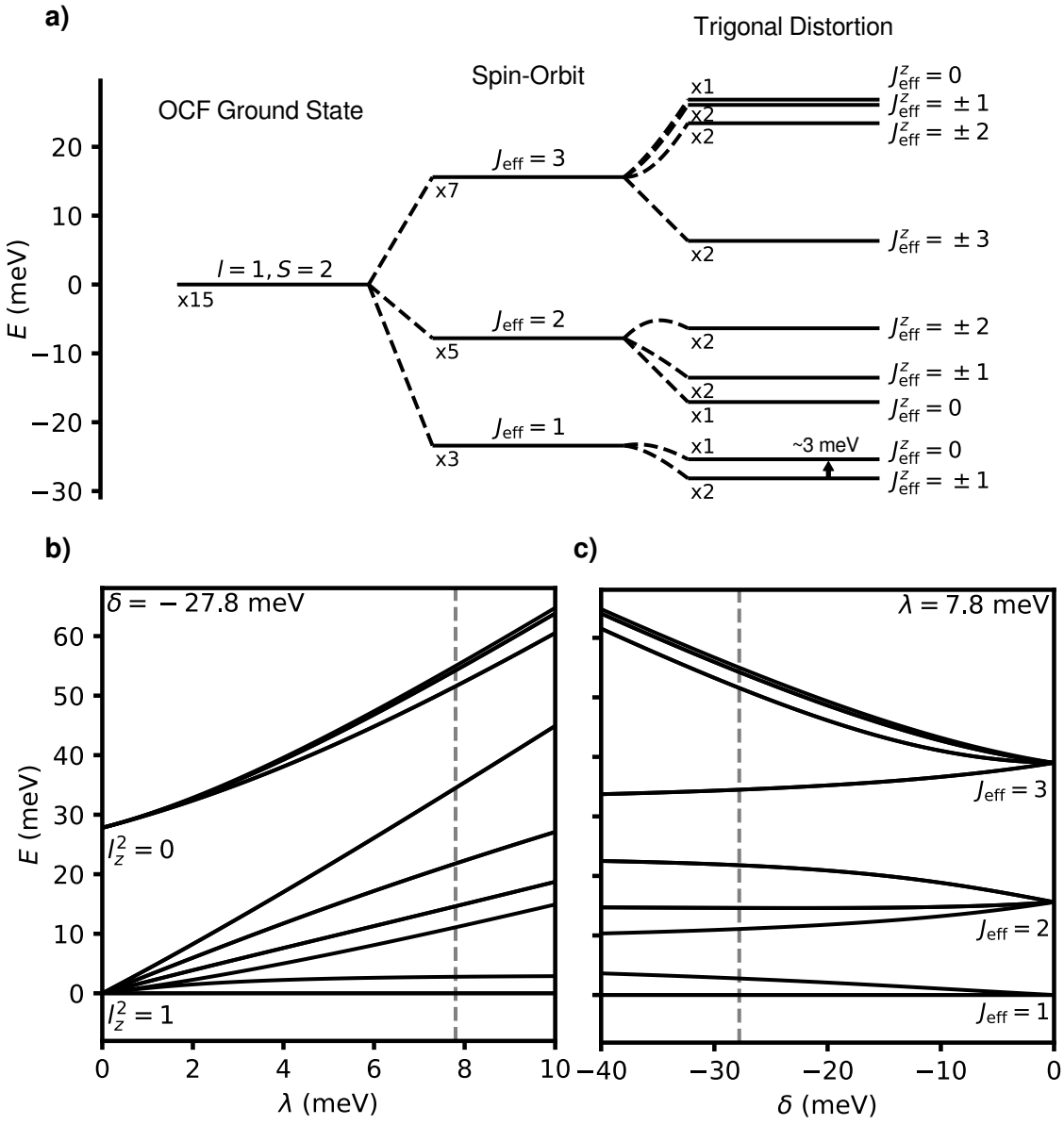


Figure 7.17: a) Schematic diagram showing the level splitting of isolated Fe^{2+}ion octahedral crystal field ground state energy levels as a function of trigonal distortion and spin-orbit coupling. Labels on states show good quantum numbers for those levels. **b, c)** show evolution of energy levels with spin-orbit coupling strength λ with fixed δ and against trigonal distortion strength δ at fixed λ respectively on the 15-fold degenerate manifold of $l = 1$, $S = 2$ states. Dashed vertical lines indicate the values closest to the experimental situation according to [4].

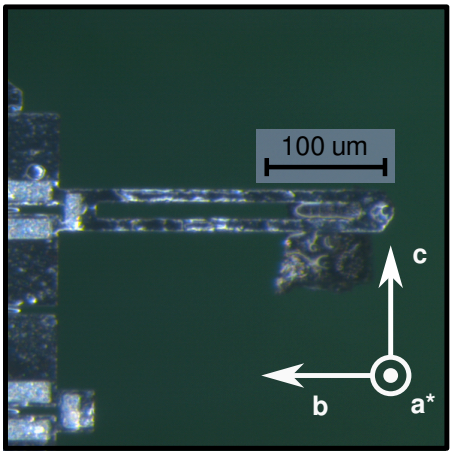


Figure 7.18: Photograph of $FeTiO_3$ single crystals mounted on piezoresistive cantilever for torque measurements. Overlaid symbols and arrows show crystallographic $\boldsymbol{a}, \boldsymbol{b}, \boldsymbol{c}$ axes.

the $\boldsymbol{c}$ axis. These transitions are only present for large $-D(J^z_{\text{eff}})^2$-type anisotropy, while XXZ easy-axis antiferromagnetism will always favour a spin-flop transition.

Strictly, the above single-ion anisotropy of a octahedral cubic environment with trigonal distortion assumes a $\bar{3}m$ point group for the Fe^{2+}ion. The full symmetry allowed anisotropy for the 3 point group is however [13, 16]

$$B^0_2O^0_2 + B^0_4O^0_4 + B^{-3}_4O^{-3}_4 + B^3_4O^3_4 \tag{7.30}$$

7.2.2 Torque magnetometry studies of $FeTiO_3$

Piezoresistive cantilever torque magnetometry was performed on single crystals of $FeTiO_3$ in order to explore the anisotropy of the material. A photo of the sample reported throughout this section can be seen in Figure 7.18.

Figure 7.19 shows how the torque profiles in the $\boldsymbol{a}^*\boldsymbol{c}$ plane change with temperature through the magnetic phase transition. At all temperatures the profile is a good fit to

$$\tau(\theta) = \tau_2 \sin 2(\theta - \theta_0) \tag{7.31}$$

where θ is measured from the $\boldsymbol{c}$ axis towards the a^* axis and θ_0 is interpreted as an offset between the nominal $\boldsymbol{c}$ orientation and the true orientation. In the high-temperature paramagnetic region, the gradient through the $\boldsymbol{c}$ axis is negative, indicating that it is a

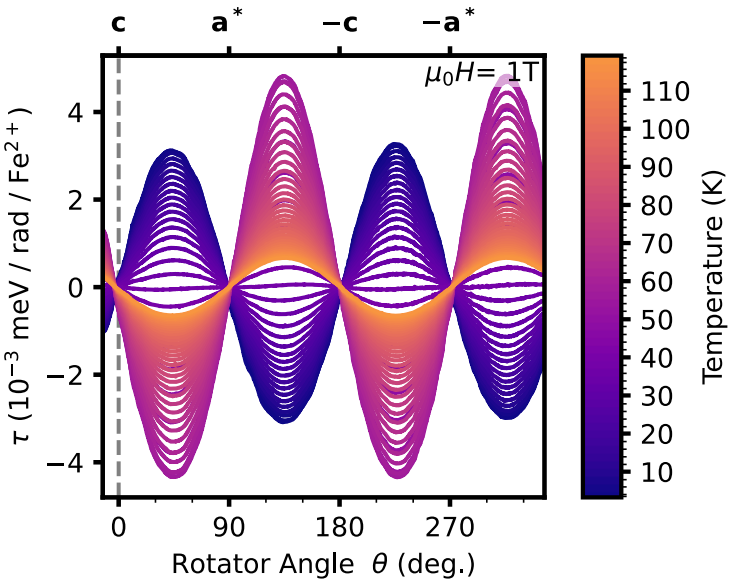


Figure 7.19: Waterfall plot showing magnetic torque vs rotator angle in the $\boldsymbol{a}^*\boldsymbol{c}$ plane for temperatures between 2 K and 120 K and an applied magnetic field of 1 T. Top labels indicate angles where the magnetic field direction is aligned parallel to a crystallographic axis. Dashed line indicates $\boldsymbol{H} \parallel \boldsymbol{c}$. Traces are raw torque piezocantilever voltages converted to absolute units as described in the text.

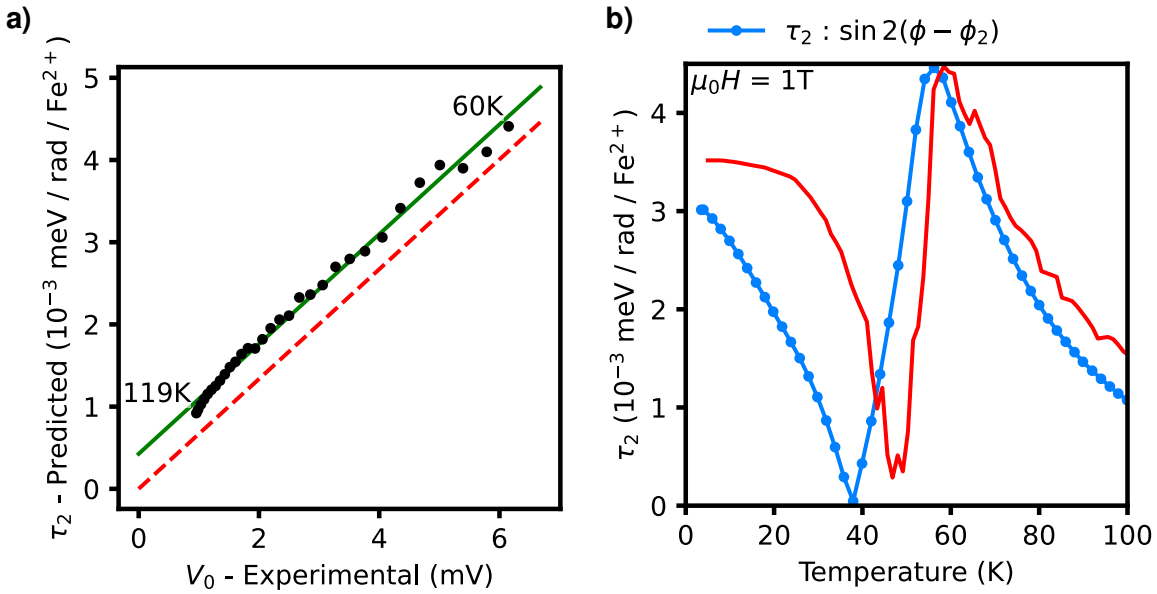


Figure 7.20: **a)** Plot showing fitted torque amplitudes in $\boldsymbol{a}^*\boldsymbol{c}$ plane against predicted torque amplitudes from published susceptibility data [12] with linear fit (green line), and linear fit with zero intercept (red dashed line). **b)** Plot showing evolution of (cyan points) fitted torque amplitudes, (red curve) predicted torque amplitudes from published susceptibility data [12] for rotations in $\boldsymbol{a}^*\boldsymbol{c}$ plane against temperature.

stable equilibrium. This is expected as the susceptibility measured along the $\boldsymbol{c}$ axis $\chi_{\parallel}$ is larger than the in-plane susceptibility $\chi_{\perp}$.

Figure 7.20 shows the plot of fitted piezocantilever voltage amplitude $V_2(T)$ against predicted torque $\frac{1}{2}B^2\left(\chi_{\parallel}(T)-\chi_{\perp}(T)\right)$ for temperature range $60\,\mathrm{K} < T < 110\,\mathrm{K}$, the green line shows a linear fit to these data. The dashed red line shows a line with the same gradient and zero intercept, this fit was used to calibrate the absolute value of the torque as described in the previous section. At the phase transition the difference $\chi_{\parallel}-\chi_{\perp}$ is maximised, which is seen as a peak in the amplitude in the torque at $58\,\mathrm{K}$ in Figure 7.20**b)**. As the temperature cools further below the transition the torque amplitude drops as the out-of-plane susceptibility is suppressed by the antiferromagnetic order. At approximately $39\,\mathrm{K}$ the torque in minimised at $\chi_{\perp} \approx \chi_{\parallel}$. This temperature is lower than the $46\,\mathrm{K}$ expected from the susceptibility data. The most likely cause of this disagreement is local sample heating; as domain reorientation while the sample is rotated in field could cause the sample to be heated above the bath temperature. At lower temperatures than this the stability of the axes changes, such that the system in unstable for fields close to $\boldsymbol{c}$, and stable for fields in the plane. This is because the out-of-plane susceptibility $\chi_{\parallel}$ has been suppressed below the in-plane value $\chi_{\perp}$. The evolution of this torque in the paramagnetic phase $T > T_N$ was used to calibrate the magnitude of the torque for these crystals by comparing the measured torque to the predicted value from $\frac{1}{2}B^2(\chi_{\perp}-\chi_{\parallel})\sin 2\theta$ as was described in the previous section, all further results in this chapter are on the same lever sample pair, although the results were verified on a second sample.

In order to explore the existence of in-plane anisotropy in $FeTiO_3$, angular dependence of torque was measured for rotations in the $\boldsymbol{ab}$ plane. Figure 7.21 shows how the magnetic torque measured in the $\boldsymbol{ab}$ plane varies with applied magnetic field at $2\,\mathrm{K}$. A dashed vertical line indicates where field is parallel to the $\boldsymbol{a}^*$ direction. These show a very clear 6-fold torque signal such that the system is in a stable equilibrium for fields close to the $\boldsymbol{a}^*$ direction and an unstable equilibrium for fields close to $\boldsymbol{b}$. This suggests that the local energy environment for the spins in minimised for spins parallel to $\boldsymbol{a}^*$, that is parallel to the bond directions. This matches the case for $CoTiO_3$. Unlike in the case for $CoTiO_3$, this six-fold torque signal shows no change in the phase of the signal as field

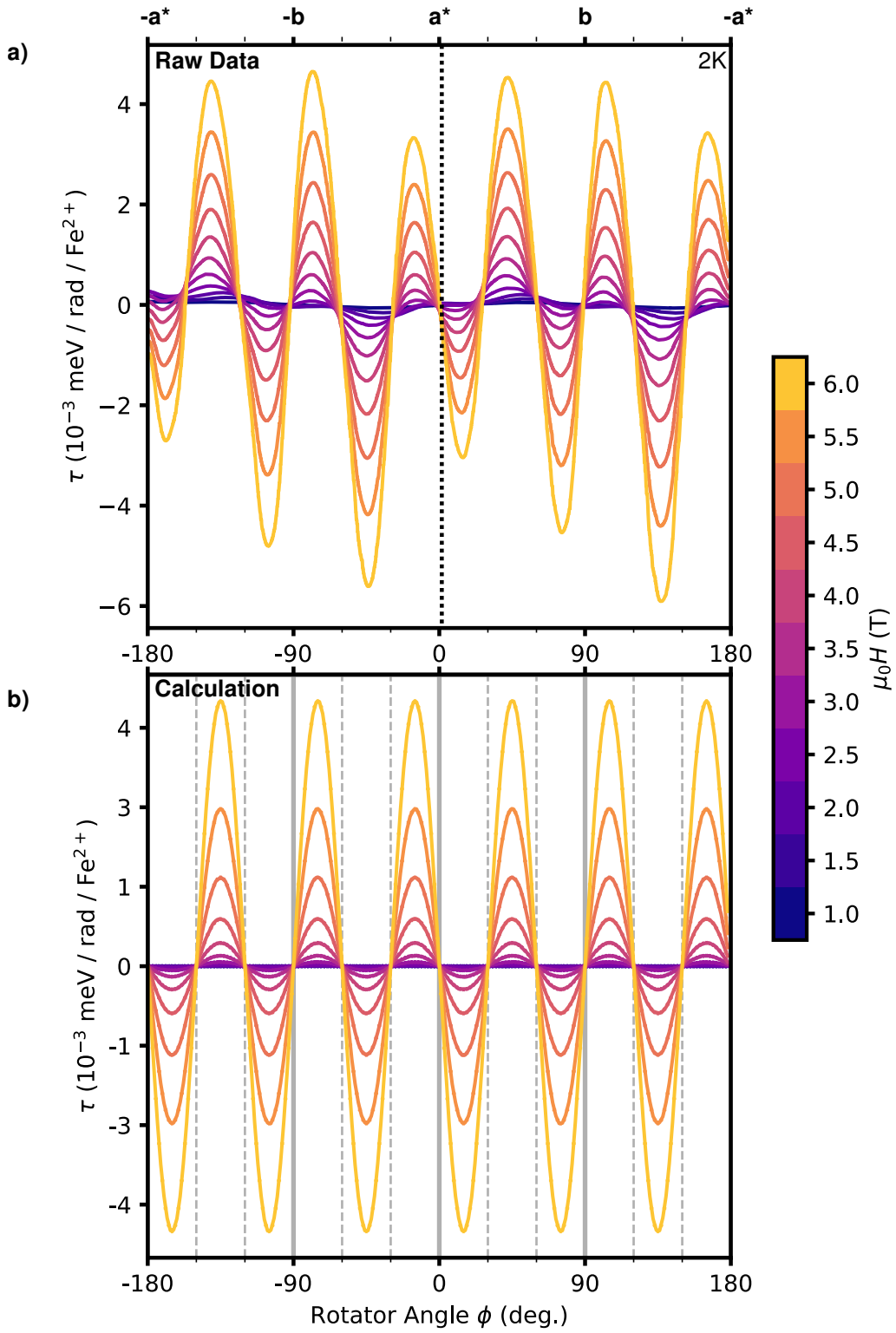


Figure 7.21: a) Waterfall plot showing magnetic torque vs rotator angle ϕ for applied magnetic fields between 1 T and 6 T in the $\boldsymbol{ab}$ plane of $FeTiO_3$, measured at the experimental base temperature of 2 K. Top labels indicate angles where the magnetic field direction is aligned parallel to a crystallographic axis. Traces are raw torque piezocantilever voltages converted to absolute units as described in the text. **b)** Waterfall plot showing calculated magnetic torque vs rotator angle ϕ for applied magnetic fields between 1 T and 16 T in the $\boldsymbol{ab}$ plane, with ϕ measured from the $\boldsymbol{a}^*$ axis. Dashed vertical line corresponds to field along the $\boldsymbol{a}^*$ axis. Calculation details are in the text.

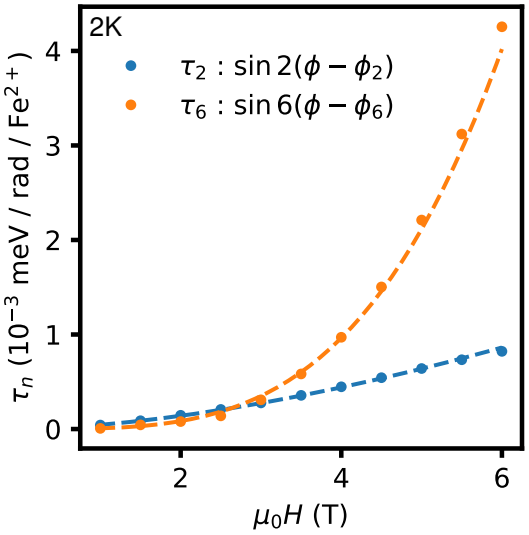


Figure 7.22: Field dependence of fitted torque amplitudes from Eqn. 7.22a in the range $1\,\mathrm{T} \leq \mu_0 H \leq 6\,\mathrm{T}$. Dashed lines indicate fit to the form $(\mu_0 H)^{\alpha_n}$, with $\alpha_2 \approx 1.8$ and $\alpha_6 \approx 3.5$.

increases, and the magnitude increases monotonically. This is because in $FeTiO_3$, the spins are canting from the $\boldsymbol{c}$ axis, so their projection in the $\boldsymbol{ab}$ plane is directly towards the magnetic field, it is not dependent on field magnitude.

The largest field I was able to test with this setup was $6\,\mathrm{T}$, this is because the growing torques became a danger of breaking the magnetometer levers. At this field, the amplitude of the 6-fold component of the torque is $\tau_6 = 4.2 \times 10^{-3}\mathrm{meV rad}^{-1}/\mathrm{Fe}^{2+}$, approximately 5 times larger than the largest value measured in $CoTiO_3$. Although the moments do not lie in-plane, so the full scale of the anisotropy is not exerting a torque on the sample, the observed size of the τ_6 component of the torque allows a lower bound to be placed that $|\Lambda_0| > 7 \times 10^{-4}\mathrm{meV}/\mathrm{Fe}^{2+}$. However, it should be noted that the value for the energy scale in $CoTiO_3$ was determined at $16\,\mathrm{T}$, when the magnetisation was nearly saturated. At $6\,\mathrm{T}$, far below the saturation field of the material, only a small part of the anisotropy energy will be seen, suggesting the six-fold clock anisotropy energy in $FeTiO_3$ is much larger than in $CoTiO_3$.

The field scaling of this torque parameter was determined by plotting the amplitude of the six-fold torque τ_6 against the magnetic field, as can be seen in Figure 7.22. These amplitudes were fitted to the form

$$\tau_n \sim (\mu_0 H)^{\alpha_n} \tag{7.32}$$

with the curves for the fitted parameters overlaid on the figure. The exponent for the six-fold anisotropy $\alpha_6 \approx 3.5$. If the origin of the anisotropy was single-ion, then it should have the form from Eqn. (7.15)

$$E_A = \Lambda_0 \sin^6\theta \cos 6(\phi - \phi_6) \tag{7.33a}$$

$$= \Lambda_0 \left(\frac{M_{xy}}{M_{sat}}\right)^6 \cos 6(\phi - \phi_6) \tag{7.33b}$$

so a value of $\alpha_6 = 6$ would be expected as $M_{xy} = \chi_\perp \mu_0 H_{xy}$. This is larger than the value found experimentally, providing further support that the anisotropy does not originate in single-ion effects.

Figure 7.21**b)** shows the results of a calculation, performed as in the case of $CoTiO_3$, with exchange parameters taken from [4]. To this I added an anisotropy energy of the form in Equation 7.14, with $\Lambda < 0, \phi_6 = 0°$, such that individual spins minimise their energy by pointing along nearest-neighbour bond directions. These show qualitative agreement with the data, with a six-fold contribution to the torque of the same sign and phase as is seen in the data. The calculations results also predict a torque that increases with the magnetic field faster than seen experimentally with exponent $\alpha_n = 6$, larger than the fitted value of 3.5.

Figure 7.23 shows the temperature evolution of the magnetic torque measured in the $\boldsymbol{ab}$ plane measured at $6\,\mathrm{T}$, between $100\,\mathrm{K}$ and $2\,\mathrm{K}$. In the high temperature regime, a 2-fold torque signal can be seen. This 2-fold signal is symmetry disallowed for the $\boldsymbol{ab}$ plane because of the rhombohedral symmetry of the crystal. For this reason I attribute this signal primarily to a small misalignment, such that the rotation plane is skewed from the $\boldsymbol{ab}$ plane. Fits to the 2-fold component of the signal seen in Figure 7.23**b)** show a peak, associated with the onset of magnetic order. This can be understood as a projection of this much larger easy-axis anisotropy into the measurement plane. As the temperature cools below the transition, a large 6-fold component of torque can be seen, increasing monotonically as temperature decreases. Figure 7.23**b)** shows the evolution with temperature of the fitted components of the torque signal. As can be seen, the six-fold component can be detected only below the magnetic phase transition.

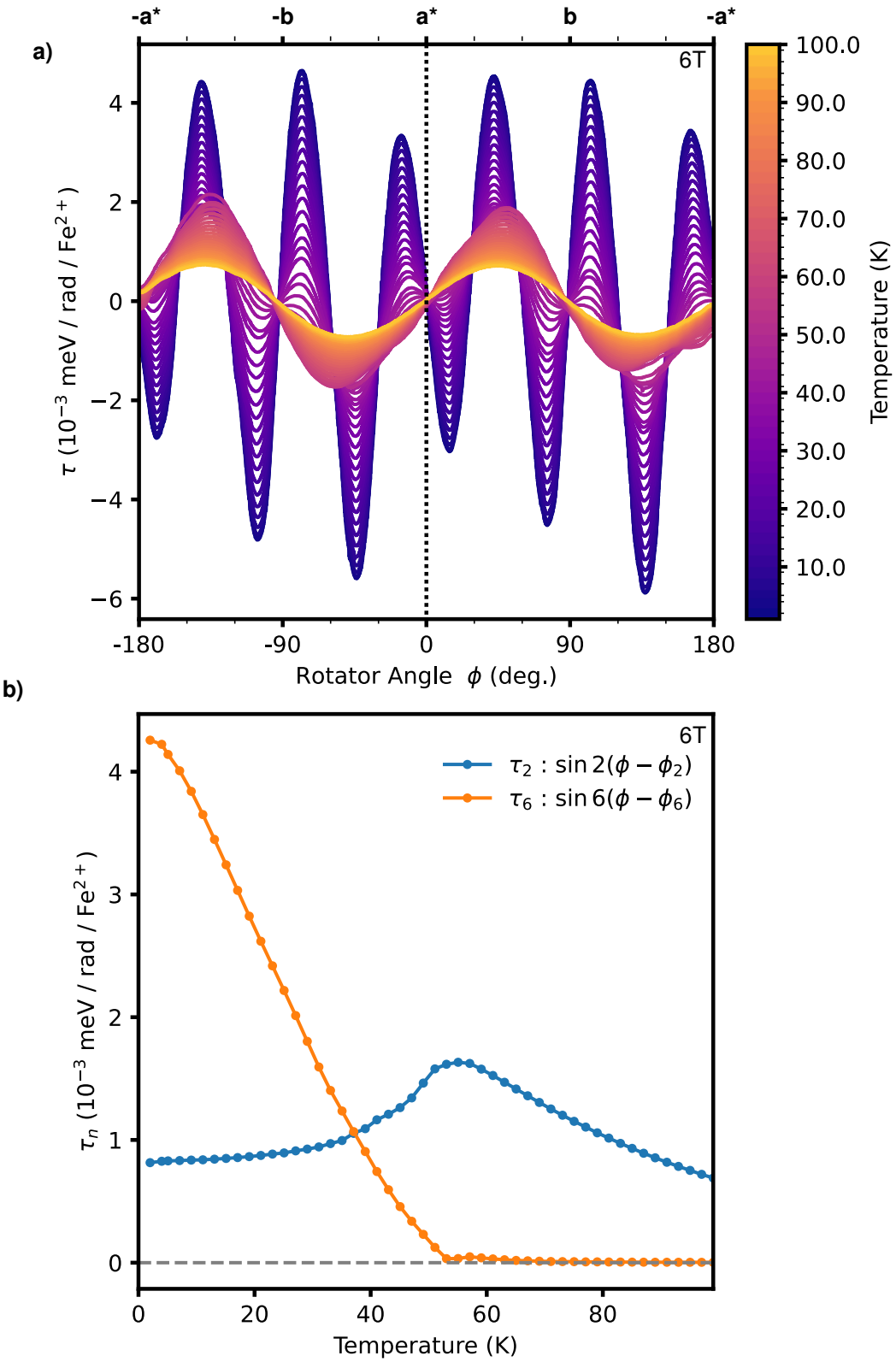


Figure 7.23: a) Angular and temperature dependence of magnetic torque the ab plane between 2 K and 120 K with an applied magnetic field of 6 T. Top labels indicate angles where the magnetic field direction is aligned parallel to a crystallographic axis. Traces are raw torque piezocantilever voltages converted to absolute units as described in the text. **b)** Evolution of fitted torque amplitudes from Eqn. 7.22a against temperature in the range $2\,\mathrm{K} \leq T \leq 100\,\mathrm{K}$.

The lowest order single-ion anisotropy term which could induce a $\cos 6\phi$ energy profile is the $O_6^{\pm 6}$ Stevens operator. The d-orbital valence electrons of Fe^{2+}do not permit any high order $O_n^q, n > 4$ terms in the CEF Hamiltonian. Because of this, the 6-fold torque profile seen at low temperatures in $FeTiO_3$ cannot have a single-ion anisotropy origin. This is further evidenced by the temperature dependence of the 6-fold component of the torque, which has onset alongside magnetic order, as can be seen in Figure 7.23. From this evidence I suggest that the anisotropy seen must originate from magnetic interactions and set in alongside the onset of the magnetic order, through quantum fluctuations inducing an angular dependence of the anisotropy energy or a spin-orbital exchange mechanism as proposed in $CoTiO_3$ [3].

7.3 Conclusions

Despite their differences in spin orientations, both of the two systems discussed in this chapter, easy plane $CoTiO_3$ and easy axis $FeTiO_3$ show clear evidence of a 6-fold modulation in energy in the $\boldsymbol{ab}$ plane visible in the low-temperature piezocantilever torque magnetometry measurements. In both cases, the six-fold torque is only detected in the ordered phase. I have been able to rule out the most straightforward origins of the energy profile; single ion anisotropy of the required form is not allowed, and exchange anisotropy up to bilinear terms will not cause such a modulation in energy at the mean field limit. What remains as explanations are more exotic phenomena such as quantum fluctuations lifting the degeneracy of spin orientations in the $\boldsymbol{ab}$ plane, or spin-orbital exchange. The data presented in this chapter should provide some additional clues for future theoretical work which seeks to understand the origin of the magnetic anisotropy in these materials, which may in turn improve our understanding of the origins of anisotropy in magnetic systems more broadly.

References

[1] K. Kidoh et al. “Electron density distribution in an ilmenite-type crystal of cobalt (II) titanium (IV) trioxide”. In: *Acta Crystallographica Section B: Structural Science* 40.2 (1984), pp. 92–96.

[2] R. Newnham, J. Fang, and R. Santoro. “Crystal structure and magnetic properties of $CoTiO_3$”. In: *Acta Crystallographica* 17.3 (1964), pp. 240–242.

[3] M. Elliot et al. “Order-by-disorder from bond-dependent exchange and intensity signature of nodal quasiparticles in a honeycomb cobaltate”. In: *Nature Communications* 12.1 (2021), p. 3936.

[4] M. Elliot. “Inelastic neutron and resonant elastic x-ray scattering studies of honeycomb quantum magnets”. PhD thesis. University of Oxford, 2022.

[5] A. Abragam and B. Bleaney. *Electron paramagnetic resonance of transition ions*. Clarendon Press, 1970.

[6] M. Hoffmann et al. “Magnetic phase diagram, magnetoelastic coupling, and Grüneisen scaling in $CoTiO_3$”. In: *Physical Review B* 104.1 (2021), p. 014429.

[7] J. J. Stickler et al. “Magnetic resonance and susceptibility of several ilmenite powders”. In: *Physical Review* 164.2 (1967), p. 765.

[8] A. Balbashov et al. “Electric and magnetic properties of titanium-cobalt-oxide single crystals produced by floating zone melting with light heating”. In: *Low Temperature Physics* 43.8 (2017), pp. 965–970.

[9] B. Yuan et al. “Dirac magnons in a honeycomb lattice quantum XY magnet CoTiO 3”. In: *Physical Review X* 10.1 (2020), p. 011062.

[10] J. Goldstone. “Field theories with «Superconductor» solutions”. In: *Il Nuovo Cimento (1955-1965)* 19 (1961), pp. 154–164.

[11] H. Watanabe, H. Yamauchi, and H. Takei. “Magnetic anisotropies in $MTiO_3$ (M= Co, Ni)”. In: *Journal of Magnetism and Magnetic Materials* 15 (1980), pp. 549–550.

[12] H. Kato et al. “Metamagnetic phase transitions in $FeTiO_3$”. In: *Journal of the Physical Society of Japan* 51.6 (1982), pp. 1769–1777.

[13] H. Kato et al. “First-order magnetization process in oblique-easy-axis antiferromagnet $FeTiO_3$”. In: *Journal of Magnetism and Magnetic Materials* 90 (1990), pp. 67–68.

[14] H. Kato et al. “On the obliqueness of the easy axis in collinear antiferromagnetic $FeTiO_3$”. In: *Solid State Communications* 45.8 (1983), pp. 669–672.

[15] Y. Yamaguchi et al. “Re-examination of the magnetic structure of $FeTiO_3$”. In: *Solid State Communications* 59.12 (1986), pp. 865–868.

[16] D. J. Newman and B. Ng. *Crystal field handbook*. Vol. 43. Cambridge University Press Cambridge, 2000.

8

Concluding Remarks

This thesis presented magnetic characterisation results on four closely related materials. The first two discussed were the honeycomb and hyperhoneycomb polymorphs of Na_2PrO_3 . These have tricoordinated lattices of $j_{\text{eff}} = 1/2$, $4f^1$ moments, which have attracted recent theoretical interest as candidate platforms to host Kitaev physics. In both cases, this is the first time that single-crystal samples of the material have been magnetically characterised.

The second two materials discussed were the isostructural honeycomb transition metal titanites $CoTiO_3$ and $FeTiO_3$, investigating the recent proposal that easy-plane antiferromagnet $CoTiO_3$ displays in-plane anisotropy driven by bond-dependent exchange interactions and a quantum zero-point fluctuations mechanism. Using single crystal torque magnetometry, I directly observe a six-fold in-plane anisotropy in the ordered phase, with an energy scale comparable with the value predicted from inelastic neutron scattering. I contrast this with the easy-axis antiferromagnet $FeTiO_3$, where I observe the same effect in the ordered phase. In both cases, single-ion anisotropy can be rejected as the origin of the effect, leaving quantum zero-point fluctuations driven by bond-dependent exchange interactions as the most likely origin.

Honeycomb α-Na_2PrO_3 orders magnetically at $4.6\,\mathrm{K}$ into a canted antiferromagnetic structure, which has a clear fingerprint in the angular dependence of torque in three orthogonal crystal planes. I propose two minimal models which can stabilise this structure, one with XXZ Ising-like exchange interactions, and a second model with Heisenberg J and symmetric off-diagonal exchange Γ. In both cases, a symmetry-allowed unbalanced Dzyaloshinskii–Moriya interaction on the honeycomb bonds causes canting

of the moments in the ac plane. Using torque magnetometry, I directly observe a spin-flop transition at high magnetic field, consistent with both magnetic models, and find a peculiar non-monotonic field dependence of crossover between spin-flop and paramagnetic phases.

Hyperhoneycomb β-Na_2PrO_3 orders at $5.2\,\mathrm{K}$ into a much more complex four sublattice non-collinear antiferromagnetic structure. I report temperature dependence of AC calorimetry and torque magnetometry consistent with a sharp transition to the magnetic structure observed in powder neutron diffraction. I explore a proposed minimal model which stabilises this structure consisting of Heisenberg J and symmetric off-diagonal exchange Γ on nearest-neighbour bonds. I show that this model predicts a spin-flop transition with a particular field orientation and use pulsed-field torque magnetometry to observe this spin-flop transition directly in β-Na_2PrO_3 single crystals.

Between the two proposed minimal models for α-Na_2PrO_3 , the model with XXZ interactions is arguably the simplest. However, given the evidence supporting a $J\Gamma\Gamma'$ model in the polymorph β-Na_2PrO_3 , and the shared structural motifs between the two materials, it is worth considering if both materials may be described by very similar models of bond-dependent exchange interactions. Additionally, both materials were theoretically predicted to host strong bond-dependent Kitaev interactions, and in neither case is clear evidence of this seen. Understanding the origin of these interactions will be important to understanding the physics of cooperative magnetism in $4f$ rare-earths.

To date, a huge amount of research effort has gone into investigating transition metal compounds as candidates for strong bond-dependent exchange in the search for experimental realisation of a Kitaev quantum spin liquid. This has been very successful in finding exotic magnetic phases of various types, however no conclusive evidence has been found for a true Kitaev-QSL. The results in this thesis show clear experimental evidence that magnetic rare-earths can also host strong bond-dependent exchange interactions, and provides further support that these may be fertile ground in the search for exotic magnetic phases driven by bond-dependent interactions.

Appendices

A

Appendix - Magnetic order and high-field magnetic phase transitions in hyper-honeycomb β-Na_2PrO_3

A.1 Character tables

This appendix presents the irreducible representations, character tables, and $\boldsymbol{q} = 0$ magnetic basis vectors for the hyperhoneycomb Pr^{4+}lattice in β-Na_2PrO_3 for magnetic field applied parallel and perpendicular to the orthorhombic crystal axes $\boldsymbol{a}, \boldsymbol{b}, \boldsymbol{c}$. These are used in the discussion of the calculated magnetic phase diagrams in Section **??**, especially in regards to Figure **??**. In all tables, a primed symmetry operation corresponds to the unprimed symmetry operation followed by time-reversal. For example $2'_y$ denotes a 2-fold rotation around y followed by time-reversal. All coordinated are in orthorhombic setting with origin choice at $\bar{1}$.

Table A.1: Irreducible representations (irreps), character table, and magnetic basis vectors for space group $Fddd$ with applied magnetic field parallel to crystallographic $\boldsymbol{a}$ axis. In character table '+' indicates $\chi = 1$, '-' indicates $\chi = -1$.

$(\boldsymbol{B} \parallel \boldsymbol{a})$	E	2_x	$\bar{1}$	d_x	$2'_y$	$2'_z$	d'_y	d'_z	Basis Vectors
$\Gamma_1^+(\boldsymbol{B} \parallel \boldsymbol{a})$	+	+	+	+	+	+	+	+	F_x, G_y
$\Gamma_2^+(\boldsymbol{B} \parallel \boldsymbol{a})$	+	-	+	-	-	+	-	+	F_y, G_x
$\Gamma_3^+(\boldsymbol{B} \parallel \boldsymbol{a})$	+	+	+	+	-	-	-	-	G_z
$\Gamma_4^+(\boldsymbol{B} \parallel \boldsymbol{a})$	+	-	+	-	+	-	+	-	F_z
$\Gamma_1^-(\boldsymbol{B} \parallel \boldsymbol{a})$	+	+	-	-	+	+	-	-	C_x, A_y
$\Gamma_2^-(\boldsymbol{B} \parallel \boldsymbol{a})$	+	-	-	+	-	+	+	-	C_y, A_x
$\Gamma_3^-(\boldsymbol{B} \parallel \boldsymbol{a})$	+	+	-	-	-	-	+	+	A_z
$\Gamma_4^-(\boldsymbol{B} \parallel \boldsymbol{a})$	+	-	-	+	+	-	-	+	C_z

Table A.2: Irreducible representations (irreps), character table, and magnetic basis vectors for space group $Fddd$ with applied magnetic field parallel to crystallographic $\boldsymbol{b}$ axis. In character table '+' indicates $\chi = 1$, '-' indicates $\chi = -1$.

$(\boldsymbol{B} \parallel \boldsymbol{b})$	E	2_y	$\bar{1}$	d_y	$2'_z$	$2'_x$	d'_z	d'_x	Basis Vectors
$\Gamma_1^+(\boldsymbol{B} \parallel \boldsymbol{b})$	+	+	+	+	+	+	+	+	F_y, G_x
$\Gamma_2^+(\boldsymbol{B} \parallel \boldsymbol{b})$	+	-	+	-	-	+	-	+	F_z
$\Gamma_3^+(\boldsymbol{B} \parallel \boldsymbol{b})$	+	+	+	+	-	-	-	-	G_z
$\Gamma_4^+(\boldsymbol{B} \parallel \boldsymbol{b})$	+	-	+	-	+	-	+	-	F_x, G_y
$\Gamma_1^-(\boldsymbol{B} \parallel \boldsymbol{b})$	+	+	-	-	+	+	-	-	C_y, A_x
$\Gamma_2^-(\boldsymbol{B} \parallel \boldsymbol{b})$	+	-	-	+	-	+	+	-	C_z
$\Gamma_3^-(\boldsymbol{B} \parallel \boldsymbol{b})$	+	+	-	-	-	-	+	+	A_z
$\Gamma_4^-(\boldsymbol{B} \parallel \boldsymbol{b})$	+	-	-	+	+	-	-	+	C_x, A_y

Table A.3: Irreducible representations (irreps), character table, and magnetic basis vectors for space group $Fddd$ with applied magnetic field parallel to crystallographic $\boldsymbol{c}$ axis. In character table '+' indicates $\chi = 1$, '-' indicates $\chi = -1$.

$(\boldsymbol{B} \parallel \boldsymbol{c})$	E	2_z	$\bar{1}$	d_z	$2'_x$	$2'_y$	d'_x	d'_y	Basis Vectors
$\Gamma_1^+(\boldsymbol{B} \parallel \boldsymbol{c})$	+	+	+	+	+	+	+	+	F_z
$\Gamma_2^+(\boldsymbol{B} \parallel \boldsymbol{c})$	+	-	+	-	-	+	-	+	F_x, G_y
$\Gamma_3^+(\boldsymbol{B} \parallel \boldsymbol{c})$	+	+	+	+	-	-	-	-	G_z
$\Gamma_4^+(\boldsymbol{B} \parallel \boldsymbol{c})$	+	-	+	-	+	-	+	-	F_y, G_x
$\Gamma_1^-(\boldsymbol{B} \parallel \boldsymbol{c})$	+	+	-	-	+	+	-	-	C_z
$\Gamma_2^-(\boldsymbol{B} \parallel \boldsymbol{c})$	+	-	-	+	-	+	+	-	C_x, A_y
$\Gamma_3^-(\boldsymbol{B} \parallel \boldsymbol{c})$	+	+	-	-	-	-	+	+	A_z
$\Gamma_4^-(\boldsymbol{B} \parallel \boldsymbol{c})$	+	-	-	+	+	-	-	+	C_y, A_x

Table A.4: Irreducible representations (irreps), character table, and magnetic basis vectors for space group $Fddd$ with applied magnetic field perpendicular to crystallographic axis $\boldsymbol{n} \in \{\boldsymbol{a}, \boldsymbol{b}, \boldsymbol{c}\}$. In character table '+' indicates $\chi = 1$, '-' indicates $\chi = -1$. Also present in text as Table **??**.

	E	$\bar{1}$	$2'_{\boldsymbol{n}}$	$d'_{\boldsymbol{n}}$	$\boldsymbol{n} = \boldsymbol{c}$	$\boldsymbol{n} = \boldsymbol{b}$	$\boldsymbol{n} = \boldsymbol{a}$
$\Gamma_1^+(\boldsymbol{B} \perp \boldsymbol{n})$	+	+	+	+	G_x, G_y, F_x, F_y	F_x, F_z, G_y	G_x, F_y, F_z
$\Gamma_2^+(\boldsymbol{B} \perp \boldsymbol{n})$	+	+	-	-	G_z, F_z	G_x, G_z, F_y	F_x, G_y, G_z
$\Gamma_1^-(\boldsymbol{B} \perp \boldsymbol{n})$	+	-	+	-	A_x, A_y, C_x, C_y	C_x, C_z, A_y	A_x, C_y, C_z
$\Gamma_2^-(\boldsymbol{B} \perp \boldsymbol{n})$	+	-	-	+	A_z, C_z	A_x, A_z, C_y	A_y, A_z, C_x

Table A.5: Irreducible representations (irreps), character table, and magnetic basis vectors for space group $Fddd$ with applied magnetic field in general orientation. In character table '+' indicates $\chi = 1$, '-' indicates $\chi = -1$.

	E	$\bar{1}$	Basis Vectors
$\Gamma^+(\boldsymbol{B})$	+	+	$\boldsymbol{G}, \boldsymbol{F}$
$\Gamma^-(\boldsymbol{B})$	+	-	$\boldsymbol{C}, \boldsymbol{A}$